THERMO-MECHANICAL FATIGUE CRACK GROWTH OF A POLYCRYSTALLINE SUPERALLOY

A Thesis
Presented to
The Academic Faculty

By

Benjamin Scott Adair

In Partial Fulfillment
Of the Requirements for the Degree
Master of Science in the
George W. Woodruff School of Mechanical Engineering

Georgia Institute of Technology

December, 2010

THERMO-MECHANICAL FATIGUE CRACK GROWTH OF A POLYCRYSTALLINE SUPERALLOY

Approved by:

Dr. W. Steven Johnson, Advisor
School of Materials Science and Engineering, George W. Woodruff School of Mechanical Engineering
Georgia Institute of Technology

Dr. Stephen D. Antolovich
School of Materials Science and Engineering, George W. Woodruff School of Mechanical Engineering
Georgia Institute of Technology

Dr. Richard W. Neu
George W. Woodruff School of Mechanical Engineering, School of Materials Science and Engineering
Georgia Institute of Technology

Date Approved: 10 November 2010

ACKNOWLEDGMENTS

I owe much thanks to Dr. Steve Johnson and Dr. Stephen Antolovich for their extensive guidance throughout this project. I have learned more than I ever imagined from their continual support and mentoring. I would also like to thank Dr. Richard Neu for being on my committee, reviewing my work and providing his technical insight.

Without the financial support of Pratt & Whitney this research would have never been possible, for that I am greatly appreciative. I am also extremely grateful for the technical oversight provided by Dr. Alexander Staroselsky.

The support provided by fellow graduate students, Robert Amaro, Vince Barker, Mike Hirsch and Brian Woodworth was immeasurable and much appreciated. I am also much indebted to Rick Brown for sharing his testing wisdom accrued over many years in the Mechanical Properties Research Lab and also to Richard Schaffer of ECE micromachining for his help in laser etching the specimens. I would also like to express my sincere gratitude for my family and friends; they gave me the support I needed to leave a good paying career and return to graduate school.

TABLE OF CONTENTS

LIST OF TABLES

LIST OF FIGURES

LIST OF SYMBOLS AND ABBREVIATIONS

a	Crack Length
AES	Auger Electron Spectroscopy
APB	Anti-Phase Boundary
APBE	Anti-Phase Boundary Energy
ASTM	American Society for Testing and Materials
BFM	Boundary Force Method
C	Paris Equation Coefficient
CBO	Cycles between Overload
CT	Compact Tension
da/dN	Fatigue Crack Growth Rate (m per cycle)
Δa	Change in Crack Length
ΔK	Stress Intensity Range
DS	Directionally Solidified
E	Modulus of Elasticity
EDM	Electrical Discharge Machining
EDS	Energy-Dispersive X-ray Spectroscopy
EIFS	Equivalent Initial Flaw Size
ENSIP	Engine Structural Integrity Program
η	Efficiency
f(a/b)	Correction Factor
FCC	Face Centered Cubic
FCG	Fatigue Crack Growth
FCGR	Fatigue Crack Growth Rate
FCP	Fatigue Crack Propagation
FCPR	Fatigue Crack Propagation Rate
G	Energy Release Rate
γ	Gamma Phase Matrix of Superalloy
γ'	Strengthening Precipitate Phase

HIP	Hot Isostatic Pressing
K	Stress Intensity Factor
K_C	Fracture Toughness (Critical Stress Intensity Factor)
K_{IC}	Plane Strain Fracture Toughness
$K_{opening}$	Crack Opening Stress Intensity Factor
K_{max}	Maximum Stress Intensity Factor
K_I	Opening Stress Intensity Factor
K_{II}	In-Plane Shear Stress Intensity Factor
K_{III}	Out-of-Plane Shear Stress Intensity Factor
m	Paris Equation Exponent
n	Walker's Equation Exponent
N	Number of Cycles
NDI	Nondestructive Inspection
OAR	Oxygen Affected Region
OLR	Overload Ratio
π	Pi (3.1415)
P/M	Powder Metallurgy
PSCL	Predicted Safe Cycle Limit
R	Load Ratio
RFC	Retirement for Cause
SEM	Scanning Electron Microscopy
SENT	Single Edge Notch Tension
SIF	Stress Intensity Factor
σ	Remotely Applied Stress
S-N	Stress-Life
T	Temperature
TMF	Thermo-Mechanical Fatigue
UHV	Ultra-High Vacuum
XPS	X-ray Photoelectron Spectroscopy
XRD	X-ray Diffraction
<001>	Family of Primary Crystallographic Directions

[001]	A Primary Crystallographic Direction
{001}	Family of Crystallographic Planes

SUMMARY

A study was done to determine the temperature and load interaction effects on the fatigue crack growth rate (FCGR) of polycrystalline superalloy IN100. Temperature interaction testing was performed by cycling between 316°C and 649°C in blocks of 1, 10 and 100 cycles. Load interaction testing in the form of single overloads was performed at 316°C and 649°C. Constant amplitude, overload and changing temperature tests were performed at 20 and 0.33 Hz and in lab air conditions ranging from 22°C up to 649°C. After compiling a database of constant temperature, constant amplitude FCGR for IN100, fatigue crack growth predictions assuming no load or temperature interactions were made. Experimental fatigue crack propagation data was then compared and contrasted with these predictions. Through the aid of scanning electron microscopy the fracture mechanisms observed during interaction testing were compared with the mechanisms present during constant temperature, constant amplitude testing. One block alternating temperature interaction testing grew significantly faster than the non-interaction prediction, while ten block alternating temperature interaction testing also grew faster but not to the same extent. One hundred block alternating testing grew slower than non-interaction predictions. It was found that as the number of alternating temperature cycles increased, changes in the γ' morphology (and hence deformation mode) caused changes in the environmental interactions thus demonstrating the sensitivity of the environmental interaction on the details of the deformation mode. SEM fractography was used to show that at low alternating cycles, 316°C crack growth was accelerated due to crack tip embrittlement caused by 649°C cycling. At higher alternating cycles the 316°C cycling quickly grew through the embrittled crack tip but then grew slower than expected due to

the possible formation of Kear-Wilsdorf locks at 649°C. Overload interaction testing led to full crack retardation at 2.0x overloads for both 316°C and 649°C testing. 1.6x overloading at both temperatures led to retarded crack growth whereas 1.3x overloads at 649°C created accelerated crack growth and at 316°C the crack growth was retarded.

CHAPTER 1: INTRODUCTION

1.1: Motivation

Gas turbine engines are constantly being pushed to their operational limits in the pursuit of more thrust and better fuel economy. These operational limits are set by the advanced engineering materials used in the combustor and turbine areas of these engines. Due to their ability to maintain excellent mechanical properties at temperature nickel based superalloys are the material of choice for use in the hot section of gas turbine engines. Superalloys are a carefully developed composition that over time has gone from twelve or more elements to many less since the function of each is understood and tailored to the needs of the application. These superalloys come in polycrystalline, directionally solidified and single crystal forms. Turbine disk materials are commonly made with polycrystalline material, while the turbine blades that they hold are made out of single and directionally solidified materials that can see and withstand temperatures up to 1150°C and beyond. Disks see larger loads but are exposed to cooler working environments than the blades with temperatures usually being below 1000°C.

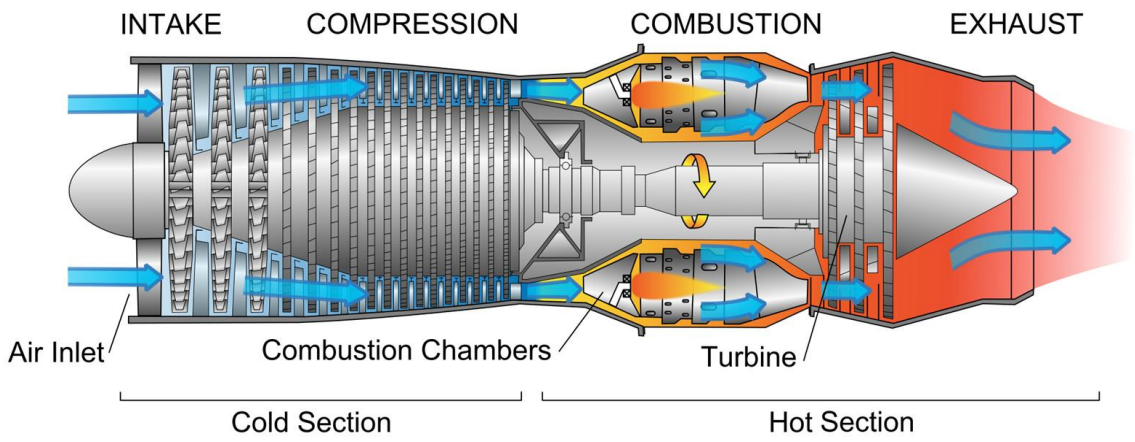

Figure 1.1: Schematic of a Basic Turbojet Gas Turbine Engine [1]

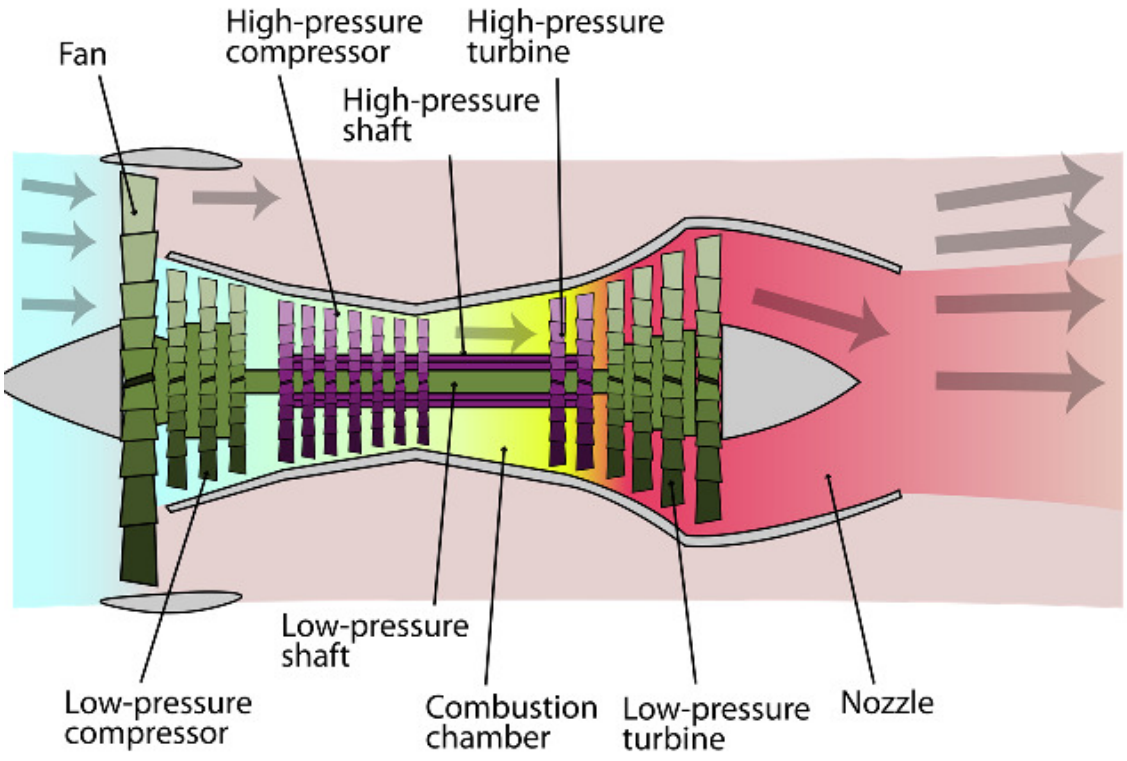

Figure 1.2: Schematic of a Basic Turbofan Gas Turbine Engine [1]

Two types of gas turbine engines can be seen in Figure 1.1 and Figure 1.2. The first is a schematic of a turbojet while the second is a schematic of a turbofan. In a gas turbine engine air first enters the compressor where pressure is increased before being mixed

with fuel and ignited in the combustor. This expanding gas is used to impart mechanical energy into a turbine which powers the compressor via a shaft. Thrust is created by the momentum difference between the incoming ambient air and the hot exhaust gas. Gas turbine engine efficiency calculated using the Carnot cycle is a function of unity subtracted by the input gas temperature over the combustor gas temperature as seen in Equation 1.1.

$$\eta = 1 - \frac{T_2}{T_1} \tag{1.1}$$

It is certainly not feasible to decrease the input gas temperature of airborne applications so in order to increase efficiency the combustor gas temperature has to be increased. This increase in temperature is made possible by the continued technological advances of superalloys. These advances are not only material in nature but also through better understanding of failure modes, underlying mechanisms and enhanced life prediction models.

A thorough understanding of the thermal mechanical fatigue crack growth behavior of hot section superalloys is crucial to being able to quell chunk liberation turbine engine concerns. This was reinforced by the failure of a General Electric CFM56 turbofan engine on a Boeing 737 during October of 2000, due to a chunk of turbine blade separating and causing damage downstream [2]. A more recent failure attributed to chunk liberation occurred on June 2, 2006 at Los Angeles International Airport. A GE engine on an American Airlines Boeing 767 had a failure of the high pressure turbine

stage 1 disk. It was shown that as a result of an intergranular fatigue crack during a high powered ground run of the engines a chunk of disk material was liberated causing catastrophic failure of the left engine seen in Figure 1.3 [3].

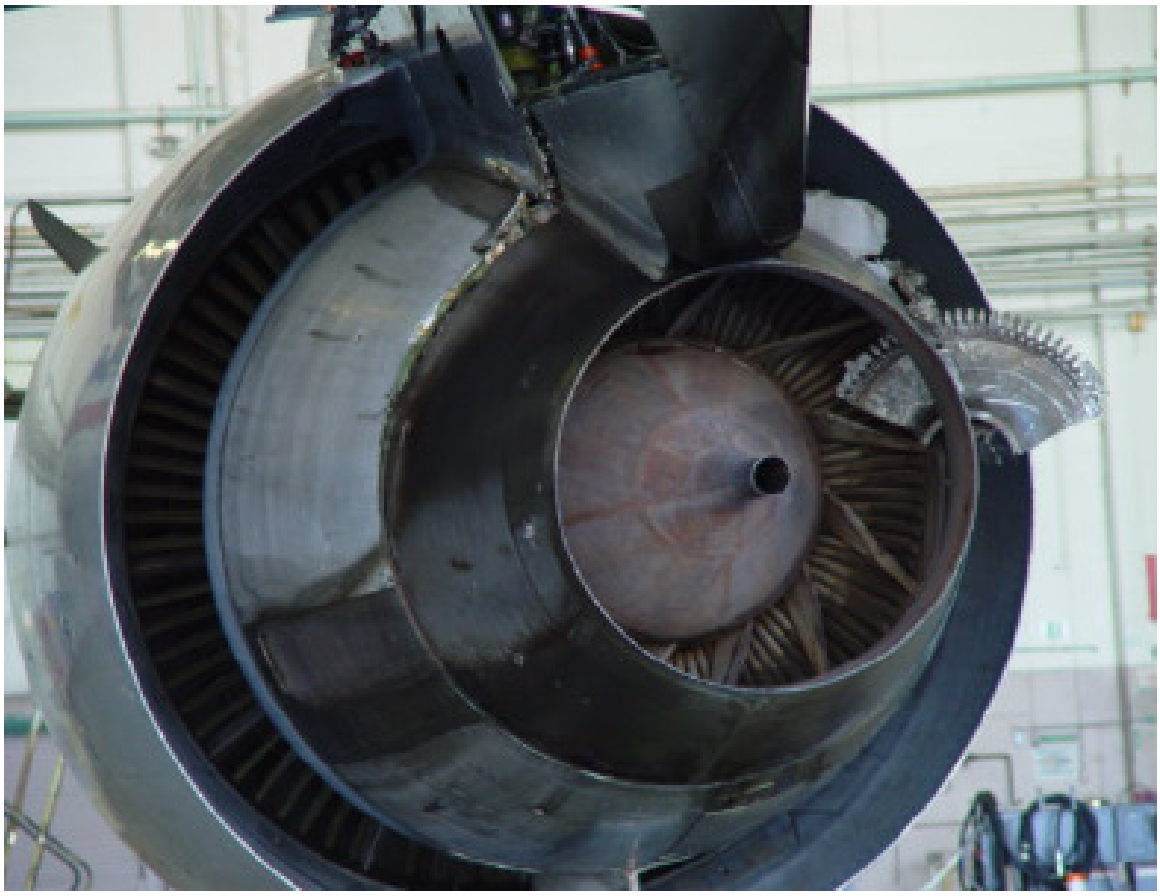

Figure 1.3 Jet Engine Disk Failure at Los Angeles International Airport [3]

Furthermore retirement for cause needs to be based on a proper understanding of fatigue crack propagation [4]. Better understanding of the fatigue crack growth will lead to superior lifetime estimation in superalloys which will lead to more intuitive inspection intervals that can be introduced to prevent this from happening.

1.2: Research Objectives

Superalloys in gas turbine engines are exposed to strenuous flight profiles involving large temperature and load cycling. This thermo-mechanical cycling introduces many frequency, load and temperature interaction effects that have not been thoroughly looked into. In order to add to the currently available body of knowledge this project focuses on the TMF crack growth characterization of polycrystalline IN100 through the use of single edge notch tension, (SENT), and compact tension, (CT), specimens with the following objectives:

1. CT specimens will be tested isothermally at room temperature using constant amplitude cyclic loading. This in order to get a base da/dN vs. ΔK using a proven stress intensity solution.
2. SENT specimens will be tested isothermally at 22°C, 316°C, 482°C and 649°C using constant amplitude cyclic loading. These data points will form the basis of the IN100 library which will be compared to existing published data.
3. SENT specimens will be tested isothermally at 0.33 Hz and 20 Hz using constant amplitude cyclic loading. The effect of frequency due to increased exposure to environmental effects will be isolated by this test.
4. SENT specimens will be tested bithermally at 316°C and 649°C using constant amplitude cyclic loading with alternating block cycles of 1, 10 and 100. The effect of temperature interaction will be considered to determine crack growth interactions between high and low temperature fatigue.
5. SENT specimens will be tested at 316°C and 649°C while applying single repeated overloads of 2.0x, 1.6x and 1.3x every 800 cycles. The retardation caused by overloads will be examined at different overload ratios and temperatures.
6. Fracture surfaces will be examined using a scanning electron microscope to determine failure modes and mechanisms. The stress intensity factor range, ΔK,

will be compared between all specimens tested to compare and contrast mechanisms.

7. Specimens will be examined using optical microscopy and scanning electron microscopy to determine oxidation effects. This examination will determine at what temperatures oxygen diffusion takes place. A model to separate environmental effects out from fatigue will be investigated.

1.3: Thesis Overview

The first chapter discusses the motivation for this thermo-mechanical fatigue crack growth of a polycrystalline superalloy project. This chapter also includes a list of the research objectives of this study. A relevant background is provided in the second chapter that discusses the history, composition, microstructure, processing and mechanical properties of superalloys. Also provided is an overview of the most common fatigue analysis and fatigue crack service life prediction methodologies. In addition the second chapter contains an in depth review of the thermo-mechanical fatigue crack growth behavior of superalloys. This section discusses the varied factors that are responsible for the fatigue crack growth rate. A section discussing current oxidation analysis of superalloy techniques is included as well in the literature review. Experimental methods are discussed in the third chapter. This chapter includes details about the material, specimen design and preparation and the thermo-mechanical testing process. Non-interaction crack growth modeling is presented and discussed in the fourth chapter. Experimental results are presented in the fifth chapter. This chapter includes results from a material analysis and a discussion on the stress intensity factor solution for the specimen used in this study. Lastly the experimental results chapter discusses the

isothermal constant amplitude and temperature and load interaction fatigue crack growth rates and fracture surface morphology. Conclusions and future recommendations can be found in the sixth chapter.

CHAPTER 2: LITERATURE REVIEW AND BACKGROUND

2.1: Superalloys

2.1.1: History

With the invention of the jet engine in the 1930's by Frank Whittle there was demand for materials that could withstand the high turbine entry temperatures. Starting in the 1940's, the turbine entry temperature had increased so much that a new high temperature alloy had to be created to withstand the harsh gas turbine engine environment. This new high temperature material had to fulfill several requirements:

1. The material needed to have excellent mechanical properties at high temperatures especially as it approached its melting point.
2. It needed to be able to resist time dependent deformation such as creep when loaded at high temperatures for long dwell periods.
3. This material would also have to be able to withstand a corrosive operating environment due to the byproducts of combustion.

Many materials can satisfy two of these requirements but very few can satisfy all three. For example titanium, which is used for compressor blades and discs, is lightweight and strong, but has poor oxidation resistance. On the other hand ceramics are creep and oxidation resistant but have low toughness and are fairly brittle. Due to their creep oxidation resistance ceramics have found use as thermal barrier coatings that increase the operational limit of Superalloy components.

Several different base alloying elements such as cobalt, nickel and tungsten were looked at but nickel was chosen as the solvent of choice because of several factors:

1. Nickel has an extremely stable face centered cubic lattice structure that does not go through any phase changes from room temperature up to its melting point of 1453°C.
2. Nickel is also very tough and ductile which makes it resistant to fatigue and fracture.
3. The diffusion rate for nickel is very low which affords it excellent creep resistance.

Some other materials are better than nickel in certain areas but when factoring in price and density nickel clearly emerges as the base alloying element for superalloys. With the base alloying element of nickel chosen Nimonic alloy 75 was the first Superalloy developed in support of the Whittle gas turbine engine. As seen in Figure 2.1 the first superalloys where wrought for all components. In the mid 1950's the introduction of vacuum induction melting and casting at Special Metals in Utica, NY, prevented aluminum and titanium from oxidizing which allowed the production of cast alloys that had fewer contaminants. Since then casting technologies have advanced so that alloys can be directionally solidified (DS) so that there are no transverse grains and eventually led to the casting of single crystals that have no grain boundaries. Due to the added expense of using and verifying grain selection processes, polycrystalline materials are still very prevalent as lower temperature turbine disk materials.

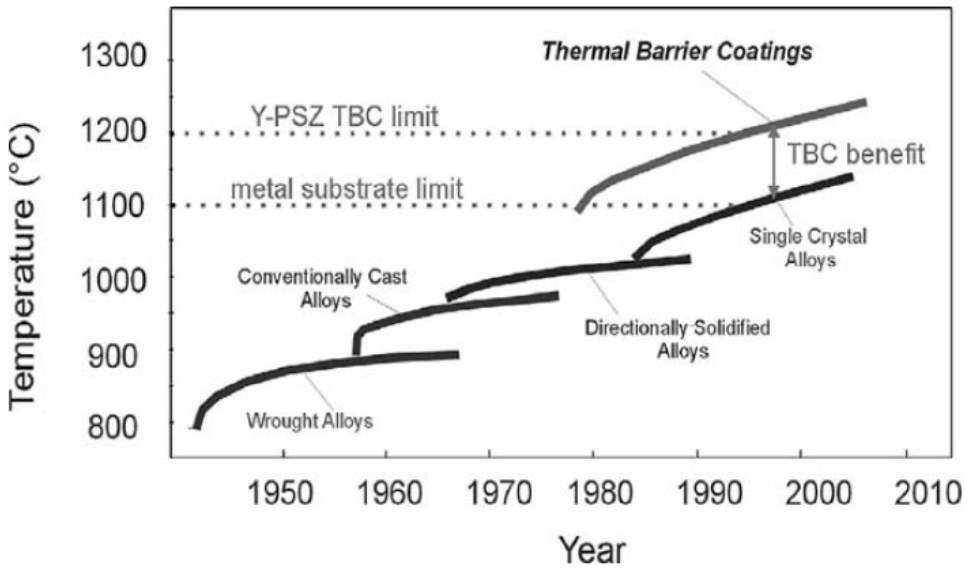

Figure 2.1: Increase of Turbine Entry Temperature TET Made Possible by Gains in Alloy and Manufacturing Technologies [5]

2.1.2: Composition

There are many different superalloys composed of a similar pool of elements but each having a slightly different percent weight configuration. This is primarily due to gas turbine engine manufacturers and material suppliers coming up with there own proprietary blends. The numerous superalloys can also be attributed to the many different alloying elements which can be seen for some common wrought and cast alloys in Table 2.1 and Table 2.2. Removing or slightly tweaking a single alloying element can have a large effect on the mechanical properties. A common trend is for superalloys to be composed of approximately 55% nickel by weight followed by chromium, cobalt, tungsten, aluminum, molybdenum and titanium in decreasing percent weight order.

In comparing wrought to cast superalloys it can be seen that iron is no longer used in any cast superalloys whereas cast superalloys are now using more rhenium and tantalum. In

comparing polycrystalline (IN100) to single crystal (PWA1494) superalloys, some elements such as carbon and boron which strengthen grain boundaries and zirconium which promotes grain boundary cohesion are absent from the grain boundary free, single crystal materials.

Table 2.1: Some Compositions of Wrought Superalloys [5]

Alloy	Cr	Co	Mo	W	Nb	Al	Ti	Ta	Fe	Hf	C	B	Zr	Ni
Astroloy	15.0	17.0	5.3	-	-	4.0	3.5	-	-	-	0.06	0.030	-	Bal
Hastelloy S	15.5	-	14.5	-	-	0.3		-	1.0	-	-	0.009	-	Bal
Haynes 230	22.0	-	2.0	14.0	-	0.3		-	-	-	0.10	-	-	Bal
Incoloy 925	20.5	-	-	-	-	0.2	2.1	-	29.0	-	0.01	-	-	Bal
Inconel 718	19.0	-	3.0	-	5.1	0.5	0.9	-	18.5	-	0.04	-	-	Bal
LSHR	13.0	21.0	2.7	4.3	1.5	3.5	3.5	1.6	-	-	0.03	0.030	0.050	Bal
Nimonic 75	19.5	-	-	-	-	-	0.4	-	3.0	-	0.10	-	-	Bal
N18	11.5	15.7	6.5	0.6	-	4.35	4.35	-	-	0.45	0.02	0.015	0.03	Bal
Pyromet 860	13.0	4.0	6.0	-	0.9	1.0	3.0	-	28.9	-	0.05	0.01	-	Bal
Rene 95	14.0	8.0	3.5	3.5	3.5	3.5	2.5	-	-	-	0.15	0.010	0.05	Bal
Udimet 500	18.0	18.5	4.0	-	-	2.9	2.9	-	-	-	0.08	0.006	0.05	Bal
Waspaloy	19.5	13.5	4.3	-	-	1.3	3.0	-	-	-	0.08	0.006	-	Bal

Table 2.2: Some Compositions of Cast Superalloys [5]

Alloy	Cr	Co	Mo	W	Al	Ti	Ta	Nb	Re	Ru	Hf	C	B	Zr	Ni
CM247LC	8.0	9.3	0.5	9.5	5.6	0.7	3.2	-	-	-	1.4	0.07	0.015	0.010	Bal
CMSX-10	2.0	3.0	0.4	5.0	5.7	0.2	8.0	-	6.0	-	0.03	-	-	-	Bal
GTD-111	14.0	9.5	1.5	3.8	3.0	5.0	3.15	0.07	-	-	-	0.1	0.014	0.007	Bal
GTD-222	22.5	19.1	-	2.0	1.2	2.3	0.94	0.8	-	-	-	0.08	0.004	0.02	Bal
IN100	10.0	15.0	3.0	-	5.5	4.7	-	-	-	-	-	0.18	0.014	0.06	Bal
IN-792	12.4	9.2	1.9	3.9	3.5	3.9	4.2	-	-	-	-	0.07	0.016	0.018	Bal
Mar-M246	9.0	10.0	2.5	10.0	5.5	1.5	1.5	-	-	-	1.5	0.15	0.015	0.05	Bal
PWA1480	10.0	5.0	-	4.0	5.0	1.5	12.0	-	-	-	-	-	-	-	Bal
PWA1484	5.0	10.0	2.0	6.0	5.6	-	9.0	-	3.0	-	0.1	-	-	-	Bal
PWA1497	2.0	16.5	2.0	6.0	5.6	-	8.25	-	5.95	3.0	0.15	0.03	-	-	Bal
Rene 80	14.0	9.0	4.0	4.0	3.0	4.7	-	-	-	-	0.8	0.16	0.015	0.01	Bal
Rene N6	4.2	12.5	1.4	6.0	5.75	-	7.2	-	5.4	-	0.15	0.05	0.004	-	Bal

Cast superalloys can be broken down into four different generations depending on the amounts of elements rhenium and ruthenium. First generation superalloys such as IN100 and GTD-222 do not have any rhenium or ruthenium. Whereas second generation

superalloys such as PWA1484 have approximately 3% rhenium. For third generation superalloys, such as Rene N6 and CMSX-10 the amount of rhenium was increased to approximately 6%. PWA1497 is a fourth generation superalloy which has the addition of ruthenium in the composition mix. Rhenium increases the superalloys' melting temperature which leads to greater thermal stability of the gamma matrix and gamma prime phase which increases creep performance through impediment of diffusion. Ruthenium increases the solubility of high temperature elements in the gamma prime phase, which improves stability leading to additional strength at high temperatures for superalloys [6].

2.1.3: Microstructure

Superalloys all have a common microstructure which consists of the following phases, which can be seen in Figure 2.2 and Figure 2.3.

Gamma Phase (Denoted γ) – This is the extremely stable FCC matrix material that the other phases, carbides and borides exist in. Elements such as cobalt, chromium, molybdenum, ruthenium and rhenium can be found in this phase [7-9]

Gamma Prime Phase (Denoted γ') – This precipitate phase contains elements such as aluminum, titanium and tantalum. This phase is called gamma double prime when talking about nickel-iron superalloys and superalloys with large quantities of niobium [7-9].

Carbides and Borides – Carbon and boron react with other elements to form these strengthening agents which can be found along the grain boundaries of the gamma

phase. The presence of these along the grain boundaries hinder grain boundary sliding greatly increasing the rupture strength at high temperatures [7, 9].

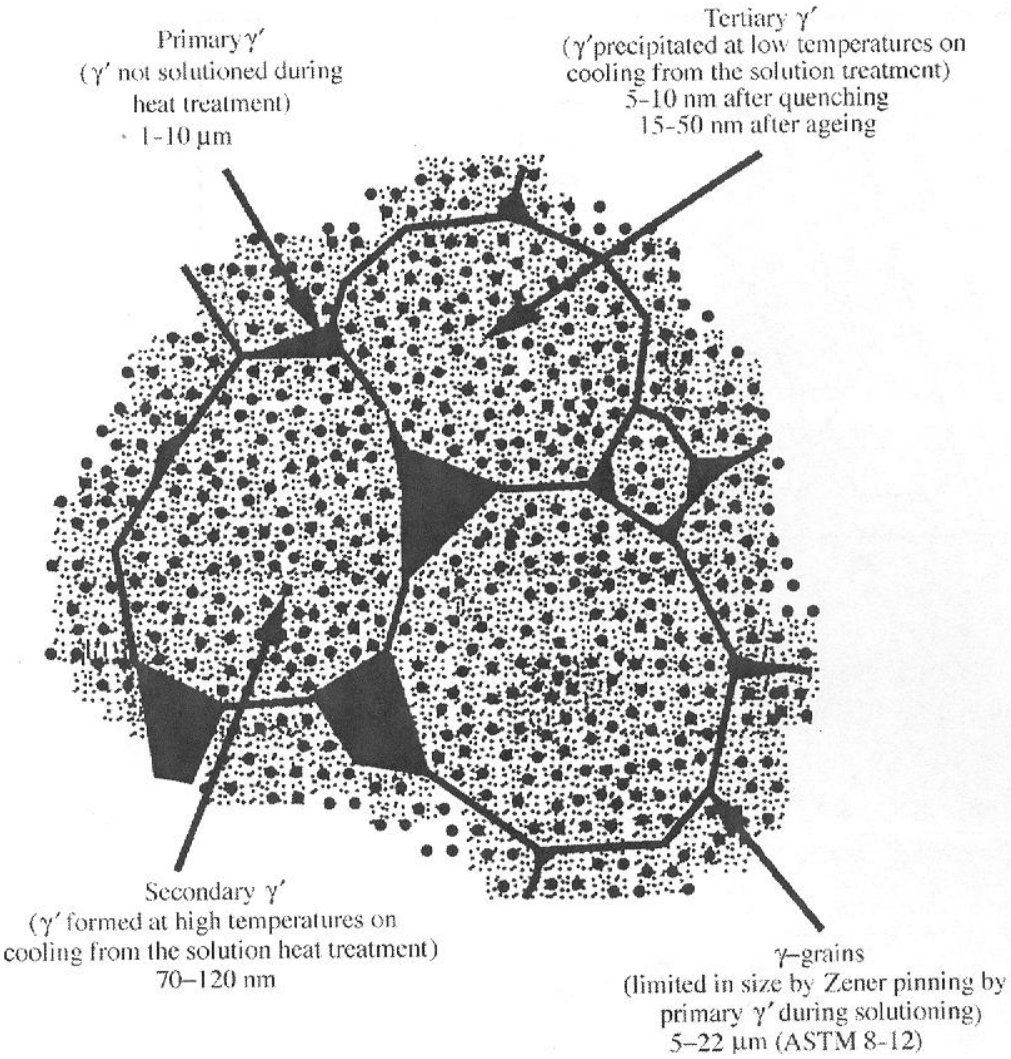

Figure 2.2: Distribution of the γ' Phase in a Polycrystalline Superalloy [8]

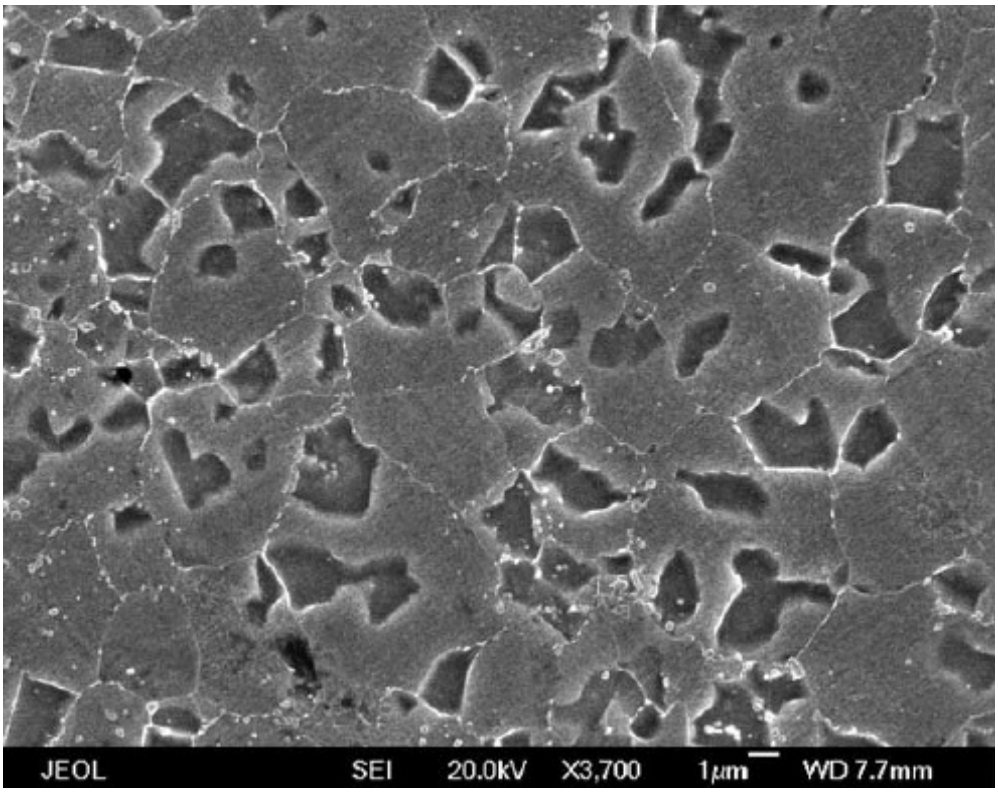

Figure 2.3: IN100 Microstructure Showing the γ Grain Boundaries as White Lines, Darker Areas are Primary γ' Phase and White Dots are Carbides [10]

2.1.4: Processing of Powdered Metallurgy Superalloys

With the advent of heavily alloyed varieties of superalloys the casting portion of vacuum induction melting and casting was no longer possible due to segregation during the melting process leading to cracking during thermal-mechanical working [8]. Powdered metallurgy (P/M) was first brought in for superalloy processing in 1970's when these alloy rich compositions started to emerge [11]. Following vacuum induction melting the material is turned into a powder through the use of inert gas atomization [12]. The powder is then sieved to remove any large unwanted particles and consolidated in a can then degassed and sealed. The powdered metal can then either be hot isostatic pressed (HIP) or extruded before being forged [8]. This process can be seen in Figure 2.4.

Powdered metallurgy allowed for the development of superalloys with a fine grain size and better property homogeny. Superalloys that were usually cast and not necessarily considered heavily alloyed also benefitted from the emergence of P/M, such as IN100 [13].

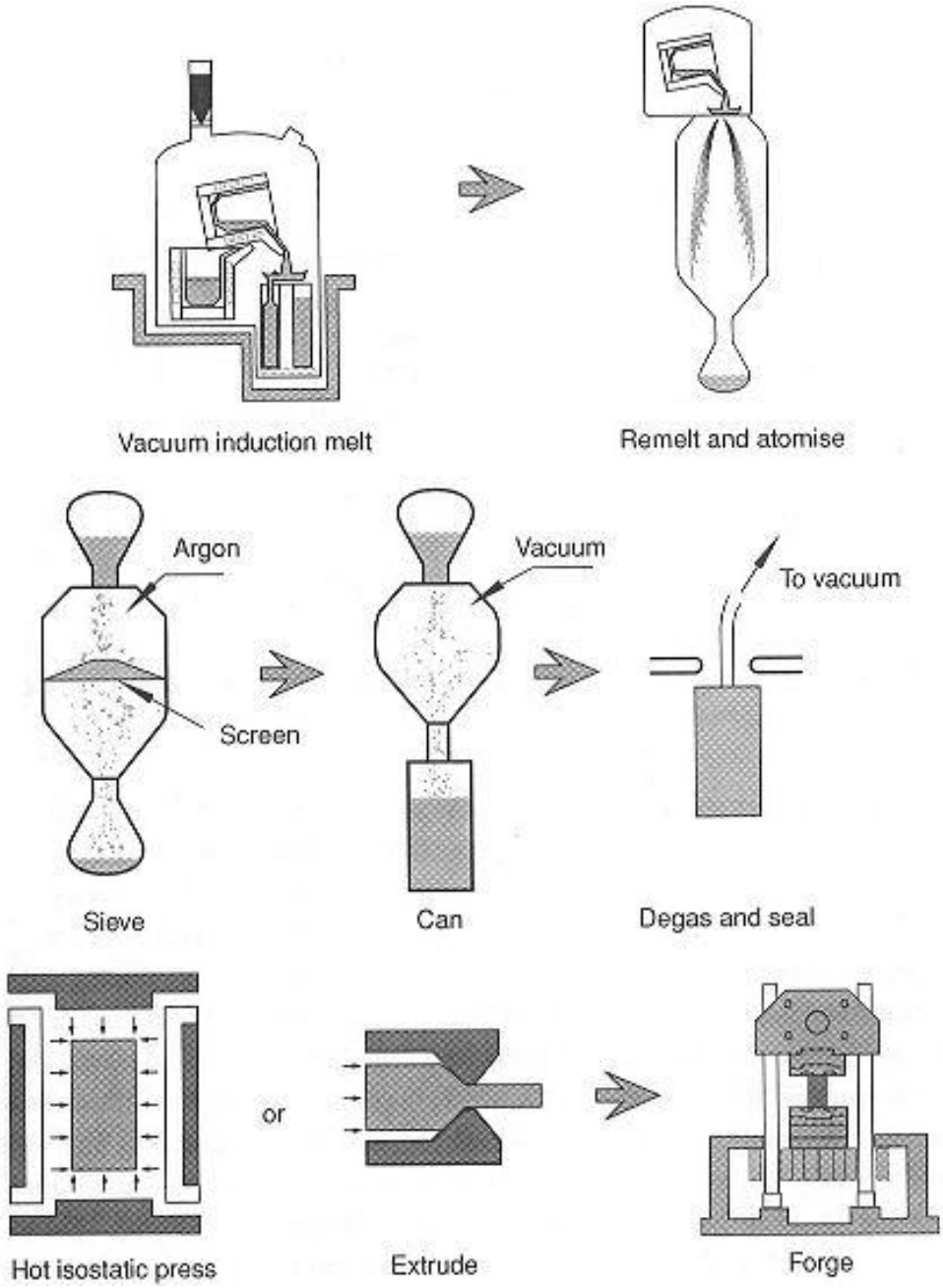

Figure 2.4: The Production of Turbine Disk Alloys by Powder Metallurgy [8]

2.1.5: Mechanical Properties

Superalloys unique combination of composition and microstructure are what give superalloys their exceptional mechanical properties at high temperature. These properties are so valuable that lattice block and metallic foam superalloys are being developed to create light weight structural components [14]. Superalloys maintain creep strength and damage tolerance at high temperatures by severely impeding dislocations, the carriers of creep, from entering the gamma prime phase. Dislocations traveling through the gamma phase have to travel in pairs through what is known as order strengthening. The particle cutting stress required for the second dislocation to remove the anti-phase boundary (APB) formed by the first is very high leading to what is known as order strengthening.

Superalloys are quite rare in the fact that unlike most alloys the yield strength increases with temperature up to about 800°C seen in Figure 2.5. The reasons for this are still not fully understood, but the general consensus is that the main source of strength increase occurs in the gamma prime phase. In this phase the cross slip of dislocations from the octahedral to cubic plane combined with the above mentioned APB order strengthening are primarily responsible for yield strength increasing with temperature. These entanglements are known as Kear-Wilsdorf locks named so after the scientists who first discovered them [15]. These locks have been found to be reversible with only a small percentage of the work hardening created at high temperature remaining at lower temperatures. Above 800°C a preference for thermally activated slip on the cubic plane leads to a sudden drop in yield strength.

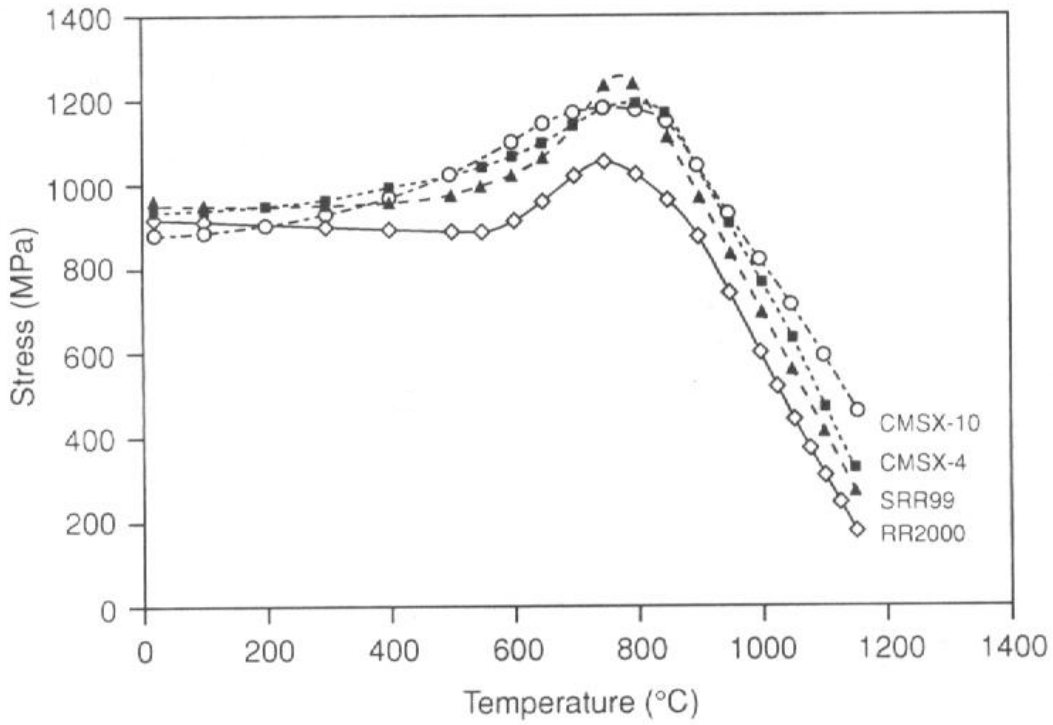

Figure 2.5: Yield Stress as a Function of Temperature for Several Single Crystal Superalloys [8]

2.2: Fatigue Analysis

Fatigue is characterized as the repeated cyclic loading of structures or components leading to damage or premature failure. In general these stresses are well below the materials yield strength making life prediction even more difficult. Add in cyclic temperature effects and you have thermo-mechanical fatigue the single largest contributor of failure in turbine engine superalloys. The fatigue life of a component is broken into three parts; initiation, propagation and fracture stages. Three main fatigue life prediction methods exist; stress-life, strain-life and fracture mechanics.

2.2.1: Stress-Life Approach

Stress-life is by far the oldest approach to fatigue life prediction. First used by the German engineer Wohler in the 1850's to predict failure of railroad axles, it was the most widely used approach for over 100 years later [16]. Wohler is credited with the creation of S-N curves, which can be plotted linearly on a log-log scale as alternating stress versus cycles to failure. An example of an S-N curve can be seen in Figure 2.6. Stress-life works well for simplified geometries under high cycle fatigue, in low cycle situations where plasticity is encountered a different method is required. Stress-life takes into account both initiation and propagation of a crack up to component failure.

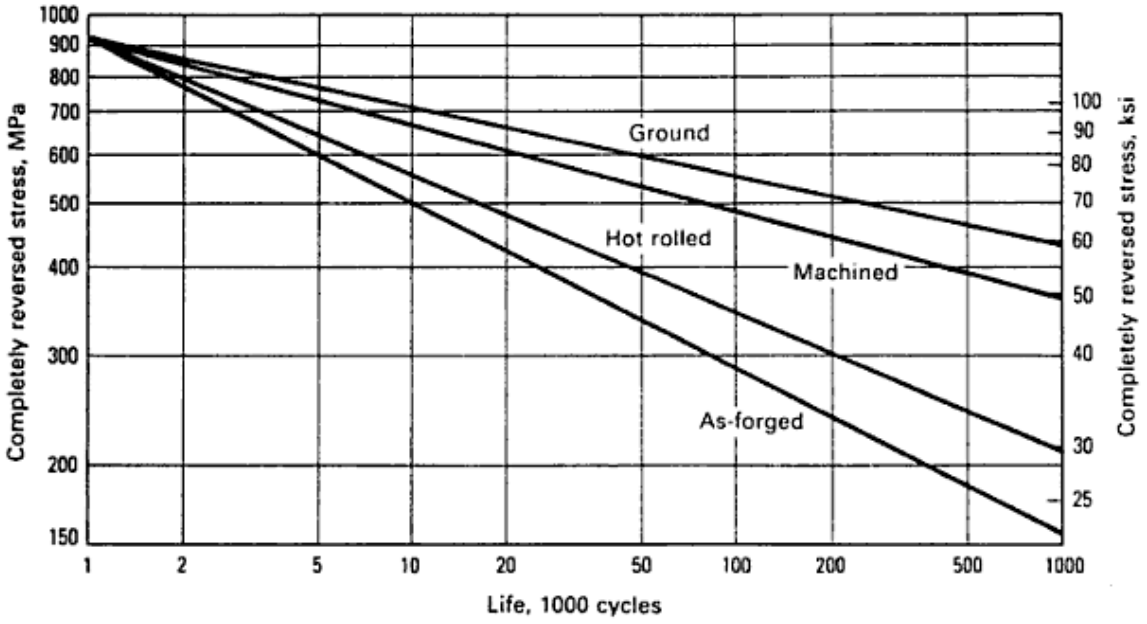

Figure 2.6: S-N Curve Showing the Effect of Surface Condition on the Fatigue Life of Steel [17]

2.2.2: Strain-Life Approach

In the 1950's Coffin and Manson discovered that strain-life could also be plotted linearly on log-log scale as strain amplitude versus cycles to failure [17, 18]. An example of a

strain-life curve can be seen in Figure 2.7. Strain life is the preferred approach for areas encountering plasticity, complicated geometries and notched components. Strain control is used around notches due to strain being a more fundamental indicator of damage, especially for materials that do not work harden. No rational design would have large component cross sections experience plasticity but in localized areas such as notches plasticity can occur. Strain-life is mostly used for determination of crack initiation and but can also be used to model fatigue crack propagation rates [19, 20].

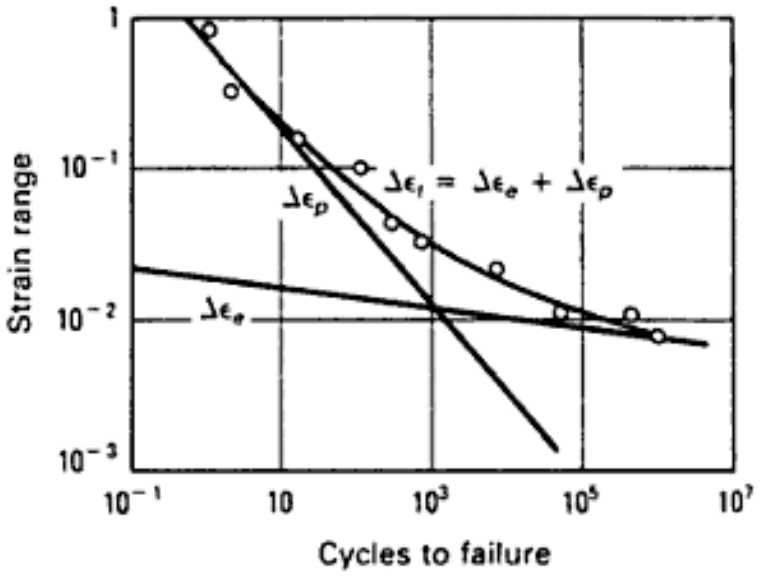

Figure 2.7: Strain-Life Curve Showing Strain Range Versus Cycles to Failure [21]

2.2.3: Fracture Mechanics Approach

Griffith first postulated in 1920 that crack propagation will occur if the total energy of the system is decreased by doing so [22]. This simple energy balance was only accurate for brittle materials so separately in the late 1940's Irwin and Orowan added a term to account for the plastic deformation found in ductile materials [23, 24]. George Irwin

rearranged and defined the strain energy release rate as G, which is the energy required to create a new area of crack extension. In 1956 Irwin made several more discoveries showing that stresses near a crack tip can be calculated with Equation 2.1 [25].

$$\sigma = \frac{K}{\sqrt{2\pi r}} f \tag{2.1}$$

Where K is the stress intensity factor, f is a loading, crack length and geometry correction factor and r is the distance from the crack tip. George Irwin also realized that G is related to the stress intensity factor, K though Equation 2.2.

$$G = \frac{K^2}{E} \tag{2.2}$$

Equation 2.1 can be reordered to solve for the stress intensity factor, seen in Equation 2.3.

$$K = \sigma\sqrt{\pi a} f \tag{2.3}$$

Where σ is the far field stress, a is the crack length and again f is a loading, crack length and geometry correction factor. There are multiple K solutions for many different loading and specimen geometries [26]. The three modes of loading that can be applied to a crack are seen in Figure 2.8.

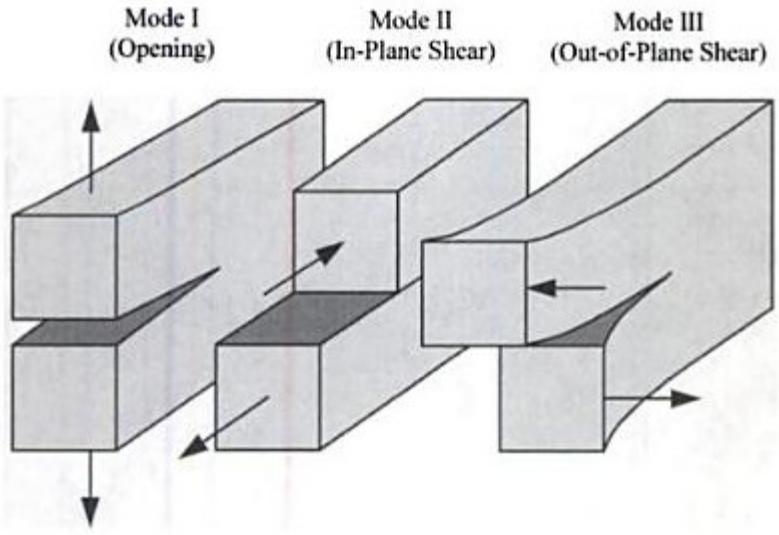

Figure 2.8: The Three Different Crack Tip Loading Modes; K_I, K_{II} and K_{III} [27]

The fracture mechanics approach is purely used for the propagation portion of fatigue. After initiation of the crack, growth data is taken by measuring the crack length as a function of the number of applied cycles. As can be seen in Figure 2.9 much of the fatigue life is spent with the crack length relatively small. Increased crack length leads to an increase in growth rate. This can be seen more clearly when the derivative of a as of function of N is taken to provide da/dN.

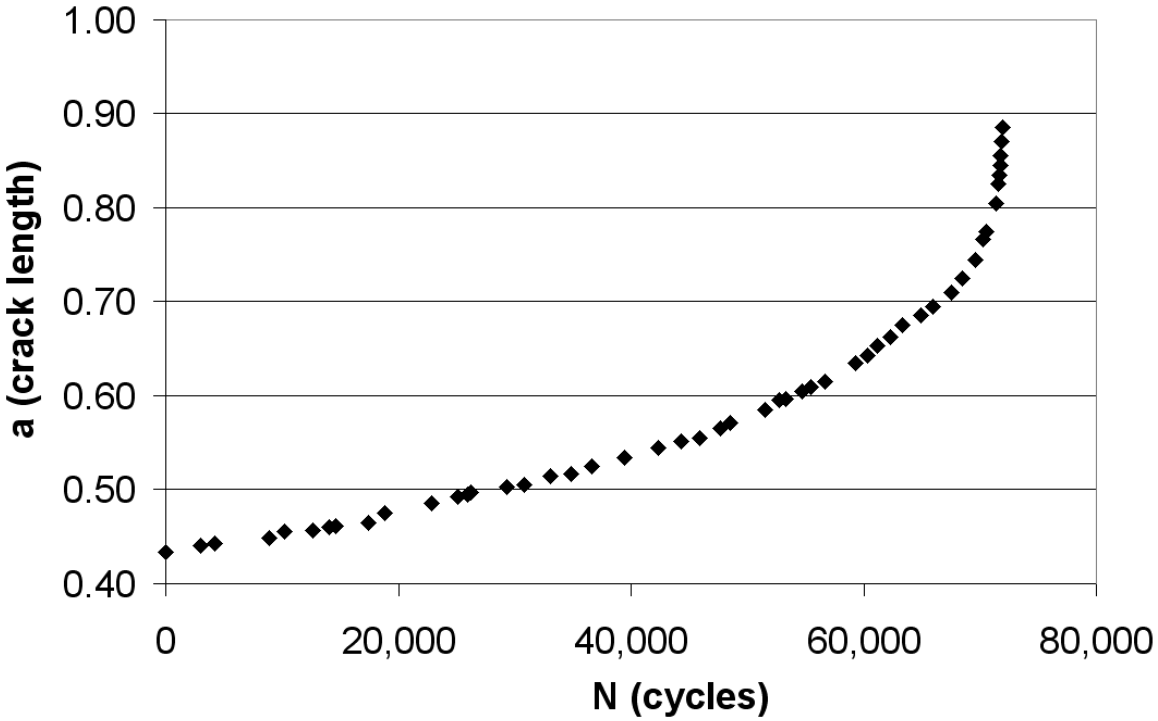

Figure 2.9: Constant Amplitude Crack Growth Data

$$\Delta K = \Delta\sigma\sqrt{\pi a}\, f \qquad \textbf{(2.4)}$$

da/dN can then be plotted as a function of ΔK, which is seen as Equation 2.4. ΔK is the difference between the max and min stress intensity factor also known as the stress intensity factor range. When plotted on a log-log plot and only when viewed sideways the data takes the form of a sigmoidal function. This curve can be split into regions I, II and III as seen in Figure 2.10.

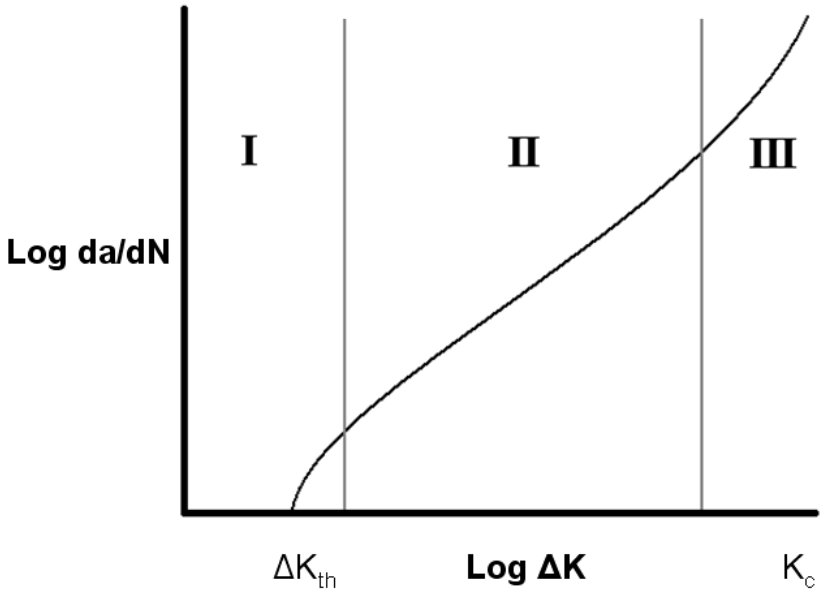

Figure 2.10: Three Regions of Crack Growth Rate

Region I is referred to as near threshold area of the da/dN vs. ΔK curve. Below the stress intensity threshold crack growth does not occur. Threshold is material dependent and also depends on many factors such as R ratio, frequency and temperature. It would be ideal to design components to be exposed only to stress's below the threshold stress intensity. Due to the low stress required to achieve this, it is often impractical to accomplish this. Even then there are small cracks that may still form and propagate ten times faster than long cracks below this threshold level.

Region III is known as the fast fracture area of the da/dN vs. ΔK curve. Once crack growth enters this region it is very difficult to predict this very short and unstable portion of propagation life. For this reason the region is usually ignored during engineering design. The critical stress intensity, K_c, is more commonly known as the critical fracture toughness and once reached leads to fracture.

Region II is where most of the crack propagation life takes place and can be plotted linearly as logarithmic da/dN versus logarithmic ΔK. The idea of using the fracture mechanics approach and applying it to fatigue crack growth was proposed by Paris, Gomez and Anderson in 1961 [28]. Building on this and realizing the log-log linearity of Region II, Paris and Erdogan proposed a power law fitted equation in 1963 seen as Equation 2.5 [29].

$$\frac{da}{dN} = C\Delta K^m \tag{2.5}$$

C is known as the Paris equation coefficient and m is known as the Paris equation exponent. C and m values for various materials can readily be found in publications with most values of m for Superalloys falling between 2 and 4. The below equation forms the basis for most fracture mechanics based life estimation models. Knowing the current crack length, a, C and m the change in crack length per cycle can be calculated and added iteratively using Equation 2.6.

$$\frac{da}{dN} = C\left(\Delta\sigma\sqrt{\pi a}\,f\right)^m \tag{2.6}$$

Many variations of the Paris equation have been developed for various reasons including the ability to also model Region III and to take into account R ratio effects. Two of the more popular equations are the Forman's and Walker's equations seen as Equations 2.7 and 2.8 respectively [30-32].

$$\frac{da}{dN} = \frac{C\Delta K^m}{(1-R)K_c - \Delta K} \quad \textbf{(2.7)}$$

$$\frac{da}{dN} = C\left[(1-R)^m K_{\max}\right]^n \quad \textbf{(2.8)}$$

2.3: TMF Crack Growth Behavior of Superalloys

There is an abundance of published data showing mostly clear TMF crack growth trends for polycrystalline superalloys. When talking about thermo-mechanical fatigue crack growth testing of polycrystalline superalloys there are several parameters that influence the crack growth rate. There are parameters relating strictly to the materials microstructure such as γ' precipitate size and grain size on the other hand there are parameters resulting from operating conditions such as R ratio, frequency, temperature and environment.

2.3.1: Precipitate Size and Distribution

As mentioned above it is well known that the gamma prime phase is responsible for giving superalloys their superior strength at high temperature. This is primarily through the phases' ability to disrupt the translation motion of dislocations. It has been shown that fine and course γ' react differently during plastic deformation; the underlying failure mechanism of fine precipitates is by shearing and course γ' fail by a process known as Orowan looping [33]. It is reasonable to believe that changing the size and distribution of the gamma prime phase through the chemical composition and heat treatment would have a profound effect on the fatigue crack growth rate [34]. There have been many tests performed looking at the effect of gamma prime manipulation on FCGR, with sometimes

contradicting results. Antolovich and Jayaraman performed fatigue crack growth rate testing on two different sized gamma prime Waspaloy materials [35, 36]. Through testing it was shown that lessening the precipitate size from 100 nm to 10 nm resulted in decreased FCGR of almost 5x [37]. Testing by Bowman showed that the fatigue crack propagation rate can be slowed by decreasing the volume fraction of gamma prime and by decreasing the precipitate size [38]. Work performed by Boyd-Lee has shown that increased uniformity in the distribution of gamma prime leads to a slower FCGR [39]. Conversely, testing performed by Gayda and Miner on P/M Astroloy showed that the fatigue crack growth rate decreased as the gamma prime size and volume fraction were increased through aging to increase strength [40]. These results could have been confounded by changing both the gamma prime size and volume fraction. Even though the effect of changing precipitate size and distribution is not entirely clear the general consensus is that decreasing gamma prime size and the volume fraction decreases the FCGR.

Work done by Telesman et al. on a low solvus, high refractory superalloy showed that a super-solvus heat treatment slowed the FCGR by a factor of 10x over a sub-solvus heat treatment. This work also showed that the super-solvus heat treatment had much more effect on the FCGR than any chemical composition change of the microstructure [41]. On top of that it has been shown that cooling rates of turbine disks play a large part in gamma prime precipitate size. Gabb et al. noticed that uneven cooling between the disk bore and rim led to a variation of precipitate sizes, with the faster cooling rim having a desired uniform precipitate size. On the other hand, the slower cooling bore had a

bimodal mix of large and small size precipitates [42]. Reed states that to create strength and fatigue resistance the gamma prime phase should be optimized with γ' forming agents Al, Ti and Ta to achieve a volume fraction between 40% and 55% and heat treatments should be appropriately applied to ensure a homogeneous allocation [8]. Supporting this statement the yield stress and creep performance as a function of fraction of strengthening phases can be seen in Figure 2.11 and Figure 2.12, respectively.

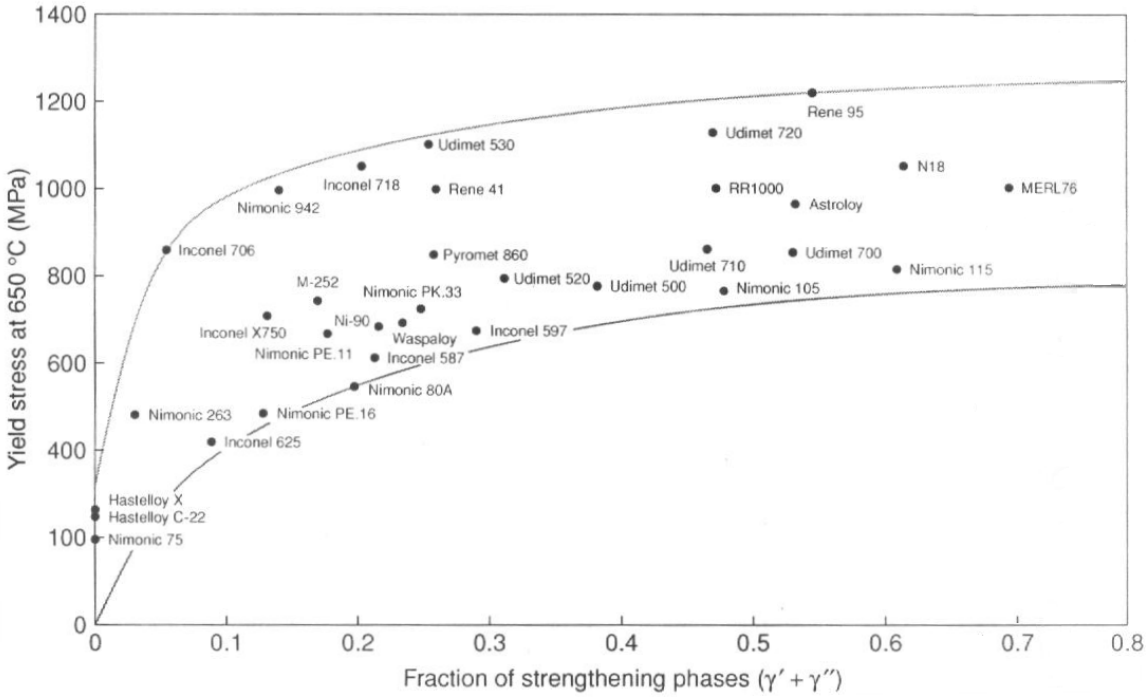

Figure 2.11: Variation of the Yield Stress at 650°C with the Total Fraction of the γ' and γ'' Strengthening Phases, for a Number of Common Turbine Disc Alloys [8]

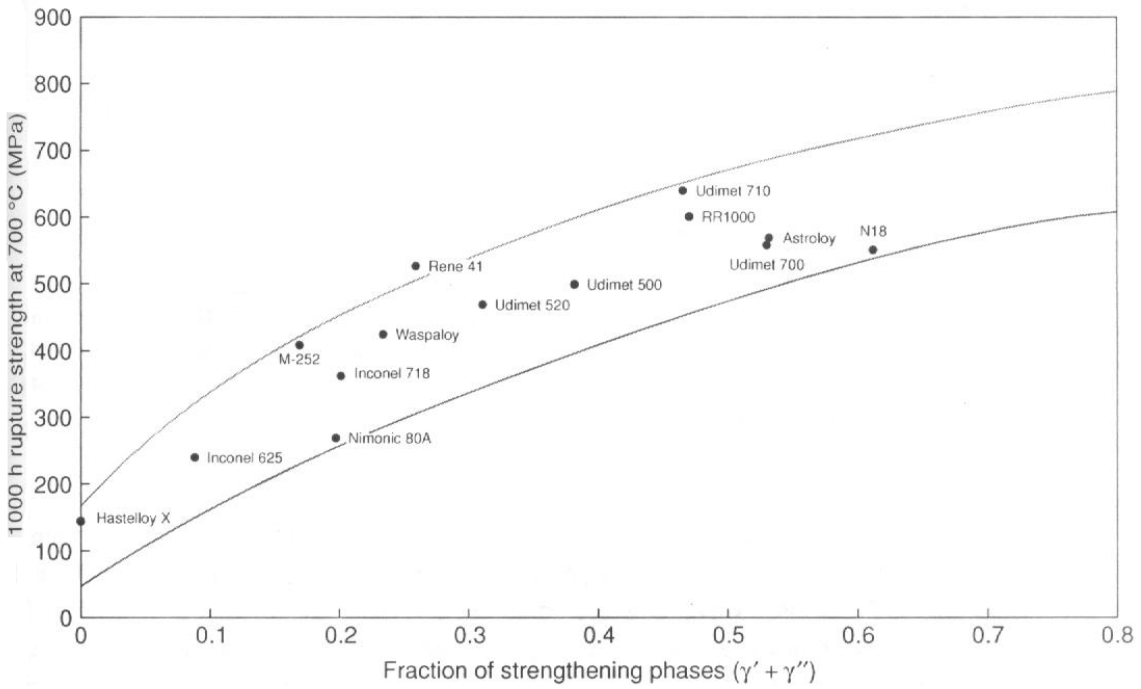

Figure 2.12: Variation of the 1000 h Creep Rupture Strength at 700°C with the Total Fraction of the γ' and γ" Strengthening Phases, for a Number of Common Turbine Disc Alloys [8]

2.3.2: Grain Size

The importance of controlling grain size has been established by many researchers. Gayda and Miner ran tests on P/M Astroloy, recording crack propagation rates in air and vacuum at 0.33 Hz at 650°C. They found that fine grained specimens, smaller than 20 microns, showed a faster crack growth rate than specimens with larger grains [40]. Bain et al. performed studies with Udimet 720 using different heat treatments to produce materials with ASTM grain sizes of 8.5, 4, 3 and 0. Testing performed at 425°C showed a clear trend with the smaller grains resisting FCG better than the large grains, especially in the threshold regime [43]. Everitt et al. looked at the high temperature fatigue crack growth in N18, RR1000, Udiment 720i and 720i large grain P/M disk superalloys. All four materials were tested at 650°C with R=0.1 and a 1-1-1-1 trapezoidal waveform. The most fatigue crack growth resistant material was RR1000, followed by Udiment 720i

large grain, N18 and Udiment 720i. In this case Udiment 720i LG has the largest grains followed by N18, RR1000 and Udiment 720i. Knowing that the larger grains tend to resistance fatigue crack growth this order made sense except for RR1000. The authors concluded that some other chemical composition or microstructural feature such as carbide distributions enables RR1000 to resist FCG the most [44]. On the other hand the influence of grain size was not as clear as shown by Caton et al. Testing performed by Caton, Larsen and Rosenberger showed that specimens with greatly different grain structures did not show much variability in fatigue crack growth rates. On the other hand it was found that specimens with similar grain structures had differing crack growth rates up to 5x. These results led Caton and others to conclude that there were some other microstructural characteristics, such as chemical composition or precipitate size, controlling the crack growth rate in these specimens [45]. Testing performed by Mall et al. on the fretting fatigue behavior of IN100 looked at the crack initiation and propagation behavior of materials with 3 and 7 micron gamma grain size. Fatigue crack initiation and growth resistance was shown to increase with decreasing grain size. This is possibly attributable to the lack of environmental access to the crack initiation site [46].

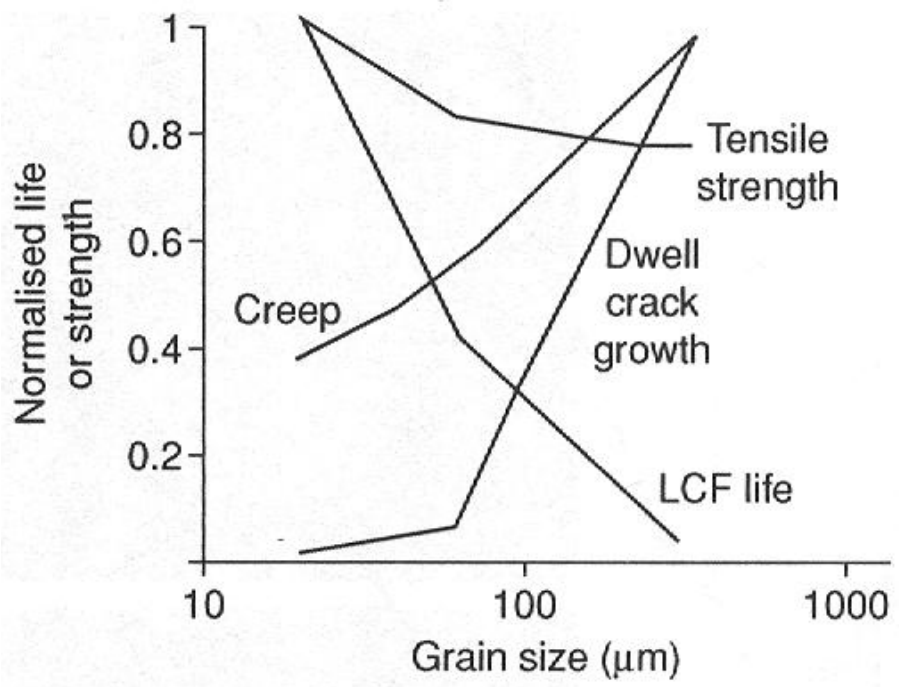

Figure 2.13: Schematic Illustration of the Important Properties of Turbine Disc Alloys and Their Dependence Upon Grain Size [47]

Caton et al. mentioned that it has been shown that superalloy grain structure can vary greatly throughout a turbine disk and even vary significantly from disk to disk [45]. This has also been reported by Gabb et al., where it was found that grain boundaries near the rapidly cooled rim had fairly straight boundaries [42]. Closer to the bore where the disk cooled slowly, microscopy showed grain boundaries that were more serrated. In spite of all the controversy, the general consensus is that yield strength and fatigue crack initiation resistance has an inverse relation with grain size. On the other hand creep strength and fatigue crack growth resistance has been shown to have a direct relationship with grain size [47]. These relationships can be seen in Figure 2.13. Realizing this, the need to have fine grains near the bore of the disk for high yield strength and courser grains at the rim of the disk for creep strength and FCG resistance has led to what is

known as dual heat treatments [48]. The whole turbine disk is first heat treated sub-solvusly to impart the desired bore area finer grain size. A more sophisticated thermal gradient producing furnace is then used to keep the bore relatively cool while super-solvusly heat treating the rim to remove gamma primes and their grain-pinning effect. This produces the desired coarser grains required in the rim region of turbine disks. Optical micrographs of these two different heat treatments can be seen in Figure 2.14 and Figure 2.15.

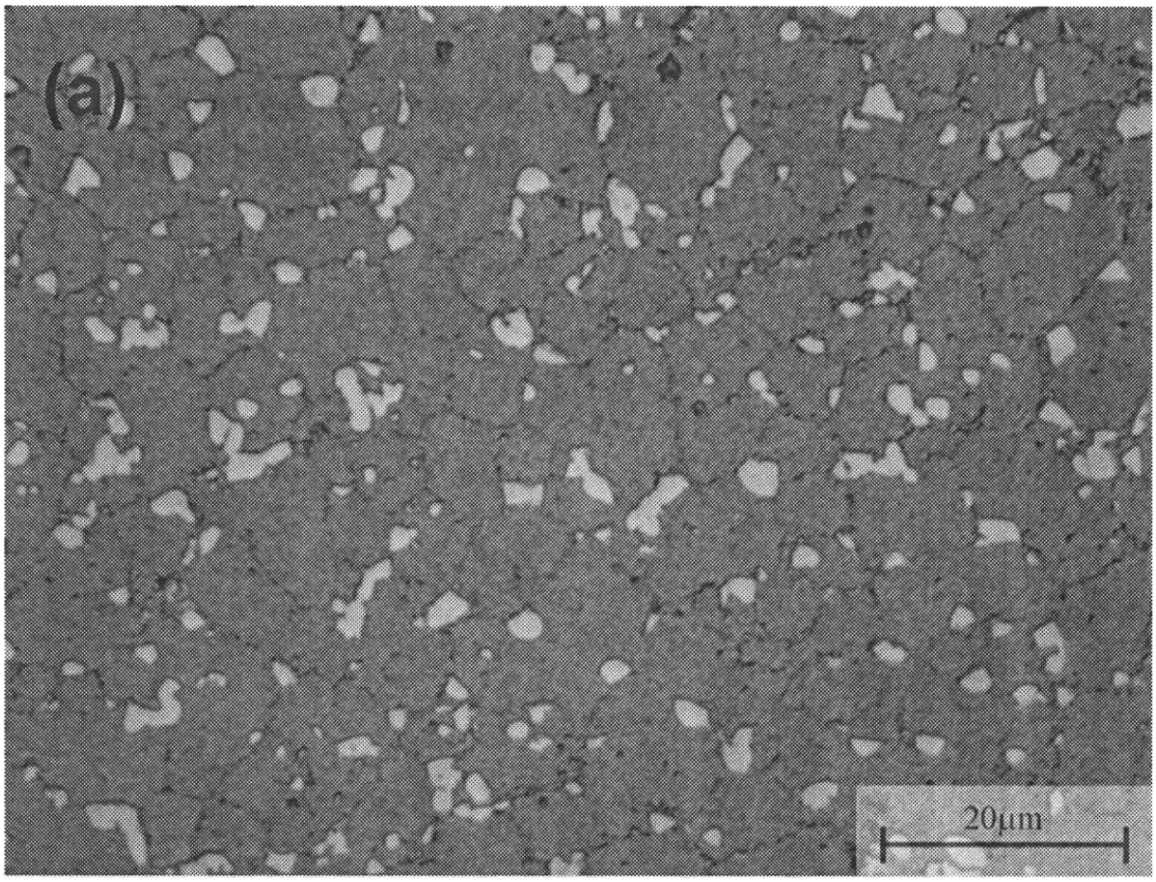

Figure 2.14: Sub-Solvus Heat-Treated for 4 h at 1130°C (Solvus Temperature is 1150°C) [8]

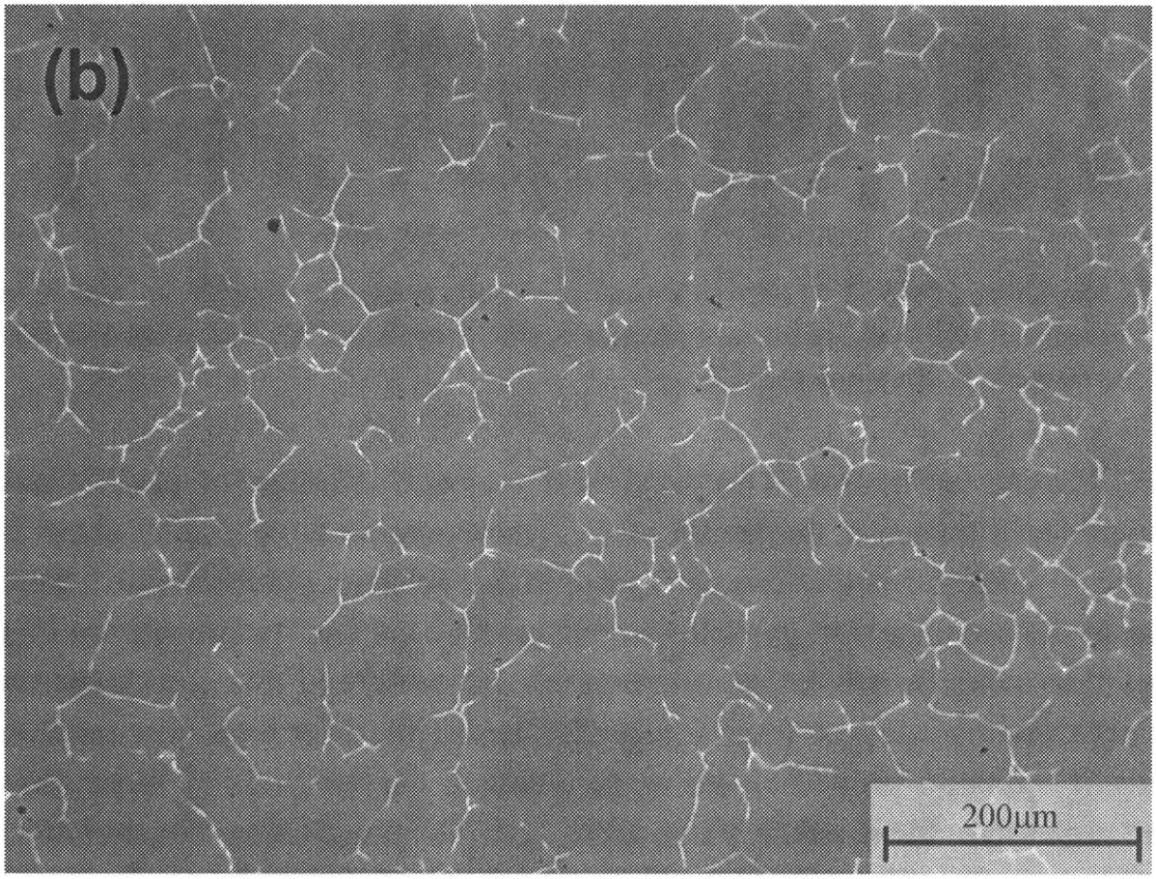

Figure 2.15: Super-Solvus Heat-Treated for 4 h at 1170 °C (Solvus Temperature is 1150°C) [8]

2.3.3: Environment and Operating Conditions

2.3.3.1: Temperature

The role that temperature plays on the fatigue crack growth rate has been extensively studied for many different P/M superalloys. Larsen et al. work with IN100 compact tension specimens validated the commonly held notion that increasing temperature leads to an increase in crack growth rate [49]. This trend can be seen in Figure 2.16. Gabb et al. looked at the effect of temperature on the TMF crack growth rate of powdered metallurgy ME3, also known as Rene 104 [42]. Their research showed that the crack growth rate increased with temperature at R ratios of -0.25, 0.05, 0.25 and 0.5. In going

from 25°C to 650°C the crack growth rate increased almost ten times. A 90 second dwell at maximum stress was used to determine the effect of temperature on the dwell crack growth rate. The dwell crack growth rates at R ratios of 0 and 0.05 also increased with temperature although with a stronger correlation showing the strong effect that environment plays on crack growth rate.

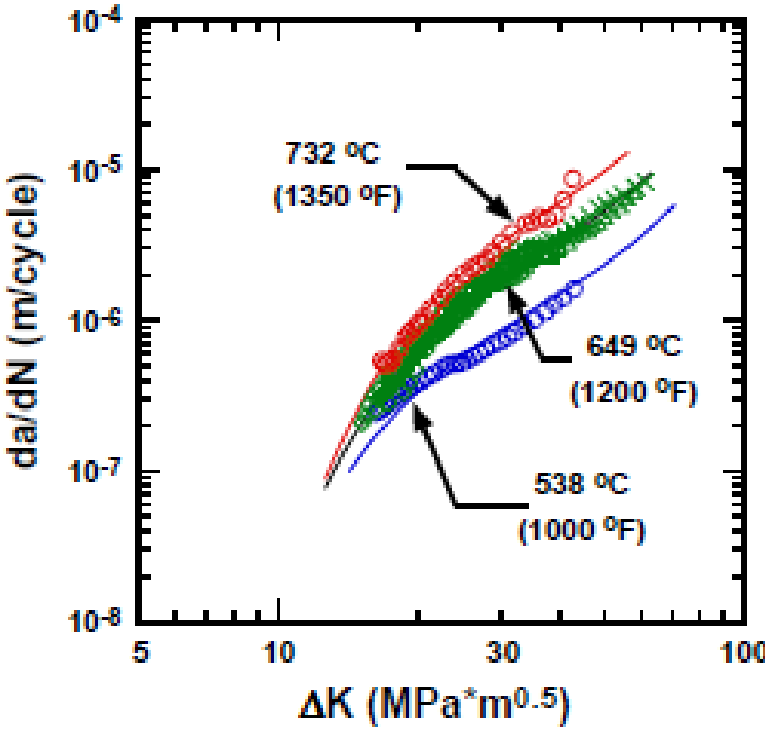

Figure 2.16: Effect of Temperature on Crack Growth in IN100; R = 0.1, Frequency = 0.167 Hz [49]

The fatigue crack growth rates of superalloys change with temperature and environment due to the underlying change in damage mechanism. At room temperature and low ΔK values, heterogeneous slip promotes FCG along {111} crystallographic planes. This, 'planar slip', is due to only a few slip systems being activated at these lower temperatures. This heterogeneous slip behavior can also be seen at higher temperatures

for high cyclic frequencies. As temperature increases and more slip systems become active the slip becomes more homogeneous with the FCG happening along {001} crystallographic facets. In addition to increasing temperature this homogeneous slip is also seen at larger ΔK values. Micromechanisms of fracture also change with increasing temperature and as a function of environment and frequency. At low temperatures fracture is predominantly transgranular. This transgranular fracture extends up to high temperatures at high cyclic frequencies and in the absence of an oxidizing environment. At low cyclic frequencies in high temperature oxidizing environments, chemical attack occurs at the grain boundaries promoting intergranular fracture [8, 27, 50, 51].

2.3.3.2: Oxygen

Numerous studies have shown that the environment, in particular the presence of oxygen at the crack tip increases the crack growth rate [52-54]. It is well known that turbine blades and disks operating in very hot corrosive environments have shorter lives than similar components running in hot only environments. Hancock reasoned for the environment to have any effect on fatigue crack growth rates it has to have access to the crack tip and when environmental factors are present the effect is more pronounced on initiation life than propagation life [55]. Earlier testing by Hoffelner showed that the fatigue crack growth rate of IN738LC and IN939 was unaffected by synthetic flue ash in SO_2 and SO_3 when compared to the rates in air [56]. The effect of environment was also looked at by Hancock on polished round bar Nimonic alloy 90 specimens. Testing performed by Hancock showed that Nimonic alloy 90 specimens tested at 850°C had fatigue lives reduced by as much as 2x when tested in a sea salt environment. Hancock

attributed these differences to initiation and propagation concluding that components with existing surface cracks would not be as affected by environment as components without preexisting cracks [55]. Andrieu et al. leveraging off extensive work showing that environmental crack growth rate increase is the result of oxygen at the crack tip, worked with Inconel 718 to show the role that oxygen plays on the crack growth rate. Andieu work with compact specimens at 0.05 Hz, R = 0.1 and 650°C showed that it took 5000 cycles in air while it took 65,000 cycles to grow the same crack length in a vacuum. Also looked at was the effect of adding a 600 second hold time at minimum load showed increased crack growth over the continuous 0.05 Hz test in air [57].

2.3.3.3: Frequency

It has been shown that changing frequency is of little significance at room temperatures and under vacuum, clearly showing frequency is a magnifier of the previously mentioned effects of temperature and environment. Larsen's work with IN100 along with many other have shown that frequency has an inverse relationship with FCGR, where with decreasing frequency comes an increased crack growth rate [49]. This trend can be seen in Figure 2.17. At lower frequencies the crack tip is open longer allowing the temperature and environment to influence the FCGR.

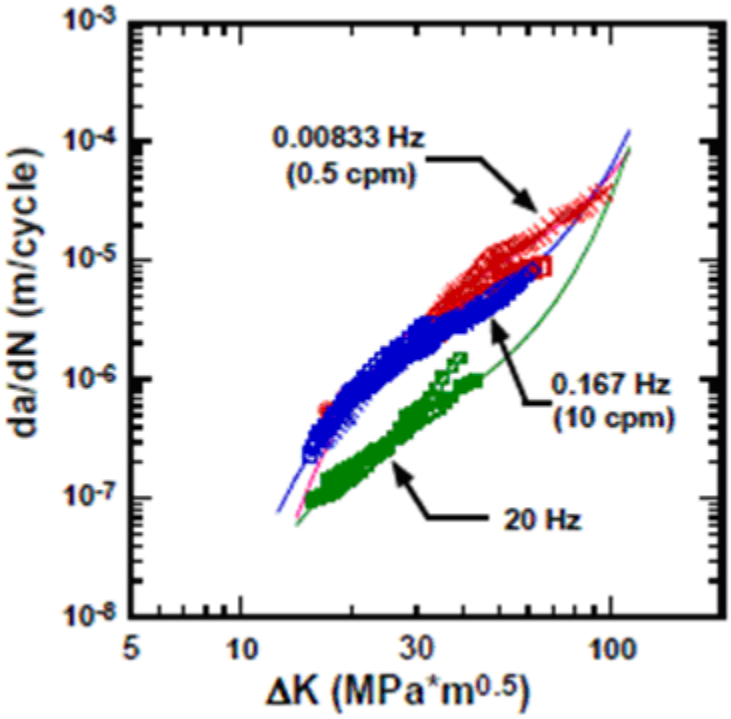

Figure 2.17: Effect of Frequency on Crack Growth in IN100; T = 649°C, R = 0.1 [49]

2.3.3.4: R Ratio

The role of R ratio on FCGR is not entirely clear with studies showing stress ratio is dominated by crack closure at lower ratios. Crack closure has been shown to be greatly dependent on temperature, environment, grain size etc. At R ratios of -0.25, 0.05, 0.25 and 0.5 Gabb et al. work with Rene 104 revealed for the most part that the FCGR tended to increase with decreasing R ratio but this trend was not very clear [42]. Conversely Larsen et al. testing of IN100 demonstrated that increasing the R ratio led to a direct increase in the fatigue crack growth rate. This relationship became more apparent with increasing R ratio showing the dominance of crack closure at lower ratios [49]. This trend can be seen in Figure 2.18. Mercer, Shademan and Soboyejo looked at the effects of R ratio for polycrystalline Inconel 718 with an average grain size of 30 microns [58].

R ratio followed the same trend as seen in Larsens' study where increased crack growth rate follows an increasing R ratio.

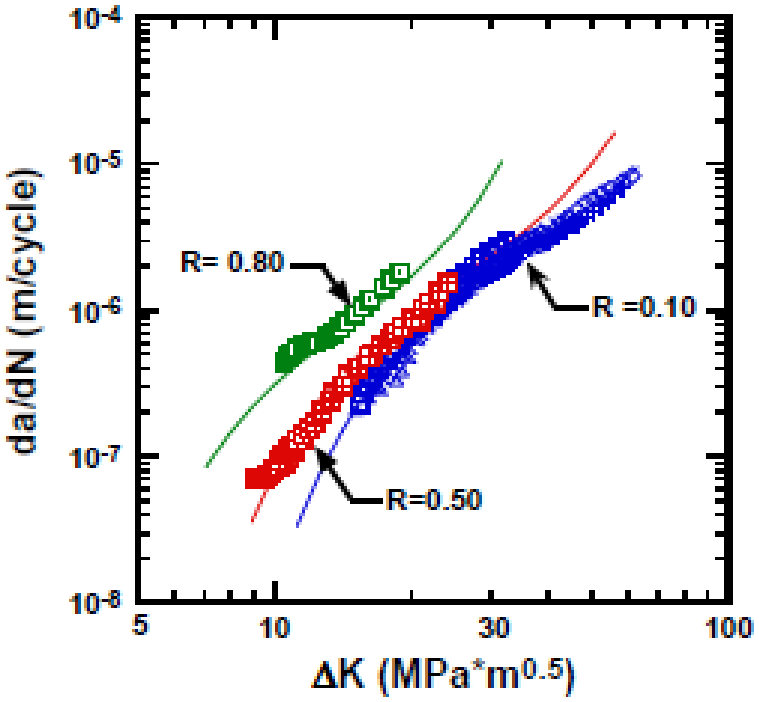

Figure 2.18: Effect of Stress Ratio on Crack Growth in IN100; T = 649°C, Freq. = 0.167 Hz [49]

3.3.3.5: Overloads

The influence of overloads on P/M superalloys is not something found in literature too often. Overloads, common in flight loading spectrums, create a large overload plastic yield zone that has to be grown through creating a period of retarded crack growth. Larsen et al. have looked into the effect of overload size and cycles between overloads on powdered metallurgy IN100 [49]. All testing was performed at 649°C at an R ratio of 0.5 and frequency of 0.167 Hz using compact tension specimens to ASTM standards. The effect of 1.25 and 1.5 overloads with 40 1.0x cycles between were also looked at, with increasing overloads leading to a decrease in the crack growth rate. This trend can be

seen in Figure 2.19. It was also shown that the smaller number of cycles between overloads (CBO) led to an increase in the crack growth rate. This trend can be seen in Figure 2.20.

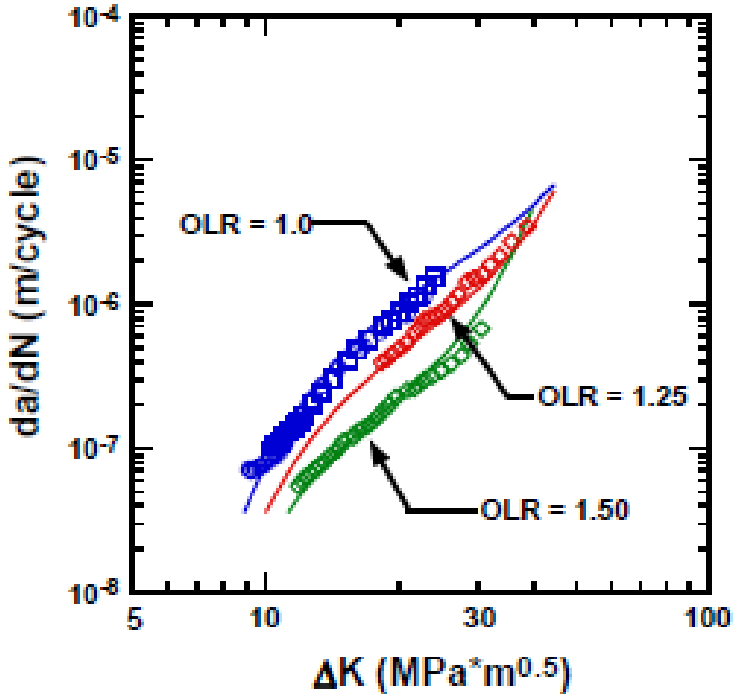

Figure 2.19: Effect of Overload Ratio (OLR) on Crack Growth in IN100; T = 649°C, R = 0.5, Freq = 0.167 Hz, CBO = 40 [49]

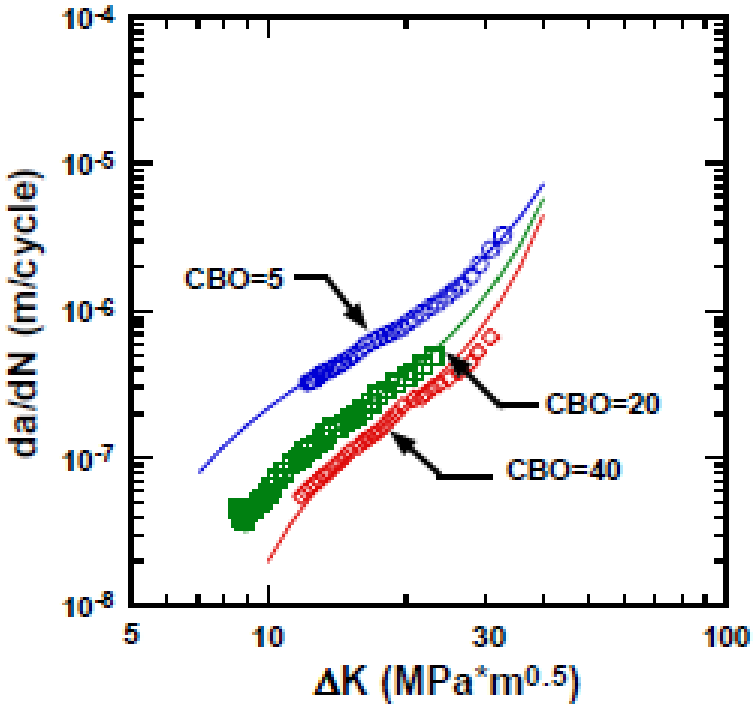

Figure 2.20: Effect of Number of Cycles Between Overloads (CBO) on Crack Growth in IN100; T = 649°C, R = 0.5, Freq = 0.167 Hz, OLR = 1.5 [49]

2.3.3.6: Slip Mode

A review of high temperature fatigue of nickel based superalloys done by Pineau and Antolovich shows the importance of not only environment but also slip mode on the fatigue crack growth rates of superalloys [50]. Looking at model alloys it was shown that an increase in planar reversible slip leads to a larger plastic yield zone at the crack tip causing a decrease in fatigue crack growth rates. Factors such as low anti phase boundary energy (APBE), low stacking fault energy, low lattice parameter mismatch and large grains promote planar reversible slip. The studies also revealed that environment promotes two different competing mechanisms. These mechanisms are composed of one that hinders fatigue crack growth and another that enhances the growth rate. Similar results have been seen in Rene 88DT and Inconel 718 [59, 60].

2.4: Oxidation Analysis of Superalloys

Oxidation due to environmental effects on nickel based superalloys is a major issue in the turbine industry. The desire for higher efficiency is pushing superalloys to their upper temperature limit. The increased oxidation that takes place at these elevated temperatures leads to an even larger thermo-mechanical fatigue crack growth rate. Surface analysis has been employed to better understand the mechanisms that lead to this increased crack propagation. Employing the use of powerful tools such as energy-dispersive x-ray spectroscopy (EDS), auger electron spectroscopy (AES) and x-ray photoelectron spectroscopy (XPS) allows for detailed analysis of these oxidation effects. AES, EDS and XPS have all been used with great success to characterize the type of oxidation and determine the extent of oxidation as a function of time and depth [53, 61, 62]. Proper understanding of these diffusion-controlled mechanisms and how they affect FCG through grain boundary oxidation and grain boundary creep is crucial in developing environmental FCG models [63].

EDS is classified as an electrons in/X-rays out surface technique. EDS is often found as an attachment on scanning electron microscope (SEM) systems. The bombardment of electrons from the SEM with atoms in the sample causes shell transitions which result in the release of an X-ray. The elemental composition of the sample can be determined by the distinctive energy of the emitted X-rays [64].

AES is classified as an electrons in/electrons out surface technique. Incident electrons of energy (2000 and up eV) are used to penetrate the surface being analyzed. Auger

electrons (2000 and less eV) are then emitted following decay of singly ionized core hole states [65]. Due to the fact that orbital energies are distinctive to an atom of a particular element, analysis of the auger electron can be used to determine the chemical composition.

XPS is classified as a photons in/electrons out surface technique. Photons of energy (1200 to 1400 eV) are used to bombard the surface being analyzed. This energy is then absorbed by electrons which then leave the surface with typical kinetic escape energies of 500 to 1400 eV [65]. Specific elements are identified by a distinctive set of XPS peaks at distinctive binding energy values.

2.4.1: Energy-Dispersive X-ray Spectroscopy

Liu et al. looked at the oxidation behavior of single crystal superalloy DD32 between the temperatures of 900°C and 1000°C in air [66]. Specimens were exposed to the elevated temperatures for 500 hours. Upon SEM/EDS examination it was found that a course grained oxide, consisting of NiO and a small amount of CoO, was found on the dendritic portions of the specimens. The EDS analysis can be seen in Figure 2.21. Cross-sections of the specimens showed that the oxide was composed of an outer layer, intermediate layer and inner layer. Similar three layer results have been found during oxidation testing of other superalloys [62, 67-69]. These layers can be seen in Figure 2.22. The intermediate layer consisted of spinels such as $CrTaO_4$ and $NiCr_2O_4$. The inner layer consisted of α-Al_2O_3. The EDS analysis used to determine the chemical composition of these oxide layers can be seen in Figure 2.23.

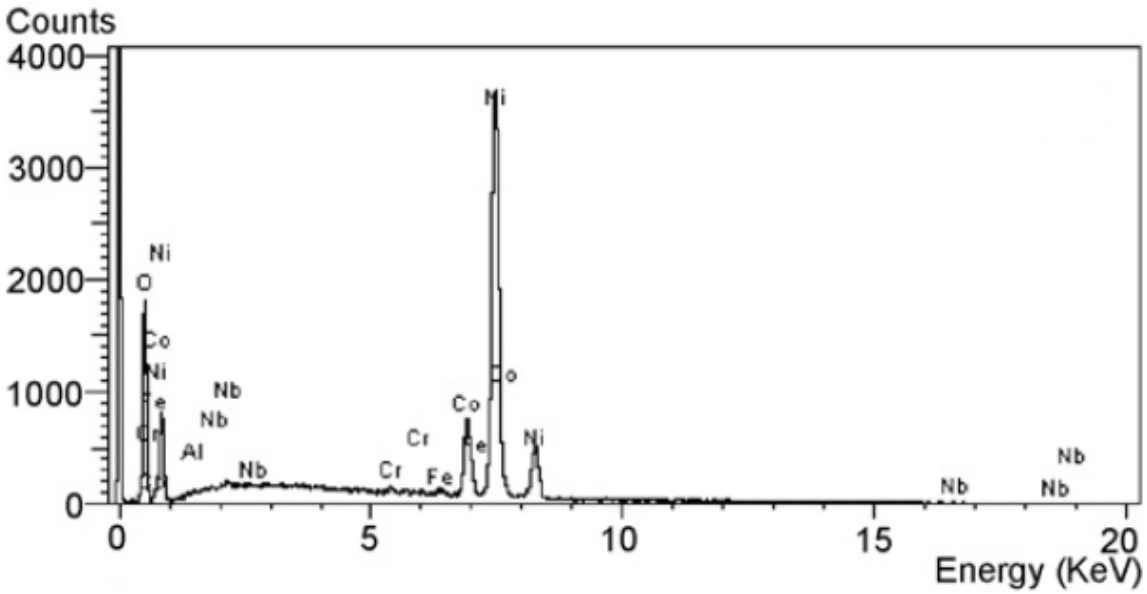

Figure 2.21: EDS Results of Dendritic Portion of Specimen after 100 hours at 1000°C [66]

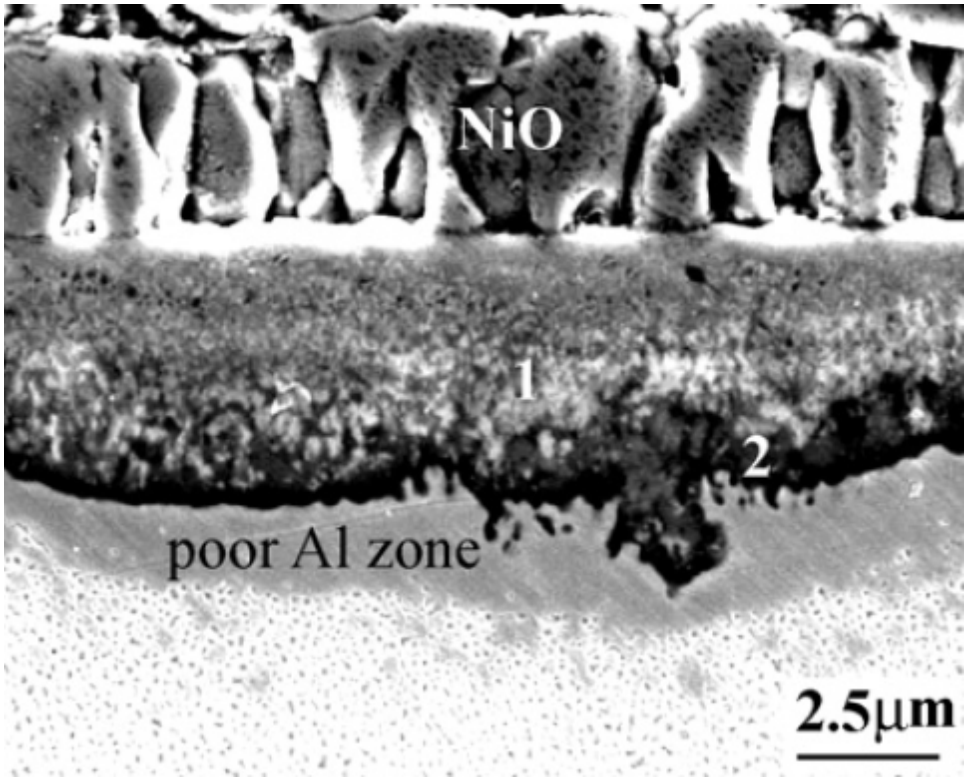

Figure 2.22: SEM Image of DD32 Specimen Cross-Section after 100 hours at 1000°C [66]

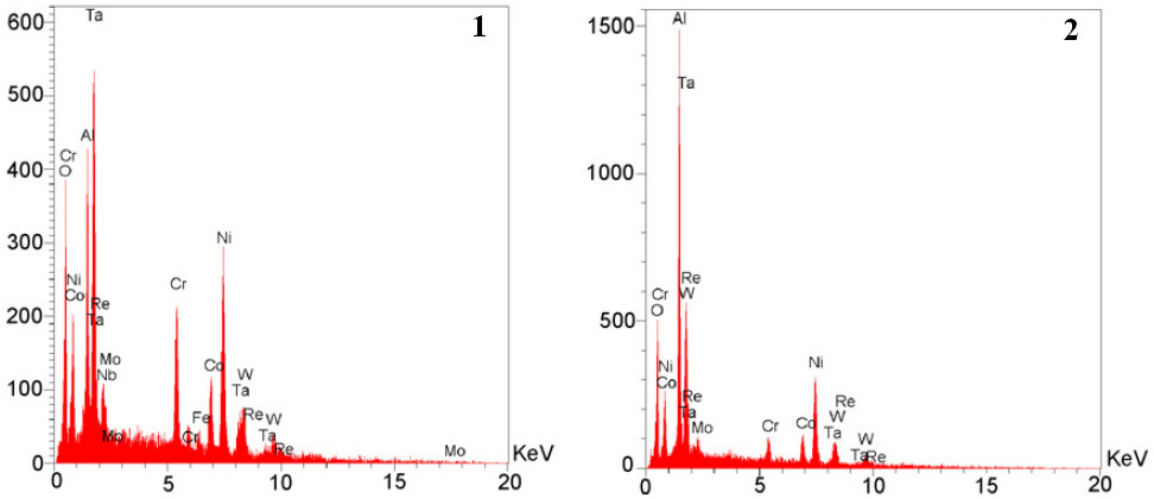

Figure 2.23: EDS Results of Specimen Cross-Section (Areas 1 and 2) after 100 hours at 1000°C [66]

2.4.2: Auger Electron Spectroscopy

Floreen and Raj's paper on environmental effects in nickel-base alloys discusses the use of AES to detect oxidation of sulfur in Ni-Mn-S alloys. They hypothesized that the release of embrittling agents, such as sulfur, from inclusions would lead to increased fatigue crack growth. This research built upon earlier work by Floreen and Kane where they grouped the mechanisms responsible for embrittlement into two different categories with the first being environmentally caused voids ahead of the crack tip and the second being grain boundary oxidation at the crack tip [70]. Specimens were exposed to 1000°C for 200 hours both in an ultra high vacuum (UHV) and air environment. The alloys were then analyzed along grain boundaries using Auger Electron Spectroscopy [61].

The results can be seen in Figure 2.24. It can be seen that the specimen exposed to air oxidized quite a bit whereas the specimen heated under UHV did not. Also interesting to note is that the oxidation is a function of distance to specimen edge; as the edge distance

increases, the oxidation decreases. This research also showed that the sulfur appeared to segregate to the alloy grain boundaries.

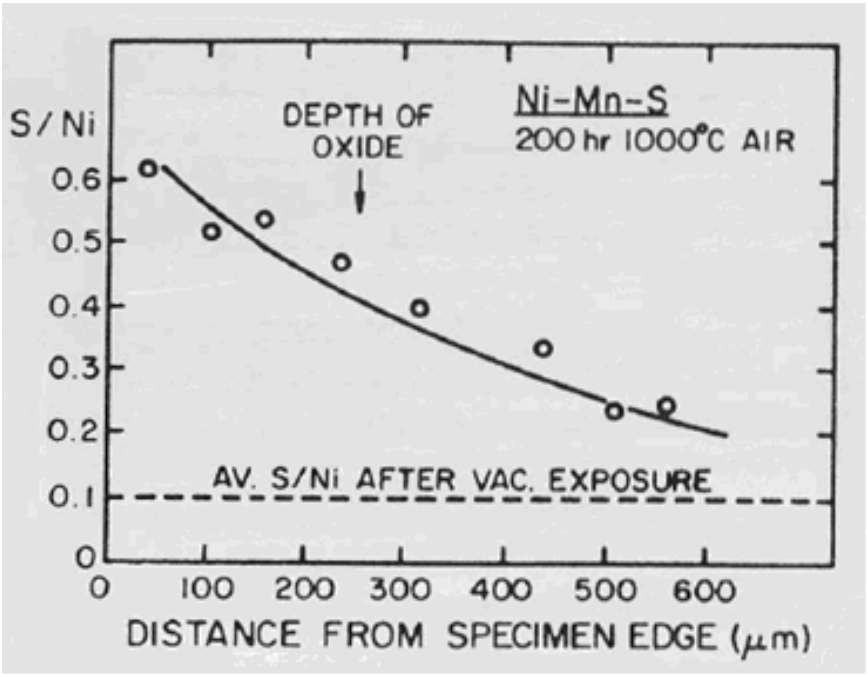

Figure 2.24: Oxide Depth as a Function of Specimen Edge Distance After 200 Hour Exposure to Air and Vacuum at 1000°C [61]

2.4.3: X-ray Photoelectron Spectroscopy

For their paper on oxygen enhanced crack growth in superalloys Wei et al used XPS to examine powdered metallurgy alloys reactivity to oxygen [53]. Three nickel based superalloy specimens were used for this study. Each specimen was cleaned by argon ion sputtering for 25 minutes prior to each oxidation experiment. The oxidation experiment consisted of heating the alloys to 973 K in an ultrahigh vacuum environment for a total of 75 minutes. The specimens were then exposed to low pressure oxygen for 45 minutes at a temperature of 973 K. XPS was performed three times; after argon ion sputtering, after UHV heating, and after low pressure oxygen heating.

The sputtered and oxidized surface XPS peak area % can be seen in Table 2.3. It can be seen that the elements Cr, Fe, Ti, Al, and Nb all oxidized from the low pressure oxygen environment. Cr, Ti, Al, and Nb also oxidized during the UHV environment. The authors proposed that the oxidation during the UHV environment was due to dissolved atomic oxygen in the sample migrating to the polished surface and out-gassing of oxygen and water from the heating element. From Table 2.3 it can clearly be seen that oxidation increases with temperature and in the presence of an oxygen rich environment.

Table 2.3: Percent Relative XPS Peaks for Alloys 1 and 3 and Inconel 718 [53]

	Ni	Cr	Co	Fe	Ti	Mo	Al	Nb
Alloy 1 (sputtered)	51.4	10.5	21.0	–	2.8	4.0	10.3	–
UHV (973 K)	31.7	19.8	17.3	–	5.7*	3.9	21.6*	–
Oxygen (973 K)	8.0	44.8*	3.8	–	10.6*	2.0	30.9*	–
Alloy 3 (sputtered)	52.8	10.3	20.2	–	1.5	4.2	7.1	4.0
UHV (973 K)	37.4	16.2	16.6	–	3.3*	4.8	15.5*	6.1*
Oxygen (973 K)	14.5	40.6*	4.4	–	5.8*	2.1	20.9*	11.8*
718 (sputtered)	59.7	15.9	–	12.9	0.9	3.8	3.1	3.6
UHV (973 K)	34.5	35.1*	–	9.3	1.5*	4.3	5.9*	9.4*
Oxygen (973 K)	2.3	64.3*	–	20.9*	0.9*	0.5	2.1*	9.0*

For the crack growth portion of this study a SEM was used to examine the oxygen affected region (OAR) [53]. The scanning electron microscope is able to image the surface of the specimen by raster scanning a high energy beam of electrons across the specimen surface. Ahead of the propagating crack tip there is a zone that reacts when coming in contact with oxygen. This oxidation causes embrittlement in the material enabling an increased crack growth rate.

This test was performed by propagating cracks in both a UHV environment and also a low pressure oxygen environment [53]. These specimens were then analyzed using SEM

and the microfractographs can be seen in Figure 2.25. Frequency testing showed that slower cycles allow more oxidation increasing the oxygen embrittlement in the specimen.

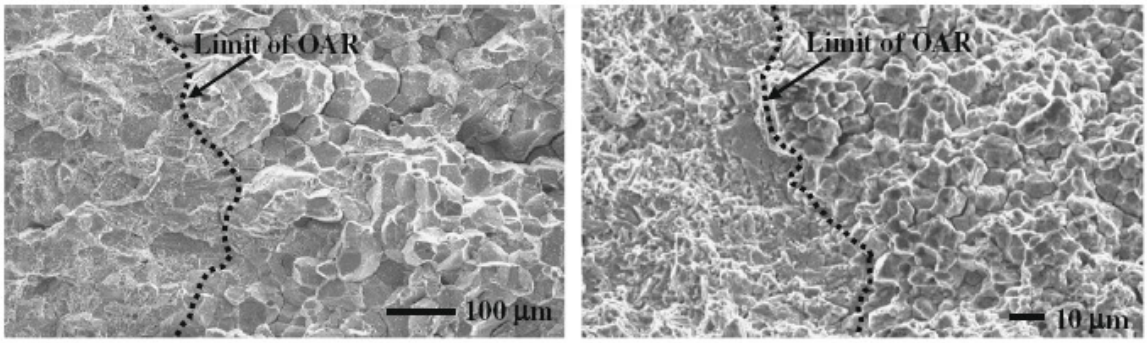

Figure 2.25: SEM Microfractographs Showing Oxygen Affected Region [53]

2.5: Fatigue Crack Service Life Prediction Methodologies

2.5.1: Safe-Life (Life-to-First-Crack)

The safe-life, also known as the life-to-first-crack approach to lifing is the most conservative of all life prediction techniques. Safe-life assumes new parts are defect free and as soon as the component reaches a predetermined cycle count, the critical gas engine element is replaced regardless of the state of the particular part. With improving NDI techniques, the acceptable crack size is decreasing, with current capabilities being between 0.75mm and 0.38mm [71-73]. In the case of turbine disks, spin tests are performed to determine the number of cycles required to grow a crack to the NDI detection limit. A predicted safe cyclic life (PSCL) is then calculated where only 1 in 750 disks would have a NDI detection limit, to 95% confidence. Assuming a scatter factor of 6, the -3σ quartile is located a factor of $\sqrt{6}$ below the geometric mean of the spin testing data, seen in Figure 2.26. This lower confidence bound corresponds to a $6^{1.645/6\sqrt{n}}$ life safety factor.

Where n is the test sample size and a 95% confidence level corresponds to 1.645. The predicted safe cyclic life of the component is then calculated using the following equation:

$$PSCL = \frac{\sqrt[n]{\prod_{i=1}^{n} N_i}}{2.449x6^{(1.645/6\sqrt{n})}} \quad \textbf{(2.9)}$$

Where $N_{i,}$ are the individual spin test results. This life prediction technique is very conservative as the crack length to promote fast fracture is most likely larger than the NDI detection limit.

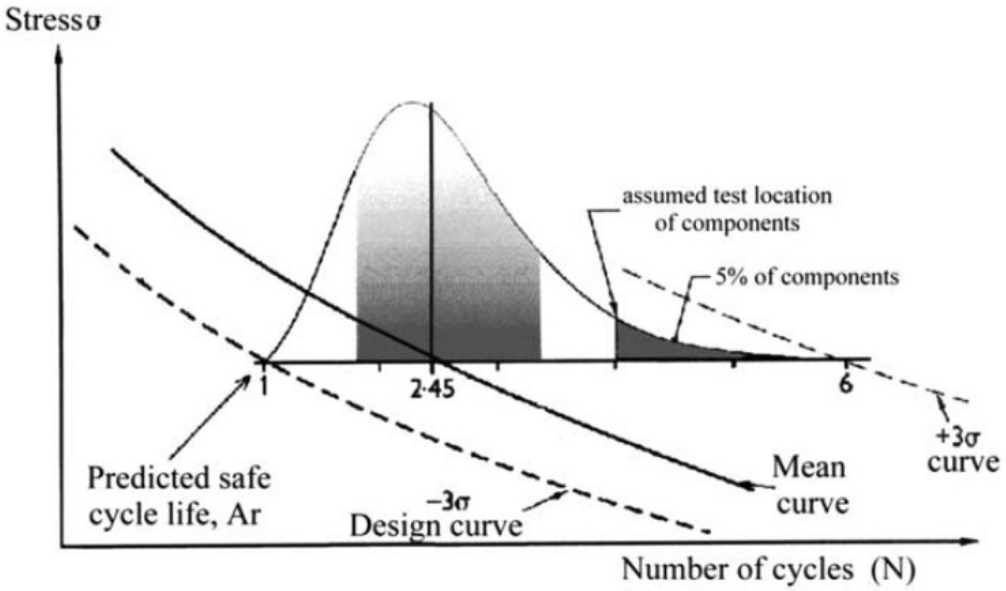

Figure 2.26: Derivation of the Material Design Curve and Predicted Safe Cyclic Life [71]

2.5.2: Damage-Tolerant (Retirement for Cause)

The damage-tolerant, also known as the retirement for cause approach came about due to the life monitoring requirements in the Engine Structural Integrity Program (ENSIP) introduced in the 1970's [74]. This lifing approach is based on the premise that even new components sometimes have flaws that grow in a predictable manner until a critical crack length is reached. This initial flaw size is assumed to be the NDI detection limit. This limit is combined with fracture mechanics and fatigue crack growth data to determine the fatigue life. Integrating the Paris expression creates the following equation for calculating the number of cycles for failure:

$$N_f = \frac{2}{(m-2)Cf^m(\Delta\sigma)^m\pi^{m/2}}\left[\frac{1}{(a_{NDI})^{(m-2)/2}} - \frac{1}{(a_{crit})^{(m-2)/2}}\right] \quad \textbf{(2.10)}$$

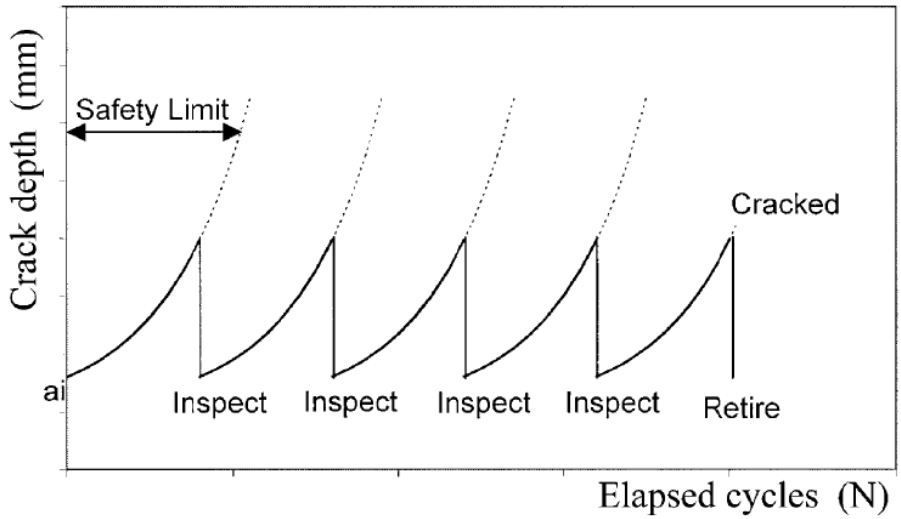

Figure 2.27: Schematic Representation of the Retirement for Cause Approach Where Inspections Are Used to Extend Damage Tolerance [71]

This calculated fatigue life is then used to set up NDI intervals as seen in Figure 2.27. The initial inspection interval is usually ½ of the calculated fatigue life. To maximize the

life of the component additional inspection intervals are added with decreasing cyclic duration. This combination of damage tolerance and risk analysis creates the foundation for the U.S Air Force retirement for cause methodology.

2.5.3: Equivalent Initial Flaw Size

The equivalent initial flaw size (EIFS) approach takes into account both initiation and propagation unlike the above mentioned damage tolerant approach that only looks at the propagation life. In that aspect this approach could be thought of as being similar to the safe-life approach but not nearly as conservative. The initiation life of a fatigue crack is very difficult to predict, being a complicated function of material type, processing, environment, geometry and loading spectrum. It is often difficult to come to a general consensus on what is the definition of a crack. The key is being able to properly determine, initiation time, which is the number of cycles it takes to reach a crack size that is detectable using NDI techniques. Being able to properly predict this adds more fidelity to a model than just setting the initial crack size to the NDI limit. Using data available the EIFS is determined by extrapolating back to a time or cycle count equal to zero. These EIFS distributions, seen in Figure 2.28, can then be used as a more precise starting point for probabilistic and damage tolerance approaches to FCG life prediction [75].

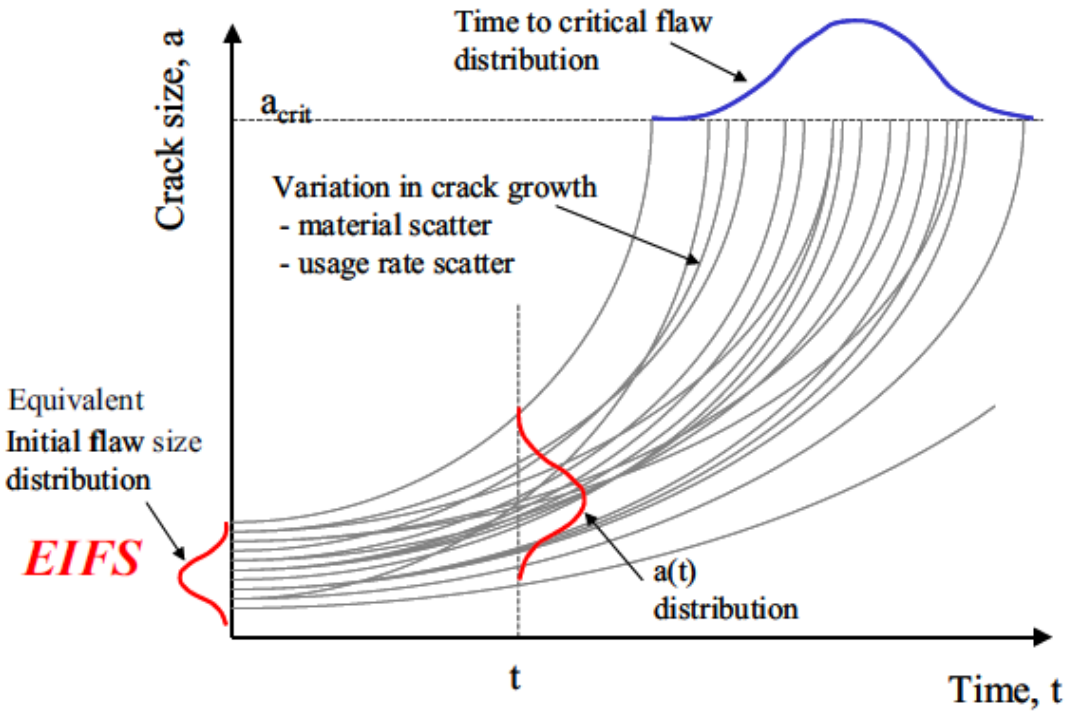

Figure 2.28: The Equivalent Initial Flaw Size Can Be Used as Starting Point for Probabilistic Life Prediction [75]

CHAPTER 3: EXPERIMENTAL METHODS

3.1: Material

Developed in the early 1960's, IN100 is a powder metallurgy (P/M) superalloy commonly used for components operating at intermediate temperatures, such as disks, spacers and seals [76]. In order to most accurately assess real world fatigue crack growth rates the material was supplied in the form of a Pratt & Whitney jet engine turbine disk in the fully heat treated state. This disk was heat treated with a solutioning treatment of 1143°C, (below the gamma prime solvus temperature of 1192°C) and oil quenched. Solutioning was followed by a two step aging heat treatment first at 982°C for an hour then forced air cooled, then held at 732°C for 8 hours then air cooled. The chemical composition of the IN100 disk evaluated can be seen in Table 3.1.

Table 3.1: Chemical Composition (in % wt.) of IN100 Disk Evaluated

	Al	B	C	Co	Cr	Mo	Ti	V	Zr	Ni
IN100	4.90	0.02	0.07	18.20	12.10	3.22	4.20	0.70	0.07	56.52

3.2: Specimens

3.2.1: Specimen Design

For this investigation the Single Edge Notch Tension (SENT) specimen configuration was chosen due to its' ease of crack measurement and ability to be gripped with water cooled hydraulic wedge grips. Specimens were cut radially from the supplied Pratt & Whitney jet engine disk as seen in Figure 3.1. The specimens used for testing are

203.2mm long, 38.1mm wide and 2.54mm thick and can be seen in Figure 3.2. For quick fatigue crack initiation, electro-discharge machining was used to create an 11.43mm long notch with a 0.1524mm root radius.

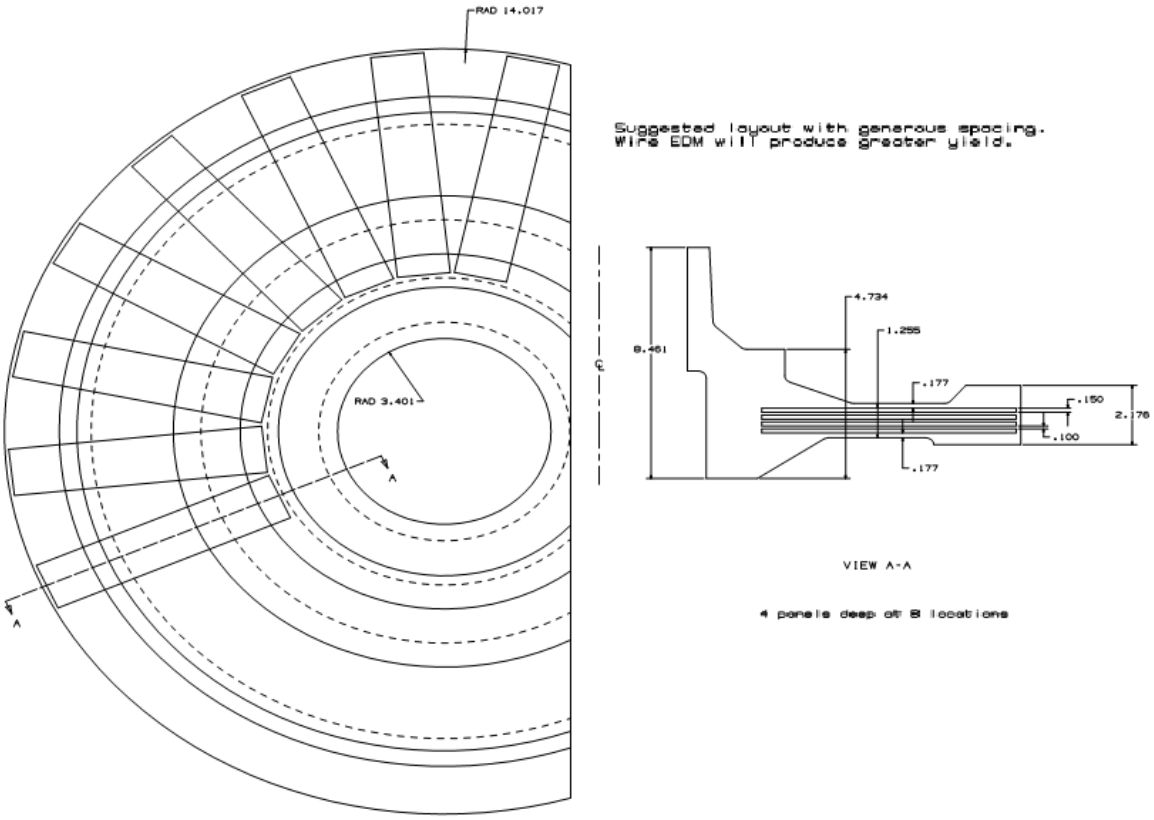

Figure 3.1: Schematic Showing How Specimens Were Cut Out of Supplied Jet Engine Disk

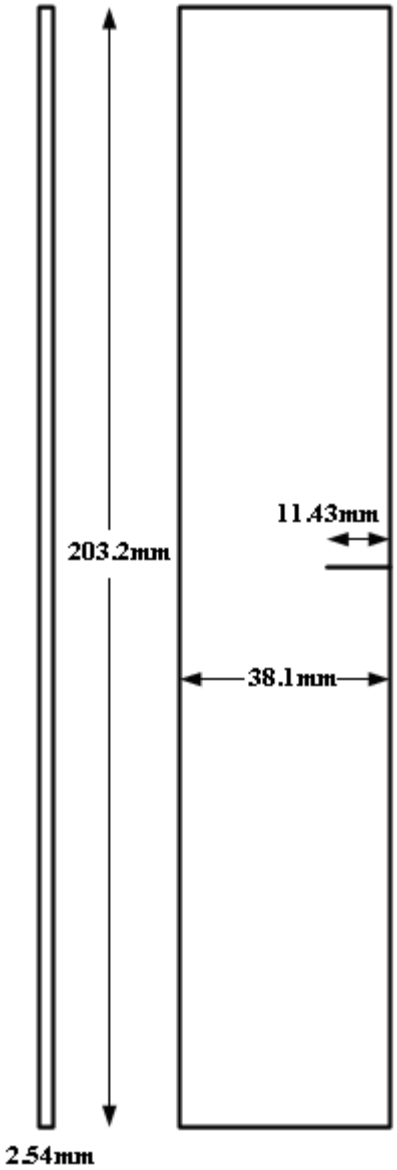

Figure 3.2: Single Edge Notch Tension Specimen with Dimensions

3.2.2: Specimen Preparation

Specimens were machined by the manufacturing division of MAR-TEST Inc. (Cincinnati, OH). A total of 10 IN100 single edge notch tension specimens were produced for fatigue crack growth testing. Low stress grinding was utilized during the production process to ensure that residual surface stresses were kept to a minimum.

For optimal viewing of the crack tip specimens were ground and polished in front of the EDM notch on the side of the specimen that was to be observed by the optical microscope. Specimens were first ground with 320 grit silicon carbide paper. This was followed up with 600 grit silicon carbide paper. Specimens were then polished using 6 and ½ micron diamond lapping paste. Polishing was aided with a Dremel tool and a felt polishing wheel.

High temperature glass insulated "K" type thermocouples were then precisely welded in the center of the specimens just below the crack path for optimal temperature control. The thermocouple position can be seen in Figure 3.3.

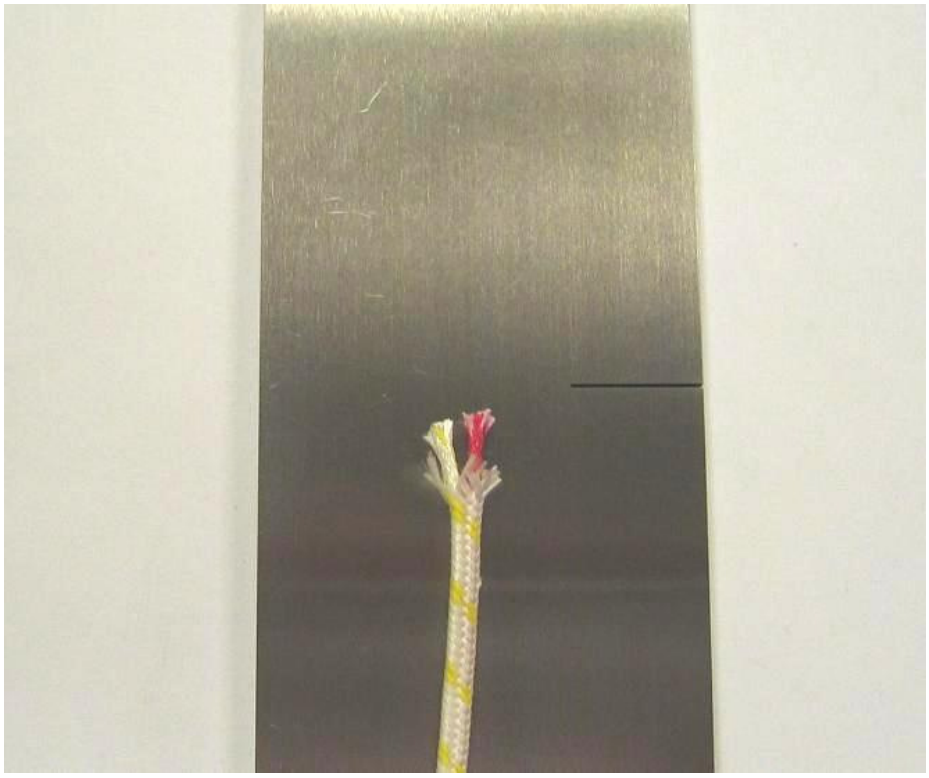

Figure 3.3: Thermocouple Placement in the Center of the Specimen Just Below the Crack Path

3.2.3: Laser Etched Gridding

To aid in measuring the crack length several different types of gridding were considered for the specimens. These very precise lines would run perpendicular to the EDM notch and need to be visible at temperatures in excess of 649°C. It was decided to have lines space every 0.254mm apart with every 2.54mm line distinguished by being wider. Gold printing and laser etching emerged as the two primary possibilities. The ability for the printing to stay attached and be visible through the accumulation of surface oxides at higher temperatures led to the selection of laser etching. Laser etching was performed by Richard Shafer in the Georgia Tech Microelectronics Research Center. The laser etching 0.254mm lines were determined to be best visible when they were made 0.0508mm wide with the 2.54mm wide lines being made 0.1016mm thick. With the depth of the etchings made to be 0.01016mm or 0.4% the thickness of the specimens no effect on crack growth would be expected. These etchings can be seen in Figure 3.4.

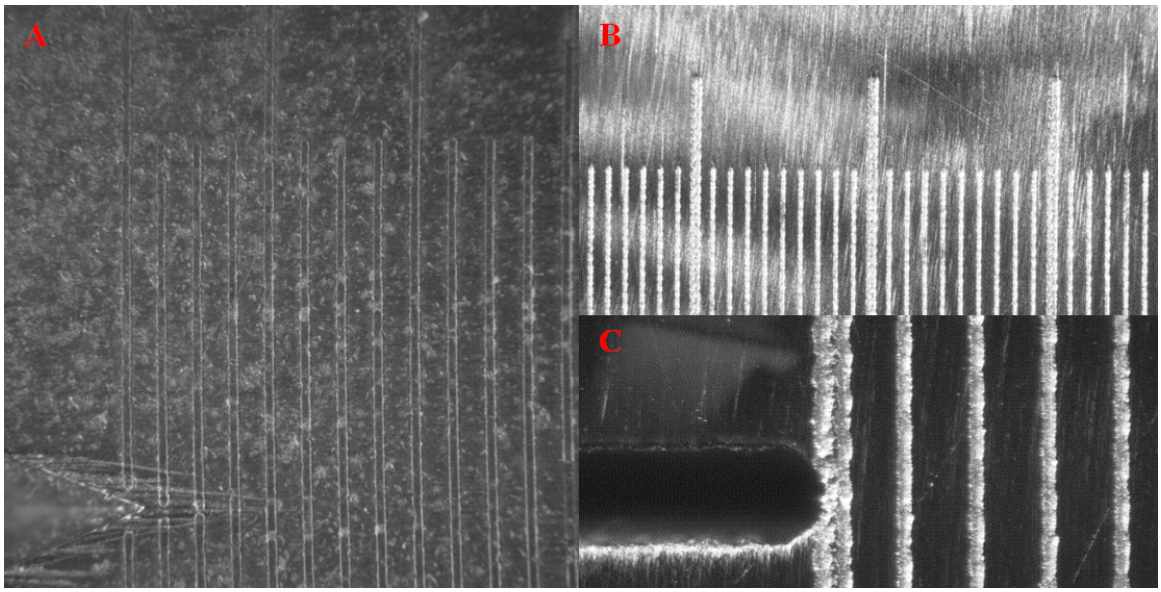

Figure 3.4: Gold Printing (A) and Laser Etching (B, C)

3.3: TMF Testing

The nickel based components in gas turbine engines are subjected to extreme fluctuations in both stress and temperature as can be seen in Figure 3.5. This combination of mechanical and thermal strains has been shown to be responsible for great damage in many engineering systems especially the gas turbine industry [77]. This combination of cyclic stress and temperature variation is known as thermo-mechanical fatigue. The understanding of the TMF crack behavior of hot section superalloys is crucial for the development of sophisticated life prediction methods. TMF testing procedures for startup, setup and shutdown can be found in Appendices A.2 through A.4, respectively.

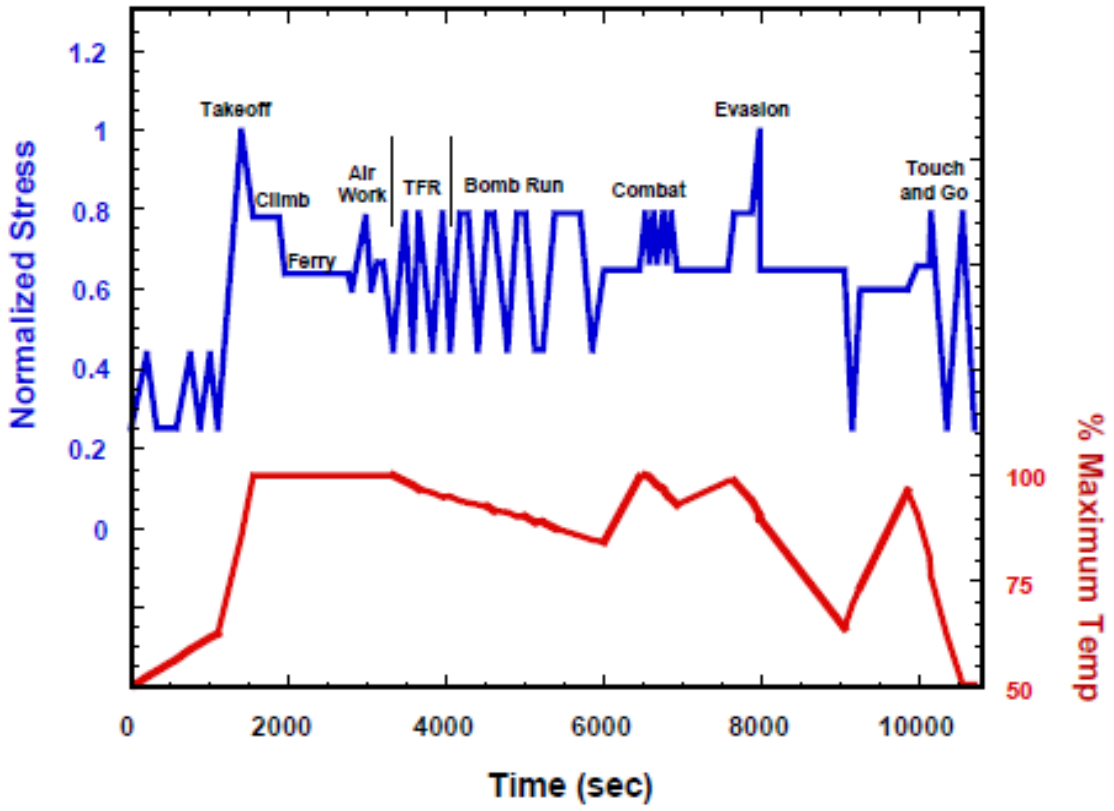

Figure 3.5: Fighter Jet Flight Spectrum Showing Cyclic Mechanical and Thermal Loading [49]

3.3.1: Test Rig

Shown in Figure 3.6 a 98 kN MTS servo-hydraulic load frame paired with a MTS TestStar IIs control system was used for testing of the SENT specimens. MTS TestStar IIs software allows for the creation of elaborate test programs featuring cyclic loading and temperature. Water cooled hydraulic wedge grips were used for rapid heat dissipation during temperature cycling. Specimens were gripped approximately 50.8mm on each end by pyramid teeth wedge grips 44.45mm wide as seen in Figure 3.7. The use of a laser level ensured that specimens were positioned in a repeatable fashion and placed squarely in the grips. Nominal grip pressure was set at 16,550 kPa.

Crack length measurement was accomplished through the use of a QM-100, Questar Microscope mounted on a three-axis Remote Measurement System platform with linear encoders. This microscope has the ability to magnify the crack tip between 50x and 300x for optimal crack length measurement. Attached to this microscope is an Edmund Optics USB 2.0 CCD camera with the ability to take still images and record video.

Figure 3.6: MTS Load Frame Used for Thermo-Mechanical Fatigue Testing

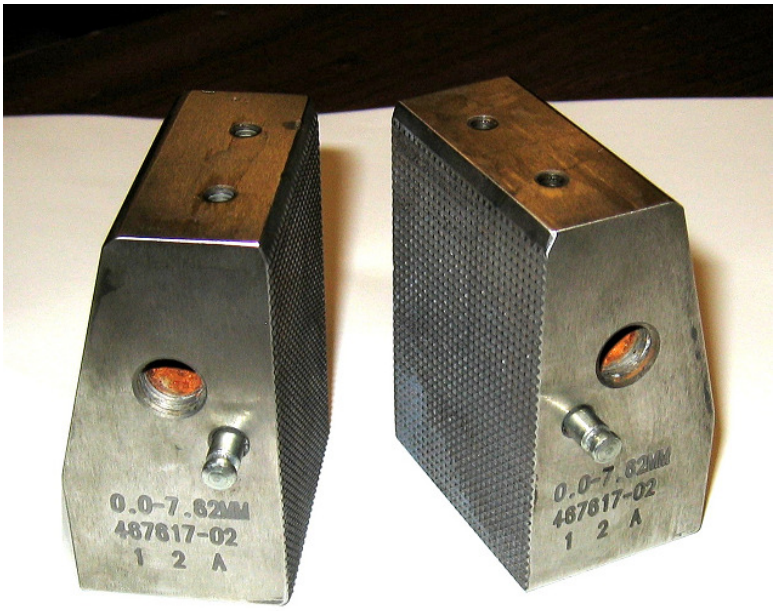

Figure 3.7: Water Cooled Pyramid Teeth Wedges

Figure 3.8: Ambrell Hotshot 3.5 kW Induction Heater (left) and Heating Station (right)

An Ambrell Hotshot 3.5 kW induction heater and heating station seen in Figure 3.8, along with high temperature glass insulated "K" type thermocouple wire was used to maintain temperatures ranging from 316°C to 649°C. An unique coil design made out of 4.76mm copper tubing was created with a 11.43mm crack viewing window with 3 turns above and below to provide uniform heat distribution. Thanks to the hard work of a previous graduate student this testing apparatus was already in place. There were just a

couple items that needed to be added to increase the functionality of this TMF test rig. Twin cooling fans controlled by the EuroTherm temperature controller were added to the TMF test rig to aid in rapid heat dissipation. These cooling fans along with the copper induction coil can be seen in Figure 3.9. Temperature inspection using an optical pyrometer showed a very minimal temperature variation of +/- 5°C across the crack plane.

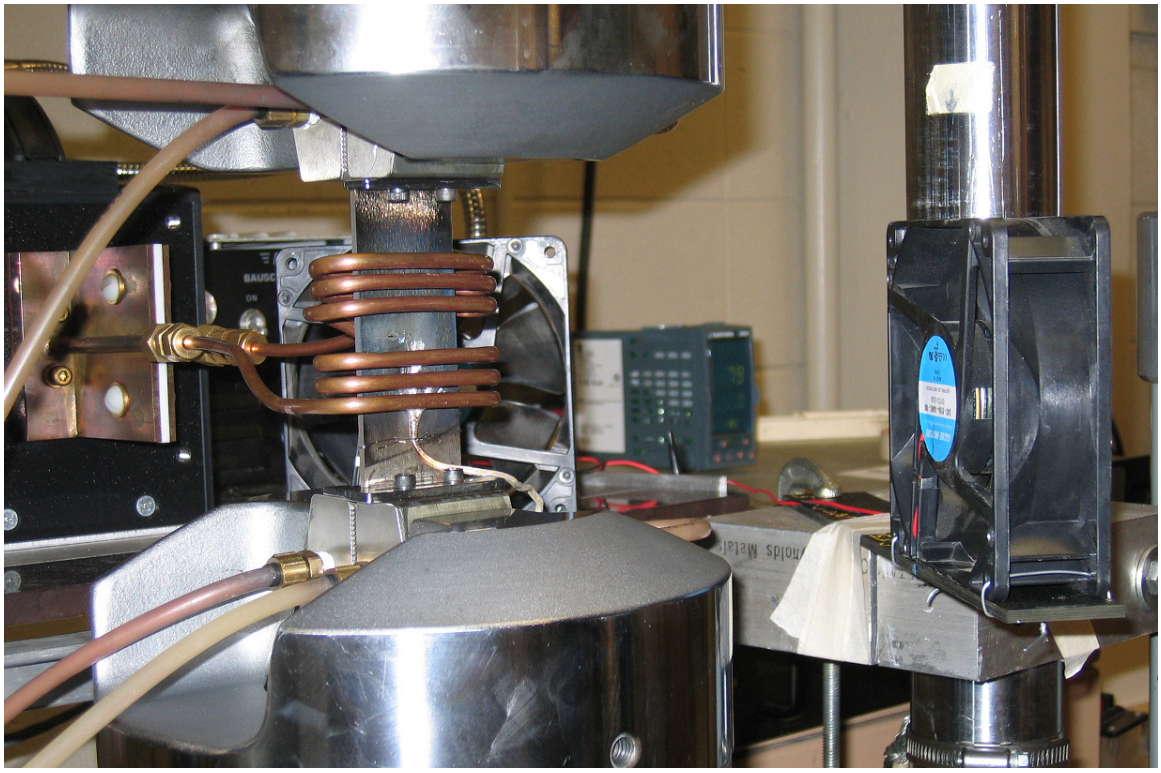

Figure 3.9: Specimen in Test Rig Showing Unique Coil Design and Twin Cooling Fans

For safety the TestStar IIs control system was set up to interlock the hydraulic pump when the applied load deviated outside of controlled limits. In the event of a specimen fast fracture failure there were also interlocks set for when the displacement deviated

outside an upper and lower limit. Improving the safety of the system a relay was added to disable the induction heater when the hydraulic interlock system was tripped.

3.3.2: Testing Standards

Fatigue crack growth testing was done in accordance with the ASTM Standard Test Method for Measurement of Fatigue Crack Growth Rates, E647-08 [78]. Below is a summary of this test method according to the ASTM standard:

> *This test method involves cycle loading of notched specimens which have been acceptably precracked in fatigue. Crack size is measured, either visually or by an equivalent method, as a function of elapsed fatigue cycles and these data are subjected to numerical analysis to establish the rate of crack growth. Crack growth rates are expressed as a function of the stress-intensity factor range, ΔK, which is calculated from expressions based on linear elastic stress analysis.* [78]

This standard lists many requirements that need to be met in order for the test to be considered a success. Several of requirements applicable to this study are as follows:

Requirement #1: Precracking must be performed on a specimen fully heat treated to the condition it is to be tested and may be executed at any convenient frequency. The fatigue precrack must be at least $1/10^{th}$ the specimen thickness, the notch height, or 1.016mm, whichever is greater. Fatigue Precracking was also performed in accordance with ASTM Standard Test Method of Linear-Elastic Plane-Strain Fracture Toughness K_{IC} of Metallic Materials, E399-09 [79].

Requirement #2: Crack measurement equipment should be capable of resolving 0.1016mm or $1/500^{th}$ the specimen width, whichever is greater. Applying reference grids

to the surface of the polished specimen decreases the chance of measurement area. It is preferred that crack length measurements are taken without test interruption.

Requirement #3: Crack measurements should be taken with a minimum crack length interval of 0.254mm. In situations where Δa must be smaller, such as near threshold, the minimum shall be ten times the crack size measurement precision.

Requirement #4: If the crack deviates more than 20° from the notch plane over a distance of $1/10^{th}$ the specimen width the data is invalid. If the crack deviates between 10° and 20°, this deviation must be reported along with the data.

Requirement #5: If crack tip tunneling is present and a crack curvature correction results in a 5% or greater change in stress intensity factor, then this correction should be applied when analyzing the test data.

CHAPTER 4: CRACK GROWTH RATE MODELING

A model, using the isothermal constant amplitude test data obtained in this study, was created to calculate crack growth cycle by cycle and was used as a baseline for subsequent fatigue crack growth interaction testing. This model can be seen in Appendix A.5. Generating a model based on the Paris equation and using Paris constants from multiple sets of test data, allows the ability to calculate non-interaction crack growth for TMF profiles with overloads and cycling temperature. Comparing the crack growth predicted with the non-interaction model to actual experimental data will show growth or retardation that can be attributed to load and temperature interactions.

Due to ease of programming, MATLAB was chosen as the numerical computing environment for modeling. Crack length calculation was done through the use of a forward iterative loop. Starting with an initial crack length the stress intensity factor was calculated. Knowing the maximum and minimum cyclic loading and using the initial crack length and previously calculated SIF, ΔK can then be calculated. Using the Paris equation (Equation 2.6), Paris constants and ΔK an increment in new crack growth can then be calculated. This increment is then added to the initial crack length and a new SIF can then be calculated based on the current crack length. This process is repeated until a critical crack length is reached for the specimen being modeled. As the modeling is done cycle by cycle at anytime the maximum and minimum cyclic loads and Paris constants can be changed to represent underloads, overloads or a change in temperature.

4.1: Temperature Interactions

The first Paris law modeling ignoring interaction effects was for the case of changing temperature between 316°C and 649°C. The effect of cycling between 316°C and 649°C every one, ten and one hundred cycles was looked at. The results can be seen in Figure 4.1. Also shown in the figure is isothermal crack growth data for the 316°C and 649°C experiments from which the Paris constants were extracted. As can be seen in Figure 4.2, when temperature interaction effects are ignored the one, ten and one hundred alternating cycle block growth rates are the same.

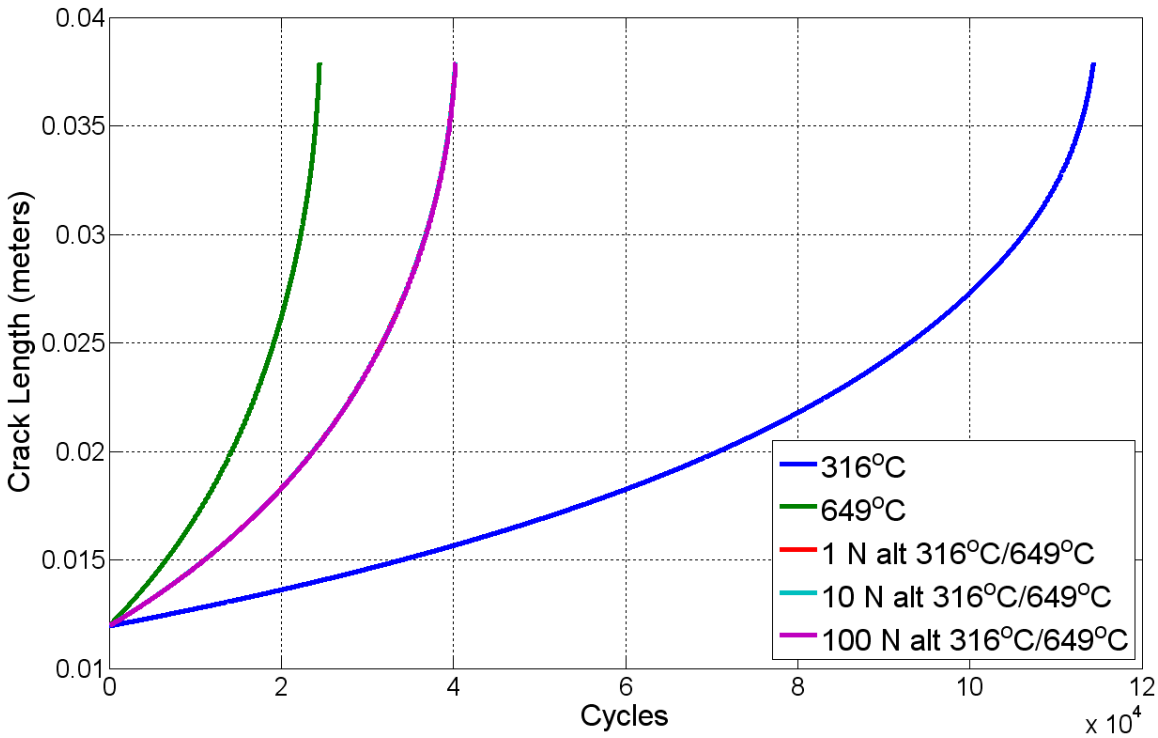

Figure 4.1: Non-Interaction Model Prediction for 1, 10 and 100 Cycle Blocks Alternating between 316°C and 649°C

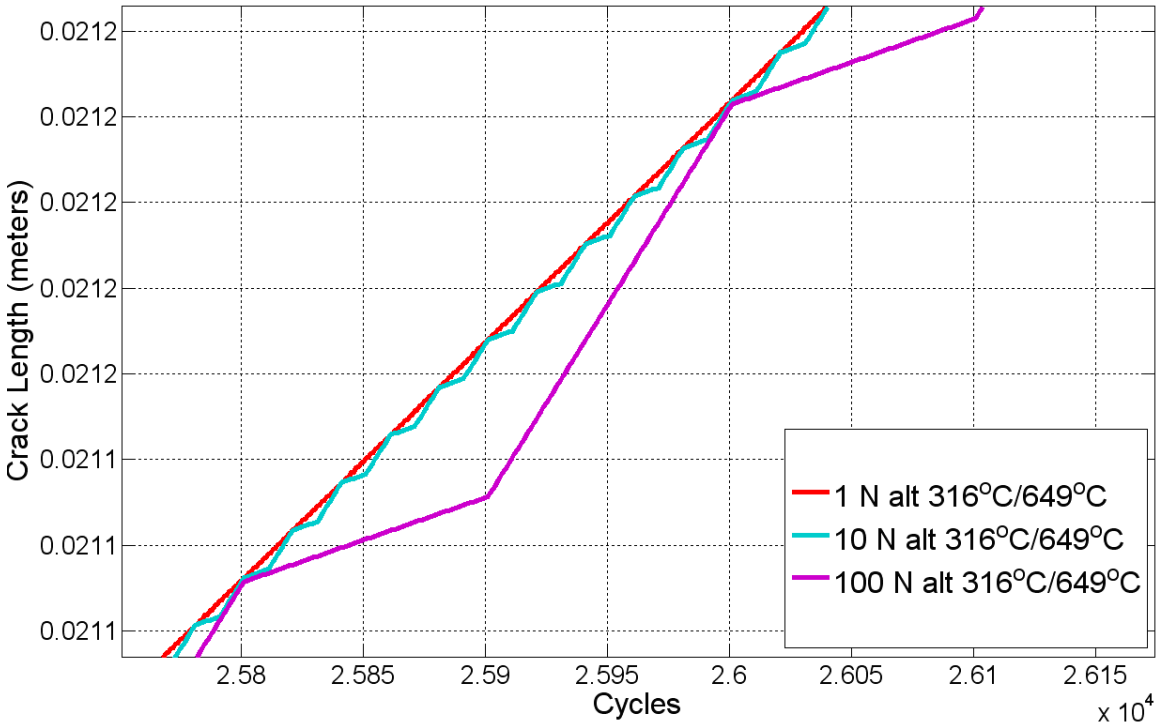

Figure 4.2: Non-Interaction Model Prediction for 1, 10 and 100 Cycle Blocks Alternating between 316°C and 649°C

4.2: Load Interactions

Non-interaction modeling was used to predict the effect of applying 1.3x, 1.6x and 2.0x overloads. Firstly Paris constants for 316°C isothermal experimental crack growth data were used to show the constant amplitude crack growth. In addition the crack growth from applying one 1.3x, 1.6x and 2.0x overload every 800 cycles at an isothermal temperature of 316°C is shown in Figure 4.3. Looking at this prediction it can be seen that all crack growth curves are very close together. Upon closer inspection in Figure 4.4, the crack growth is faster due to the overloads, with crack growth rate increasing as the size of the overload is increased. This same trend can be seen in Figure 4.5 and Figure 4.6 for the same model predictions done with isothermal 649°C data.

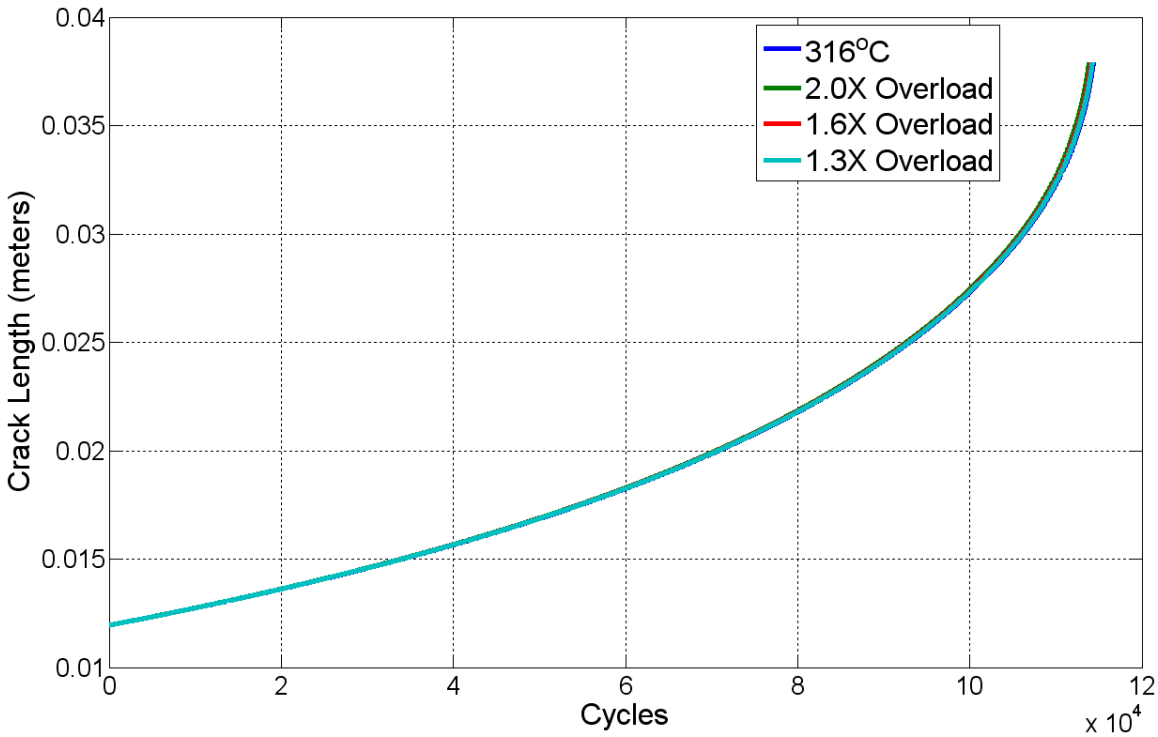

Figure 4.3: Non-Interaction Model Prediction for 1.3x, 1.6x and 2.0x Overloads Applied at 316°C

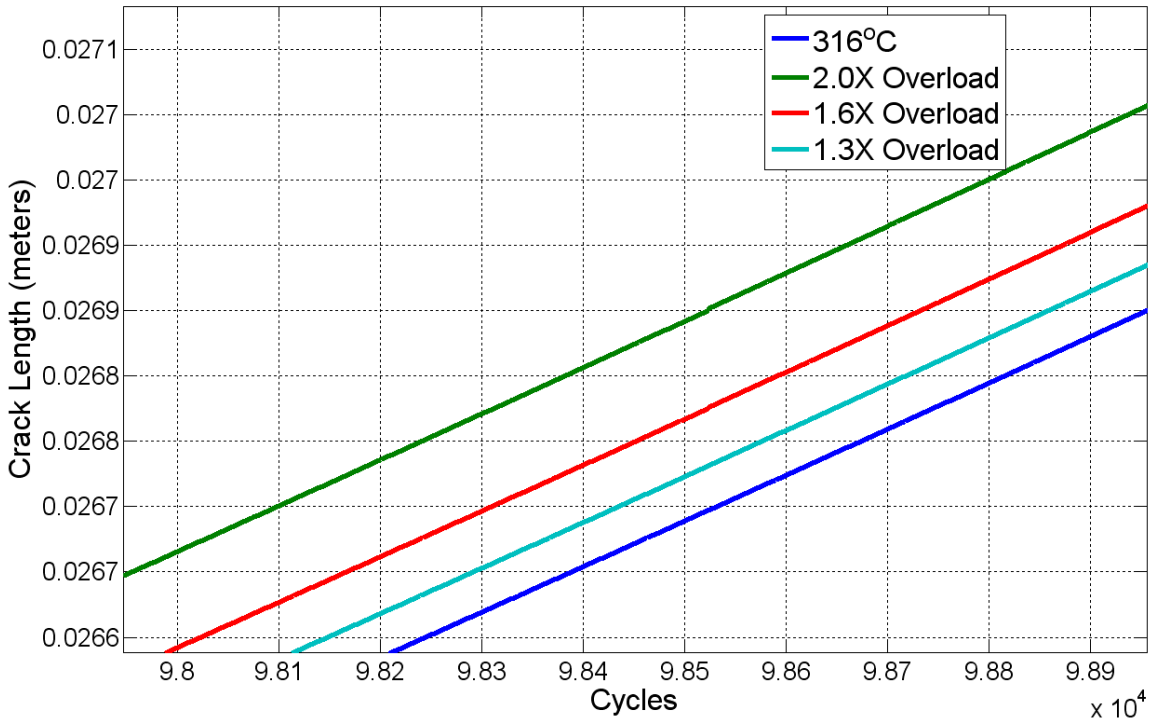

Figure 4.4: Non-Interaction Model Prediction for 1.3x, 1.6x and 2.0x Overloads Applied at 316°C

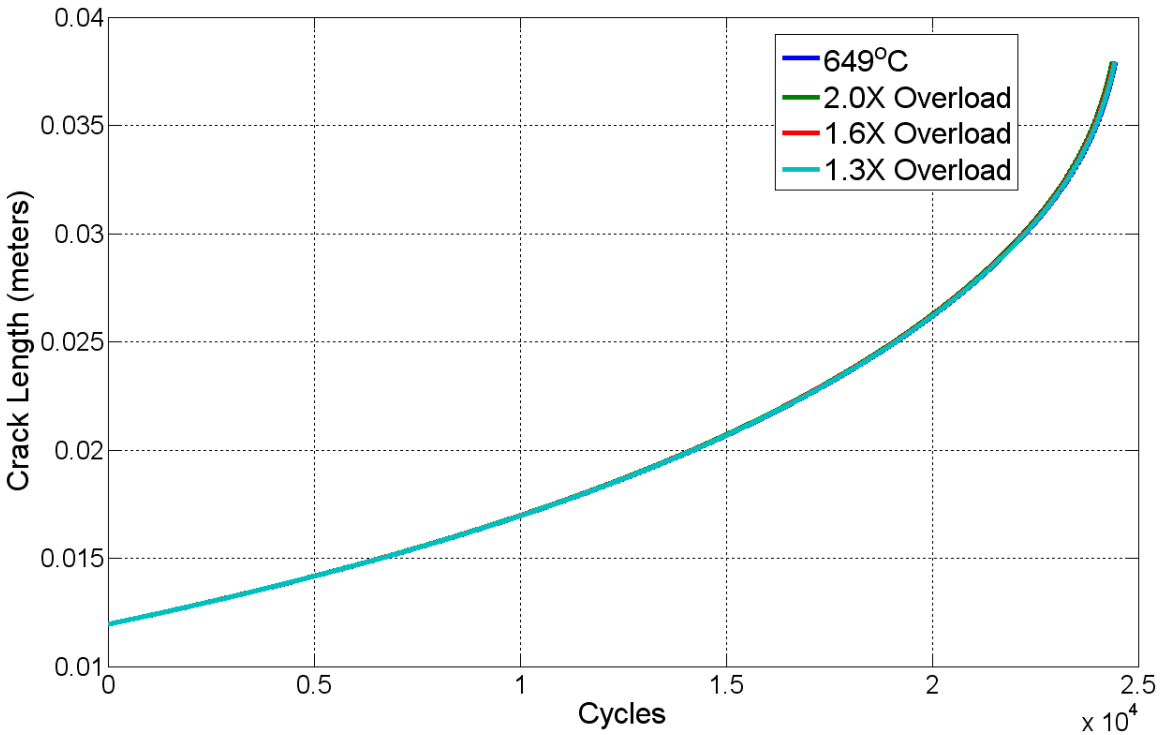

Figure 4.5: Non-Interaction Model Prediction for 1.3x, 1.6x and 2.0x Overloads Applied at 649°C

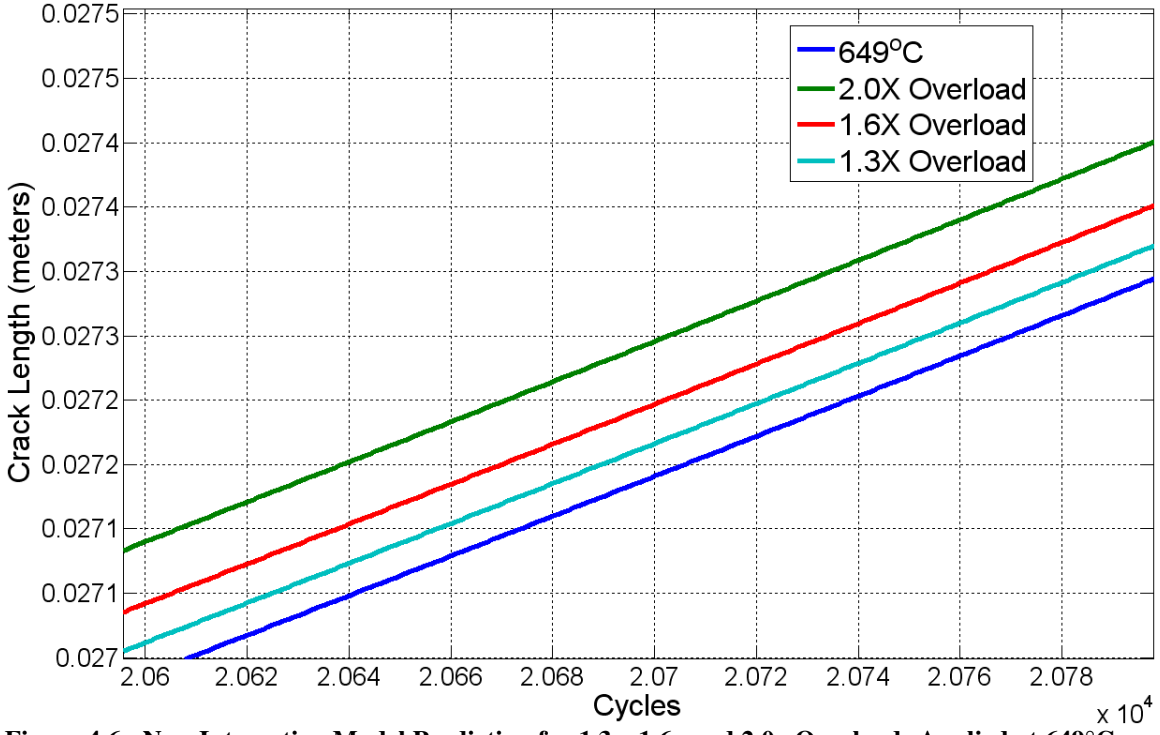

Figure 4.6: Non-Interaction Model Prediction for 1.3x, 1.6x and 2.0x Overloads Applied at 649°C

Non-interaction modeling provides a good baseline from which to compare experimentally determined load and temperature interactions. Interaction effects such as overload plastic zones, crack tip embrittlement and microstructural changes due to environmental exposure can then be quantified in terms of the differences between the non-interaction modeling and the interaction testing. This will be discussed further in the experimental results and conclusions.

CHAPTER 5: EXPERIMENTAL RESULTS

This section will start off by presenting the results of a material analysis on the IN100 disk material. The differences in a uniform stress vs. uniform displacement stress intensity factor for the SENT specimen will be discussed. Then a residual stress investigation will be presented along with the reasons for implementing marker bands. The fatigue crack growth rate data for constant amplitude isothermal testing for different temperatures, frequencies and specimen type will be discussed. This data will be compared to published FCGR data for IN100. Scanning electron microscope (SEM) fractography results will also be shown explaining the growth rate differences through the underlying failure modes and mechanisms. Following this crack growth data for load and temperature interaction tests will be shown. Fractography via SEM will show how the failure mechanisms have changed from what was seen during isothermal constant amplitude testing. An oxidation study will then be presented showing the effect of oxidation at different temperatures plays on the fatigue crack growth rate.

5.1: Material Analysis

The microstructure was examined using optical microscopy and a scanning electron microscope to evaluate the grain size, gamma prime distribution and percentage. The fine structure of IN100 makes it difficult to resolve the grain boundaries. This is even more compounded because the gamma grains are similar in size to the primary gamma primes. Specimens were prepared using the cold-mounting, grinding, polishing and etching procedure can be found in Appendix A.1. The waterless Kalling's etching

solution coupled with a scanning electron microscope worked the best for revealing the microstructure [80]. The gamma matrix grain boundary is one of the more difficult microstructural features to properly chemical etch in IN100. The grain boundaries' etching resistance leaves it raised above the surrounding microstructure [10, 81]. When the etched surface is bombarded with electrons the grain boundary appears as a white outline due to electron charging. As can be seen in optical Figure 5.1 and SEM Figure 5.2 the grain size is approximately 3-5 microns with primary gamma prime sizes of 2 microns. This agrees well with what is found in published literature for IN100 [46, 82, 83]. The two most significant phases in IN100 are the gamma prime phase consisting of primary, secondary and tertiary precipitates and the solid solution gamma matrix; creating a relative volume fraction of 60:40 as seen in Figure 5.3.

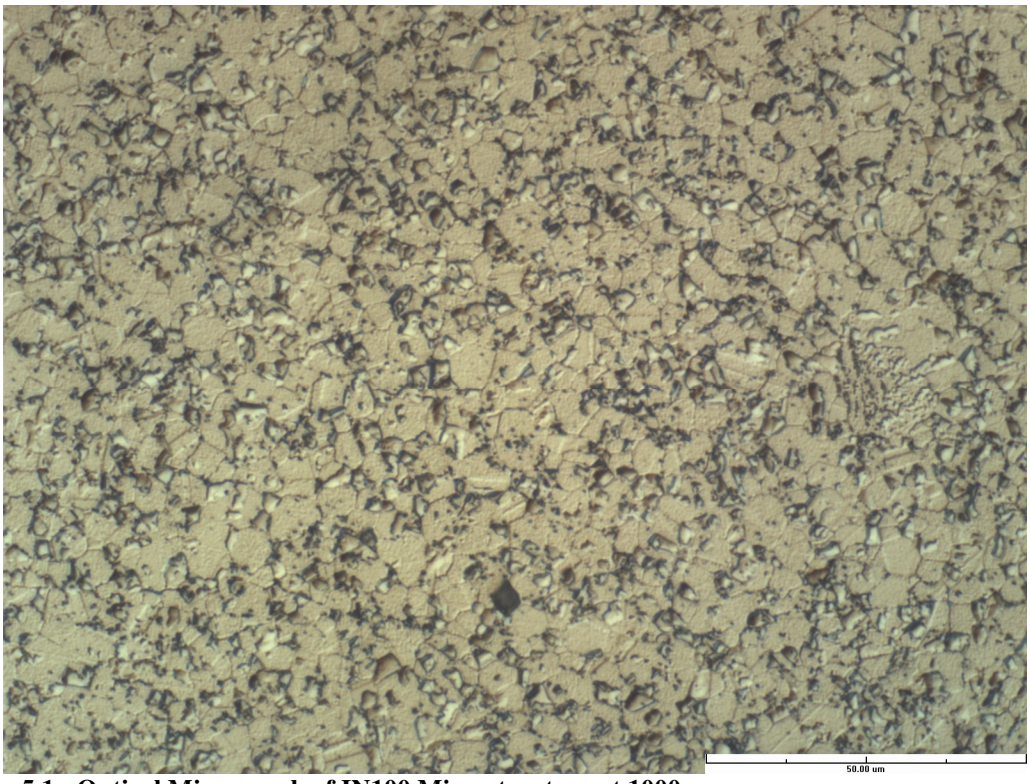

Figure 5.1: Optical Micrograph of IN100 Microstructure at 1000x

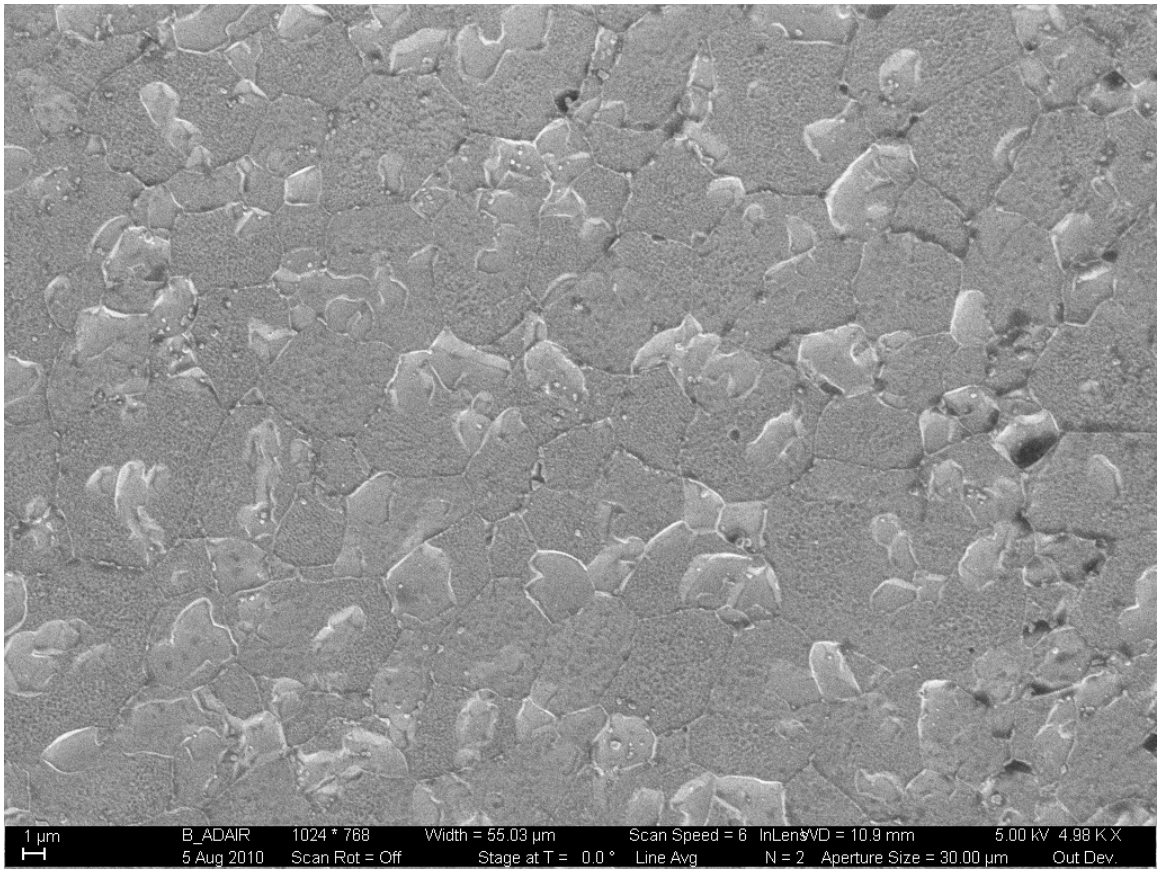

Figure 5.2: SEM Micrograph of IN100 Microstructure at 5000x

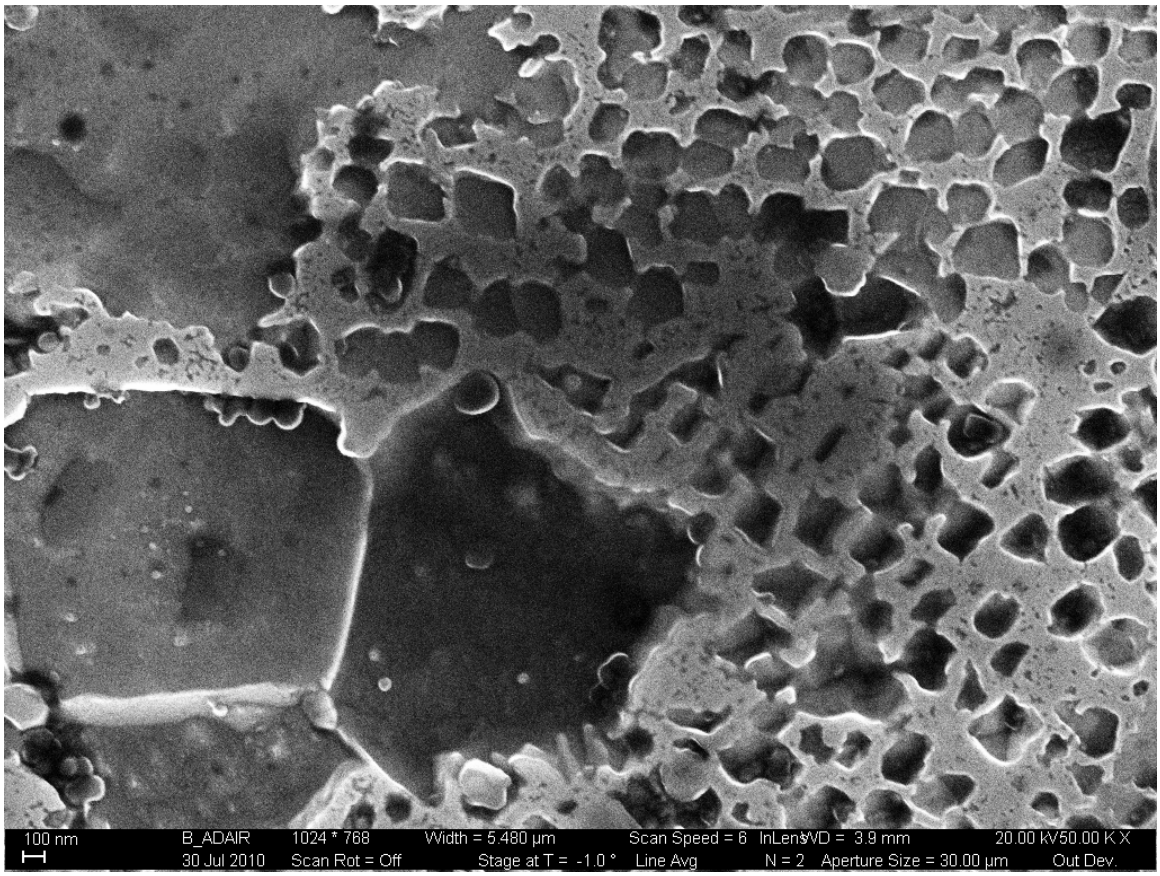

Figure 5.3: SEM Micrograph of IN100 Microstructure at 50,000x

The microstructure of the supplied IN100 was analyzed using energy-dispersive x-ray spectroscopy (EDS) to verify the elemental composition of the supplied IN100. These results show very good agreement with the IN100 composition provided by Pratt & Whitney and can be seen in Table 5.1. Aluminum, Cobalt, Titanium and Vanadium were all within 1% of the expected values, while Chromium and Molybdenum were within 2% of the values provided by Pratt & Whitney. Unsurprisingly the most abundant element, Nickel, was off the expected value the most with a difference of 3%. These minor differences are most likely due to the limited inspection area and the tendency for elements to enter preferentially either the gamma matrix or the gamma prime precipitate phase during heat treatment. Due to the very low expected amounts of Boron, Carbon

and Zirconium in IN100, 0.02%, 0.07% and 0.07% respectively, they were not detected during the EDS analysis. The EDS analysis was performed in the gamma matrix material location shown in Figure 5.4. Figure 5.5 shows the electron count as a function of binding energy measured in electron volts.

Table 5.1: EDS Determined Elemental Composition of Supplied IN100 Disk

Element	App Conc.	Intensity Corrn.	Weight %	Weigh % Sigma	Atomic %
Al K	2.65	0.6550	4.22	0.54	8.65
Ti K	4.62	1.0068	4.80	0.65	5.54
V K	0.93	0.9967	0.98	0.57	1.06
Cr K	13.13	1.0367	13.24	1.06	14.08
Co K	17.36	0.9561	18.97	1.62	17.80
Ni K	50.97	0.9946	53.56	1.98	50.44
Mo L	3.02	0.7447	4.24	1.25	2.44
Totals			100.00		

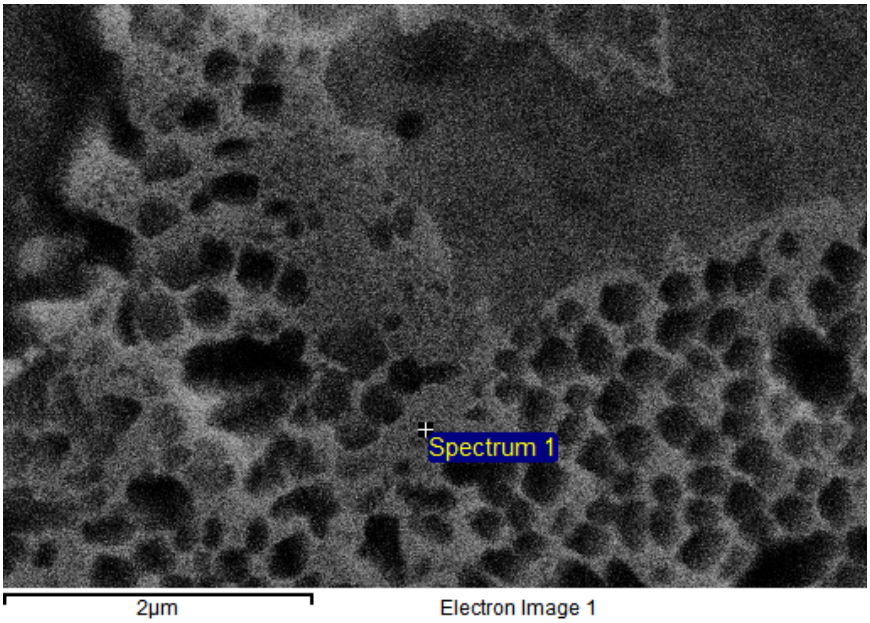

Figure 5.4: Gamma Prime Location of IN100 EDS Analysis

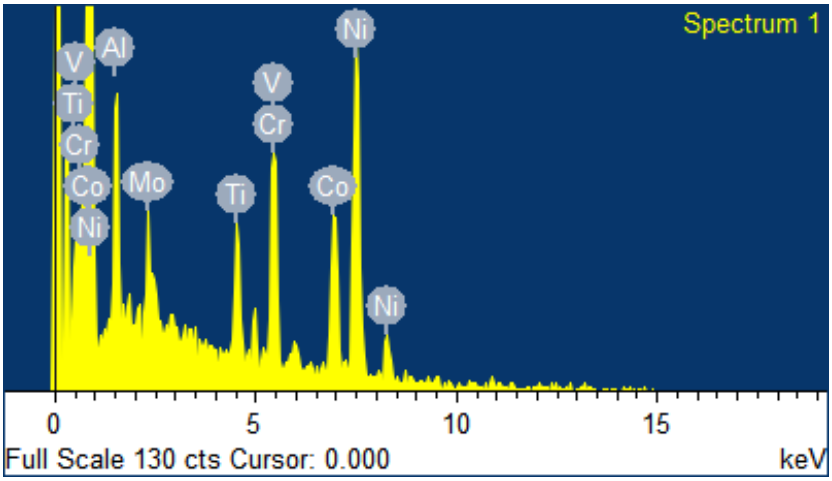

Figure 5.5: Counts as a Function of Binding Energy for IN100 EDS Analysis

5.2: Specimen

5.2.1: Uniform Stress vs. Uniform Displacement

Gripping the SENT specimens with hydraulic wedge grips creates a uniform displacement boundary condition. It is well known that a uniform stress boundary condition yields a much different stress distribution than a uniform displacement boundary condition as seen in Figure 5.6. By performing a review of published stress intensity factor solutions it became apparent that most if not all solutions were for a uniform stress boundary condition. It was determined to use a finite element program to correctly model the boundary conditions of the SENT specimens. Knowing the applied far field stress and the stress at the crack tip, it would be possible to back calculate a stress intensity factor solution.

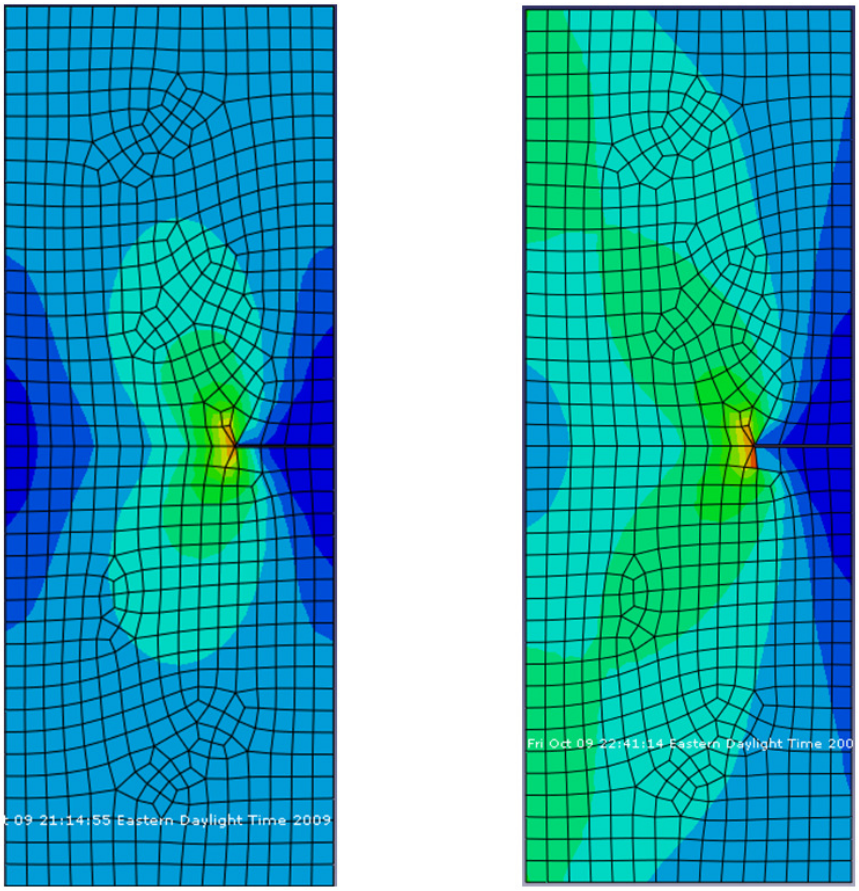

Figure 5.6: ABAQUS FEM For Uniform Stress (left) and Uniform Displacement (right)

FRANC2D is a finite element program maintained by the Cornell Fracture Group for predicting crack propagation through plane strain and plane stress two dimensional structures. The SENT specimen was modeled and meshed using a simple pre-processor that is included with FRANC2D called CASCA. The crack tip mesh can be seen in Figure 5.7. Using FRANC2D the appropriate boundary conditions were applied to mimic the uniform displacement conditions imposed by the hydraulic wedge grips. The notch was then allowed to propagate through the specimen yielding stress intensity factors as a function of crack length as seen in Figure 5.8.

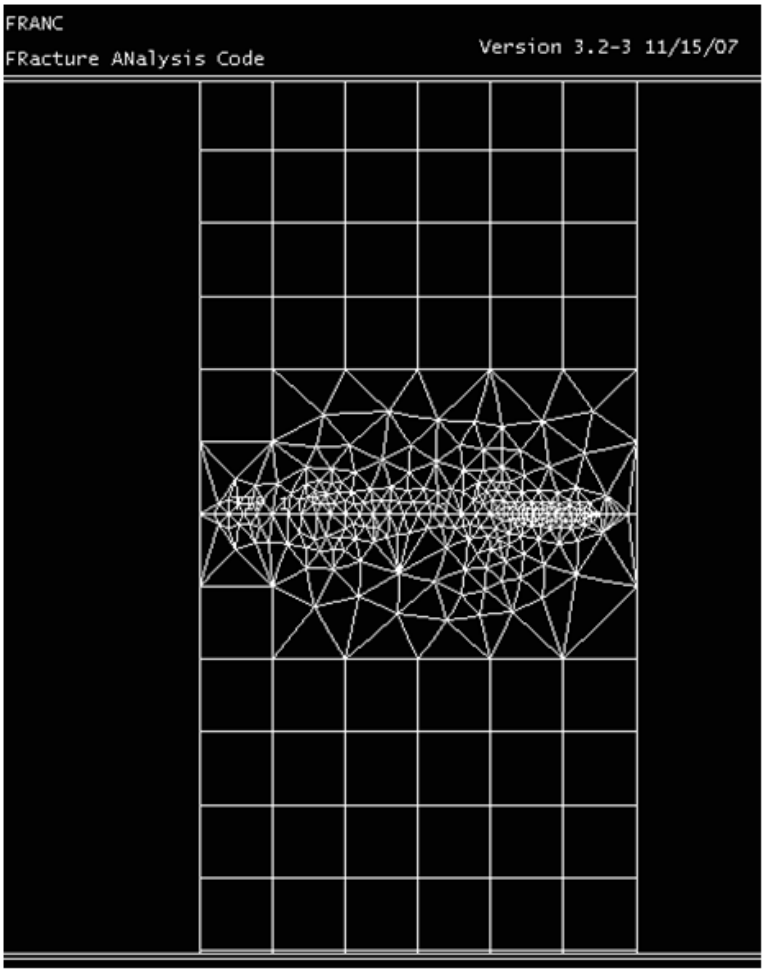

Figure 5.7: FRANC2D SENT Specimen Crack Tip Mesh

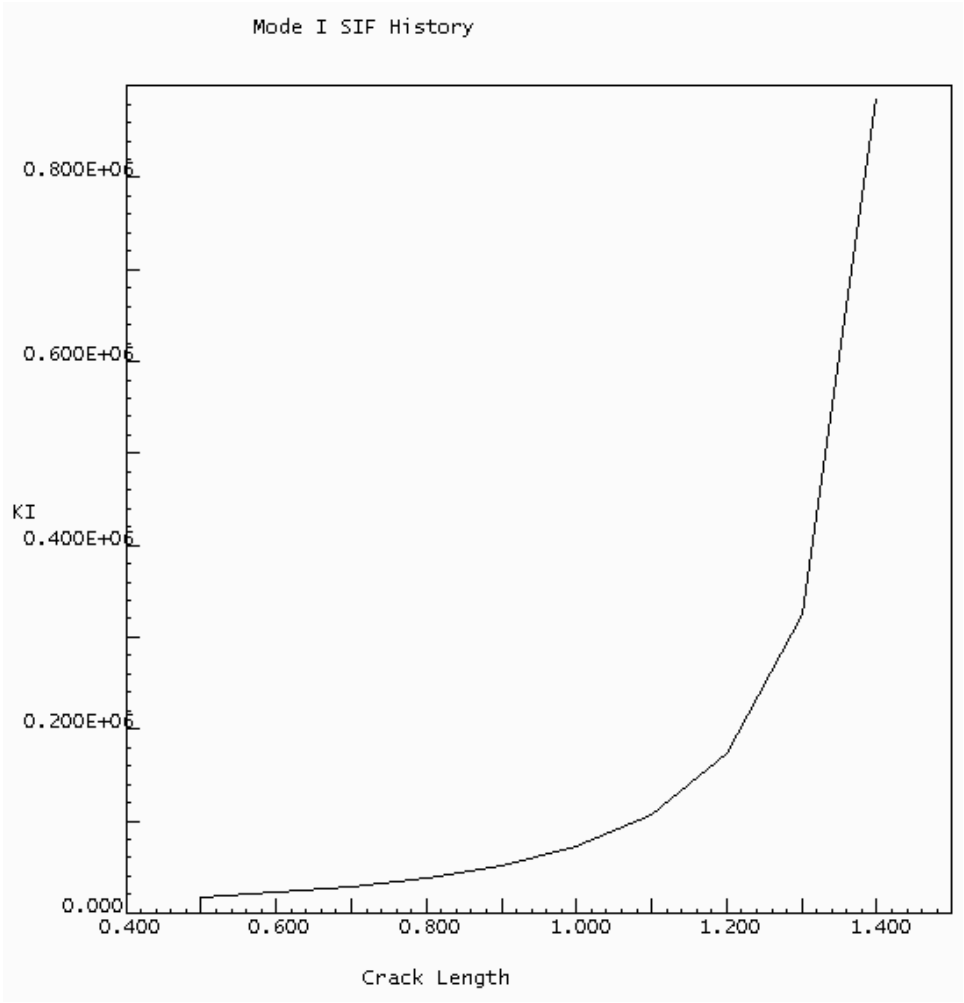

Figure 5.8: FRANC2D Stress Intensity Factor as a Function of Crack Length

For comparison purposes the correction factor, f(a/b), was also calculated using the Gross/Brown and Tada formulas, respectively Equations 5.1 and 5.2, both found in The Stress Analysis of Cracks Handbook [26].

$$f(a/b) = 1.122 - 0.231\left(\frac{a}{b}\right) + 10.550\left(\frac{a}{b}\right)^2 - 21.710\left(\frac{a}{b}\right)^3 + 30.882\left(\frac{a}{b}\right)^4 \quad \textbf{(5.1)}$$

$$f(a/b) = \sqrt{\frac{2b}{\pi a}\tan\frac{\pi a}{2b}}\,\frac{0.752 + 2.02(a/b) + 0.37\left(1-\sin\frac{\pi a}{2b}\right)^3}{\cos\frac{\pi a}{2b}} \qquad \textbf{(5.2)}$$

As can be seen in Table 5.2 the FRANC2D correction factors are very close to the uniform stress formulas from The Stress Analysis of Cracks Handbook up until a crack length over specimen width of 0.87. Realizing there might have been an error with how the boundary conditions were applied in FRANC2D, Dr. Mark James was contacted. Dr. James went to graduate school at Cornell University and is one of the originators of the FRANC2D code. In discussions with him it became apparent that FRANC2D is not the finite element program to use for uniform displacement.

Table 5.2: Comparison of Sent Specimen Correction Factors

Crack Length/ Specimen Width	The Stress Analysis of Cracks Handbook		FRANC2D
a/b	F(a/b) Gross/Brown	F(a/b) Tada	F(a/b)
0.33	1.79	1.78	1.79
0.40	2.11	2.11	2.11
0.47	2.55	2.55	2.54
0.53	3.16	3.16	3.09
0.60	4.03	4.04	4.03
0.67	5.23	5.40	5.32
0.73	6.85	7.67	7.63
0.80	9.02	11.99	11.79
0.87	11.85	22.38	21.17
0.93	15.50	64.27	55.71

An evaluation showing stress intensity factors for full rotation, partial rotation and no rotation boundary conditions provided by Dr. James is shown in Figure 5.9. The rotating

SENT specimen SIF increases faster as a function of crack length than the no rotation specimen. The partial rotation SIF in turn increases at a rate between the no rotation specimen and full rotation specimen. Work by Wu et al. looking at the stress intensity factors for through-cracks emanating from notches in SENT specimens demonstrated a similar relationship between uniform stress and uniform displacement boundary conditions [84]. This relationship can be seen in Figure 5.10. Their analysis using the boundary force method confirmed that the uniform stress SIF increases faster than the uniform displacement SIF as a function of crack length [85].

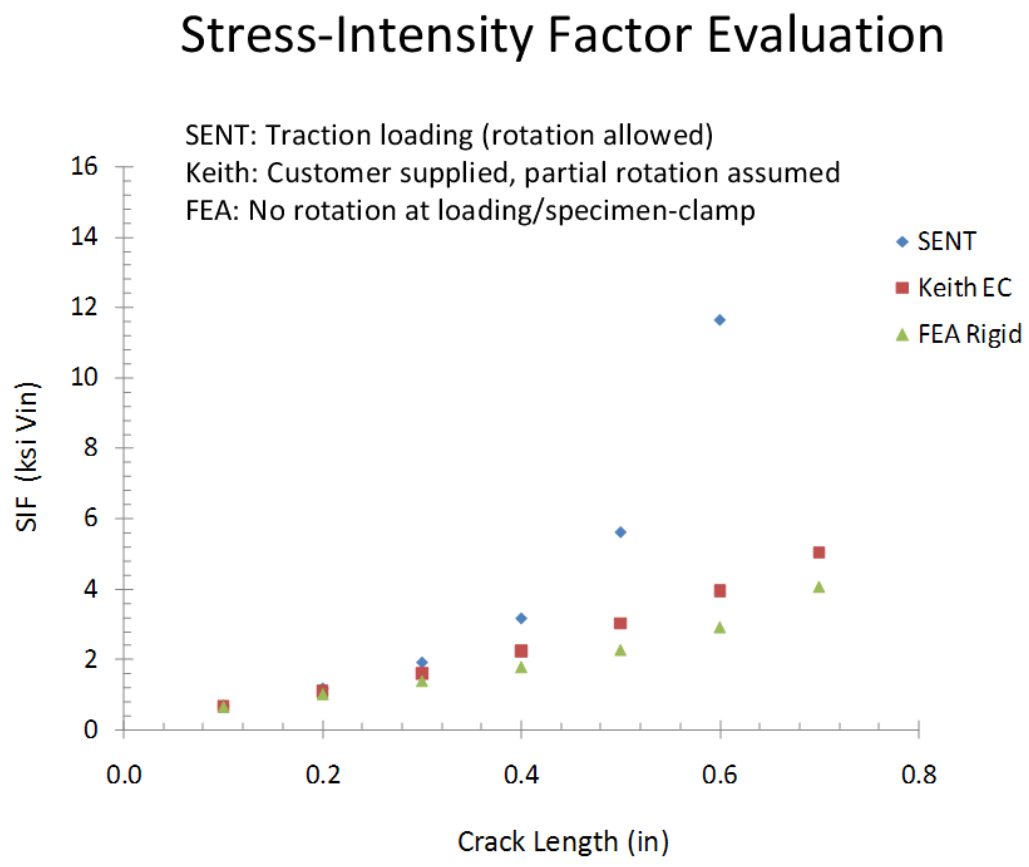

Figure 5.9: Comparison of Stress Intensity Factors for Uniform Stress and Uniform Displacement Conditions

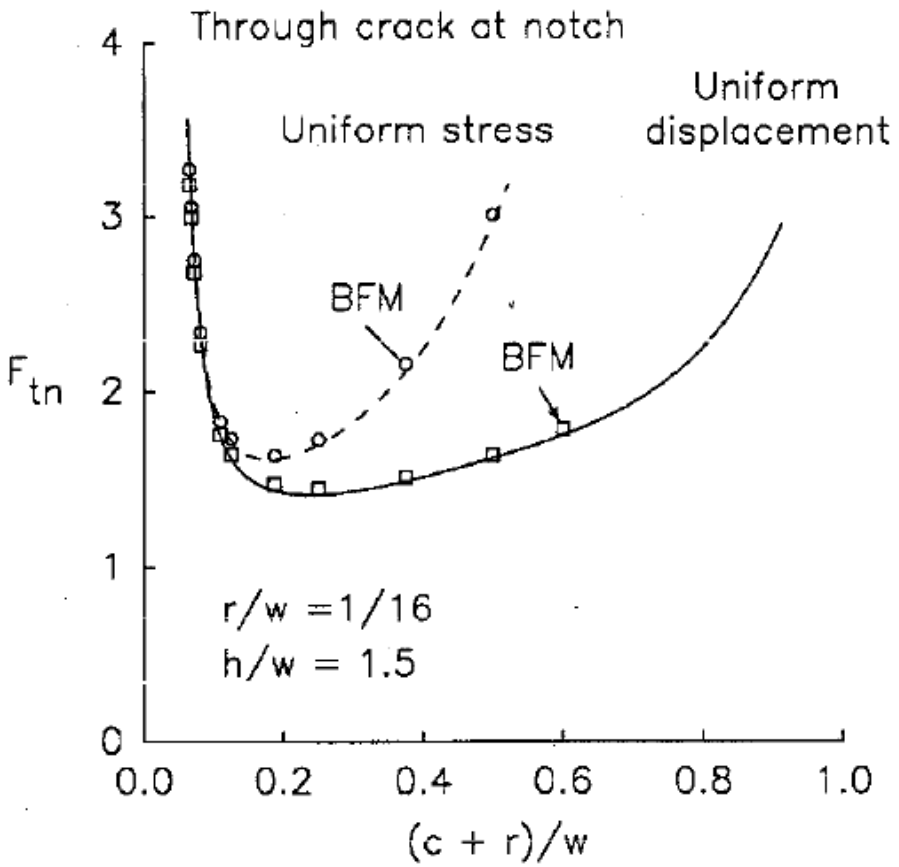

Figure 5.10: Comparison of Correction Factors Calculated Using the Boundary Force Method [84]

Dr Jim Newman Jr. at Mississippi State University was able to use his FADD2D boundary element code to plot the SIF as a function of crack length over specimen width for this studies' SENT specimen. In similar fashion to how Telesman et al. used a boundary integral equation and fitted a four-order equation to yield a solution a sixth-order equation was fitted to the FADD2D boundary element result [86]. The uniform displacement stress intensity factor used for this study plotted again the uniform stress SIF can be seen in Figure 5.11. Other methods that use FEA, weight functions and experimental data to determine the SIF for uniform displacement SENT specimens can be found in published literature [87-90]. The correction factor solution for a specimen with fixed ends is as follows:

$$f(a/b) = 1.126 - 0.504\left(\frac{a}{b}\right) + 10.473\left(\frac{a}{b}\right)^2 - 48.17\left(\frac{a}{b}\right)^3 + 112.87\left(\frac{a}{b}\right)^4 - 124.63\left(\frac{a}{b}\right)^5 + 53.327\left(\frac{a}{b}\right)^6 \quad \textbf{(5.3)}$$

Where a is the crack length and b is the specimen width. This solution was implemented for a specimen height to width ratio of 1.33.

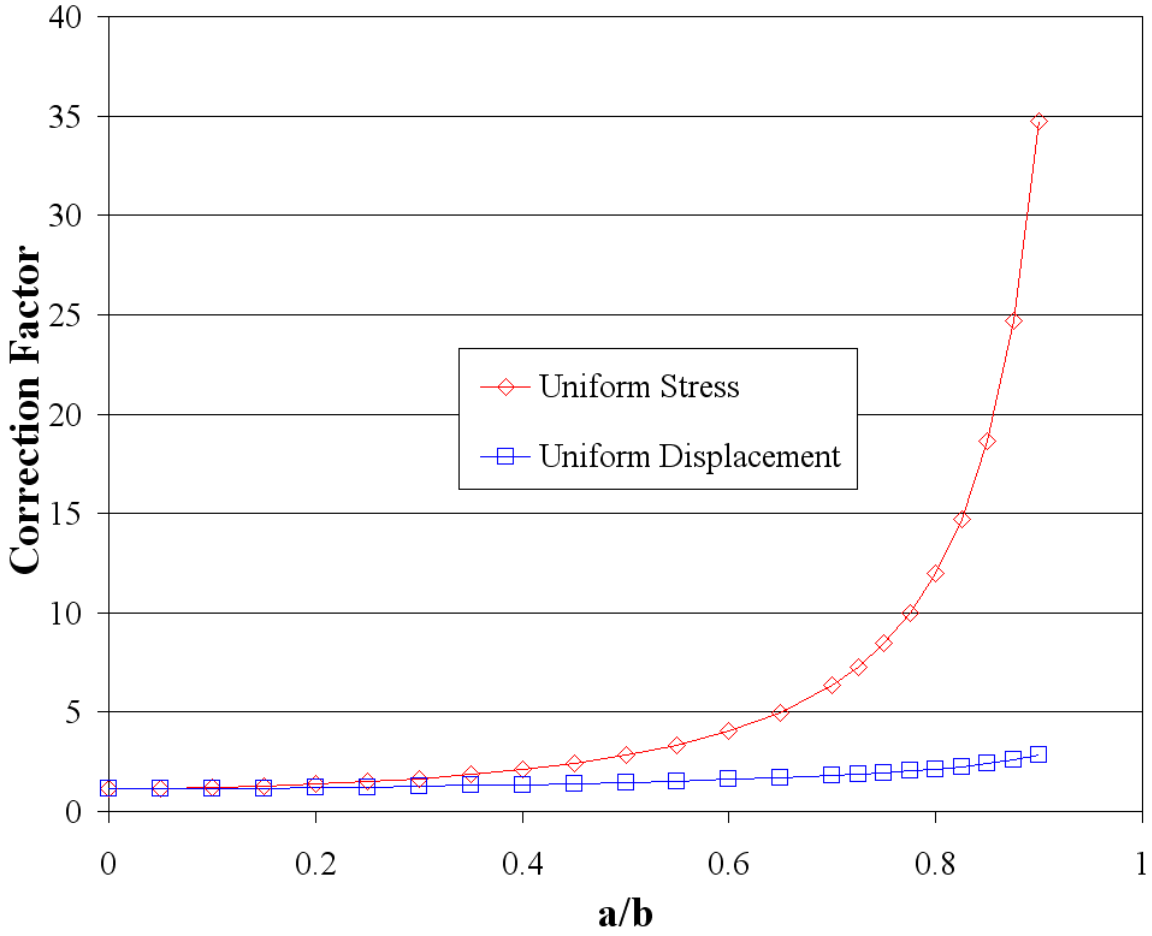

Figure 5.11: Comparison of Uniform Stress and Uniform Displacement Correction Factors for a SENT Specimen

In order to verify a correct SIF for the SENT specimen, fatigue crack growth was also performed on a compact tension specimen at room temperature. The commonly accepted uniform stress solution for a compact tension specimen is as follows [27]:

$$K = \frac{P}{b\sqrt{W}} \left(\frac{2+\left(\frac{a}{W}\right)}{\left(1-\left(\frac{a}{W}\right)\right)^{\frac{3}{2}}} \right) (0.886 + 4.64\left(\frac{a}{W}\right) - 13.32\left(\frac{a}{W}\right)^2 + 14.72\left(\frac{a}{W}\right)^3 - 5.6\left(\frac{a}{W}\right)^4 \quad \textbf{(5.4)}$$

Where P is the load, b is the specimen thickness and W is the specimen width. It will be shown later that there was excellent correlation between SENT and CT room temperature FCGR data.

5.2.2: Residual Stress Investigation

During the course of this investigation crack tip tunneling was seen on a specimen tested at 649°C and at a frequency of 20 Hz. Often times crack tip tunneling can be the result of residual surface stresses imparted during the machining process. To make sure that the specimens were properly machined; two IN100 specimens were sent to Lambda Technologies in Cincinnati, Ohio to be tested for the presence of residual surface stresses. X-ray diffraction (XRD) was used to measure the strain in the crystal lattice. Assuming a linear elastic distortion of the crystal lattice, the residual stress producing the strain can be calculated. After each measurement, electropolishing is used to expose new surfaces to determine residual stress as a function of depth. At the same time microstresses resulting from imperfections in the crystal lattice are measured. These microstresses are

used to determine the amount of plastic yielding that has taken place. This plastic yielding can be used to determine the percent of cold working that has taken place as a function of depth. Both an untested and 649°C tested specimen showed high residual surface tension as seen in Figure 5.12. However this stress went to almost zero at a depth of 0.0254mm and completely went away after a depth of 0.254mm. The percent cold work was about 27% on the surface and also went almost to zero at a depth of 0.0254mm. While the percent cold work and surface residual stress is high it is confined to such a swallow area that it will have only a negligible effect on the crack growth rate.

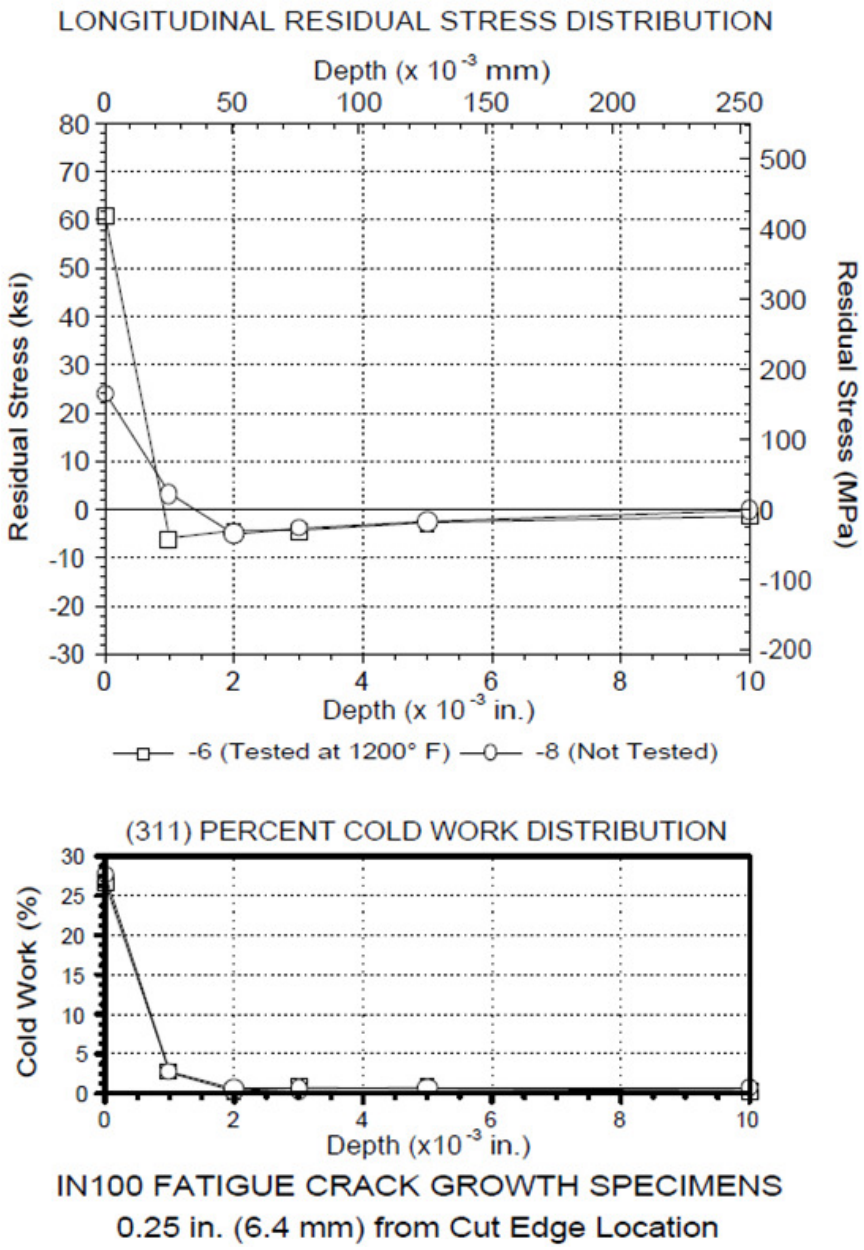

Figure 5.12: Residual Surface Stress and Percent Cold Work Distributions

5.2.3: Marker Bands

Marker bands are the preferred method for observing whether crack front tunneling is taking place. When done correctly marker bands can provide a clear picture as to whether the crack front is well behaved or not. Marker bands are creating by applying every so often a number of cycles at a higher R ratio than what the test is normally

running. This is accomplished by increasing the minimum stress and effectively decreasing the ΔK for the marker band cycles. This causes the crack growth rate to slow during marker band application. For this very reason crack growth data encompassing the marker bands needs to be discarded. Figure 5.13 shows some marker bands created by increasing the R ratio from R = 0.1 to R = 0.5 for 500 cycles every 2000 cycles. Note that the marker bands increase in thickness as the overall crack length increases leading the applied ΔK to increase. Upon fatigue surface examination the average crack front due to tunneling was measured and added to the optical crack length measurements.

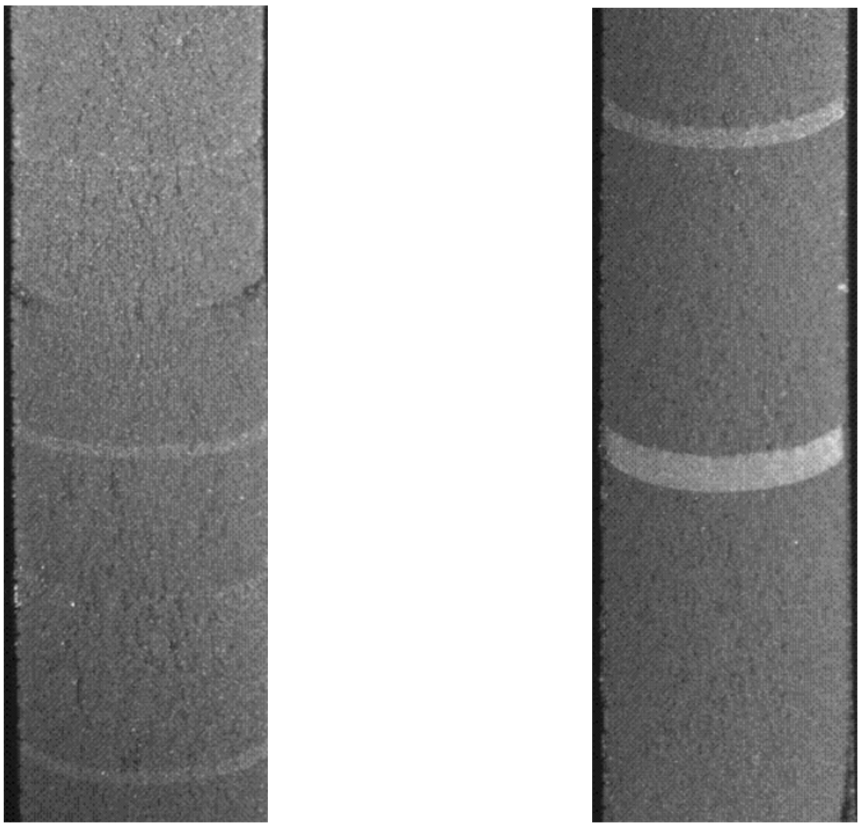

Figure 5.13: Marker Bands Showing Mild Curvature of a Well Behaved Crack Front

5.3: Isothermal Constant Amplitude Fatigue Crack Growth Testing

Isothermal constant amplitude fatigue crack growth rate testing was performed on five IN100 single edge notch tension specimens and one IN100 compact tension specimen. All testing was done at an R ratio of 0.1. The test matrix in Table 5.3 shows the test temperatures and frequencies. All specimens are the SENT configuration except for IN100-8 which is a compact tension (CT) specimen. Specimens were pre-cracked at 20 Hz at the same temperature they were tested at.

Table 5.3: Isothermal Constant Amplitude Test Matrix

Specimen	Temperature (°C)	R Ratio	Frequency (Hz)
IN100-6	649	0.1	20
IN100-10	649	0.1	0.33
IN100-1	316	0.1	0.33
IN100-8	22	0.1	0.33
IN100-2	22	0.1	0.33
IN100-3	482	0.1	0.33

For each test, crack length and number of cycles was recorded approximately every 500 cycles. This cycle interval was larger at small ΔK's and decreased as ΔK increased. Using the ASTM Standard E647 sliding three point incremental polynomial method for data reduction, da/dN was obtained and plotted along with ΔK on a log-log plot. For Paris equation fitting only ΔK from 22 MPa$\sqrt{m}$ to 44 MPa$\sqrt{m}$ was used to ensure data was only in the linear Paris region and that each specimen was fitted across an identical range. This is true for all specimens except for IN100-2 which was only tested from 25 to 32 MPa$\sqrt{m}$.

Fatigue crack growth tests were performed on IN100-10 and IN100-6 at 649°C at frequencies of 0.33 and 20 HZ, respectively. These results are shown in Figure 5.14, where the frequency effect can be clearly seen with the 0.33 Hz growth rate being approximately 5x the 20 Hz growth rate. The overall trend at elevated temperature is clear with decreased cyclic frequency comes increased crack growth rate. This trend can be attributed to stress enhanced diffusion of oxygen at the crack tip that increases due to the crack tip being open longer at slower frequencies providing more time for diffusion during each cycle. To assess the contribution of creep on the crack growth rate sustained loading at 649°C was performed. After three and a half hours of dwelling the stress relaxation was found to be very minimal at 649°C. This agrees well with what was found in other studies for similar powdered metallurgy superalloys. Tong et al. found that there was very little creep influence on the FCGR at 650°C for a Udimet series superalloy [91]. Work with polycrystalline Inconel 718 performed by Nicholas and Pineau have shown that the Riedel-Rice short time for transition from elastic behavior to viscous behavior at 650°C to be in the range of approximately 1 day to 3 years [92, 93]. This characteristic time is very large compared to this studies cycle time of 3 seconds and as such very little creep influence would be expected at 649°C in IN100.

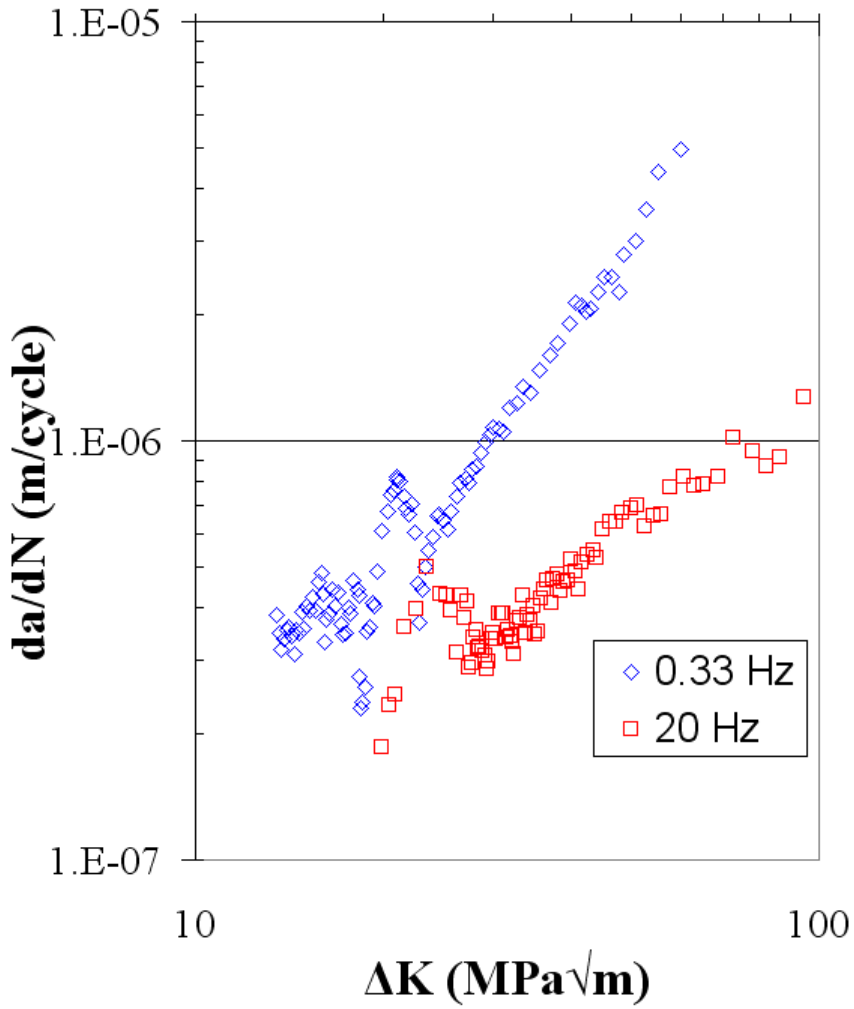

Figure 5.14: Comparison of Crack Growth Rates at a Temperature of 649°C

In addition tests were conducted at 482°C, 316°C and 22°C at a frequency of 0.33 Hz and R = 0.1. Figure 5.15 shows a comparison of fatigue crack growth rates for all specimens tested at a frequency of 0.33 Hz. A clear trend that emerges is that increasing temperature leads to an increasing crack growth rate. As can be seen in Figure 5.15 the growth rate at 316°C is about 2X the growth rate at 22°C. This trend continues with the growth rate at 649°C and 482°C being approximately 8x and 4x the growth rate at 22°C. The 22°C test data for compact tension and single edge notch tension specimens lie right

on top of each other further lending credence to the uniform displacement stress intensity factor for the SENT specimens.

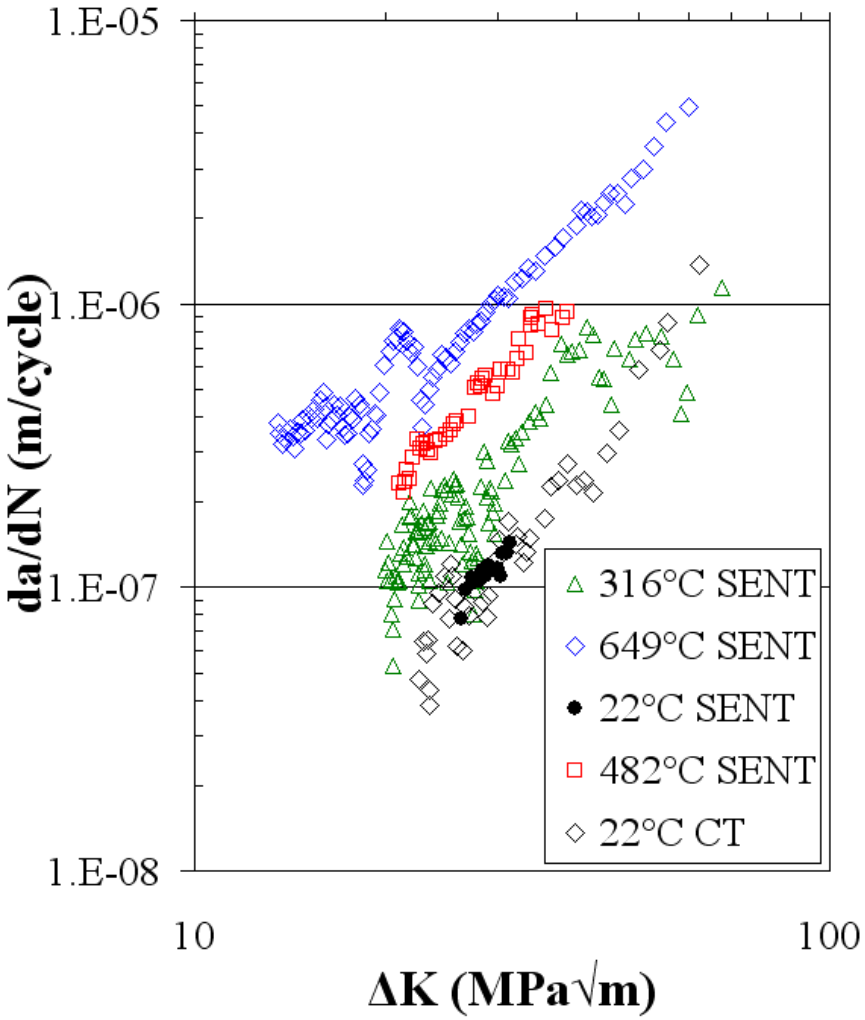

Figure 5.15: Comparison of Crack Growth Rates at a Frequency of 0.33 Hz

In Figure 5.14 and Figure 5.15 at ΔK values of 22 MPa√m and below the da/dN values show oscillations of accelerating and decreasing crack growth. These crack growth rates do not uniquely correlate to ΔK as da/dN values in the Paris regime should. This "rollercoaster" effect was not seen in any uniform stress data during the course of performing a literature review. There is much less literature presenting uniform

displacement crack growth rates but it can be seen that there is much more scatter at the lower ΔK values. This "rollercoaster" effect appears to be an interaction between competing crack tip loading modes and possible microstructural interactions. Through visual observations during testing it was noticed that the wedge grips are able to rotate relative to each other allowing an out-of-plane tearing mode to occur at the crack tip. The hydraulic wedge grips attempt to restrict rotation which is an additional boundary condition that is not present in uniform stress loading. The wedge grip out of plane rotation along with very minimal in plane rotation due to the load train not being infinitely rigid creates a very complex loading condition at the crack tip. This condition persists until the crack reaches a length were the ΔK_I, opening mode becomes the dominant driving force for crack growth around a ΔK 22 MPa$\sqrt{m}$.

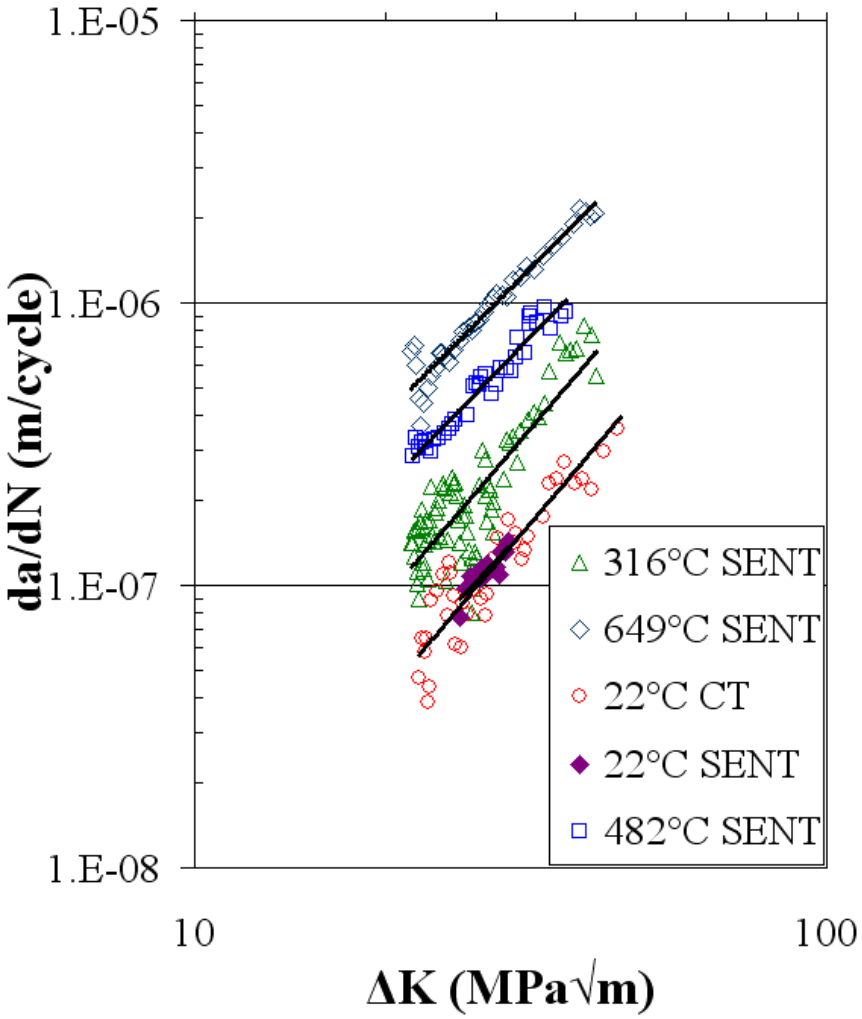

Figure 5.16: Paris Equation Fitted da/dN for All Temperatures at 0.33 Hz and R = 0.1

$$\frac{da}{dN} = C\Delta K^{m} \tag{5.5}$$

Fitting Equation 5.5 to the Paris regime crack growth data between 22 and 44 MPa√m in Figure 5.16, yields Paris exponents ranging from 2.25 to 2.64, shown in Table 5.4. Both 22°C tests are 2.40 and 2.64 respectively for the SENT and CT specimen. The 316°C test yielded an exponent of 2.62 while the 482°C test yielded an exponent of 2.31. With the 649°C test having the smallest exponent of 2.25. These Paris law exponents seem to

largely follow the rule of decreasing in magnitude with increasing temperature, though scatter could overshadow this trend. These values are very consistent with the values for IN100 found in the Damage Tolerant Design Handbook (DTDH) where most of the exponents range from 2.2 to 3.0.

Table 5.4: Paris Equation Coefficients and Exponents for Isothermal Constant Amplitude Testing

Specimen	Paris Coefficient	Paris Exponent	R^2	Temperature (°C)
IN100-10	4.68E-10	2.25	0.937	649
IN100-3	2.17E-10	2.31	0.949	482
IN100-2	3.49E-11	2.40	0.781	22
IN100-1	3.49E-11	2.62	0.701	316
IN100-8	1.52E-11	2.64	0.883	22

The Paris equation fitted data from Figure 5.16 can be seen in Figure 5.17 plotted alongside data for IN100 from the Damage Tolerant Design Handbook. The DTDH data is for testing performed between temperatures of 427°C and 649°C, between R ratios of 0.05 and 0.8 and at a frequency of 0.33 Hz and less. The specimens range in thickness from 2.54mm to 12.7mm. The R ratio = 0.1 data obtained during this study fits very well with the DTDH data considering that an increase in R ratio tends to lead to an increase in FCGR. Another thing to point out is that this study only looked at two temperatures above 427°C. An increase in temperature would also lead to an increase in FCGR.

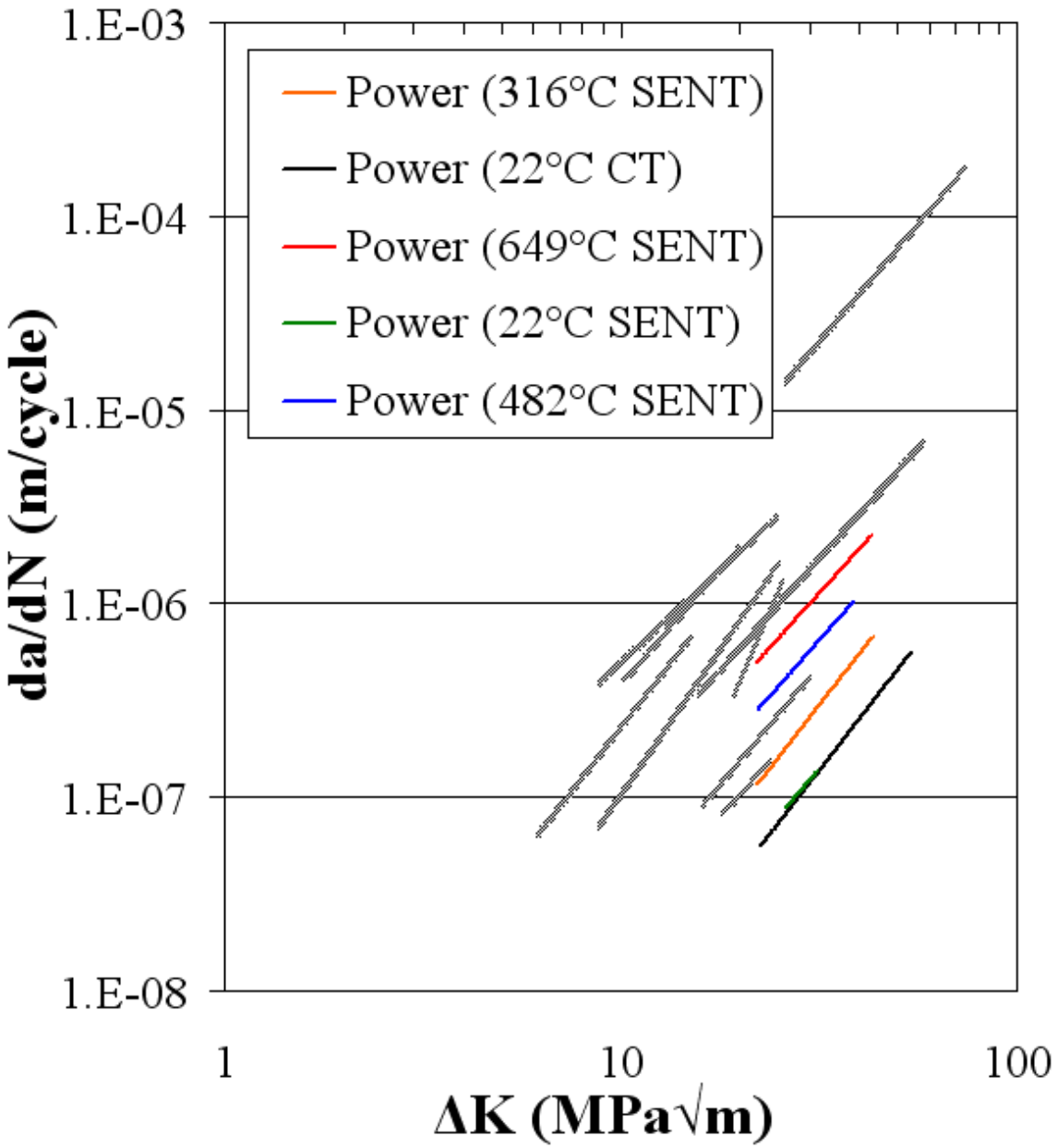

Figure 5.17: Paris Equation Fitted da/dN for All Temperatures at 0.33 Hz and R = 0.1 Compared with IN100 Damage Tolerant Design Handbook Data at All Temperatures, All R ratios, All Thicknesses and 0.33 Hz and Below [94]

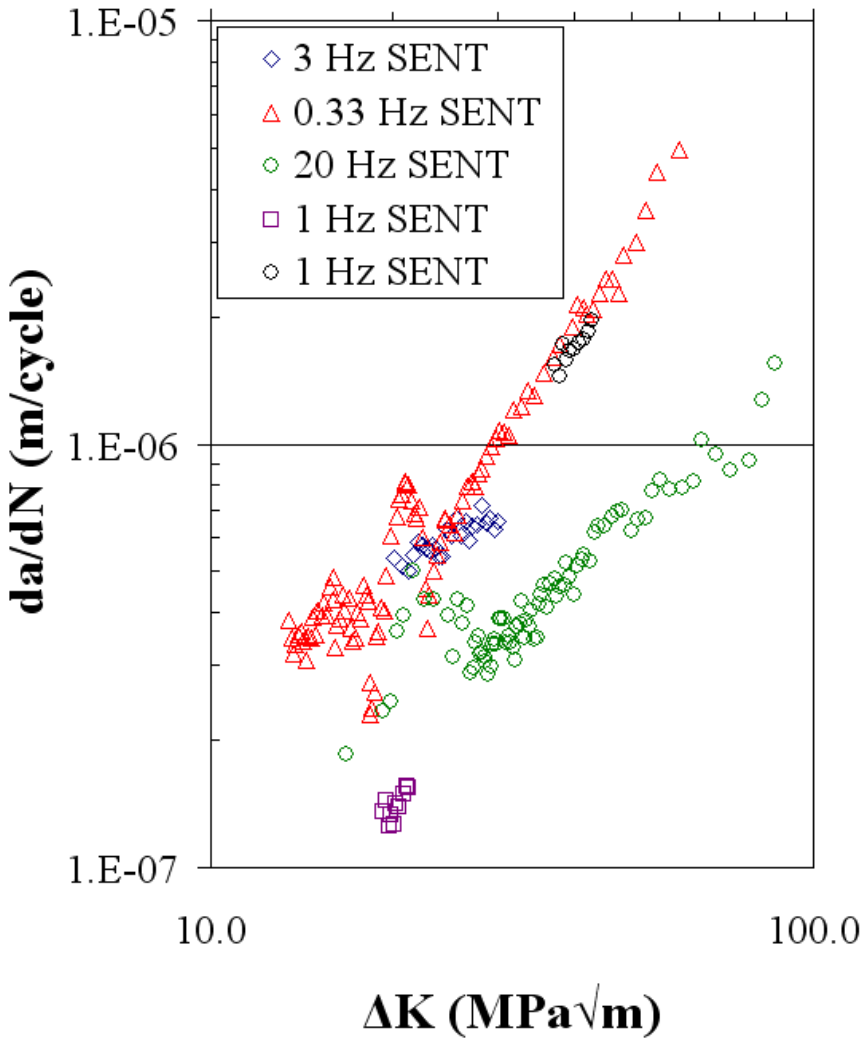

Figure 5.18: Comparison of Crack Growth Rates at a Temperature of 649°C

In order to determine a frequency faster than 0.33 Hz that provided a similar fatigue crack growth rate; frequencies of 3 Hz and 1 Hz were looked at. These frequencies were tested on a single specimen at an R ratio of 0.1 and a temperature of 649°C. Testing began at 3 Hz and can be seen as diamonds in Figure 5.18. When it became apparent that the FCGR at 3 Hz was slower than the FCGR at 0.33 Hz the ASTM load shedding procedure was employed to start 1 Hz testing at the same ΔK as the 3 Hz was started at. The FCGR at 1 Hz, seen in Figure 5.18 as squares, was severely slower than expected and was attributed

to crack closure not addressed by the ASTM load shedding technique. When the minimum and maximum loads were increased to the original levels the 1 Hz FCGR increased to what was expected. This data can be seen in Figure 5.18 as circles. It was determined that cycling at 1 Hz provides a similar FCGR as cycling at 0.33 Hz at a temperature of 649°C.

5.4: Temperature Dependent Diffusion Based FCGR Modeling

Using the isothermal constant amplitude data obtained at ΔK values of 22, 33 and 44 MPa√m for temperatures of 22°C, 316°C, 482°C and 649°C and frequencies of 0.33 Hz and 20 Hz a temperature dependent diffusion based FCGR model is proposed. Equation 5.6 shows a fatigue crack propagation model consisting of separate dominant mechanism modules as proposed by Miller, McDowell and Oehmke [95].

$$\frac{da}{dN} = \frac{da}{dN}_{fatigue} + \frac{da}{dN}_{creep} + \frac{da}{dN}_{oxidation} \quad \textbf{(5.6)}$$

Equation 5.7 provides the governing relationship for the oxidation crack growth.

$$\frac{da}{dN}_{oxidation} = C_{ox}(\Delta J_{eff})^m t^n \quad \textbf{(5.7)}$$

Christ et al. [96] expanded the prefactor in Equation 5.7 using an Arrhenius relation as shown in Equation 5.8.

$$\frac{da}{dN}_{oxidation} = C_{ox}(\Delta J_{eff})^m t^n = C\exp\left(\frac{-Q}{RT_{eff}}\right)(\Delta J_{eff})^m t^n \quad \textbf{(5.8)}$$

Using the above as a basis for a mechanistic fatigue-oxidation model correlated to IN100 crack growth data, the following relationship seen in Equation 5.9 is proposed, where ν is the test frequency.

$$\frac{da}{dN} = C\exp\left(\frac{-nQ}{RT_{eff}}\right)(\Delta K)^m\left(\frac{1}{\nu}\right)^n \quad \textbf{(5.9)}$$

Similar variants of this model have been used previously proposed in literature [91, 97]. The time exponent (n) for matrix diffusion has been rigorously determined by Wagner to be n=1/2 [98]. Reuchet et al. determined that short circuit diffusion along grain and dendritic-interdendritic boundaries followed a n=1/4 rate law [99]. Experimental results indicate that at higher temperatures the crack path is primarily intergranular, while lower temperatures produce transgranular fracture surfaces. As such it is proposed that the time exponent in Equation 5.9 be set to n=1/4 for high(er) temperatures and n=1/2 for low(er) temperatures, and a value of 1/4<n<1/2 for intermediate temperatures. An equation to determine an effective time exponent is proposed following the functional form for determining the effective diffusion coefficient for combined matrix-grain boundary diffusion proposed by Matsunaga et al. [100].

$$D_{eff} = D_L(1-f) + fD_{GB} \quad \textbf{(5.10)}$$

In Equation 5.10 D_{eff} is the effective diffusion coefficient, D_L the lattice diffusion coefficient, D_{GB} the grain boundary diffusion coefficient and f is the area fraction of grain boundaries (A_{GB}) to the total area (A_{Tot}).

$$f = \frac{A_{GB}}{A_{Tot}} \sim \frac{2\delta}{G} \tag{5.11}$$

In Equation 5.11 δ is the grain boundary width and G is equal to the grain side length (grain assumed to be square) plus δ. The effective time exponent for combined granular-transgranular crack paths is given by Equation 5.12 where $n_L = 1/2$ and $n_{GB} = 1/4$.

$$n_{eff}^{-1} = (n_L)^{-1}(1-f) + f(n_{GB})^{-1} \tag{5.12}$$

Using IN100 fatigue crack growth results at three temperatures and two frequencies, one can plot $\frac{da}{dN}\left((\Delta K)^m t^n\right)^{-1}$ versus 1/RT to determine the effective activation energy for the temperature-assisted crack propagation. The exponent m is taken as m=1 when plotting Figure 5.19.

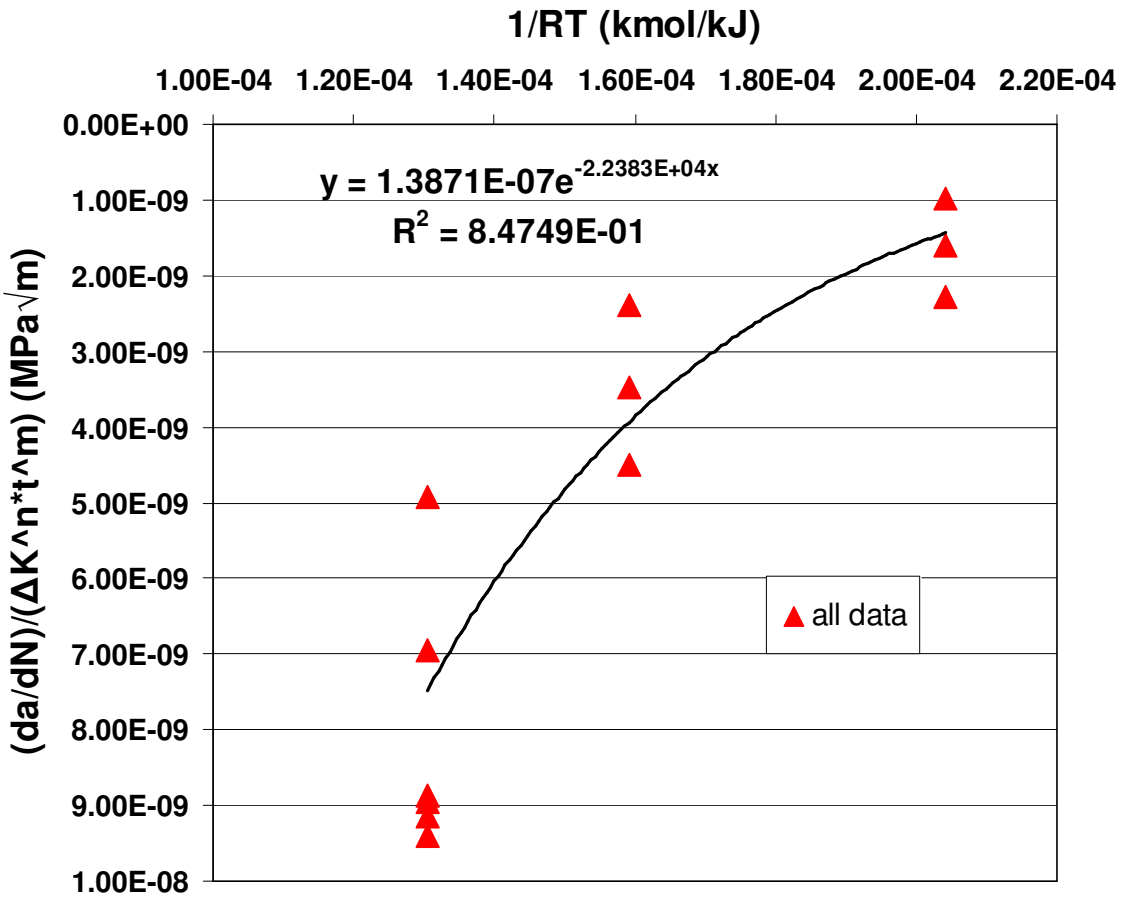

Figure 5.19: Determination of Activation Energy

The prefactor, C, and the exponential numerator, nQ, in Equation 5.9 are determined (from Figure 5.19) as C=1.39 x 10^{-7} and nQ=22,383 J/mol. The resulting activation energy for temperature assisted crack growth, at the temperatures and loads tested, is determined as 44696 < Q < 89536, depending upon the temperature of interest, and therefore the value of n. The value of activation energy determined here is reasonable compared to those determined for other polycrystalline Ni-base superalloys. Antolovich et al. [101] determined an activation energy of 40.2 kJ/mol for Rene 80, while Boismier et al. [102] determined a value of 175.9 kJ/mol for polycrystalline Mar M247.

The correlated crack propagation estimation equation can be seen in Equation 5.13.

$$\frac{da}{dN}_{oxidation} = 1.39x10^{-7} \exp\left(\frac{-n(22383)}{RT_{eff}}\right)(\Delta K)^{1.4}\frac{1}{\nu}^{n} \quad \textbf{(5.13)}$$

Model correlation is well within a factor of two, as shown in Figure 5.20.

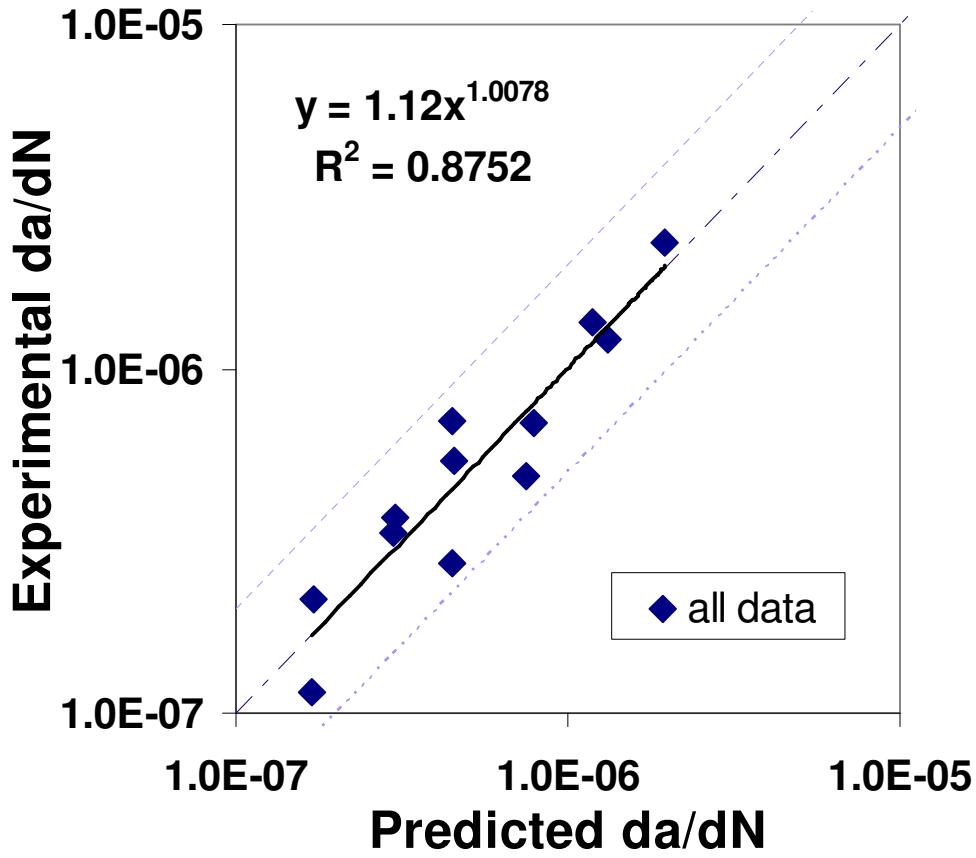

Figure 5.20: Correlation for Temperature Dependent Diffusion Based FCGR Model

5.5: Isothermal Constant Amplitude Crack Surface Morphology

Fracture surfaces were examined using a scanning electron microscope to determine the underlying failure mechanisms across temperature, frequency and ΔK. Micrographs were taken at ΔK's of 22, 33 and 44 MPa√m for each isothermal constant amplitude test specimen. Other micrographs investigating interesting features were also taken and will be discussed. Scanning electron microscopy stereo pairs are presented in Appendix A.6 to reveal the three dimensional aspects of the fatigue fracture surfaces. A table summarizing the morphology characteristics of the fatigue fracture surfaces as a function of temperature and frequency can be found in Appendix A.7.

5.5.1: IN100-6, 649°C, 20 Hz Fatigue Fracture Surface

The first specimen, IN100-6, was tested at a temperature of 649°C, R ratio of 0.1 and a frequency of 20 Hz. It can be seen in Figure 5.21 through Figure 5.23 that the high frequency this specimen was tested at prevented the high temperature environment from having a large effect. As can be seen in the SEM micrographs taken at ΔK's of 22, 33 and 44 MPa√m the fracture surface is very transgranular in nature. This transgranular surface is a mixture of fatigue striation patches and ductile rupture. As ΔK increases and the crack growth becomes more rapid the fatigue striations become less and less prevalent while the amount of ductile rupture increases.

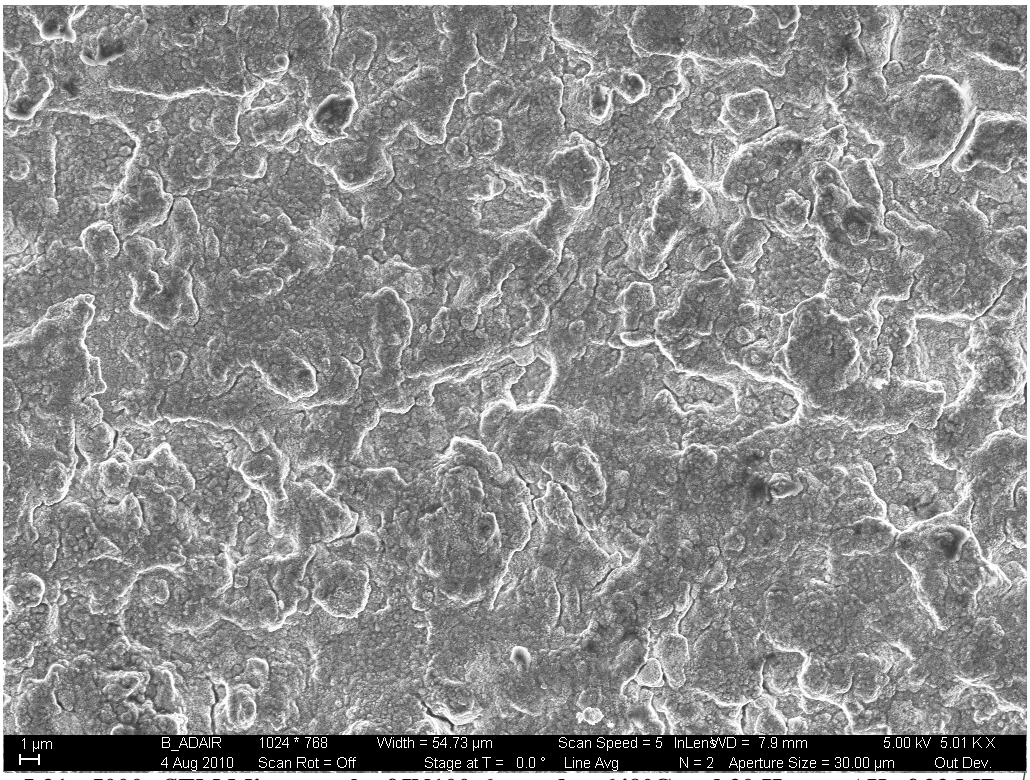

Figure 5.21: 5000x SEM Micrograph of IN100-6 tested at 649°C and 20 Hz at a ΔK of 22 MPa√m

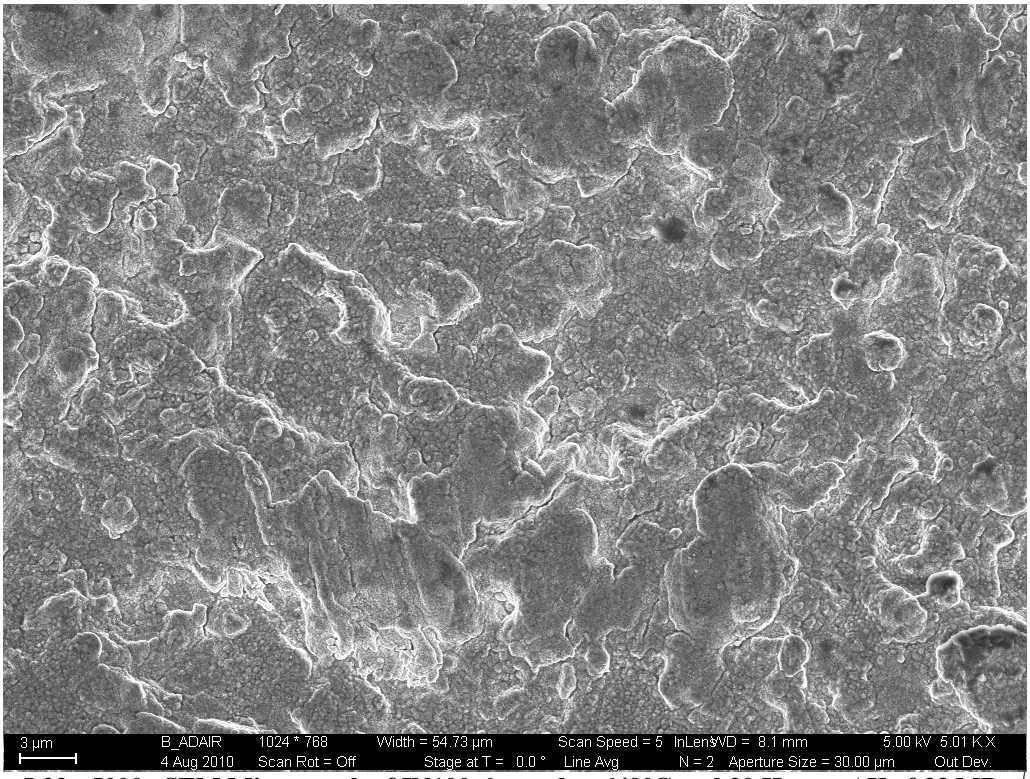

Figure 5.22: 5000x SEM Micrograph of IN100-6 tested at 649°C and 20 Hz at a ΔK of 33 MPa√m

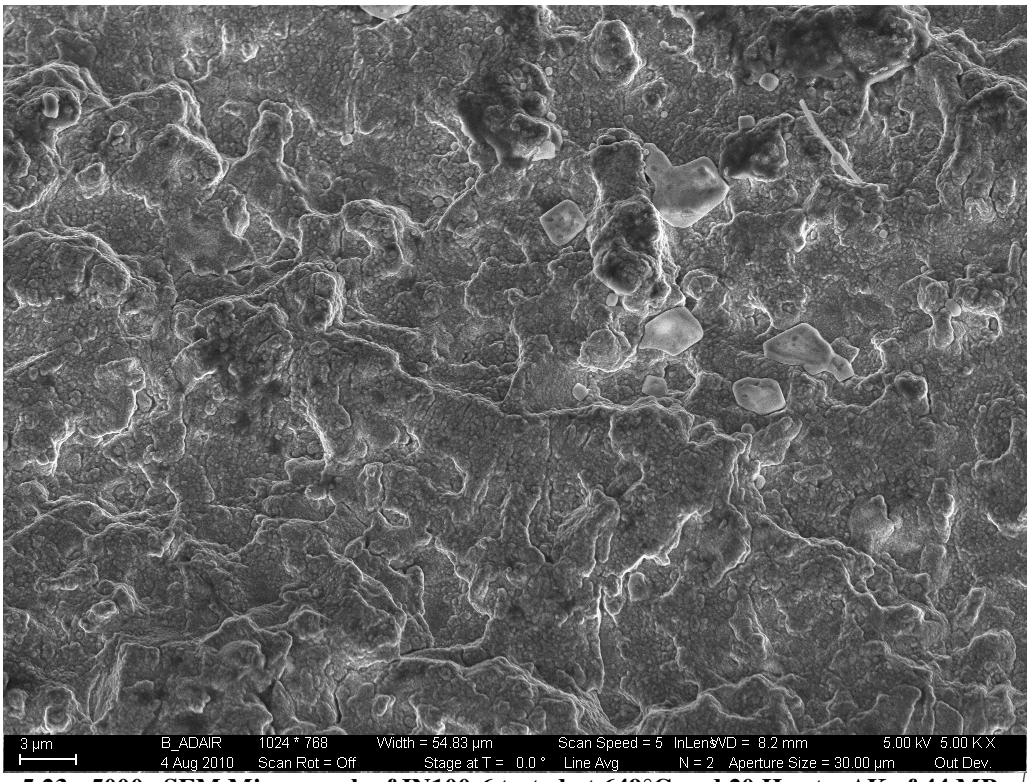

Figure 5.23: 5000x SEM Micrograph of IN100-6 tested at 649°C and 20 Hz at a ΔK of 44 MPa√m

Figure 5.24 shows an interesting artifact at a ΔK of 25 MPa√m, an area showing crack closure rubbing. This feature very clearly follows the crack front and has very clear areas of fatigue striations. From these striations it can be seen that the spacing is about three times the da/dN at that given ΔK. This strengthens the earlier mentioned concept of a mixed transgranular mode of both fatigue striations and ductile rupture. Crack growth does not necessary occur for every cycle but occurs in bursts as the Antolovich-Saxena Fatigue Crack Propagation Model takes into account [103]. Figure 5.25 taken at a ΔK of 39 MPa√m shows a portion of the flat to slant transition, where the plastic yield zone in front to the crack tip is influenced by plane stress boundary conditions.

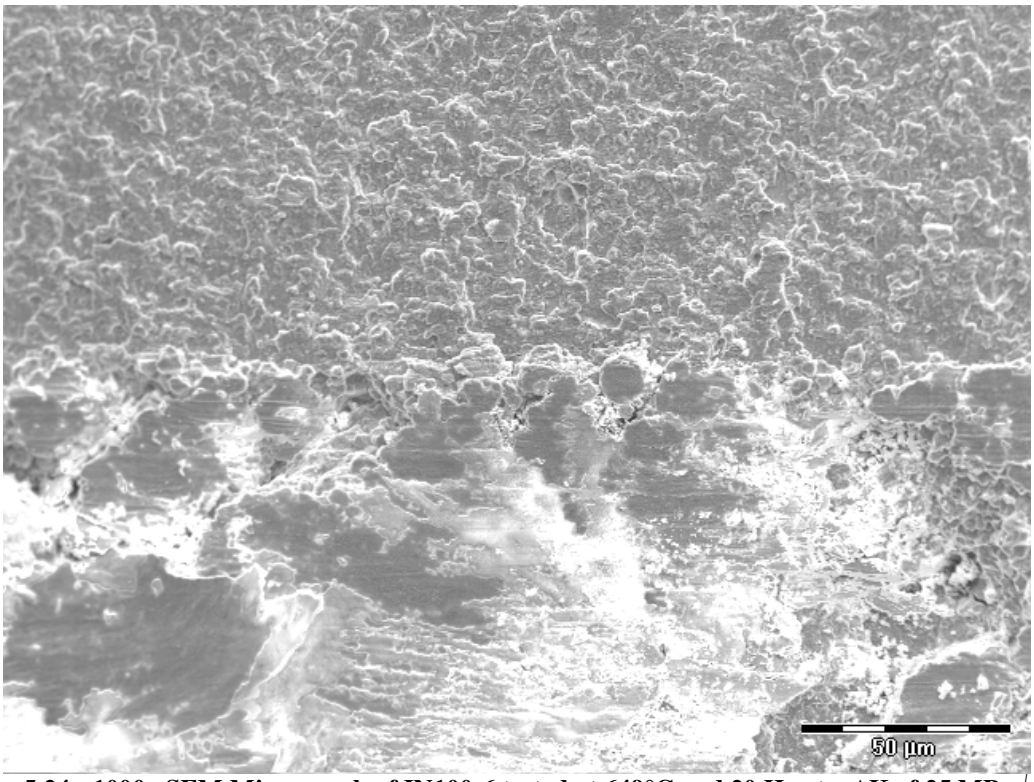

Figure 5.24: 1000x SEM Micrograph of IN100-6 tested at 649°C and 20 Hz at a ΔK of 25 MPa√m

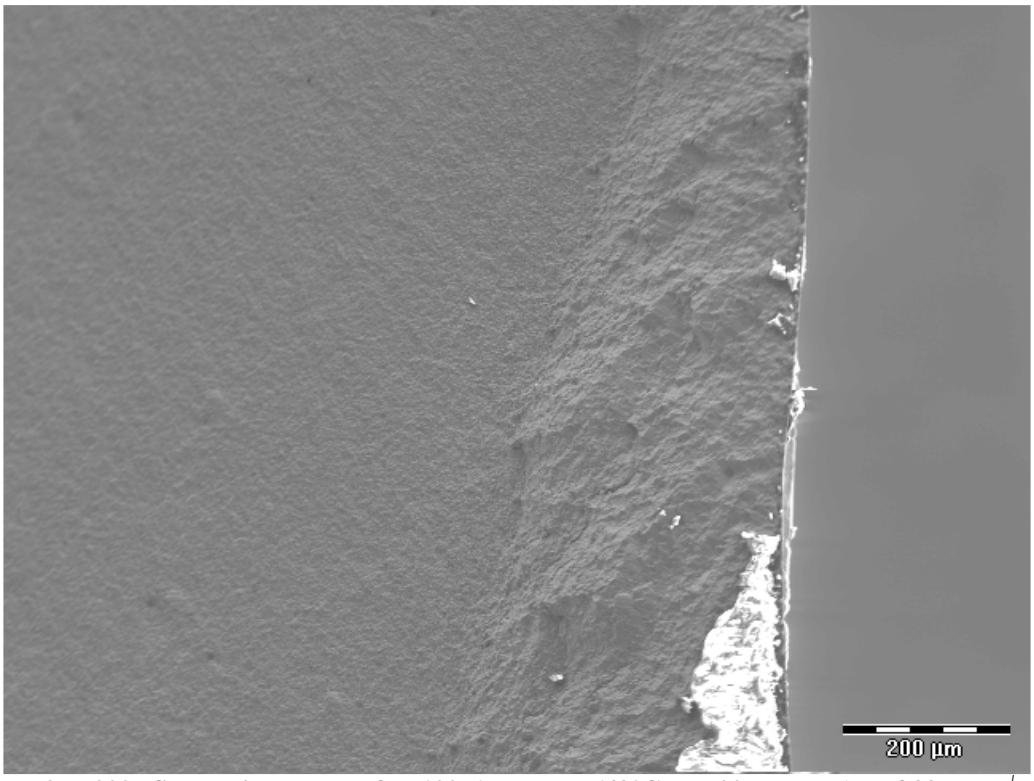

Figure 5.25: 200x SEM Micrograph of IN100-6 tested at 649°C and 20 Hz at a ΔK of 39 MPa√m

5.5.2: IN100-10, 649°C, 0.33 Hz Fatigue Fracture Surface

Specimen, IN100-10, was tested at a temperature of 649°C, R ratio of 0.1 and a frequency of 0.33 Hz. In comparison to IN100-6 the effect of frequency at high temperatures can easily be seen. Figure 5.26 to Figure 5.28 show SEM micrographs taken at ΔK's of 22, 33 and 44 MPa√m. These micrographs show the large role that environment plays at the crack tip. The failure mechanism is very intergranular in nature. It can also be seen that as ΔK increases the failure mechanism adds a very transgranular component as the crack growth rate increases. Grain boundary facet tearing normal to the crack growth direction becomes more prevalent as the stress intensity increases.

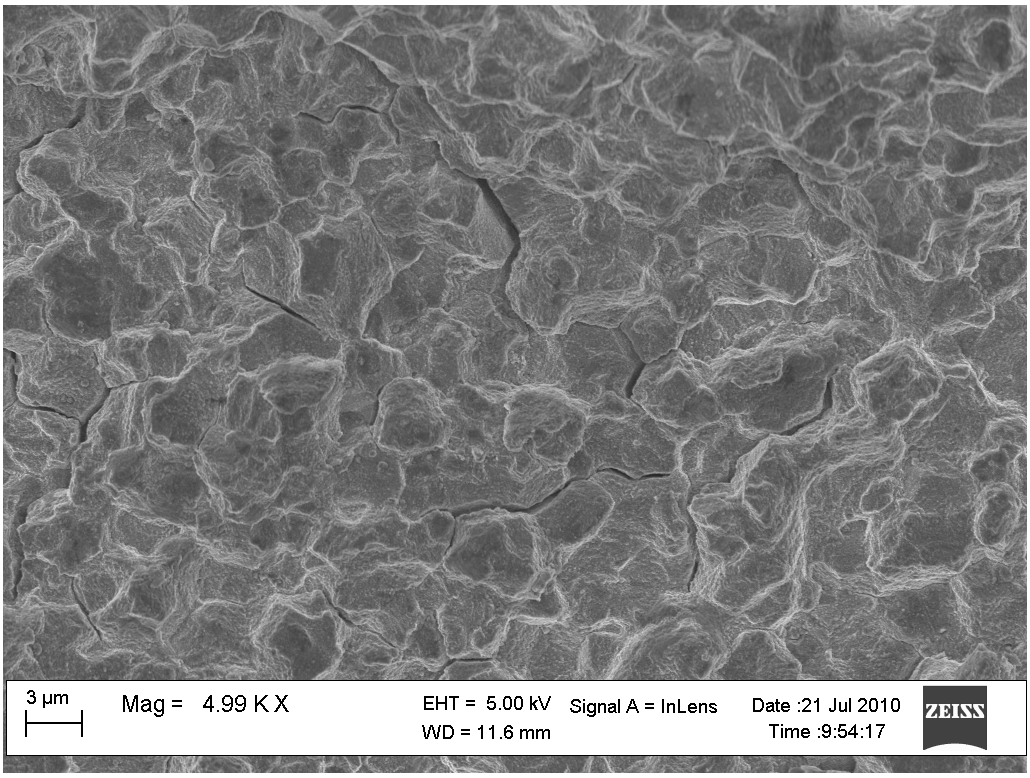

Figure 5.26: 5000x SEM Micrograph of IN100-10 tested at 649°C and 0.33 Hz at a ΔK of 22 MPa√m

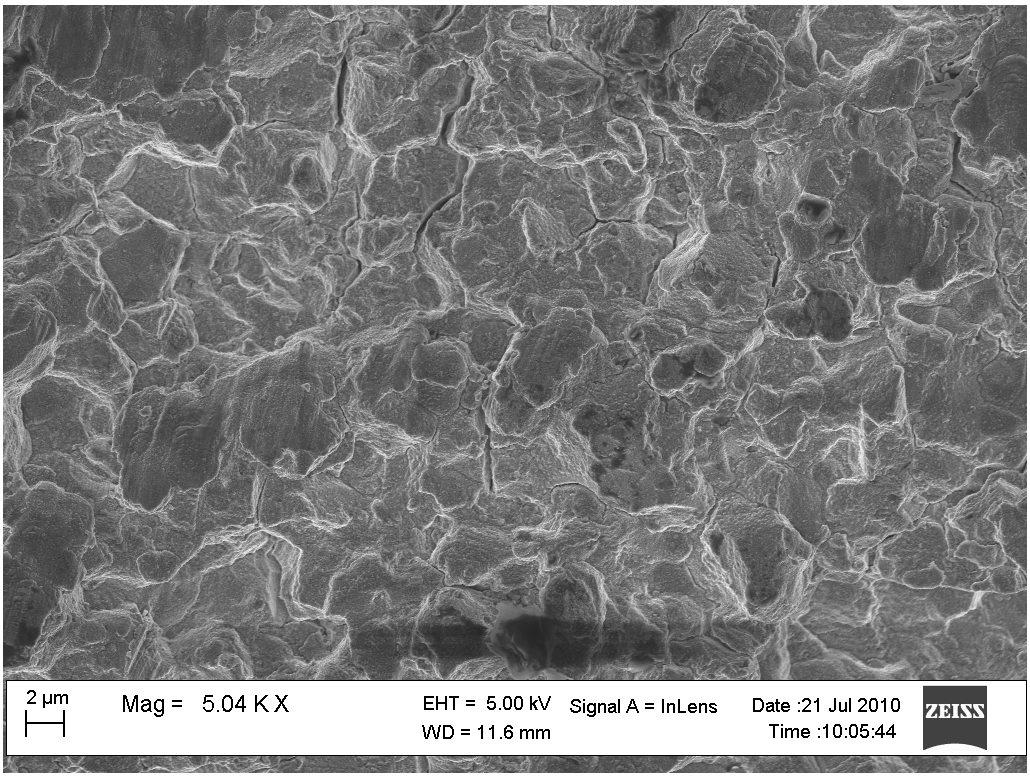

Figure 5.27: 5000x SEM Micrograph of IN100-10 tested at 649°C and 0.33 Hz at a ΔK of 33 MPa√m

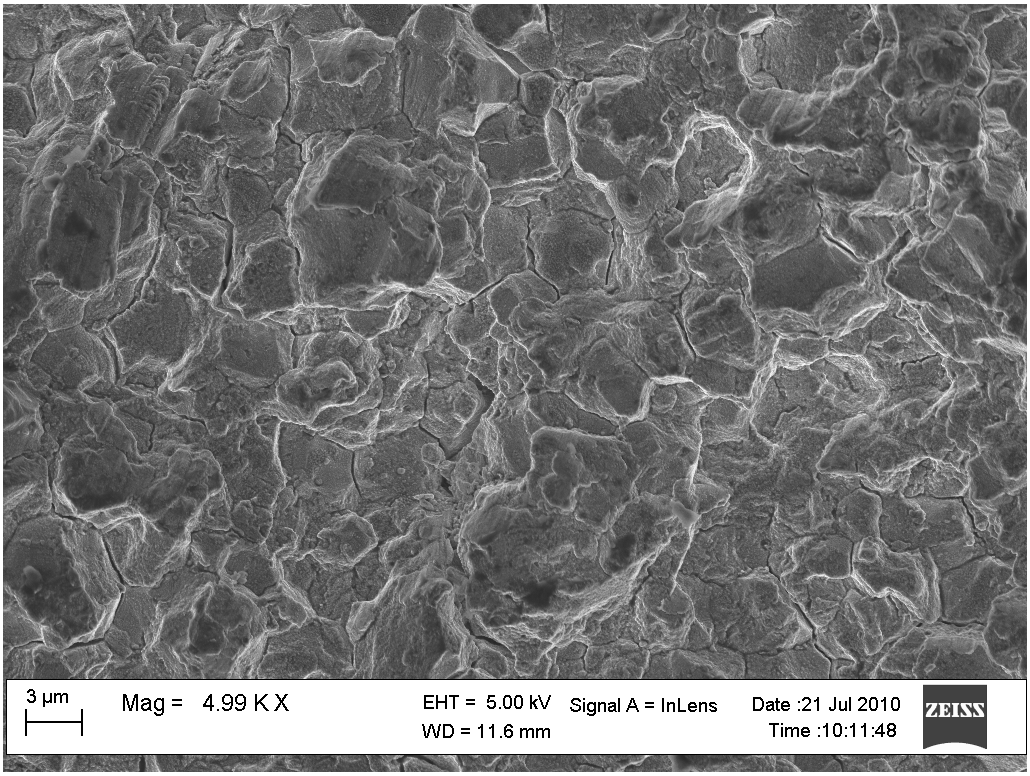

Figure 5.28: 5000x SEM Micrograph of IN100-10 tested at 649°C and 0.33 Hz at a ΔK of 44 MPa√m

Figure 5.29 shows some areas of incomplete consolidation at a ΔK of 23 MPa√m. Common in powdered metallurgy superalloys these are regions where the hot isostatic pressing (HIP) did not properly fuse the powdered material. In the right side of the micrograph an area of crack closure rubbing can be seen.

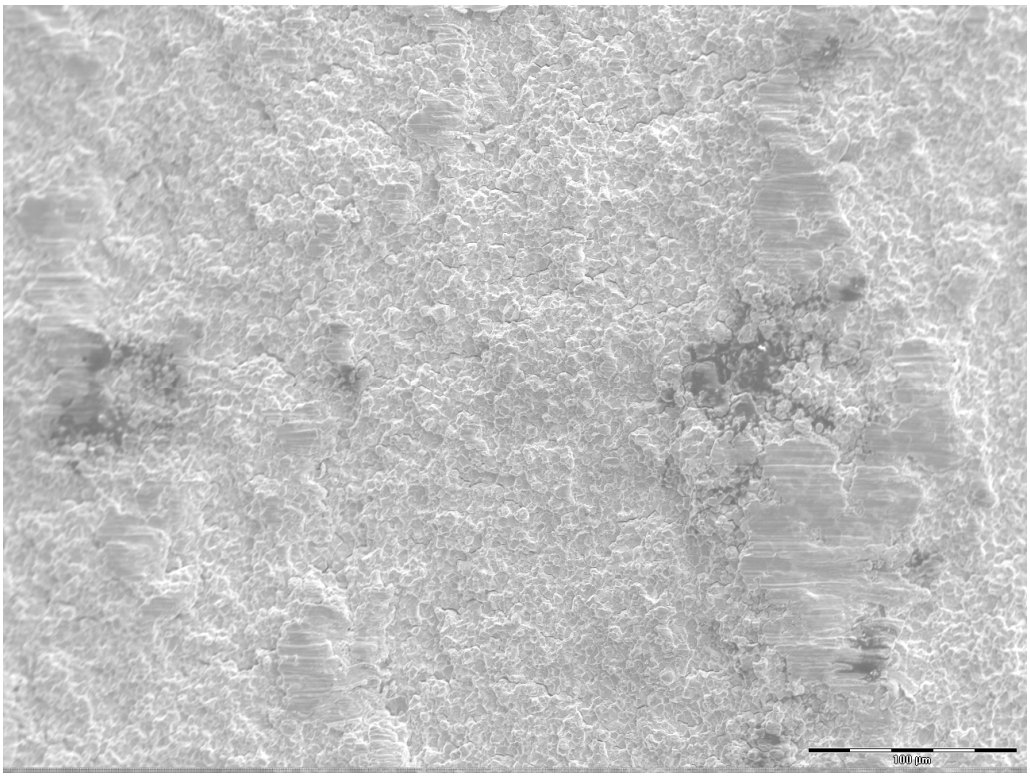

Figure 5.29: 500x SEM Micrograph of IN100-10 tested at 649°C and 0.33 Hz at a ΔK of 23 MPa√m

5.5.3: IN100-1, 316°C, 0.33 Hz Fatigue Fracture Surface

IN100-1 was tested at a temperature of 316°C, R ratio of 0.1 and a frequency of 0.33 Hz. It can be seen in SEM micrographs taken at ΔK's of 22, 33 and 44 MPa√m, Figure 5.30 through Figure 5.32, that the failure mechanism is very similar to what was seen in specimen IN100-6. Like, IN100-6, the fracture surface is very transgranular in nature with a mix of fatigue striations and ductile rupture. This demonstrates that the decrease

in temperature from 649°C has the same effect on the underlying failure mechanisms as increasing the frequency from 0.33 Hz to 20 Hz. It can also be seen that as ΔK increases from 22 to 44 MPa√m the amount of surface that failed by fatigue striations becomes more prevalent.

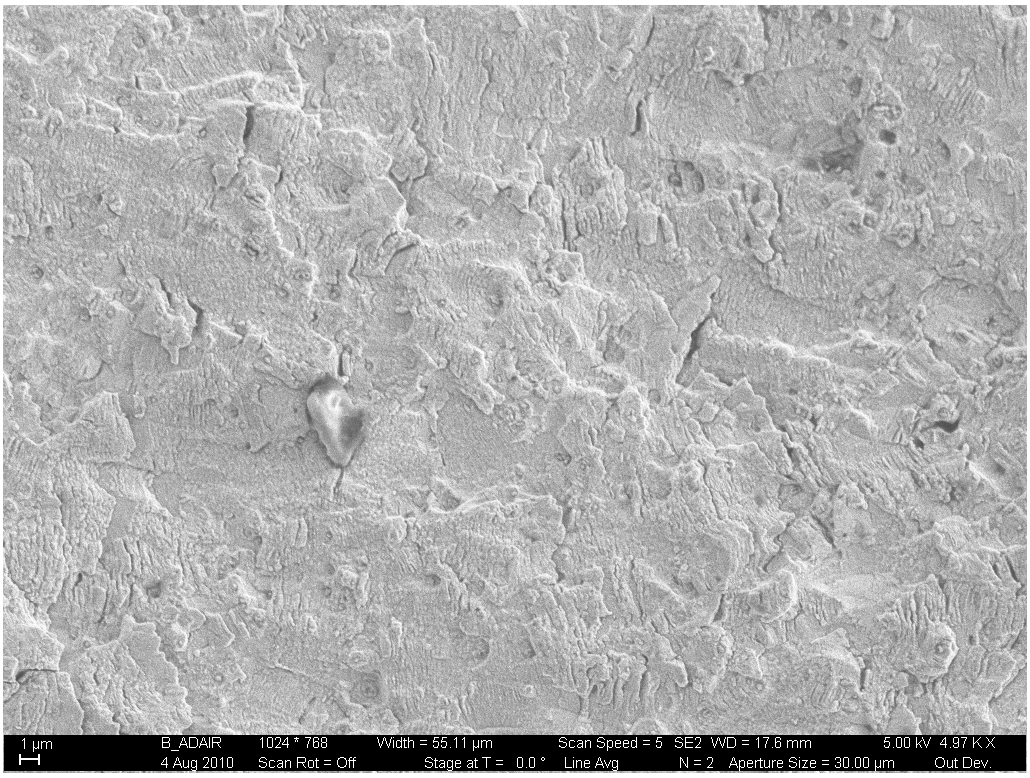

Figure 5.30: 5000x SEM Micrograph of IN100-1 tested at 316°C and 0.33 Hz at a ΔK of 22 MPa√m

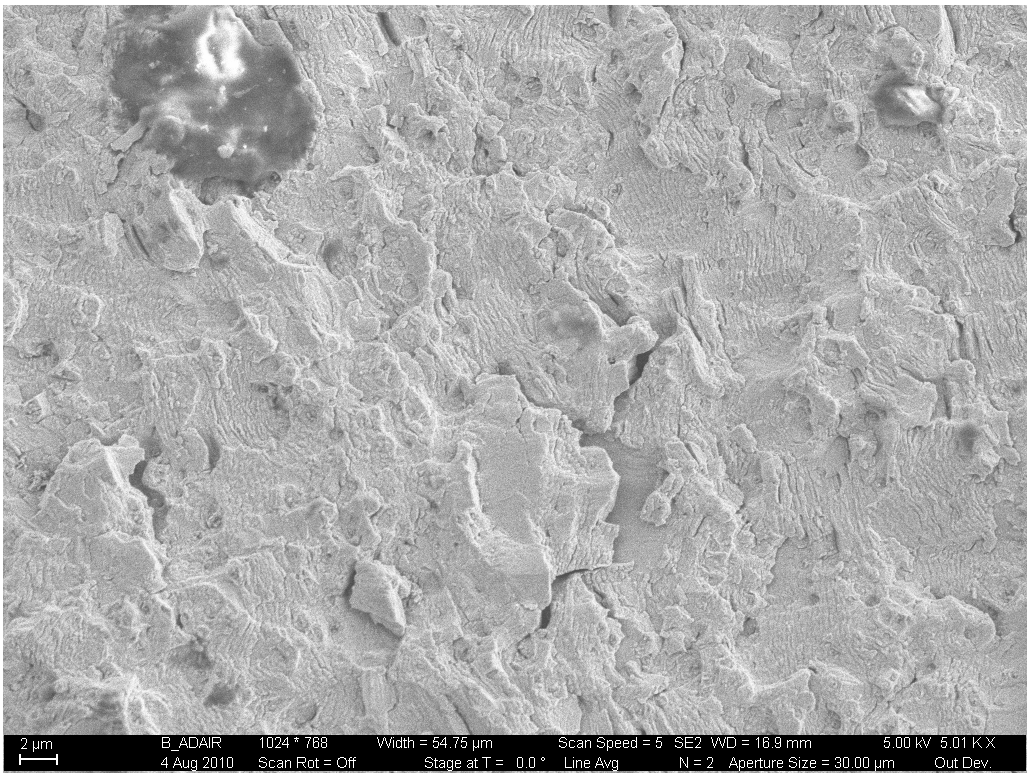

Figure 5.31: 5000x SEM Micrograph of IN100-1 tested at 316°C and 0.33 Hz at a ΔK of 33 MPa√m

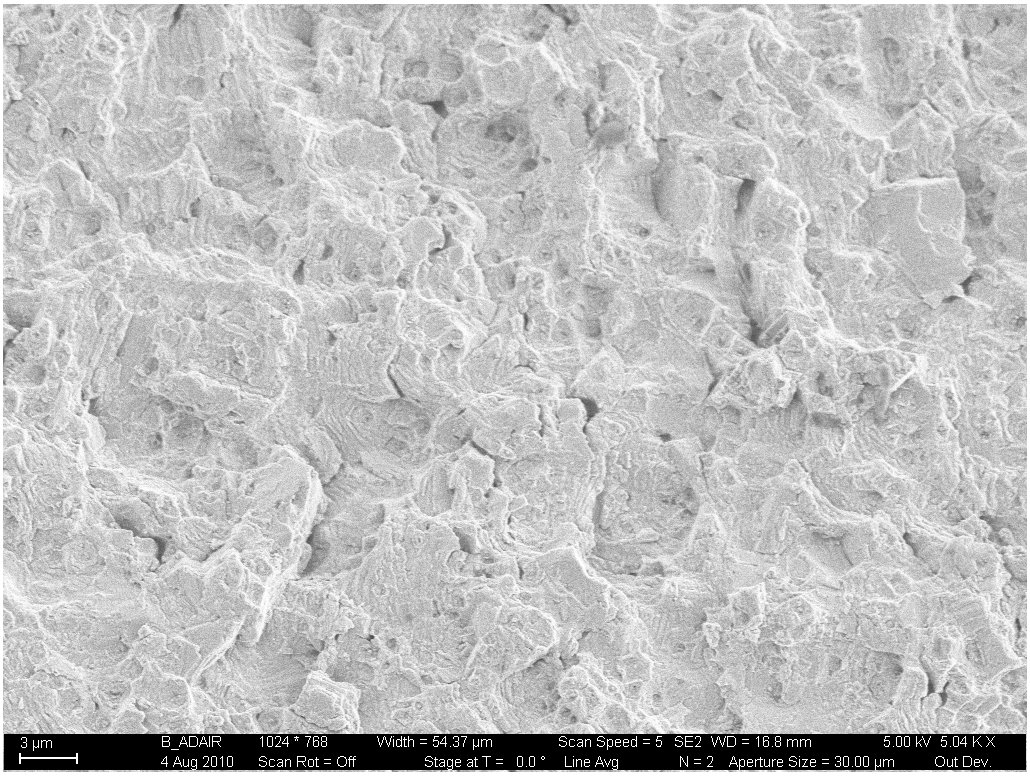

Figure 5.32: 5000x SEM Micrograph of IN100-1 tested at 316°C and 0.33 Hz at a ΔK of 44 MPa√m

Figure 5.33 illustrates an irregular crack front at a ΔK of 28 MPa√m. Most likely this was caused by some sort of inclusion that was in the void seen at the right side of the micrograph. Upon closer inspection it can be seen in Figure 5.34 that the irregular crack front formation is a slant area of all normal rupture.

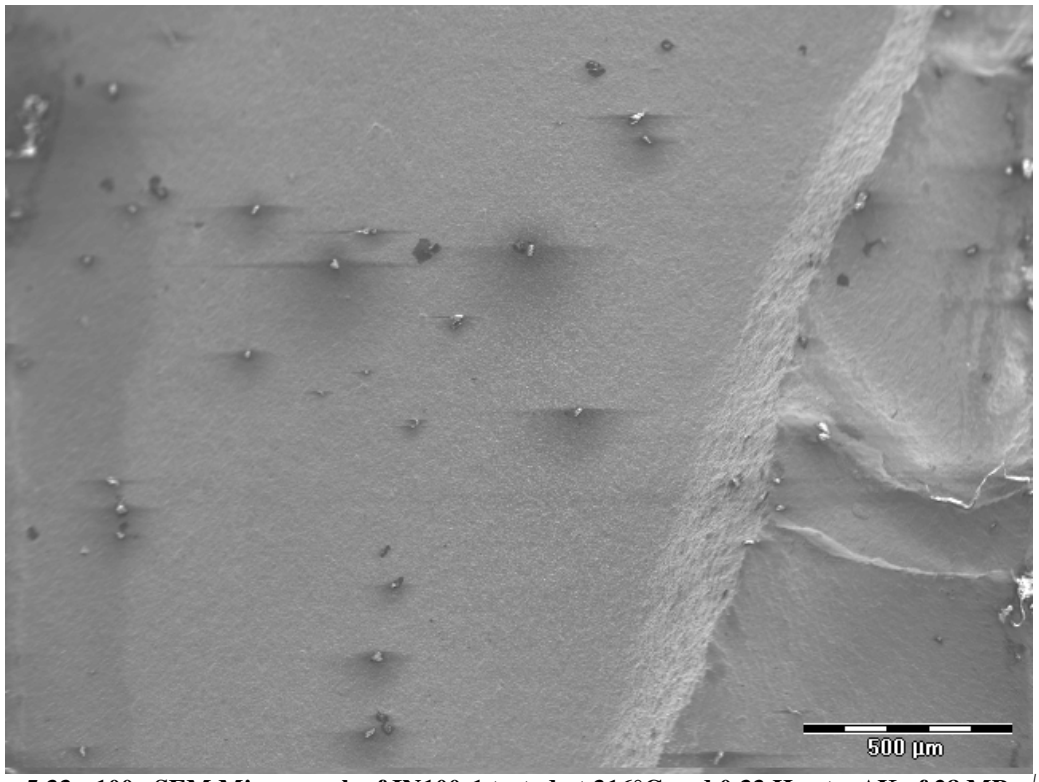

Figure 5.33: 100x SEM Micrograph of IN100-1 tested at 316°C and 0.33 Hz at a ΔK of 28 MPa√m

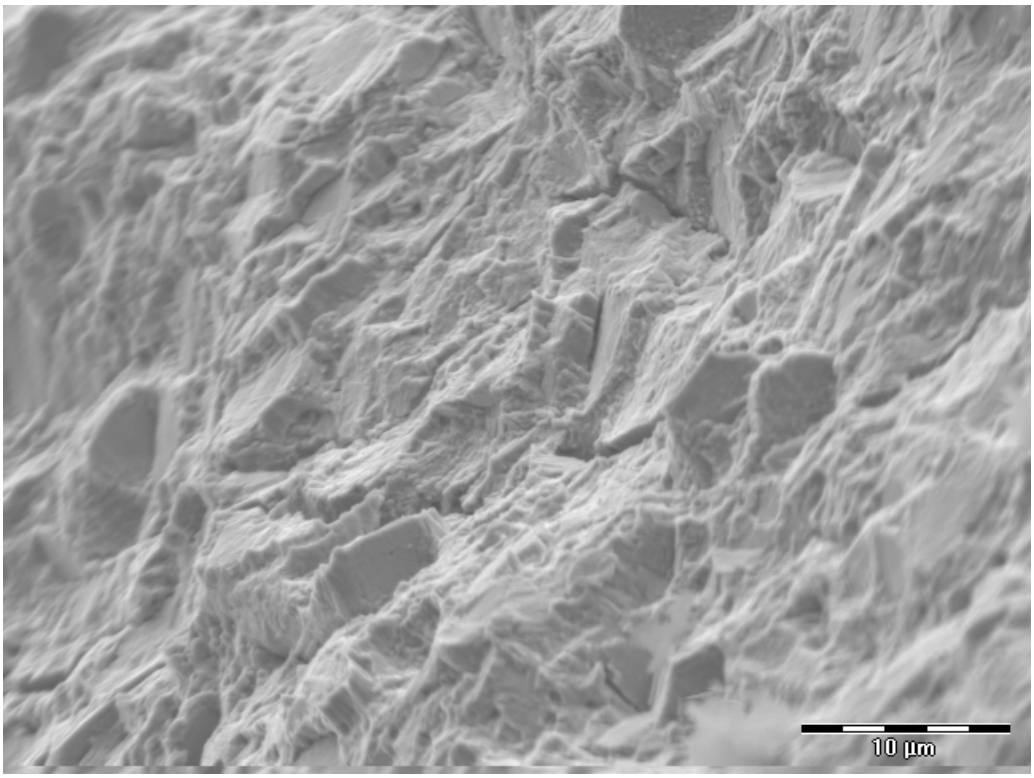

Figure 5.34: 5000x SEM Micrograph of IN100-1 tested at 316°C and 0.33 Hz at a ΔK of 28 MPa√m

5.5.4: IN100-8, 22°C, 0.33 Hz Fatigue Fracture Surface

IN100-8 was tested at room temperature with an R ratio of 0.1 and a frequency of 0.33 Hz. This compact tension specimen was created to compare room temperature crack growth rates between SENT and CT specimens to verify a correct SENT SIF equation. It can be seen in Figure 5.35 through Figure 5.37 that the low temperature this specimen was tested at created a very similar crack surface morphology that can be seen at higher frequencies coupled with elevated temperatures. As can be seen in the SEM micrographs taken at ΔK's of 22, 33 and 44 MPa√m the fracture surface is essentially transgranular in nature. Like previous fracture surfaces this transgranular surface is a mixture of fatigue striation patches and ductile rupture. The fracture surface is also composed of brittle, crystallographic features and secondary cracks. In comparison to the 316°C test

performed on IN100-1 this surface shows an even larger proportion of fatigue striations. As ΔK increases and the crack growth becomes more rapid the fatigue striations become less and less prevalent while the amount of ductile rupture increases.

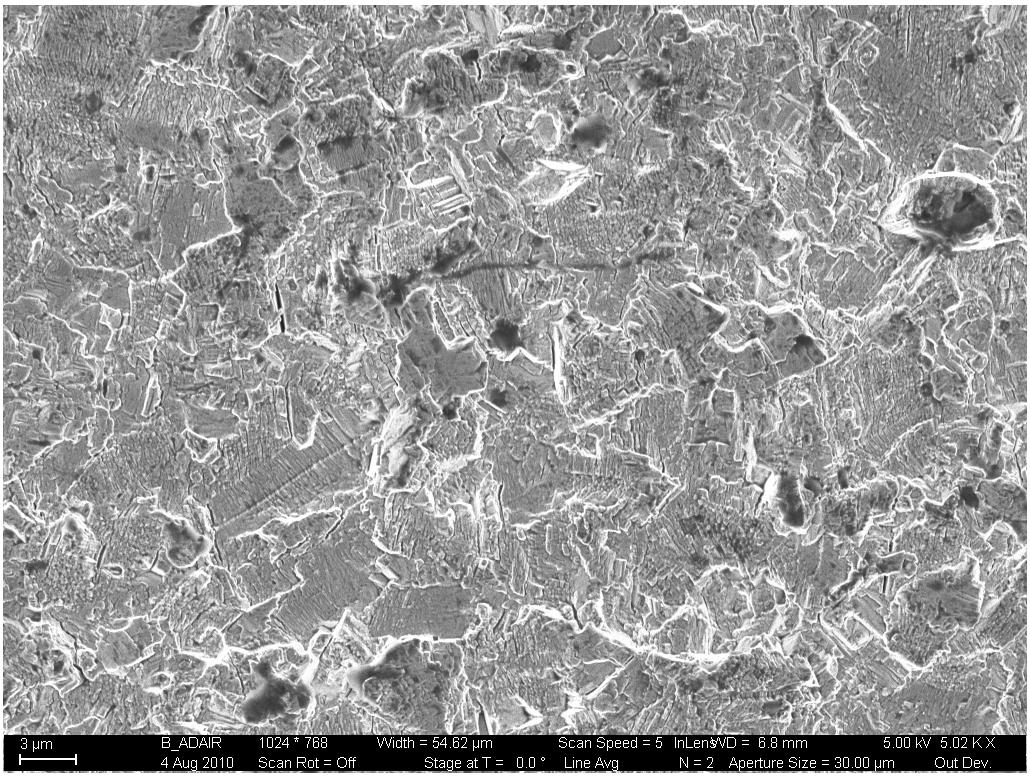

Figure 5.35: 5000x SEM Micrograph of IN100-8 tested at 22°C and 0.33 Hz at a ΔK of 22 MPa√m

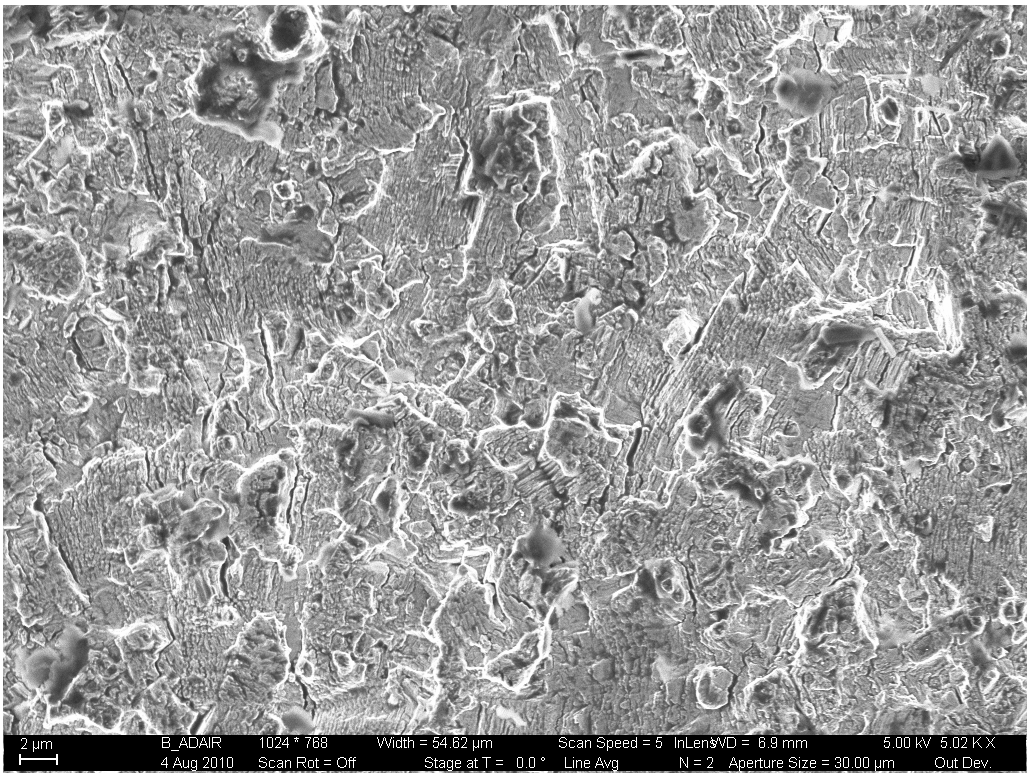

Figure 5.36: 5000x SEM Micrograph of IN100-8 tested at 22°C and 0.33 Hz at a ΔK of 33 MPa√m

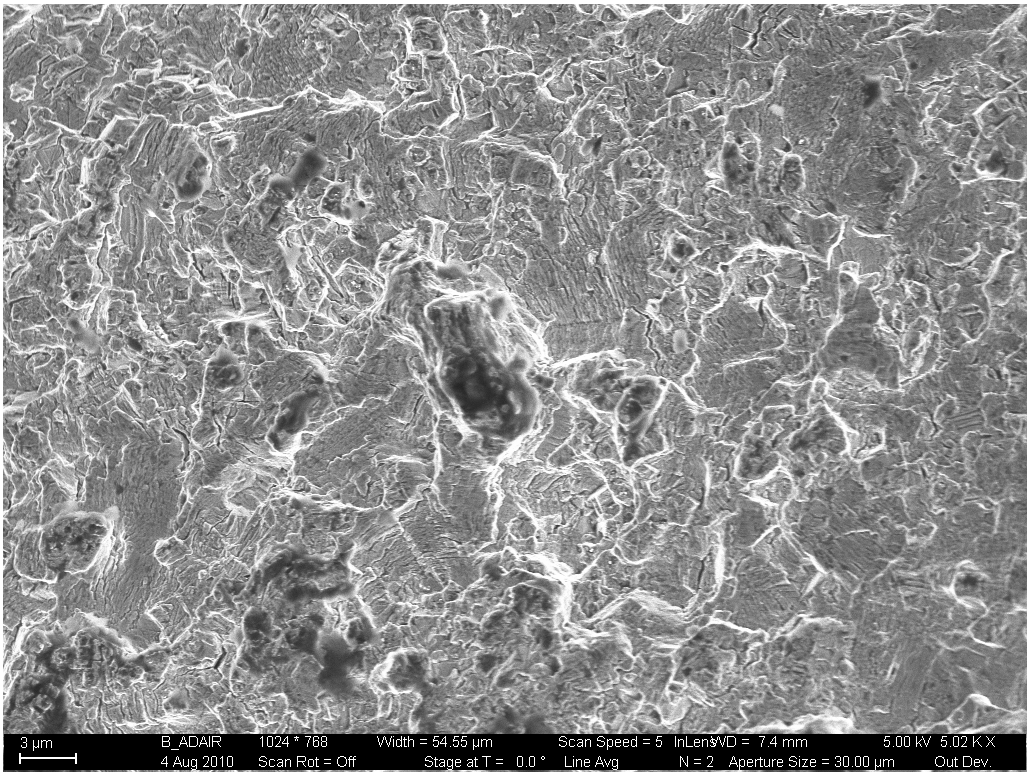

Figure 5.37: 5000x SEM Micrograph of IN100-8 tested at 22°C and 0.33 Hz at a ΔK of 44 MPa√m

5.5.5: IN100-2, 22°C, 0.33 Hz Fatigue Fracture Surface

IN100-2 was also tested at room temperature with an R ratio of 0.1 and a frequency of 0.33 Hz. It can be seen in Figure 5.38 and Figure 5.39 that the low temperature this SENT specimen was tested at created a very similar crack surface morphology that can be seen at higher frequencies coupled with elevated temperatures. As can be seen in the SEM micrographs taken at ΔK's of 26 and 32 MPa$\sqrt{m}$ the fracture surface is very transgranular in nature. Like previous fracture surfaces this transgranular surface is a mixture of fatigue striation patches and ductile rupture. There is also considerable evidence of brittle striations, crystallographic cracking and some secondary cracks along what appear to be grain boundaries. In comparison to the room temperature test performed on CT specimen IN100-8 this surface shows an even larger proportion of fatigue striations due to ΔK increasing slower in uniform displacement SENT specimens. As ΔK increases and the crack growth becomes more rapid the fatigue striations become less and less prevalent while the amount of ductile rupture increases.

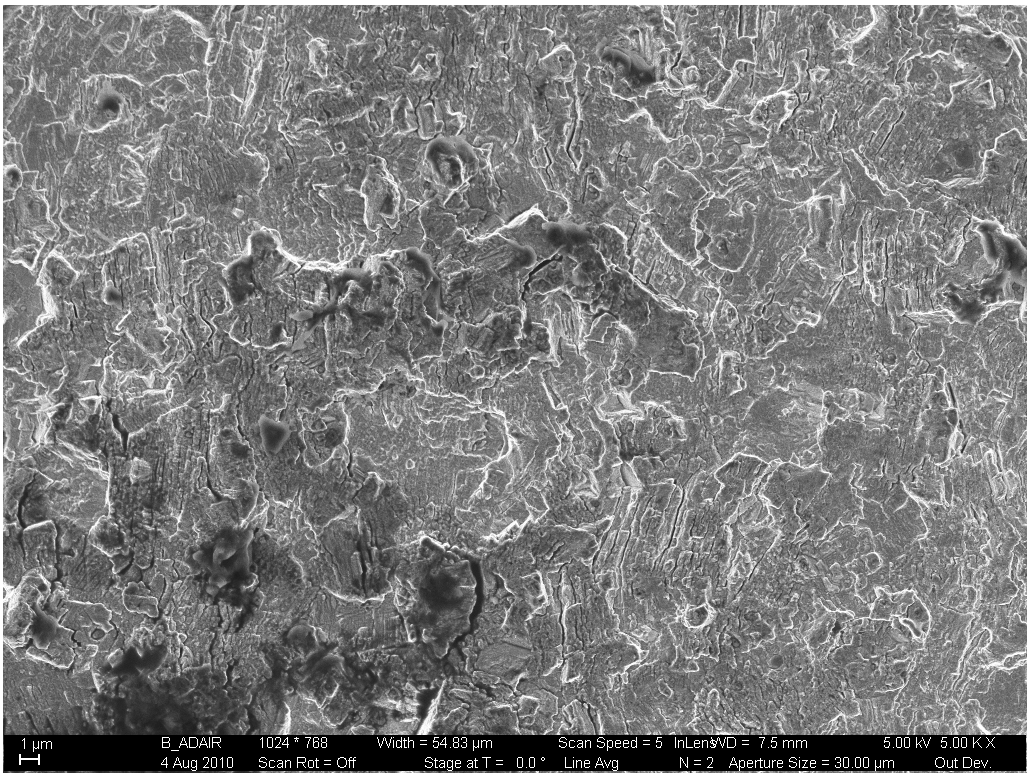

Figure 5.38: 5000x SEM Micrograph of IN100-2 tested at 22°C and 0.33 Hz at a ΔK of 26 MPa√m

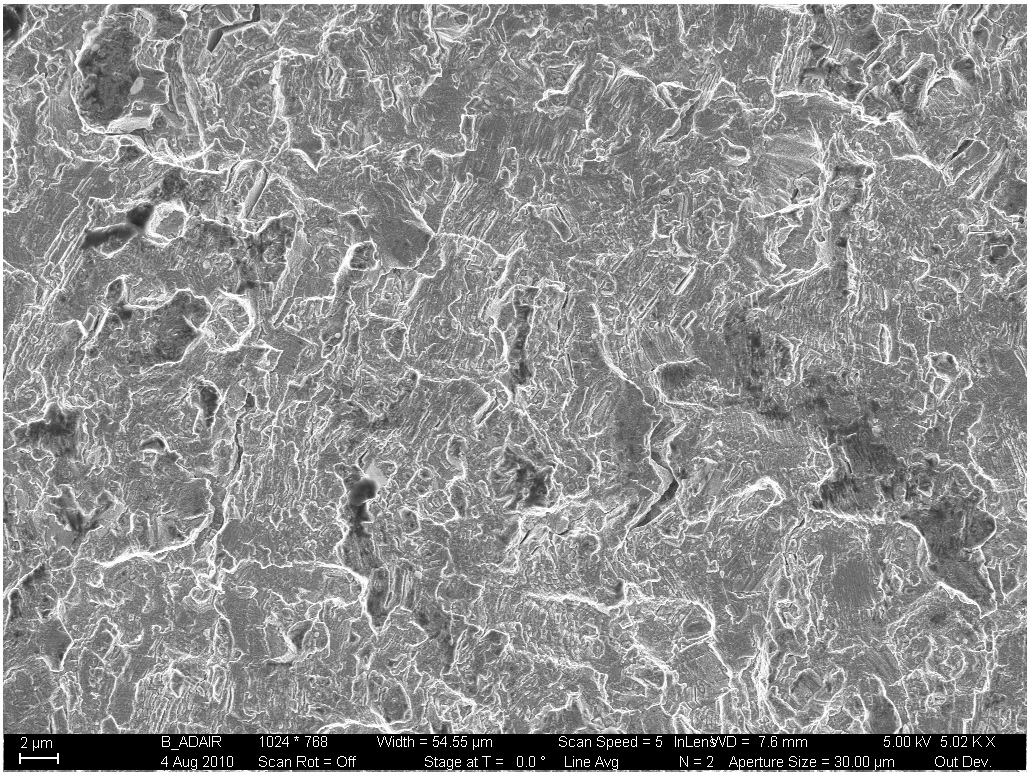

Figure 5.39: 5000x SEM Micrograph of IN100-2 tested at 22°C and 0.33 Hz at a ΔK of 32 MPa√m

5.5.6: IN100-3, 482°C, 0.33 Hz Fatigue Fracture Surface

IN100-3 was tested at a temperature of 482°C, R ratio of 0.1 and a frequency of 0.33 Hz. It can be seen in SEM micrographs taken at ΔK's of 22, 33 and 44 MPa√m, Figure 5.40 through Figure 5.42, that being tested at an intermediate temperature of 482°C created a failure mechanism that is a mix of transgranular and intergranular fracture. There is significantly increased intergranular fatigue fracture with small regions of striations and crystallographic fracture. Elements from what are normally seen at room temperature and also at slow and fast frequencies at a temperature of 649°C can be seen in this 482°C specimen. Intergranular fracture is prevalent at lower values of ΔK as can be seen in Figure 5.40. As the ΔK increases the fracture surface transitions to a more transgranular failure mechanism composed of a mix of fatigue striations and ductile rupture as can be seen in Figure 5.42. It can also be seen that as ΔK increases from 33 to 44 MPa√m the amount of surface that failed by ductile rupture becomes more prevalent due to the crack growth rate increasing.

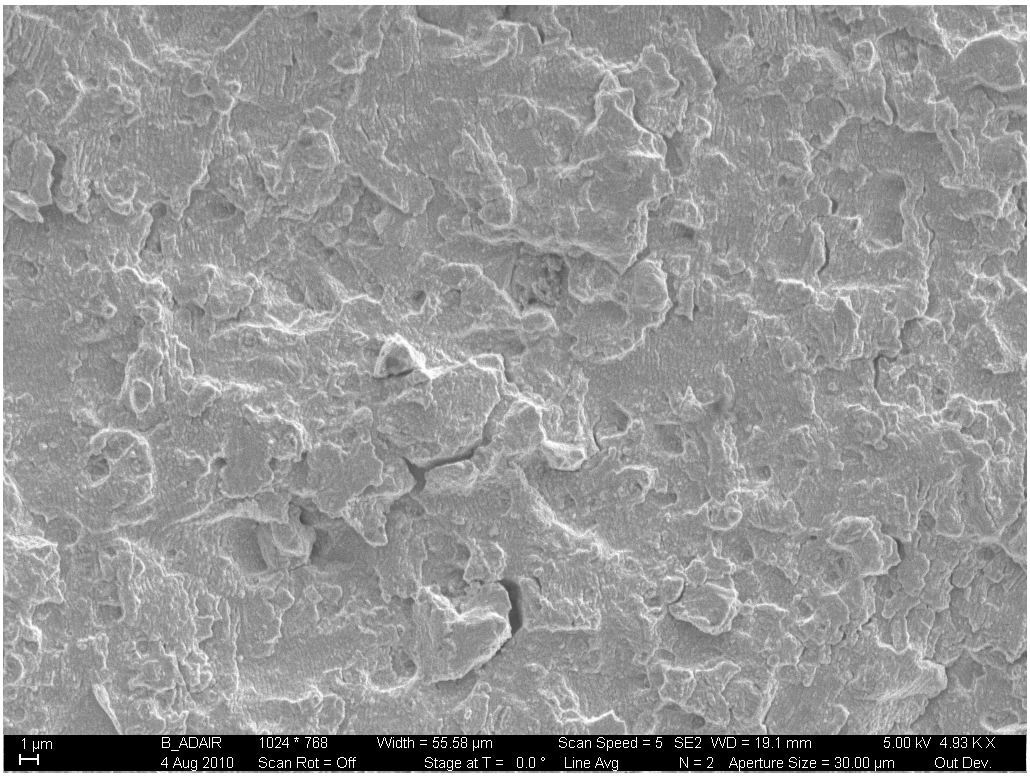

Figure 5.40: 5000x SEM Micrograph of IN100-3 tested at 482°C and 0.33 Hz at a ΔK of 22 MPa√m

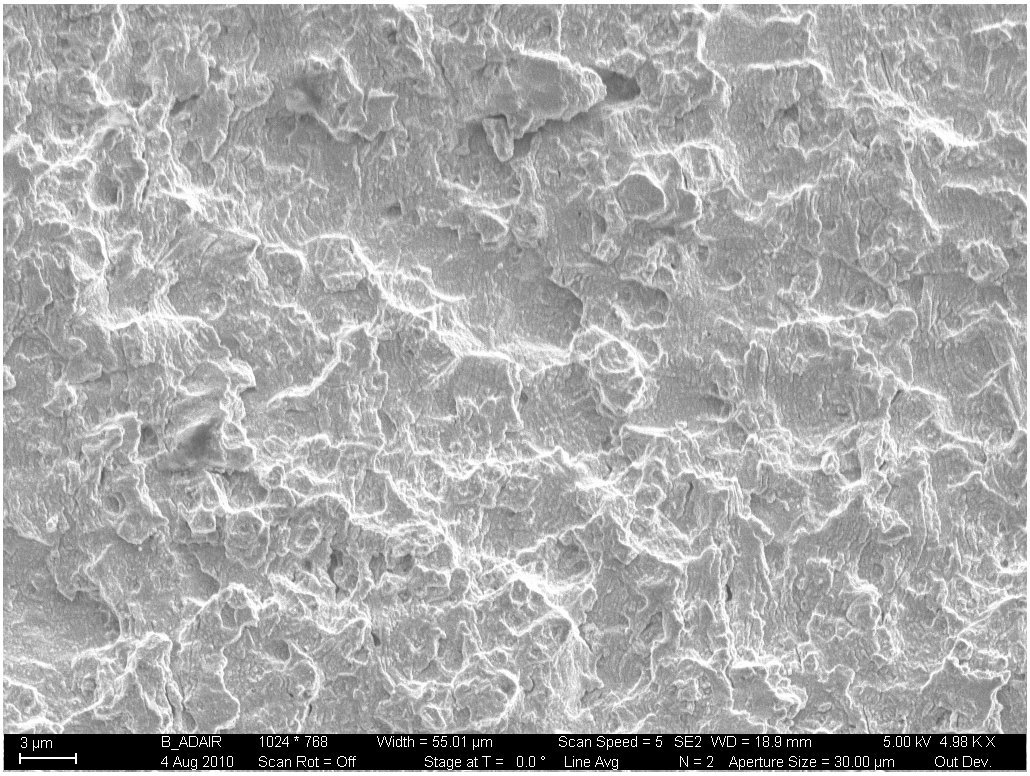

Figure 5.41: 5000x SEM Micrograph of IN100-3 tested at 482°C and 0.33 Hz at a ΔK of 33 MPa√m

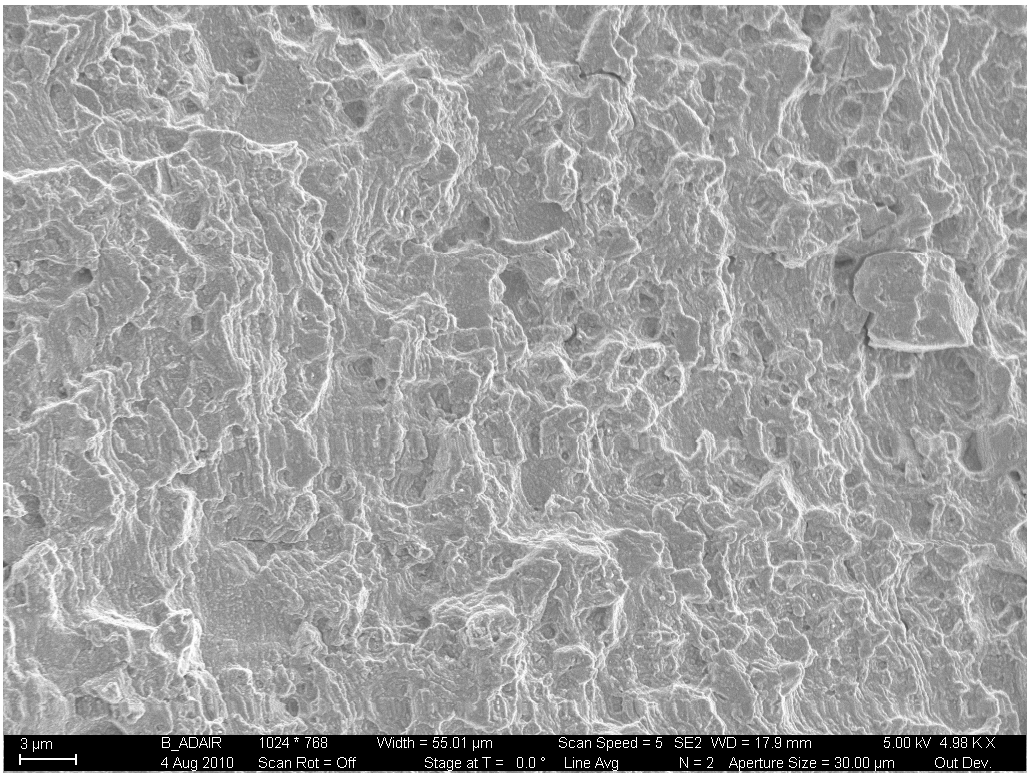

Figure 5.42: 5000x SEM Micrograph of IN100-3 tested at 482°C and 0.33 Hz at a ΔK of 44 MPa√m

5.5.7: IN100-9, 649°C, 3 and 1 Hz Fatigue Fracture Surface

IN100-9 was tested at a temperature of 649°C, R ratio of 0.1 and a frequency of 3 and 1 Hz. The effect of increasing ΔK at 3 Hz can be seen in SEM micrographs taken at ΔK's of 22 and 33 MPa√m in Figure 5.43 and Figure 5.44. The predominantly intergranular fracture surface with crystallographic facets seen in Figure 5.43 transitions to a mix of intergranular and transgranular failure mechanisms composed of a blend of fatigue striations and ductile rupture as can be seen in Figure 5.44. Testing performed at a frequency of 1 Hz also shows an increase in transgranular fracture as ΔK increases from 22 to 44 MPa√m as seen in Figure 5.45 and Figure 5.46. Testing this specimen at two different frequencies allows the effect of frequency at common ΔKs to be compared. It can be seen from Figure 5.43 and Figure 5.45 that the fractures surfaces at a common ΔK

of 22 MPa√m for 3 and 1 Hz tests have a very similar intergranular failure mechanism. From this we know that the diffusion mechanism responsible for oxidation is very fast acting and is only negated at high values of ΔK and at high frequencies.

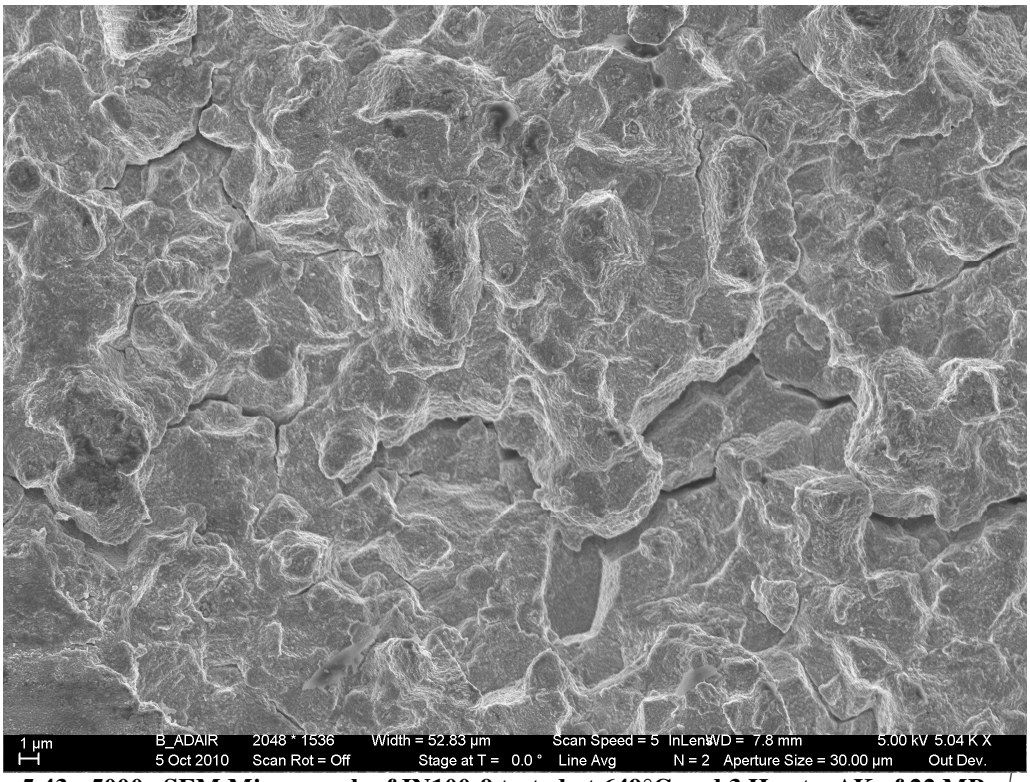

Figure 5.43: 5000x SEM Micrograph of IN100-9 tested at 649°C and 3 Hz at a ΔK of 22 MPa√m

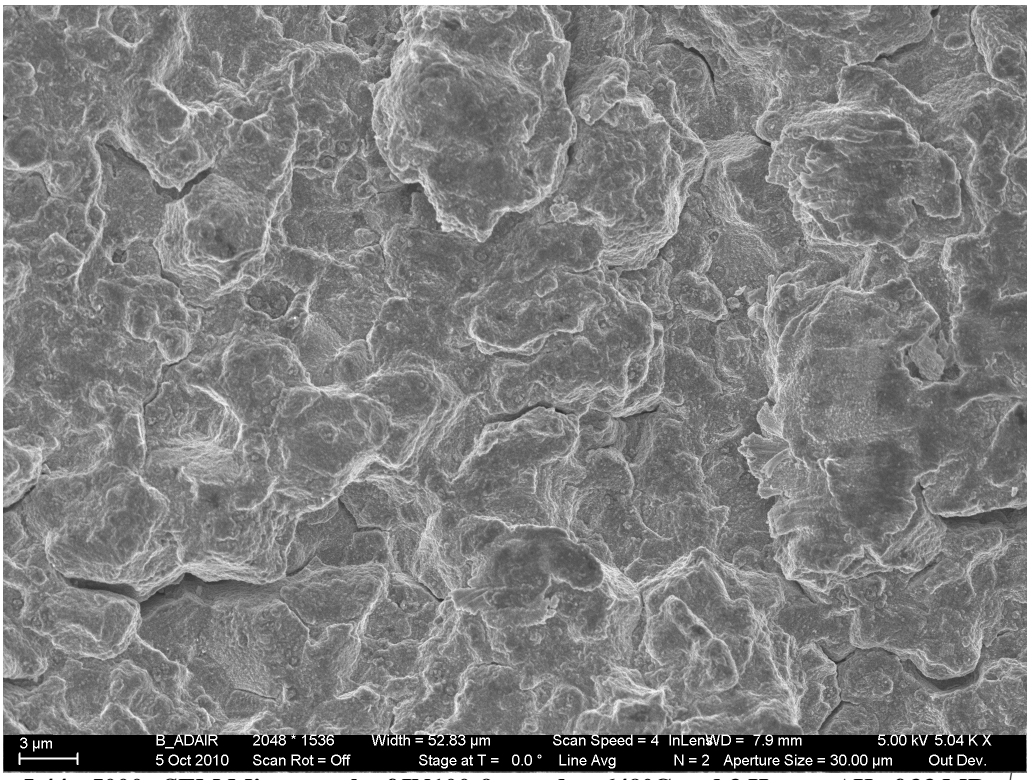

Figure 5.44: 5000x SEM Micrograph of IN100-9 tested at 649°C and 3 Hz at a ΔK of 33 MPa√m

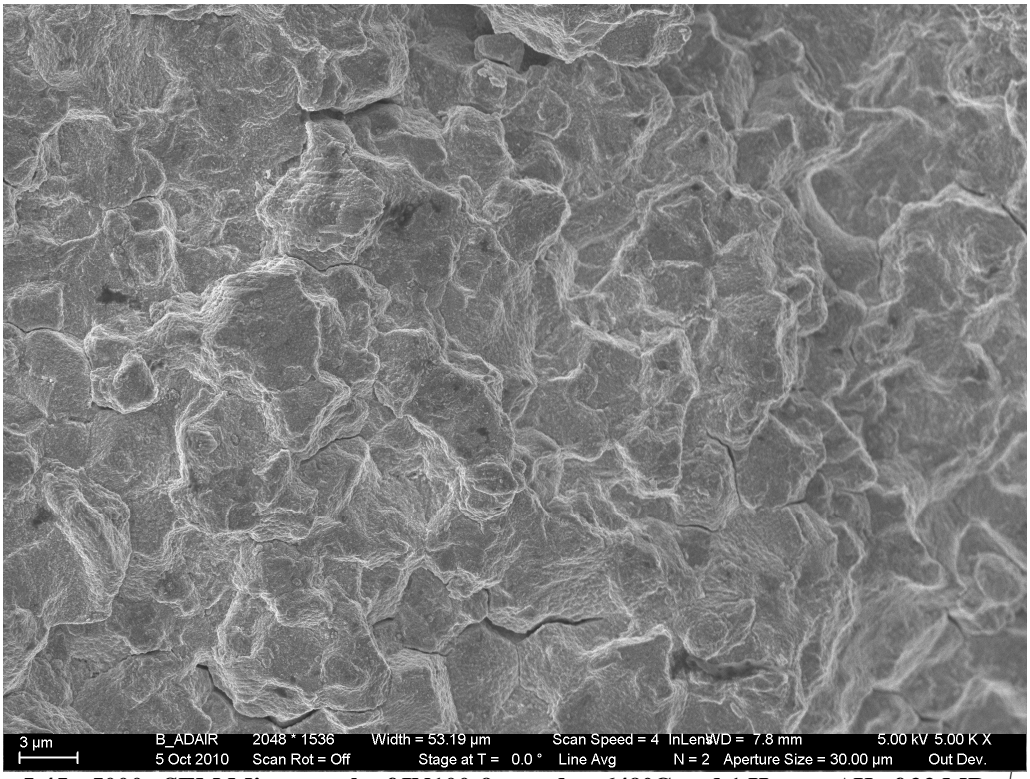

Figure 5.45: 5000x SEM Micrograph of IN100-9 tested at 649°C and 1 Hz at a ΔK of 22 MPa√m

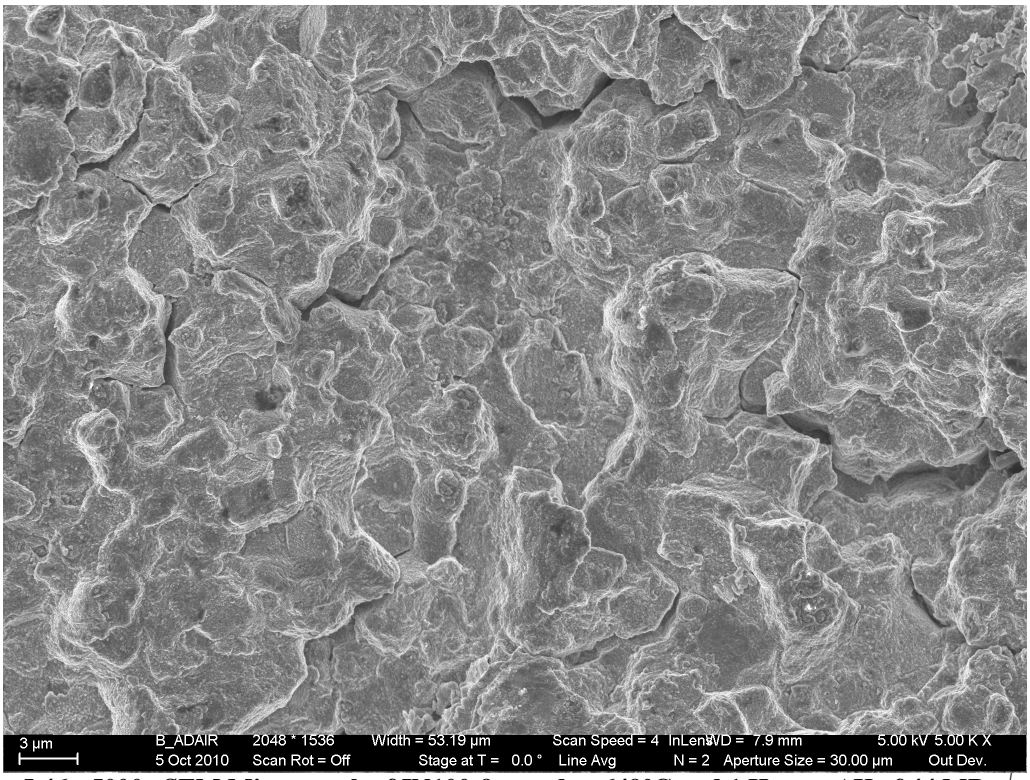

Figure 5.46: 5000x SEM Micrograph of IN100-9 tested at 649°C and 1 Hz at a ΔK of 44 MPa√m

5.6: Temperature and Load Interaction Fatigue Crack Growth Rate Testing

Temperature and load interaction fatigue crack growth rate testing was performed on four IN100 single edge notch tension specimens. All testing was done at an R ratio of 0.1. The test matrix in Table 5.5 shows the test temperatures and frequencies. All specimens were pre-cracked at 20 Hz at the same minimum temperature they were tested at. For each test, crack length and number of cycles was recorded approximately every 500 cycles. This cycle interval was larger at small ΔK's and decreased as ΔK increased.

Table 5.5: Temperature and Load Interaction Test Matrix

Specimen	Temperature (°C)	R Ratio	Frequency (Hz)
IN100-4	316/649	0.1	0.33
IN100-5	649	0.1	0.33
IN100-7	316	0.1	0.33
IN100-9	649	0.1	1

Temperature interaction testing was performed by cycling between 316°C and 649°C in blocks of 1, 10 and 100 cycles. Alternating the temperature every one cycle between temperatures caused the fatigue crack growth rate to be substantially faster than the non-interaction prediction as seen in Figure 5.47. Ten block alternating temperature interaction testing also grew faster than the non-interaction prediction but not to the same extent as the one block alternating test. This can be seen in Figure 5.48. On the other hand one hundred block alternating testing, shown in Figure 5.49, grew slower than the non-interaction prediction. It was found that as the number of alternating temperature cycles increased, changes in the γ' morphology (and hence deformation mode) caused changes in the environmental interactions thus demonstrating the sensitivity of the environmental interaction on the details of the deformation mode. With the aid of SEM fractography discussed in the next section it was shown that at low alternating cycles, 316°C crack growth was accelerated due to crack tip embrittlement caused by 649°C cycling. At higher alternating cycles the 316°C cycling quickly grew through the embrittled crack tip but then grew slower than expected due to the possible formation of Kear-Wilsdorf locks at 649°C.

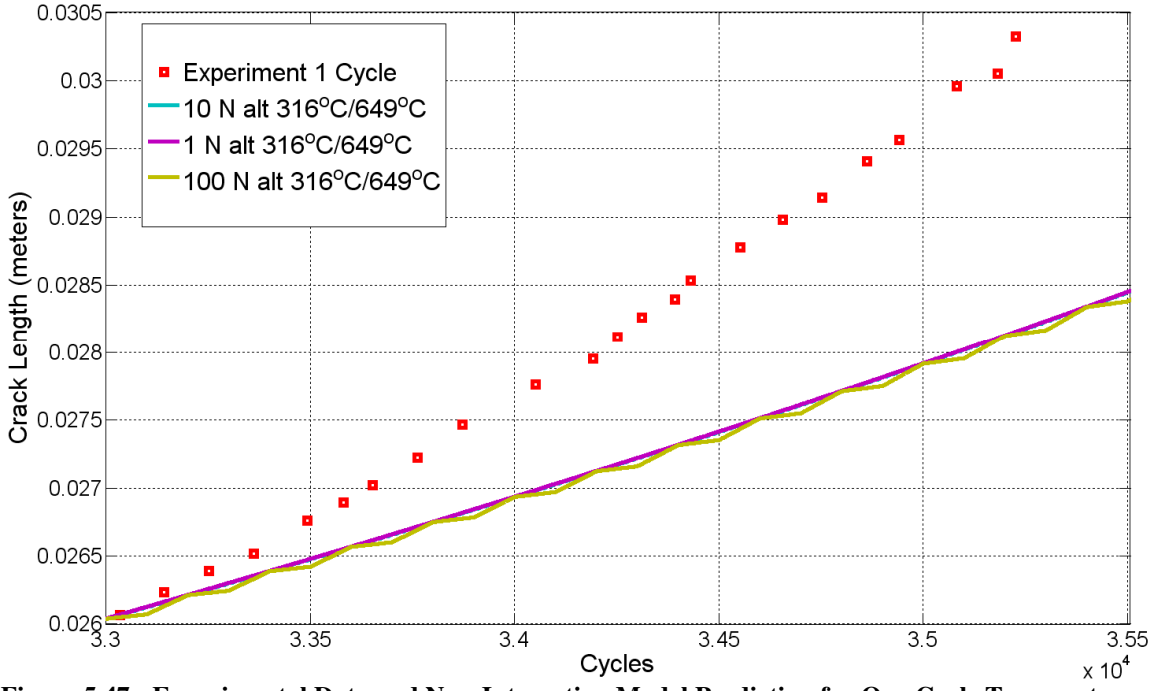

Figure 5.47: Experimental Data and Non-Interaction Model Prediction for One Cycle Temperature Interactions Between 316°C and 649°C

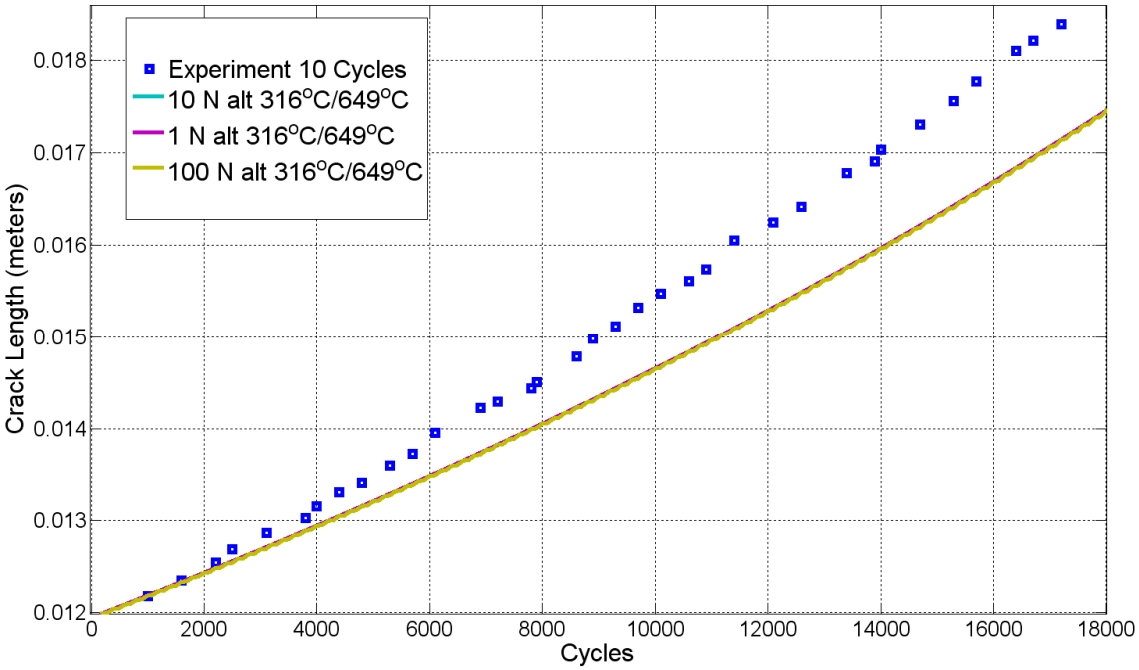

Figure 5.48: Experimental Data and Non-Interaction Model Prediction for Ten Cycle Temperature Interactions Between 316°C and 649°C

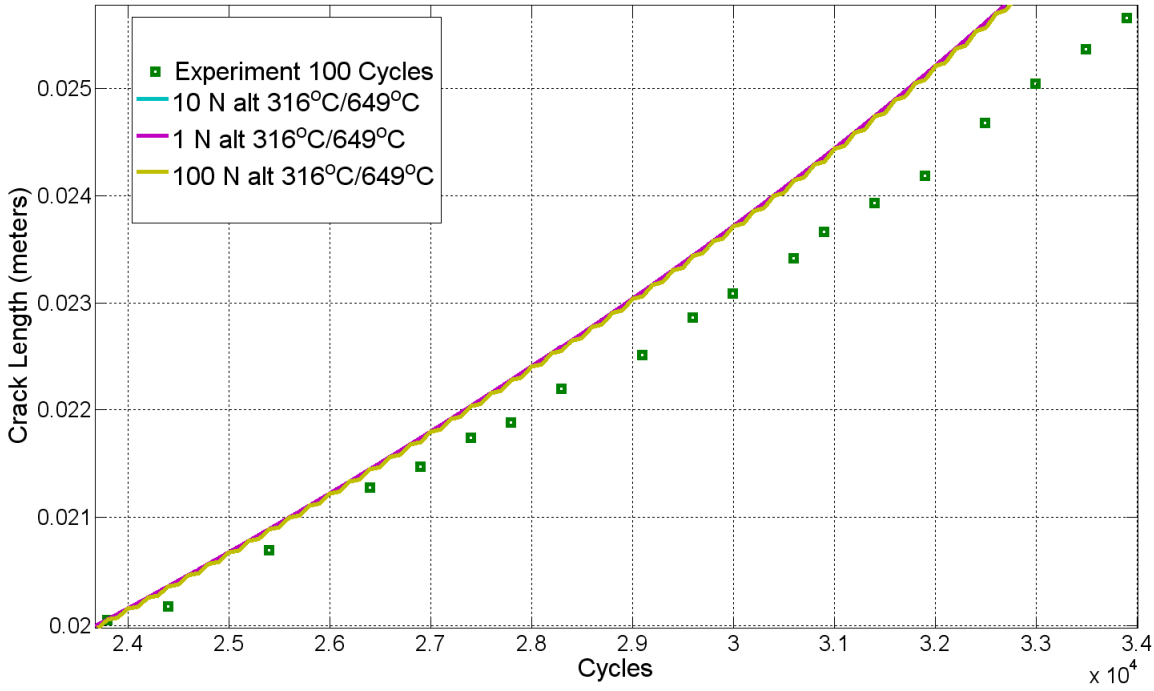

Figure 5.49: Experimental Data and Non-Interaction Model Prediction for One Hundred Cycle Temperature Interactions Between 316°C and 649°C

Load interaction testing in the form of single overloads was performed at 316°C and 649°C. Calculations showed that it would take 800 cycles for the crack to grow out of a 1.6x overload plastic zone. With this in mind overloads of 2.0x, 1.6x and 1.3x were applied every 800 cycles. This allowed the observation of fully retarded crack growth at 2.0x, crack growth that just exits retardation at 1.6x, and crack growth that quickly exits retardation at 1.3x.

During the course of overload testing an interesting crack closure phenomenon was observed. Immediately following the precracking the crack growth rate was fairly high due to the application of the first 2.0x overload and minor crack growth from the 1.0x cycles; after this first overload the crack growth rate was found to steadily decrease upon application of further overload cycles. This phenomenon can be attributed to the

stabilized $K_{opening}$ created during the 1.0x precracking. Upon additional application of overload cycles $K_{opening}$ slowly increased leading to a decreasing ΔK_{eff}. A visualization of this process can be seen in Figure 5.50. Once the 2.0x overload crack growth stabilized, da/dN then continued to increase with increasing ΔK.

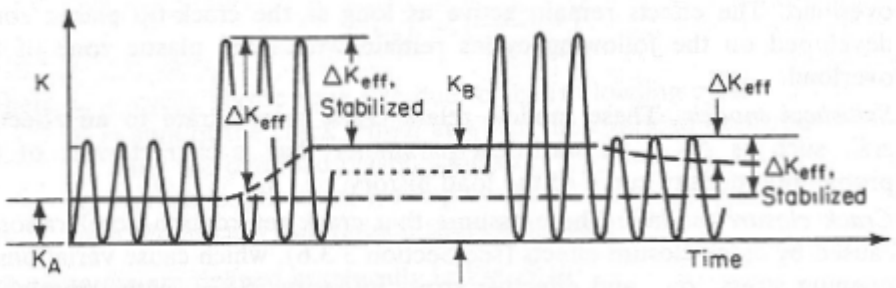

Figure 5.50: Variation in Crack Closure Stress Intensity Factor (and Variation in ΔKeff) with Variation in Load Level [16]

Overload interaction testing led to full crack retardation at 2.0x overloads for both 316°C and 649°C testing. The only growth seen during 2.0x overload testing was attributed to growth from the overload cycles. On the other hand 1.6x overloading at both temperatures led to retarded crack growth that consisted of growth from both the 1.6x and 1.0x cycles. It was found that 1.3x overloads at 649°C created accelerated crack growth when compared with constant amplitude data at the same temperature. The 1.3x overloads at 316°C was found to retard the crack growth when compared with constant amplitude data at the same temperature. This can be attributed to the less oxidation embrittlement being present at the lower temperature. These results can be seen in Figure 5.51.

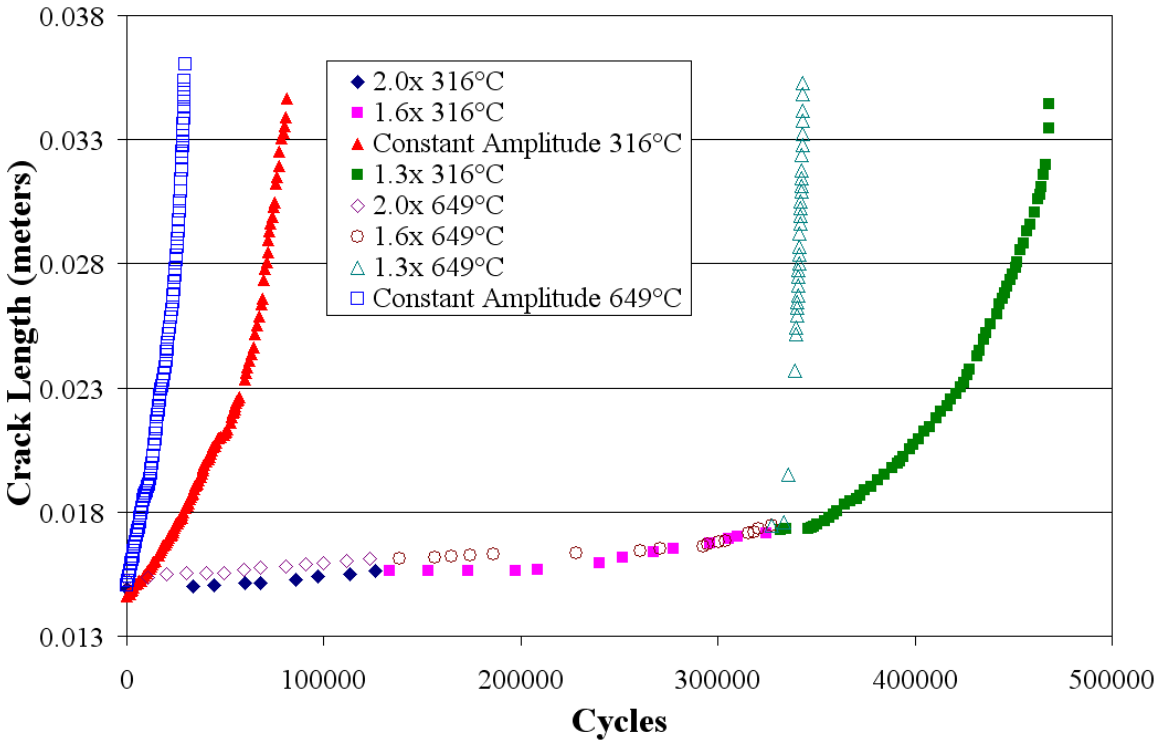

Figure 5.51: Experimental Load Interactions Data for 1.3x, 1.6x and 2.0x Overloads Applied Every 800 Cycles

Single overload testing was performed at 1 Hz, an R ratio of 0.1 and 649°C for the 1.3x and 2.0x overload case. The results of 1.3x overload can be seen in Figure 5.52. The 1.3x non-interaction prediction shows no retardation, just acceleration due to the applied overload. Looking at the experimental test data it can be clearly seen that crack growth retardation is present for approximately 500 cycles after the applied overload. After the 500 cycles the experimental data closely track the growth rate of the non-interaction prediction. The application of a 2.0x overload caused full crack growth retardation where no crack growth was measured after applying 28,000 1.0x cycles.

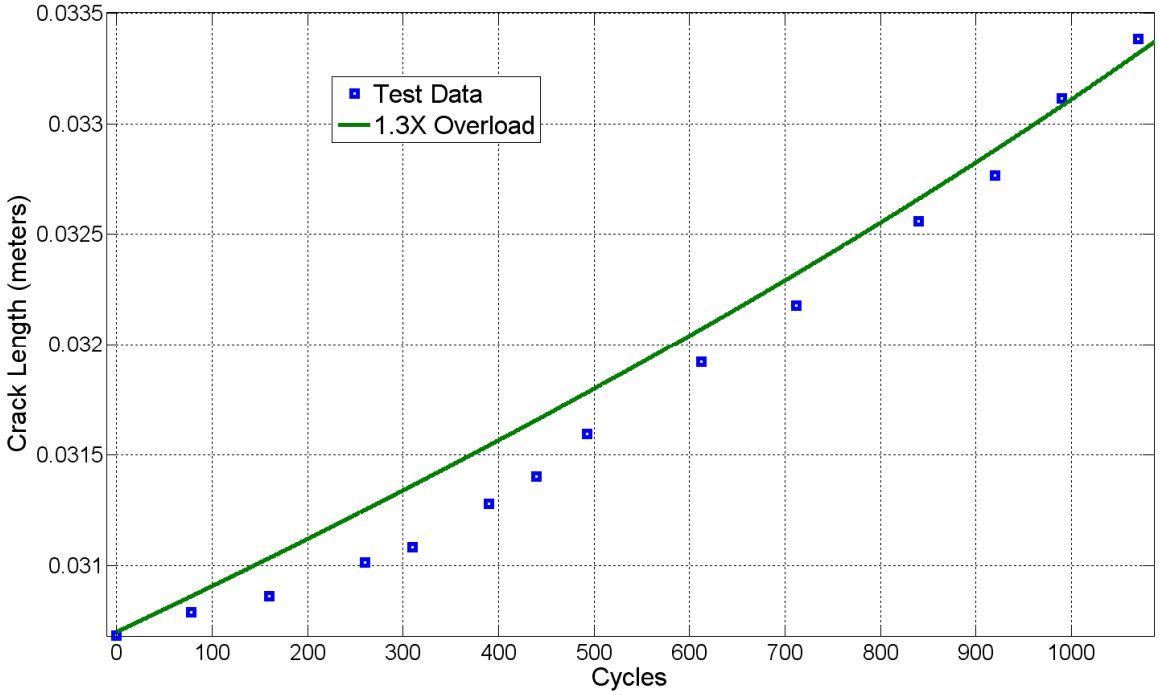

Figure 5.52: Experimental Data and Non-Interaction Model Prediction for 1.3x Overload Interaction Testing

5.7: Temperature and Load Interaction Crack Surface Morphology

5.7.1: IN100-4, 316/649°C, 0.33 Hz Fatigue Fracture Surface

Specimen IN100-4 was alternated between a temperature of 316°C and 649°C, at an R ratio of 0.1 and a frequency of 0.33 Hz. Three different alternating blocks consisting of 10, 100 and 1 cycles in that order were applied to this specimen. SEM fractographs for the alternating 10 cycle test can be seen in Figure 5.53 and Figure 5.54. The effect of 649°C crack growth on the 316°C crack growth can clearly be seen as more intergranular crack growth is present at 316°C than found in isothermal testing. The material degradation at 649°C led to embrittlement in front of the crack tip that allowed the 316°C cycles to propagate faster than predicted by the non-interaction model. The 316°C

cycling was able to break through this oxide zone after a few cycles leading to an overall crack growth rate that was slightly faster then predicted.

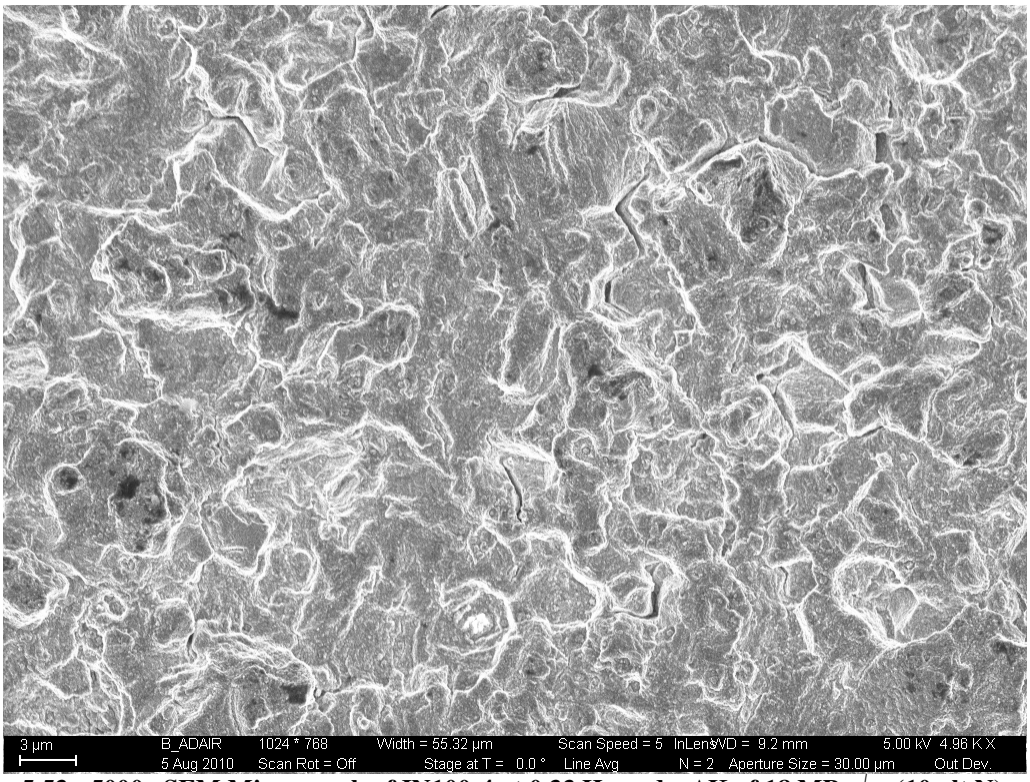

Figure 5.53: 5000x SEM Micrograph of IN100-4 at 0.33 Hz and a ΔK of 18 MPa√m (10 alt N)

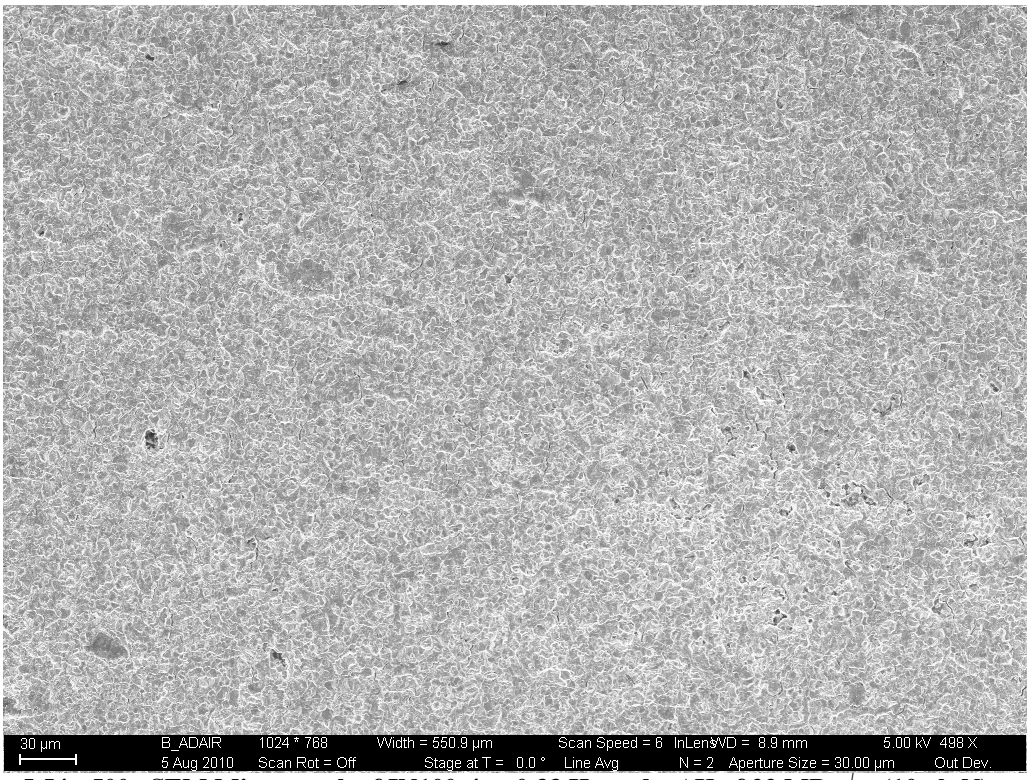

Figure 5.54: 500x SEM Micrograph of IN100-4 at 0.33 Hz and a ΔK of 22 MPa√m (10 alt N)

SEM fractographs for the alternating 100 cycle test can be seen in Figure 5.55 through Figure 5.58. In looking at Figure 5.56 and Figure 5.58 the effect of 649°C crack growth on the 316°C propagation rate can clearly be seen as more intergranular crack growth is present at 316°C than the transgranular mechanism found in isothermal testing. This phenomenon can still be seen even as ΔK increases, which would tend to promote an environment that is more favorable to transgranular fatigue crack growth.

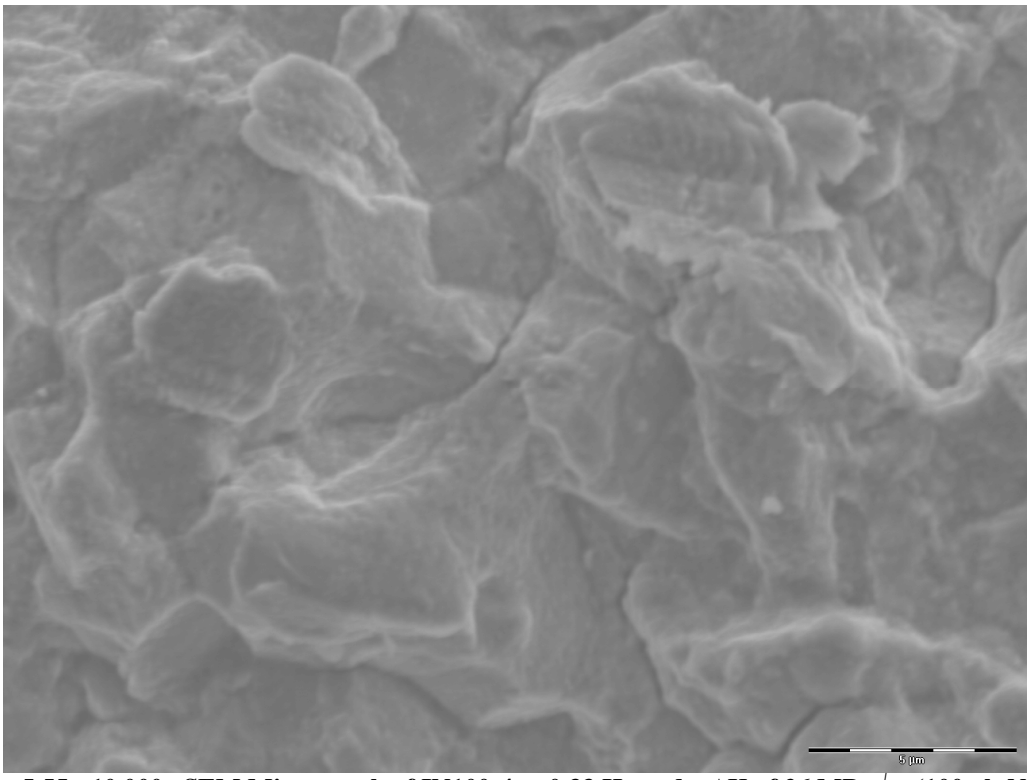

Figure 5.55: 10,000x SEM Micrograph of IN100-4 at 0.33 Hz and a ΔK of 26 MPa√m (100 alt N 649°C)

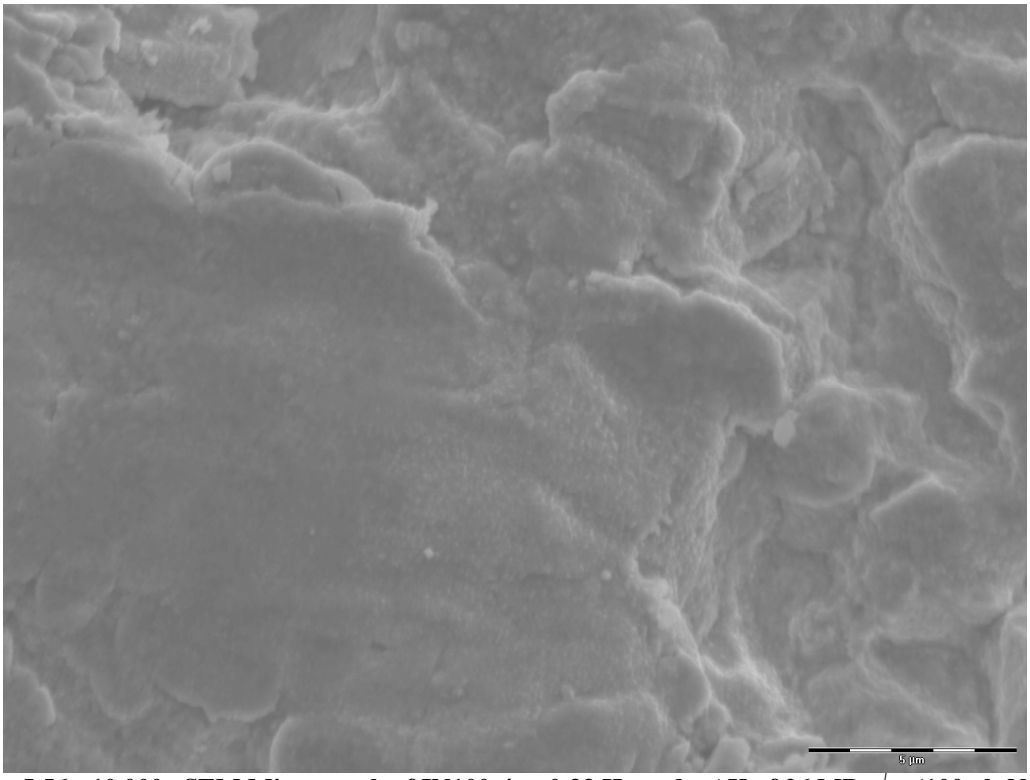

Figure 5.56: 10,000x SEM Micrograph of IN100-4 at 0.33 Hz and a ΔK of 26 MPa√m (100 alt N 316°C)

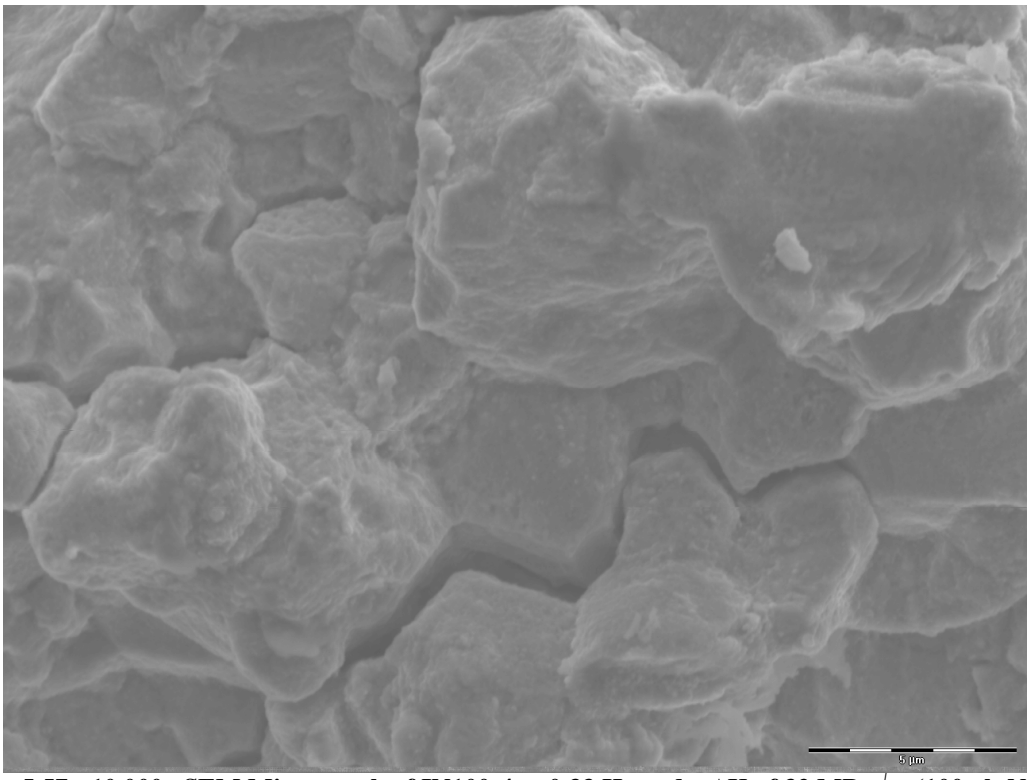

Figure 5.57: 10,000x SEM Micrograph of IN100-4 at 0.33 Hz and a ΔK of 32 MPa√m (100 alt N 649°C)

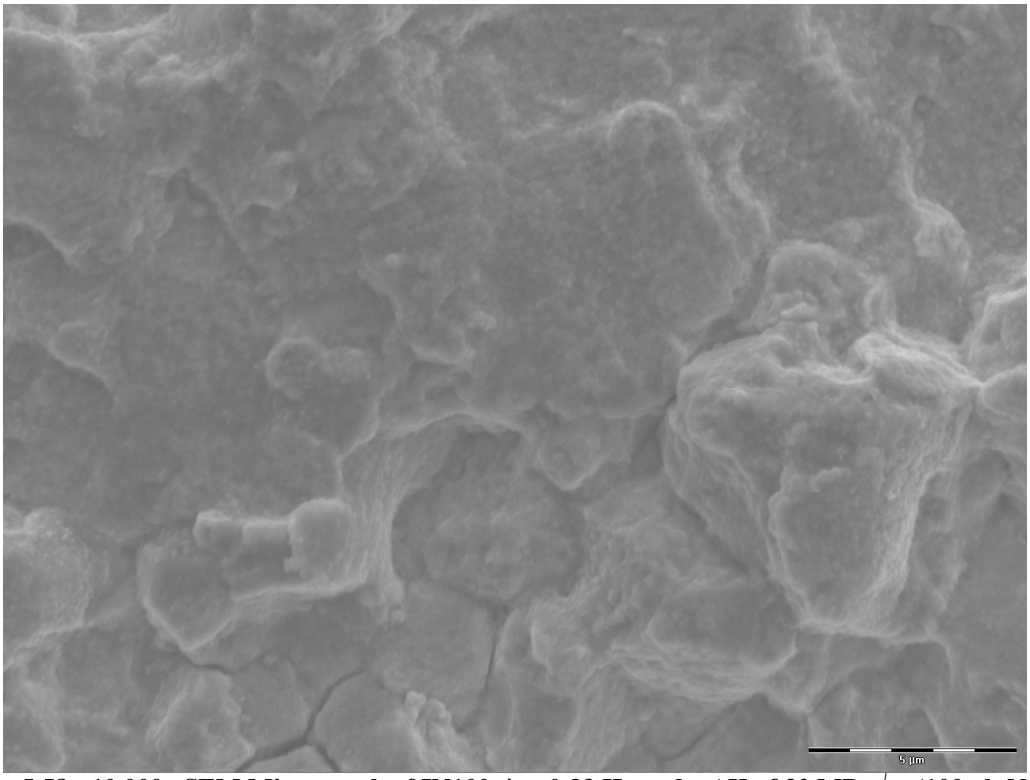

Figure 5.58: 10,000x SEM Micrograph of IN100-4 at 0.33 Hz and a ΔK of 32 MPa√m (100 alt N 316°C)

By reviewing Figure 5.59 it can be seen that there is a roughly 9x size ratio between the width of the large band and the width of the small band. The large band is fatigue crack growth attributed to 649°C while the dark smaller band can be attributed to 316°C fatigue crack growth. From isothermal testing it is known that the da/dN ratio between those two temperatures at any given ΔK is approximately 3 with 649°C isothermal testing having the larger da/dN. Knowing that the alternating 100 cycle testing grew slower than what was predicted by the non-interaction model it can be surmised that the 316°C crack growth was 3x smaller than the same 100 cycles at a constant temperature. The 316°C cycles quickly grew through the embrittled material created at 649°C but the growth was then slowed by γ' strengthening that took place at 649°C due to the formation of Kear-Wilsdorf locks [15].

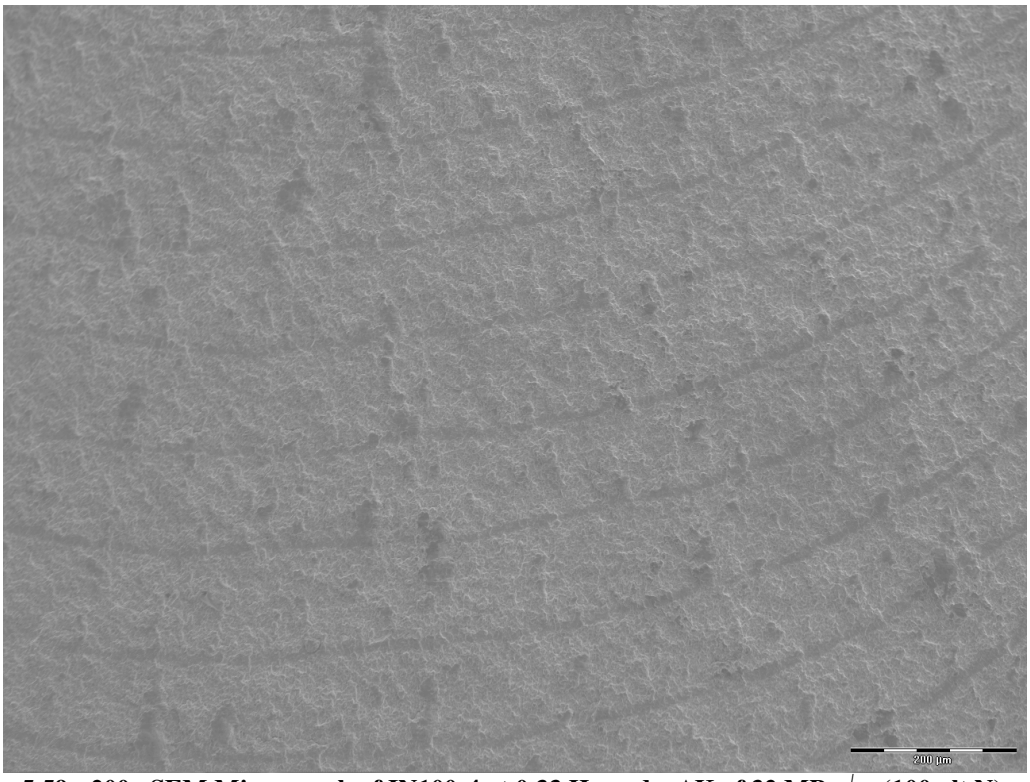

Figure 5.59: 200x SEM Micrograph of IN100-4 at 0.33 Hz and a ΔK of 32 MPa√m (100 alt N)

After the alternating 1 cycle testing was completed the specimen was subjected to maximum load for 2.5 hours at 649°C. The purpose of this test was to verify that environmental effects are not responsible for crack growth but do play a role in determining the underlying mechanism. After 2.5 hours it was discovered that the dwell test only blunted the crack tip and did not create any additional crack growth. This confirmed the notion that environmental effects are not responsible for crack growth in themselves but do change the underlying fatigue crack growth mechanism. Figure 5.60 shows the very clear environmental effect that oxidation at elevated temperature plays at the crack tip.

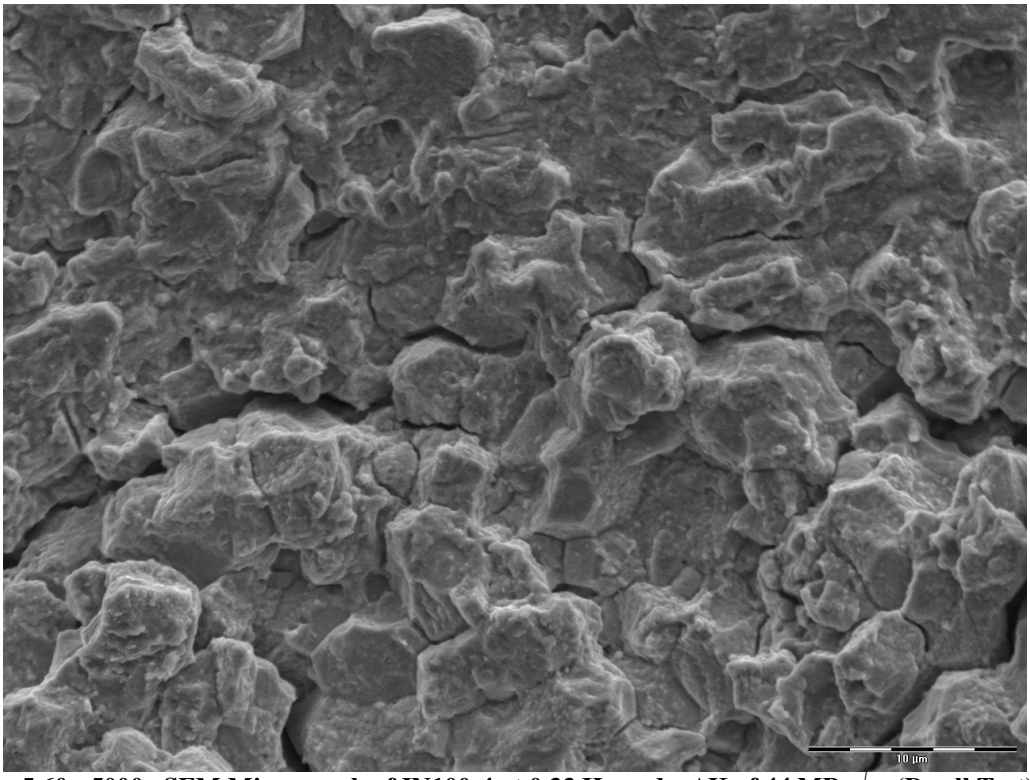

Figure 5.60: 5000x SEM Micrograph of IN100-4 at 0.33 Hz and a ΔK of 44 MPa√m (Dwell Test)

5.7.2: IN100-5, 649°C, 0.33 Hz Fatigue Fracture Surface

Overloading testing was performed on specimen, IN100-5, at a temperature of 649°C, at an R ratio of 0.1 and a frequency of 0.33 Hz. Three different overloads consisting of 2.0x, 1.6x and 1.3x cycles in that order were applied every 800 cycles to this specimen. SEM fractographs for this specimen can be seen in Figure 5.61 through Figure 5.66. In Figure 5.61 it can be seen that the 2.0x overload fracture surface is composed of a mix of intergranular fracture and ductile rupture. The crack grew in length only during the 2.0x overload cycles and this fracture surface is indicative of that.

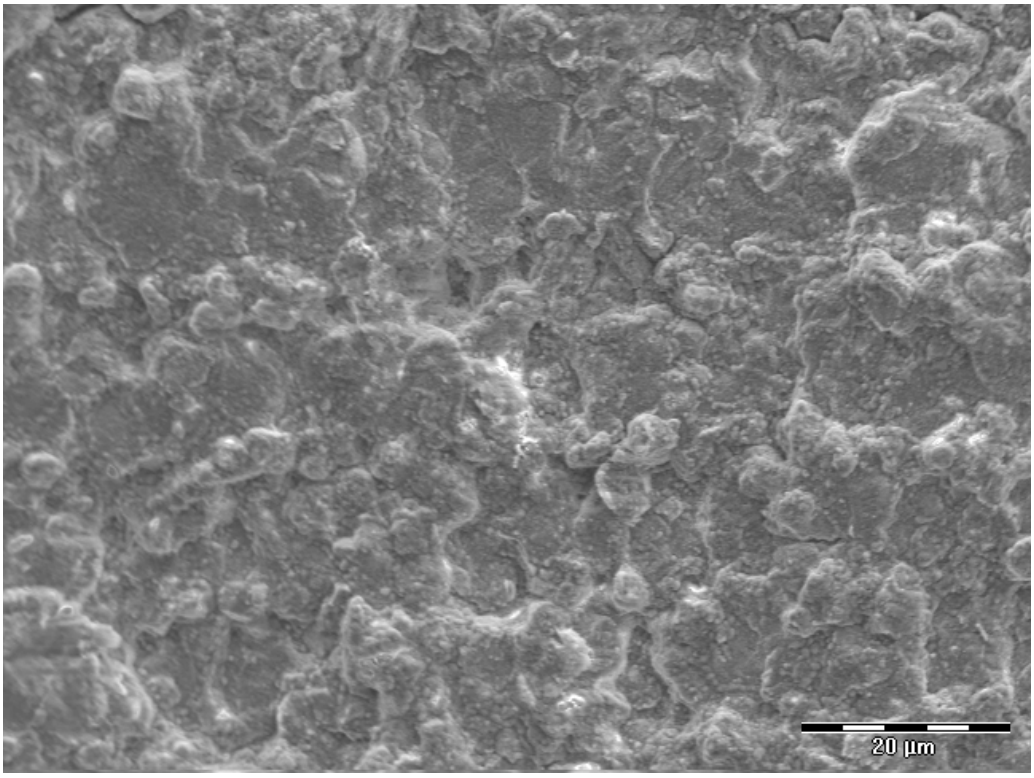

Figure 5.61: 2500x SEM Micrograph of IN100-5 tested at 649°C and 0.33 Hz at 4.08mm from Notch

The 1.6x overload cycles can clearly be seen in Figure 5.62. This initial 1.6x overload crack growth was retarded by the overload plastic zones created by the 2.0x testing. Due

to this the 1.6x crack growth was initially only caused by the 1.6x overloads. Once the 1.6x crack growth was out of the influence of the 2.0x overload zone the growth became a mix of 1.6x and 1.0x cycles. This phenomenon can best be seen in Figure 5.63 through Figure 5.65. Figure 5.63 shows the fracture surface at the beginning of the 1.6x overloading is primarily ductile rupture caused by the overloading cycles. Figure 5.64 shows all the fatigue crack growth due to the 1.6x overloading test. It can be seen that as the growth became more removed from the 2.0x overloading test that the growth rate increased due to additional growth from the 1.0x cycles. Taken near the end of 1.6x fracture surface Figure 5.65 shows clearly the intergranular crack growth from the 1.0x cycles and the ductile rupture crack growth due to the 1.6x cycles.

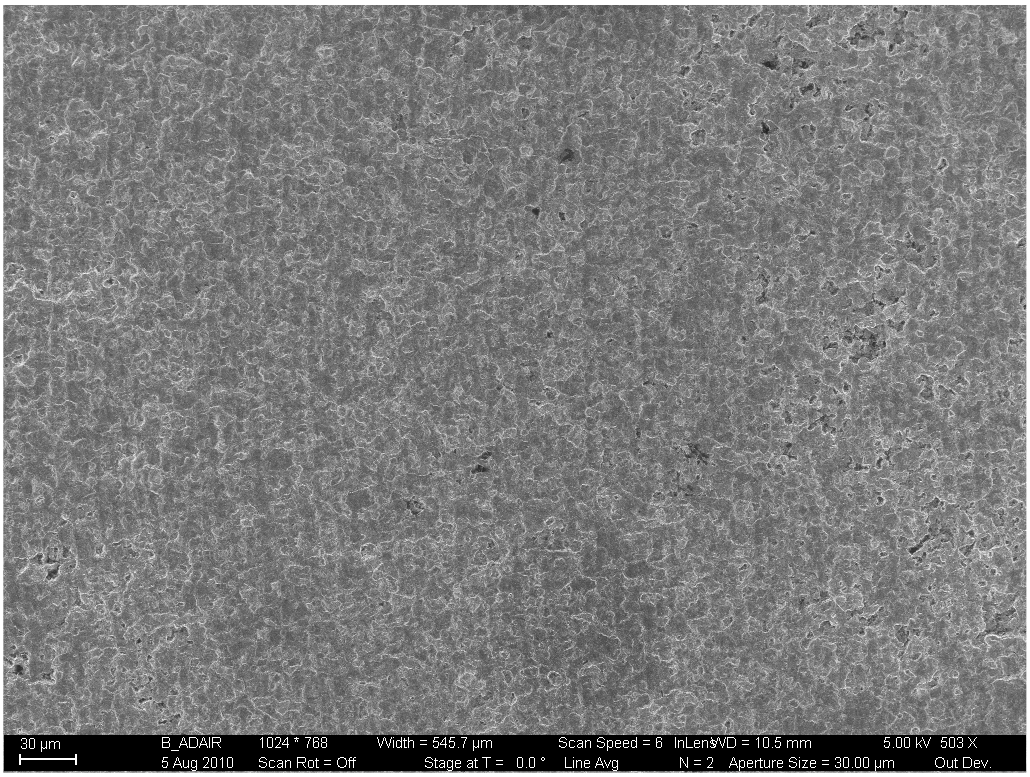

Figure 5.62: 500x SEM Micrograph of IN100-5 tested at 649°C and 0.33 Hz at 4.87mm from Notch

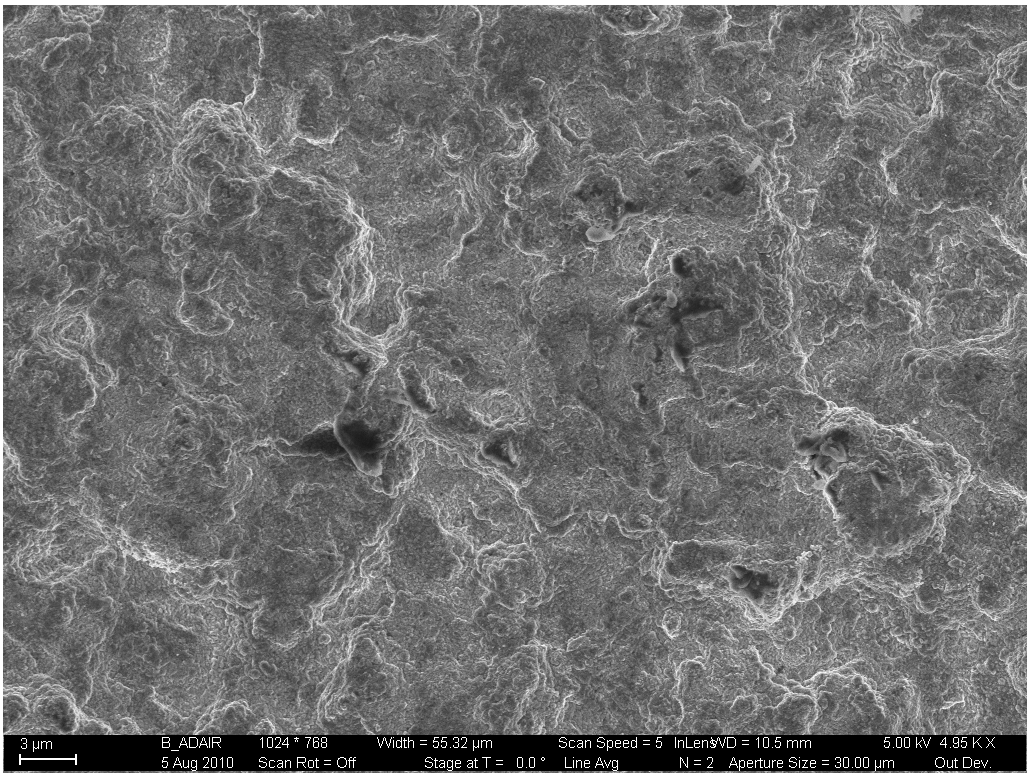

Figure 5.63: 5000x SEM Micrograph of IN100-5 tested at 649°C and 0.33 Hz at 4.87mm from Notch

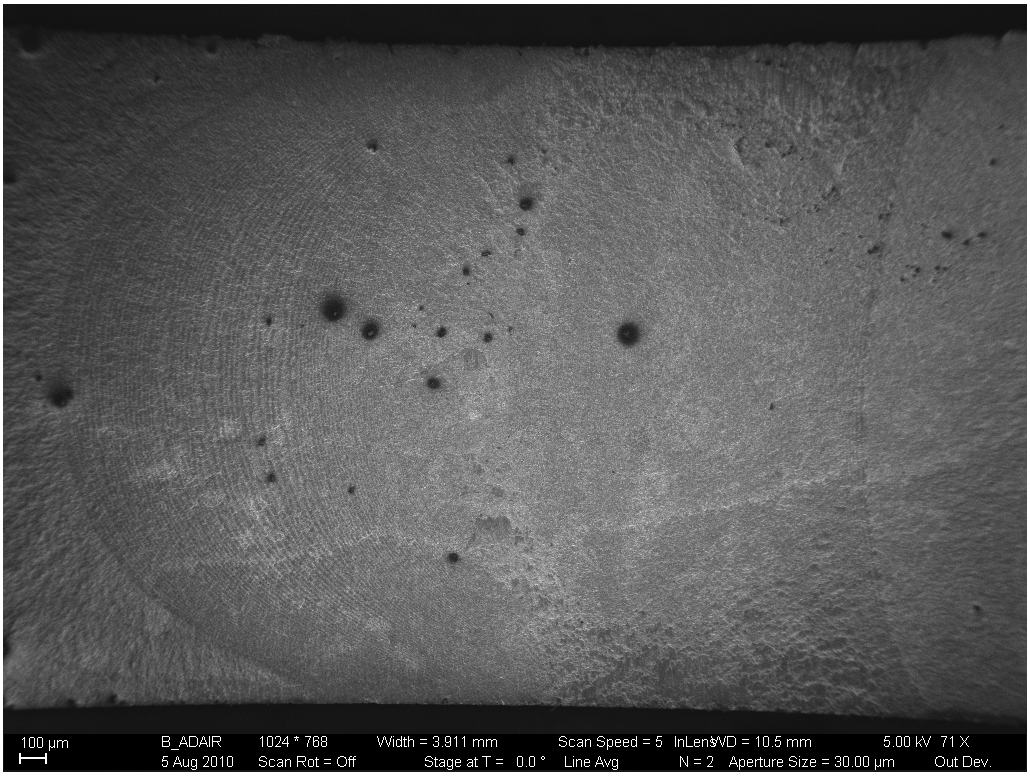

Figure 5.64: 71x SEM Micrograph of IN100-5 tested at 649°C and 0.33 Hz at 5.33mm from Notch

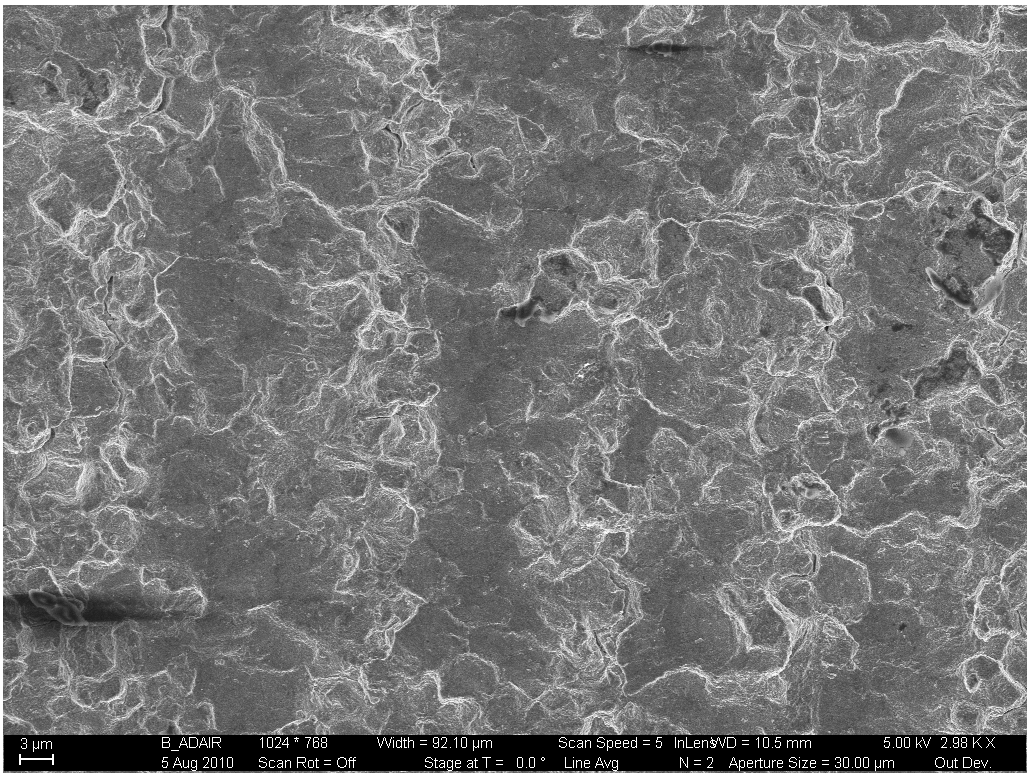

Figure 5.65: 3000x SEM Micrograph of IN100-5 tested at 649°C and 0.33 Hz at 6.44mm from Notch

Figure 5.66 reveals the predominantly intergranular fracture present during 1.3x overload cycling. The 1.3x overload cycles were not large enough to create ductile rupture but were large enough to accelerate the crack growth.

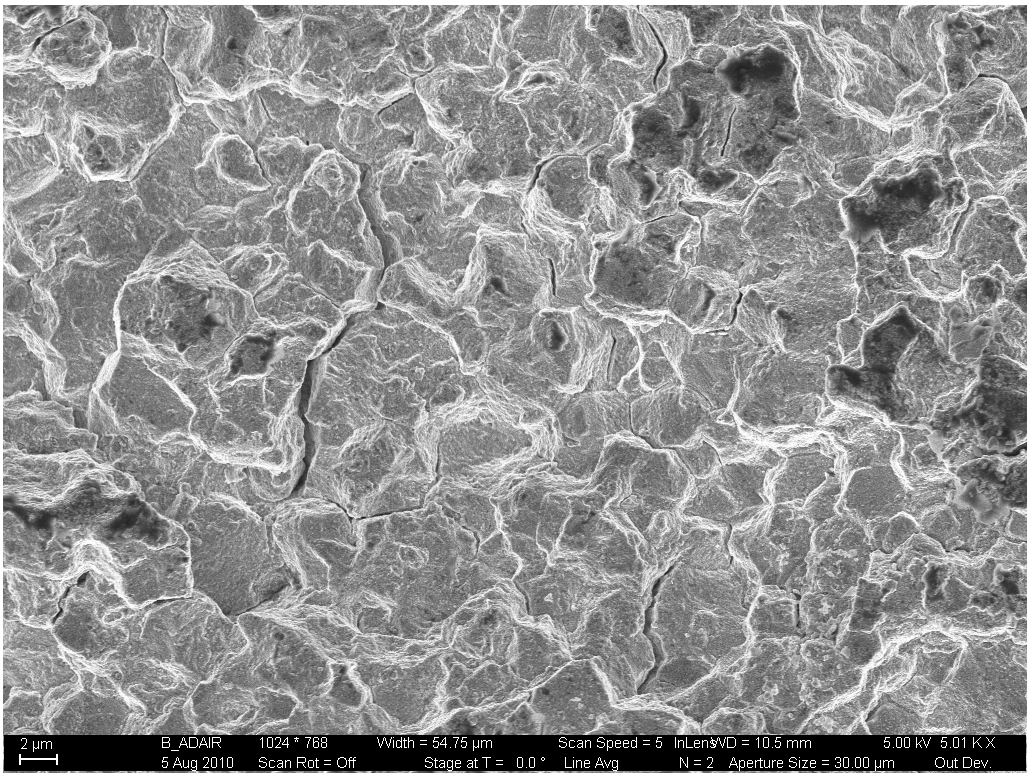

Figure 5.66: 5000x SEM Micrograph of IN100-5 tested at 649°C and 0.33 Hz at 9.52mm from Notch

5.7.3: IN100-7, 316°C, 0.33 Hz Fatigue Fracture Surface

Overloading testing was performed on specimen, IN100-7, at a temperature of 316°C, at an R ratio of 0.1 and a frequency of 0.33 Hz. Three different overloads consisting of 2.0x, 1.6x and 1.3x cycles in that order were applied every 800 cycles to this specimen. SEM fractographs for this specimen can be seen in Figure 5.67 through Figure 5.73. The 2.0x overload cycles can clearly be seen in Figure 5.67.

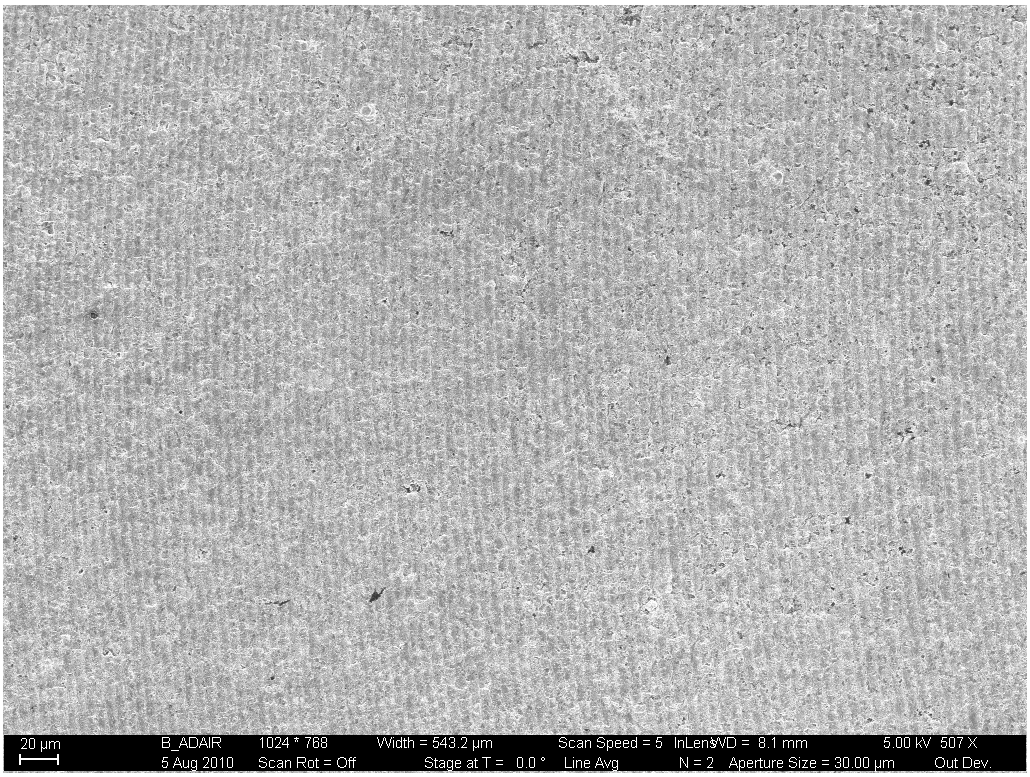

Figure 5.67: 500x SEM Micrograph of IN100-7 tested at 316°C and 0.33 Hz at 3.53mm from Notch

In Figure 5.68 showing 2.0x overload cycling it can be seen that the predominant mechanism for fatigue crack growth was ductile rupture caused by the overload cycles. This ductile rupture caused by overload cycles continues into the 1.6x overload cycles seen in Figure 5.69.

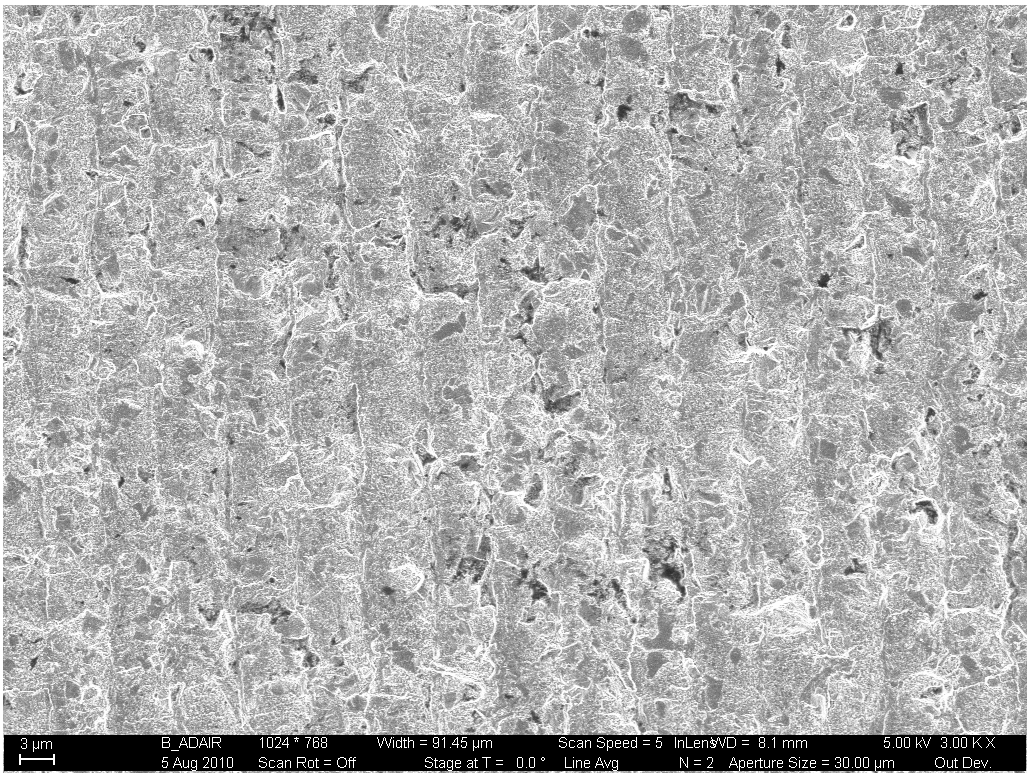

Figure 5.68: 3000x SEM Micrograph of IN100-7 tested at 316°C and 0.33 Hz at 3.53mm from Notch

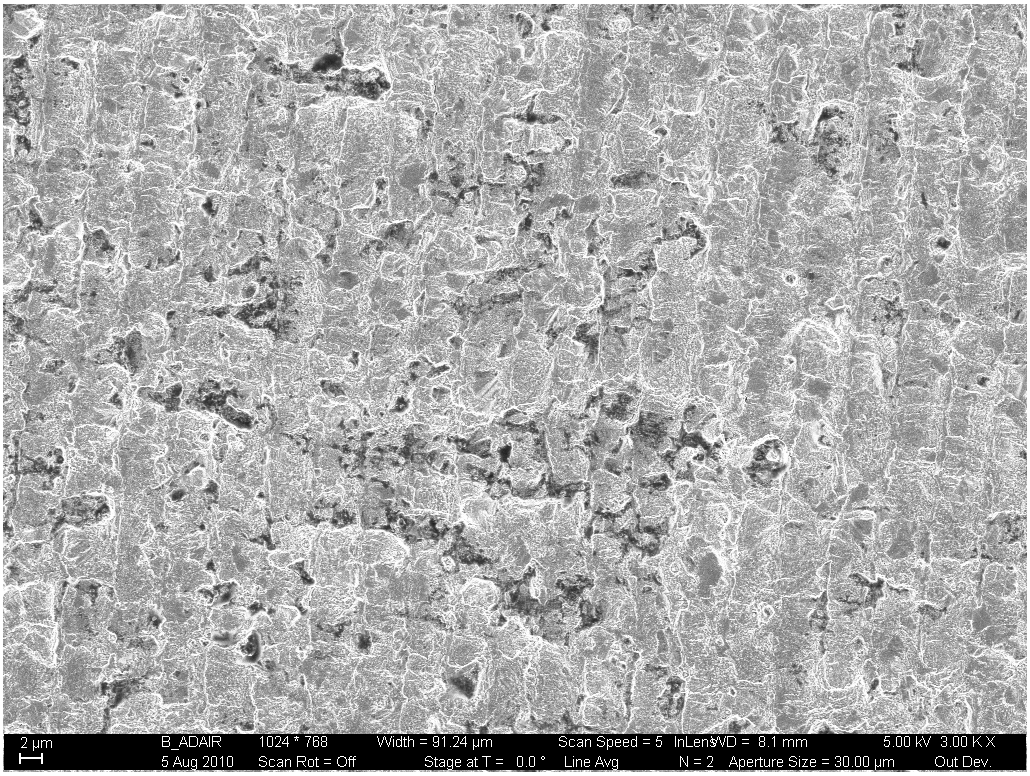

Figure 5.69: 3000x SEM Micrograph of IN100-7 tested at 316°C and 0.33 Hz at 5.00mm from Notch

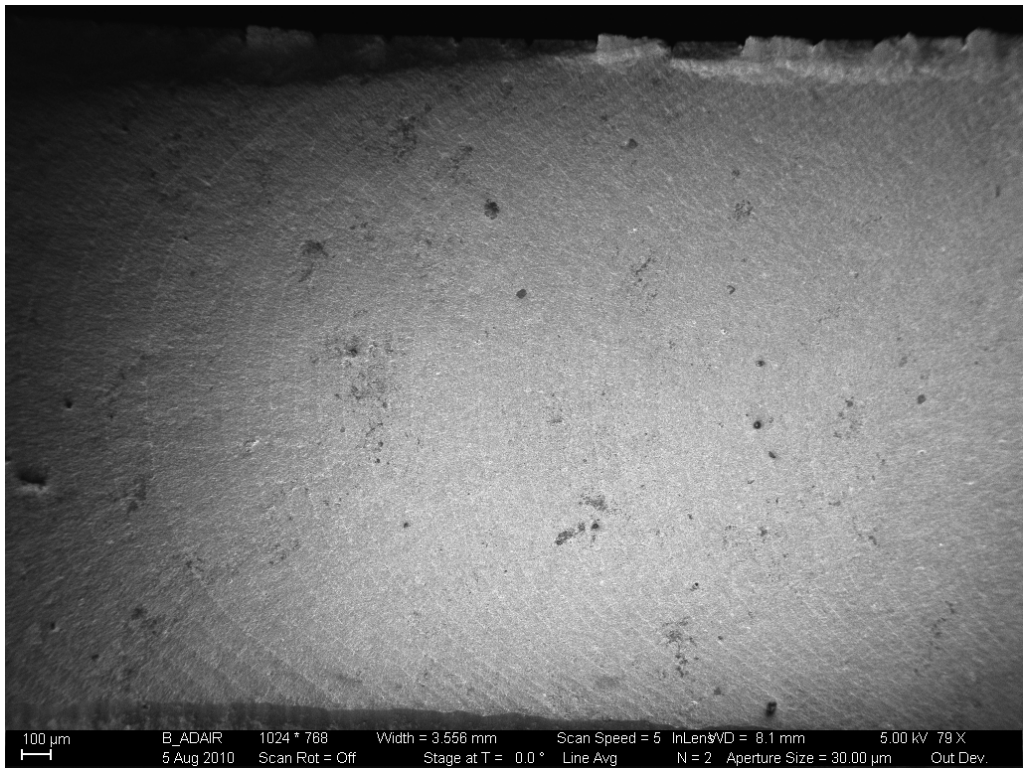

Figure 5.70: 80x SEM Micrograph of IN100-7 tested at 316°C and 0.33 Hz at 12.00mm from Notch

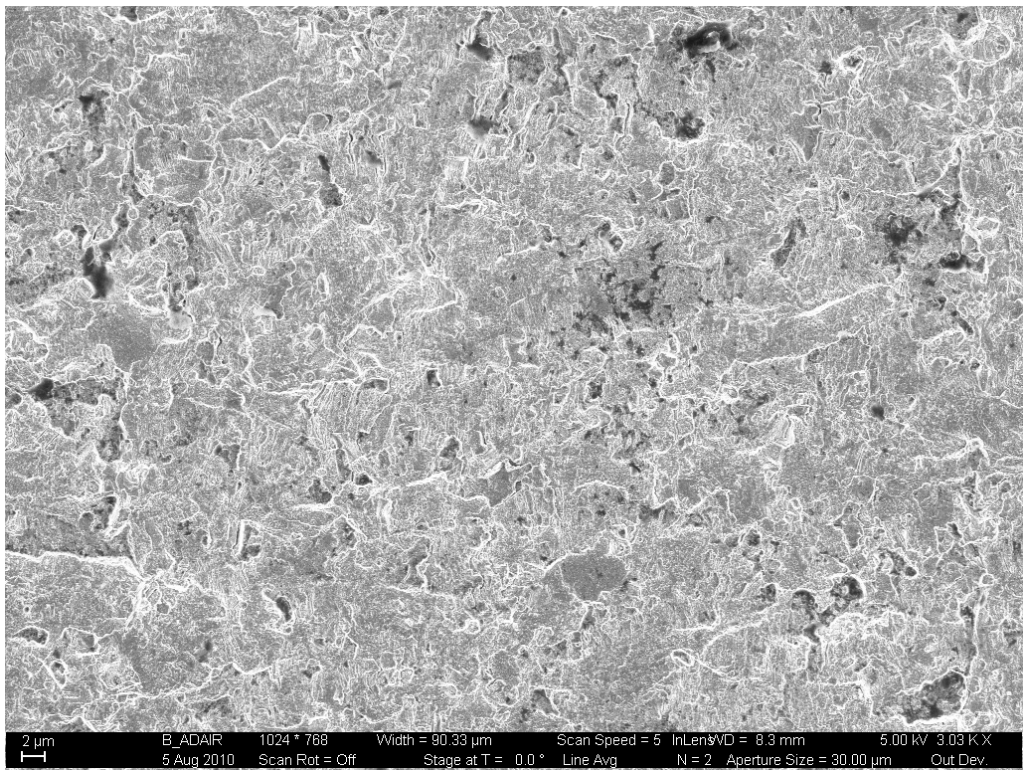

Figure 5.71: 3000x SEM Micrograph of IN100-7 tested at 316°C and 0.33 Hz at 12.00mm from Notch

Figure 5.70 and Figure 5.71 show the 1.3x overload fracture surface at 316°C. Due to testing taking place at a relatively low temperature for superalloys the presence of oxidation is very minimal. As such the failure mechanism is very transgranular in nature being a mixture of fatigue striations and rupture. More SEM fractographs showing 1.3x overload fracture can be seen in Figure 5.72 and Figure 5.73. These pictures tell a very similar story but at a higher ΔK value of 40 MPa√m. Due to the lack of oxidation at 316°C the 1.3x overloads caused a little bit of retardation leading to slightly slower crack growth than what is seen during constant amplitude testing.

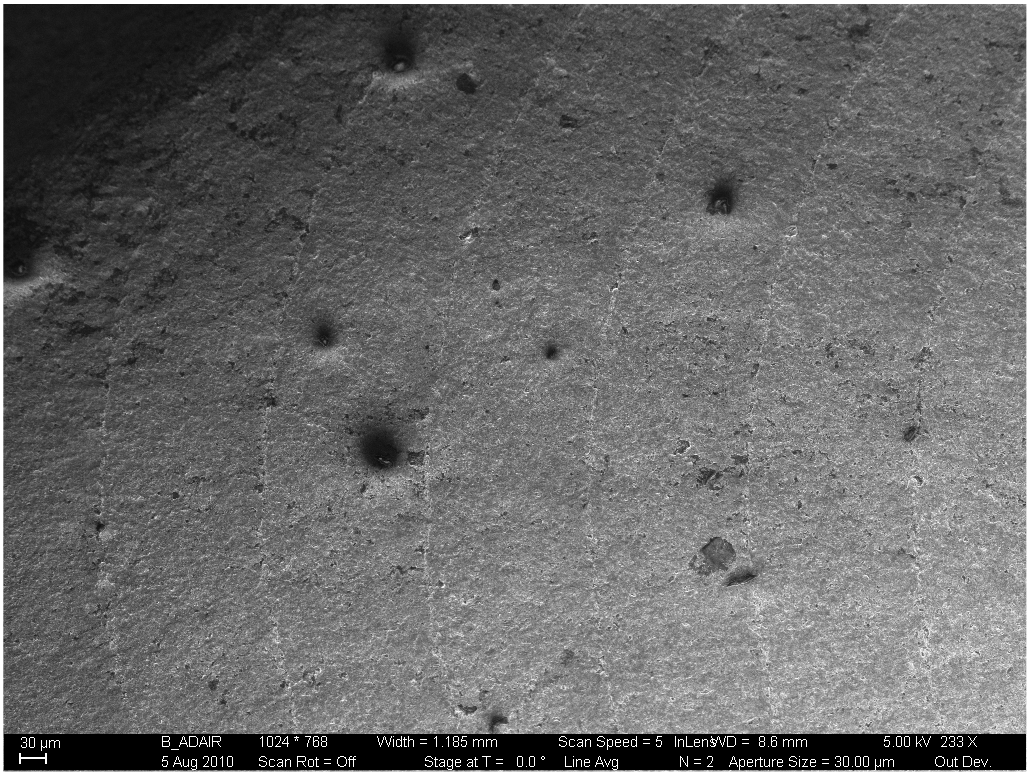

Figure 5.72: 230x SEM Micrograph of IN100-7 tested at 316°C and 0.33 Hz at 17.30mm from Notch

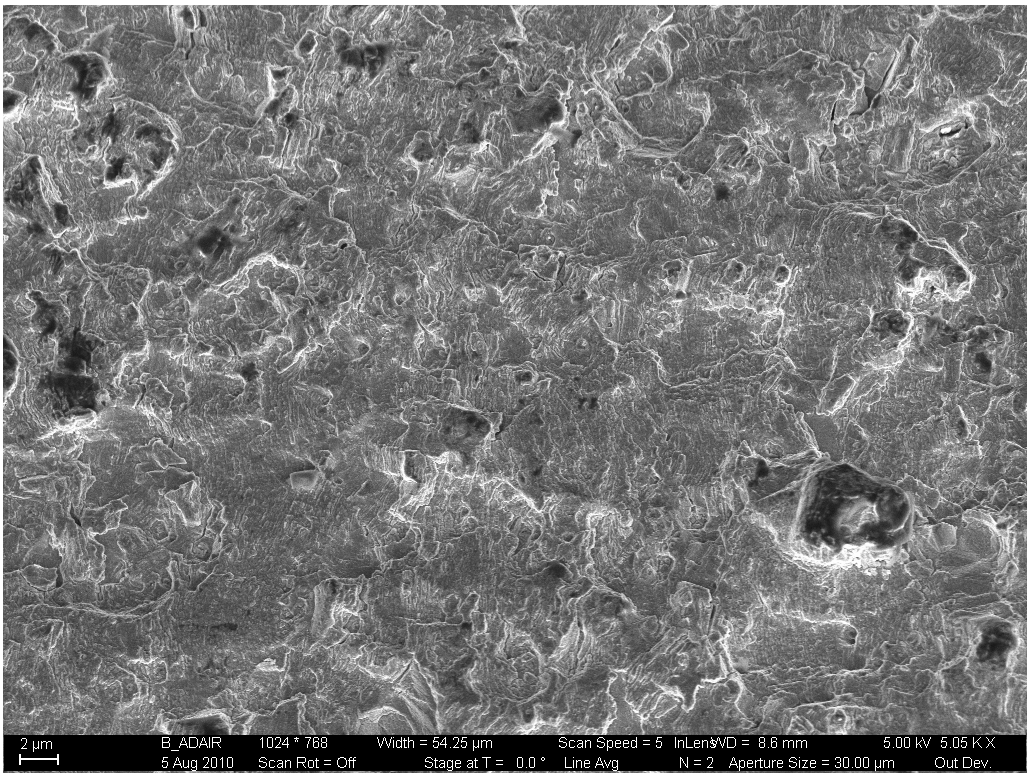

Figure 5.73: 5000x SEM Micrograph of IN100-7 tested at 316°C and 0.33 Hz at 17.30mm from Notch

5.7.4: IN100-9, 649°C, 1 Hz Fatigue Fracture Surface

Single overloading testing was performed on specimen, IN100-9, at a temperature of 649°C, at an R ratio of 0.1 and a frequency of 1 Hz. Figure 5.74 shows a region of 1.0x crack growth after application of a single 1.3x overload. As expected at this frequency and temperature the fracture surface is very intergranular in nature and appears to be unaffected by the prior overload.

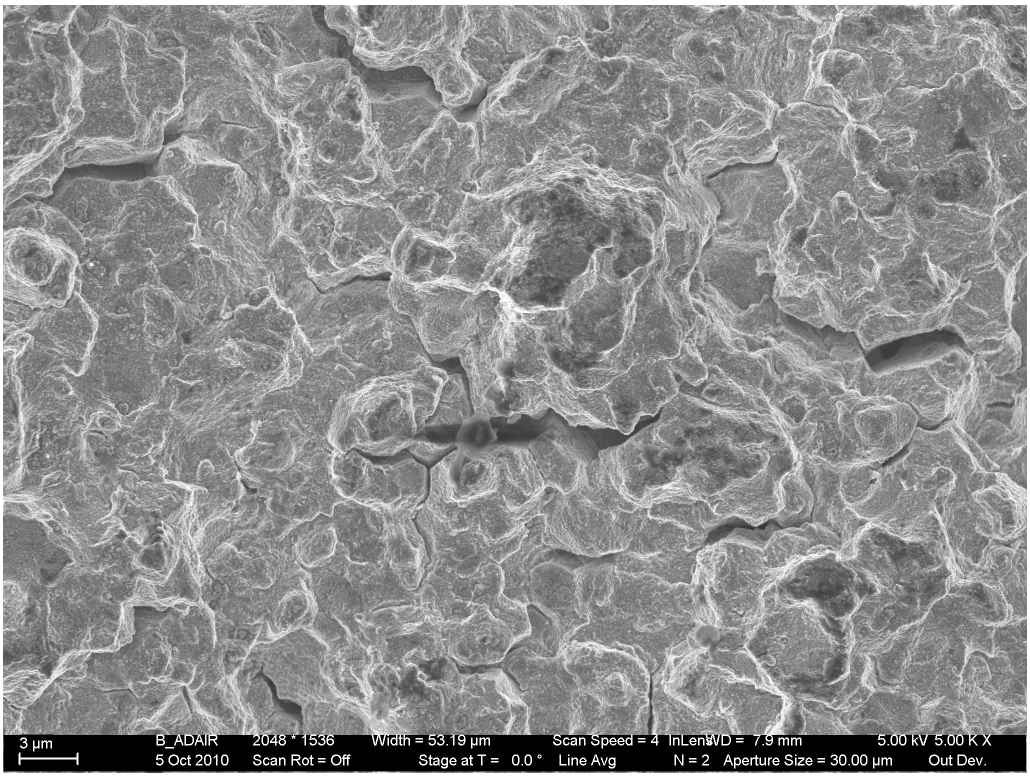

Figure 5.74: 5000x SEM Micrograph of IN100-9 tested at 649°C and 1 Hz at 18.63mm from Notch

CHAPTER 6: CONCLUSIONS AND RECOMMENDATIONS FOR FUTURE WORK

6.1: Conclusions

The purpose of this research was to investigate the fatigue crack growth rate properties of polycrystalline IN100 through the building of a database that fills a void in currently published literature. This project utilized extensive mechanical testing composed of isothermal, load interaction and temperature interaction testing. The fracture surfaces were also examined using scanning electron microscopy to better understand the crack surface morphology and crack driving mechanisms as a function of load, temperature, R ratio and frequency. The primary conclusions from this work are as follows:

6.1.1: Isothermal Constant Amplitude Conclusions

- Scanning electron microscopy showed that as temperature increased the fracture mechanism transitioned from transgranular to intergranular.
- The fracture mechanism was shown to transition from intergranular to transgranular at elevated temperatures as da/dN increased.
- Scanning electron microscopy showed that as frequency decreased at elevated temperatures the fracture mechanism transitioned from transgranular to intergranular.
- Oxygen penetration is responsible for embrittlement at the crack tip, which leads to increased fatigue crack growth rates, but required cyclic loading to have an effect.
- The crack growth was shown to happen discontinuously (i.e. in bursts); not necessarily creating striations of growth from every mechanical cycle as is commonly accepted.

6.1.2: Temperature Interaction Conclusions

- During alternating temperature cycling it was found that as the number of alternating temperature cycles increased, changes in the morphology (and hence deformation mode) caused changes in the environmental interactions thus demonstrating the sensitivity of the environmental interaction on the details of the deformation mode.
- During alternating temperature cycling it was shown that at low alternating cycles, 316°C crack growth was accelerated due to crack tip embrittlement caused by 649°C cycling. At higher alternating cycles the 316°C cycling quickly grew through the embrittled crack tip but then grew slower than expected due to the possible formation of Kear-Wilsdorf locks at 649°C.

6.1.3: Load Interaction Conclusions

- Overload interaction testing led to full crack retardation at 2.0x overloads for both 316°C and 649°C testing. The only growth seen during 2.0x overload testing was attributed to transient growth from the overload cycles.
- 1.6x overloading at both 316°C and 649°C led to retarded crack growth that consisted of growth from both the 1.6x and 1.0x cycles.
- It was found that 1.3x overloads at 649°C created accelerated crack growth when compared with constant amplitude data at the same temperature. The 1.3x overloads at 316°C were found to minimally retard the crack growth when compared with constant amplitude data at the same temperature.

6.1.4: Primary Overall Conclusions

- Environmental assisted FCG is very temperature and frequency dependent. Also as da/dN increases, less environmental enhancement (intergranular fracture) is observed.

- There is significant influence in changing temperature on resulting crack growth. This must be accounted for in any TMF crack growth life prediction model.
- There are significant load interaction (both retardation & accelerations) effects present in IN100 under TMF conditions. This also must be accounted for in TMF crack growth prediction models.

6.1.5: Secondary Overall Conclusions

- The commonly published stress intensity factor solution is for a uniform stress boundary condition. During the course of this research a SIF solution for the uniform displacement boundary condition was created.
- Due to the very fine microstructure of IN100, the matrix grain boundaries and γ' precipitates were difficult to visualize with optical microscopy. Scanning electron microscope techniques worked the best for revealing the microstructure.
- Marker bands are an excellent way to visualize the crack front and to correct for crack tip tunneling.
- In this study we verified that residual stresses, although moderate to high, were limited to a very small near surface region and had no effect on results.
- Decreasing the frequency below 1 Hz at 649°C does not lead to a noticeable increased fatigue crack growth rate due to the rapid oxygen diffusion rate. In other words the effect is saturated at 1 Hz and further decreases have a minimal effect.
- ASTM load shedding is appropriate for avoiding retardation due to the plastic yield zone in front of the crack tip but does not adequately take into account retardation due to crack closure effects.

6.2: Recommendations for Future Work

Extensive fatigue crack growth rate testing was performed to add to the current body of knowledge for IN100. The data obtained from this study filled a much needed thin specimen gap, yet much remains to be known to properly model the fatigue crack growth rate of IN100. The following recommendations, when coupled with the results from this study and existing published literature, will greatly further the cause.

- Due to a limited number of specimens it was not possible to test at all desired temperatures, R ratios, and frequencies. Additional testing at frequencies between 1 and 20 Hz, at higher R ratios and at additional temperatures between 22°C and 649°C would be very beneficial to the IN100 isothermal constant amplitude fatigue crack growth rate database.
- Performing single overload testing at additional overload ratios to pinpoint at what ratio acceleration begins and also at what ratio full retardation begins.
- Obtaining underload test data would be very beneficial for predicting flight spectrums.
- Additional temperature interaction testing needs to be done to fully understand the change in deformation mode as a function of alternating temperature cycles.
- Creating 3D fracture surface maps that can be used to determine the average surface roughness would be very helpful for quantifying transgranular and intergranular morphology changes.
- Additional oxidation studies to determine the oxide depth as a function of temperature, stress and time along the fracture surface would be very valuable for creating an environmental fatigue crack growth model.
- Additional temperature dependent diffusion FCGR modeling to account for creep at higher temperatures and to account for R ratios.
- Develop plastic yield zone and crack closure approaches to predict FCGR for realistic TMF flight spectra.

APPENDIX

A.1: Procedure for cold-mounting, grinding, polishing, and etching

Cold-mounting

1. Line plastic cup with release agent
2. Put paper cup on scale and zero scale
3. Add desired Epofix resin to paper cup
4. Multiply the mass of the resin by 3/25 (because its 25 parts resin, 3 parts hardener by mass) to determine required amount of hardener
5. Zero scale again and add calculated mass of Epofix hardener
6. Stir for a few minutes in paper cup and remove big air bubbles
7. Put specimen (and specimen holder clips if necessary) and add mount
8. Allow to harden for 12-24 hours

Grinding/Polishing

Step	Preparation Disc (Material)	Force (N)	Speed (RPM)	Suspension	Lubricant	Time (min)
Course Grind	320 AD (SiC)	30	150	None	Water	3+
Fine Grind I	1200 AD (SiC)	25	150	None	Water	5
Fine Grind II	4000 AD (SiC)	25	150	None	Water	5
Course Polish	MD Mol (Woven wool)	20	150	DiaPro Mol	None	8
Fine Polish	MD Chem-OP-S (Porous synthetic)	15	150	OP-S Suspension	None	2

** Thoroughly clean machine and the samples between each of the last 4 step!!!!!!
** If the polishing machine squeaks, put something nonmetallic (ex. folded up kimwipes) in between the sample and the force applicator or turn down the force

Etching

1.) Add 2 g of $CuCl_2$ to an empty beaker
2.) In the fume hood, add 40 mL of Ethanol
3.) Put on some gloves and add 40 mL of HCl
4.) Stir well
5.) Submerge specimen in etchant for 35-40 sec
6.) Immediately submerge in a beaker of water
7.) Rinse specimen with water and ethanol as necessary

A.2: Initial TMF Test Rig Startup Tasks

Water		Turn on induction heater's water supply (approx. 2 turns)
		Turn on water-cooled hydraulic grips' water supply (1.5 turns)
Open Station Manager		Start Station Manager program on TestStar IIs Computer
		Choose TMF-1.cfg configuration file
Turn On Hydraulics		Clear Interlock 1 by resetting it
		Power up HPS 1 to Power Low, then Power High
		Power up HSM 1 to Power Low, then Power High
Mount Specimen		Insert specimen so that it is properly positioned
		Manual Ctrl to Displacement, Enable Manual Control
		Move lower grip up (turn dial CCW) so top of specimen between top grip
		Make sure specimen aligned, Close lower grips on bottom of specimen
		Move lower grip up (turn dial CCW) so notch centered in coil gap
		Disable Manual Control, Auto Offset Force, Manual Ctrl to Force
		Enable Manual Control, Close upper grips on top of specimen
		Apply approx. 20lbf of tensile force (turn dial CW)
		Disable Manual Control
		Reposition induction heater heat station to center specimen in coil
Position Questar Microscope		Turn on light source and position so shining through coil gap from the side
		Toggle eye piece bypass switch to up (Enable eye piece use)
		Center notch tip in Questar view using positioning knobs and focus
		Toggle eye piece bypass switch to right (Disable eye piece use)
Questar RMS and Video Acquisition Startup		Switch on Power to RMS II system (two switches need to be turned on)
		Turn on surgeprotector to power up Video Processor and Questar Computer
		Open up RMS software on Questar Computer
		Open up Motion Platform and Encoder Position Windows
		Open Windows Movie Maker
		Click on Capture from video device, found under Capture Video heading
		New window will open up, Verify Dazzle DVC100 Video Device is selected
		Set video input source as Composite, Click Next to move forward
		Enter file name for video file, Choose Location to save file, Click Next
		Select Best Quality for Playback (default recommended setting), Click Next
		Use Video Processor and Motion Platform to enhance image in Preview
		Reposition light source to shine down through top of coils at incidence angle
		Use Video Processor and Motion Platform to enhance image again
Heating System Startup		Plug in power cord for temperature controller into 120Vac wall outlet
		Turn on power to heater by flipping power lever located on rear panel
		From now on, Do NOT touch coil or specimen until heater is turned off

[104]

A.3: TMF Test Procedure Setup and Initialization

MPT and Procedure Editor		Open MPT within Station Manager
		Open Procedure Editor within MPT
		When prompted, select procedure to run or create a new procedure to run
Specimen Selection		Back in MPT, select a previously created specimen -OR- choose to create new one
		In new window, select "Currently Loaded Procedure" and "Saved State: Reset"
Data File Setup		Toggle "Lock" icon back to Edit Mode ("lock" icon now displays open lock)
		Option 1: Erase "old" data file created in specimen folder: C:\tsiis\mpt\Specimens\<Selected Specimen Name>
		Option 2: In Data Acquisition Process for Procedure, change user data file name in Destination Tab to reflect new test
		Retoggle "Lock" icon back to Execute Mode
Start Test		Open any Scopes or Meters to display test data during test, setup as desired
		Position vertical crosshair of Questar image at notch/crack tip, zero Encoder Position
		Hit "Start" button on induction heater power supply front panel
		Simultaneously, Click "Program Run" in MPT on TestStar computer and "Start Capture" in Windows Movie Maker on Questar computer
		Readjust focus of Questar and image setting on Video Processor if needed
Acquire Data		For cyclic load tests: move vertical crosshair ahead of notch/crack 5mils, record cycle count for when crack reaches crosshair, then repeat
		For flight profile tests: at conclusion of every flight cycle, move vertical crosshair to crack tip, record Encoder Position values, then repeat

[104]

A.4: TMF Test Rig Shutdown Procedure

Shutdown		Click "Program Stop" in MPT on TestStar computer
		Click "Stop Capture" in Windows Movie Maker on Questar Computer
Remove Heating and Load with Function Generator		Go to Function Generator mode in Station Manager
		Select TempControl channel, setpoint & amplitude to 0.00V
		Click "Program Run," wait 5 seconds, click "Program Stop"
		Select Channel 1 channel & Force control mode, setpoint to 10lbf & amplitude to 0lbf
		Click "Program Run," wait 5 seconds, click "Program Stop"
Questar Microscope and Accessories Shutdown		Confirm video was captured and saved of the test on the Questar computer
		Close Windows Movie Maker on Questar computer
		Close Questar RMS II software on Questar computer
		Save any collected data and captured video from the Questar computer to an external hard drive
		Shut down Questar computer and power off the surge protector for the system
		Turn off power switches (two of them) for the Questar microscope RMS platform
		Turn off the light source
Turn off Heating		Turn off power switch for induction heater located on rear panel
		Unplug temperature controller once specimen temperature reaches approx. 100F
Remove Specimen from Grips		Manual Ctrl to Force, Enable Manual Control
		Lower load to a 5lbf tensile load by moving lower grip up (turn dial CCW)
		Disable Manual Control, Manual Ctrl to Displacement
		Open upper grips (turn lever CCW), Enable Manual Control
		Lower bottom grips to lowest level (turn dial CW), Disable Manual Control
		Open lower grips (turn lever CCW)
		Remove specimen from test frame
Shutdown Station Manager/ Retrieve Data		Power down HSM 1 to Power Low, then Power Off
		Power down HPS 1 to Power Low, then Power Off
		Close Station Manager
		Open folder: C:\tsiis\mpt\Specimens\<Selected Specimen Name>
		Save data file(s) saved there by Data Acquisition process(es) to a floppy
Water Off		Turn off induction heater's water supply
		Turn off water-cooled hydraulic grips' water supply

[104]

A.5: MATLAB Crack Growth Calculator

```
%%%%%%%%%%%%%%%TMF Crack Propagation Calculator%%%%%%%%%%%%%%%
%% n number of cycles
%% a crack length(inches)
%% dn change in number of cycles
%% da change in crack length
%% pmax max load(lbf)
%% pmin min load(lbf)
%% smax max stress(psi)
%% smin min stress(psi)
%% w specimen width(inches)
%% ai initial notch length(inches)
%% t specimen thickness(inches)
%% dk6 stress intensity range(ksi*in^1/2) at 600 degrees
%% dk12 stress intensity range(ksi*in^1/2) at 1200 degrees
%% f geometry correction factor

clc
close all
clear all
format long eng

w=1.502;  %specimen width
t=.102;  %specimen thickness
a(1,1)=.4703;  %initial crack length after precrack
a1(1,1)=.4703;  %initial crack length after precrack
a6(1,1)=.4703;  %initial crack length after precrack
a12(1,1)=.4703;  %initial crack length after precrack
a100(1,1)=.4703;  %initial crack length after precrack
pmax=1700;  %max load
pmin=170;  %min load
smax=pmax/w/t;  %max stress
smin=pmin/w/t;  %min stress
sr=smax-smin;  %stress range
pirt=1.7724;  %square root of pi
total=45000;  %Total number of cycles
tot=total/20;  %Total number of sets of temp blocks
n=1;  %cycle counter

%2.0X 1200F Overloads
while a(n,1)<(w-.01);
    b=1;
    c=1;
    while b<801 && a(n,1)<(w-.01);
    faw(n,1)=53.327*(a(n,1)/w)^6-
124.63*(a(n,1)/w)^5+112.87*(a(n,1)/w)^4-
48.17*(a(n,1)/w)^3+10.473*(a(n,1)/w)^2-0.5037*(a(n,1)/w)+1.1258;
    dk(n,1)=(smax-smin)*pirt*sqrt(a(n,1))*faw(n,1)/1000;
    y(n,1)=.000000131291*(dk(n,1).^(1.746187591014));
    a(n+1,1)=a(n,1)+y(n,1);
    b=b+1;
    n=n+1;
```

```
    end

    while c<2;
    faw(n,1)=53.327*(a(n,1)/w)^6-
124.63*(a(n,1)/w)^5+112.87*(a(n,1)/w)^4-
48.17*(a(n,1)/w)^3+10.473*(a(n,1)/w)^2-0.5037*(a(n,1)/w)+1.1258;
    dk(n,1)=(2*smax-smin)*pirt*sqrt(a(n,1))*faw(n,1)/1000;
     y(n,1)=.000000131291*(dk(n,1).^(1.746187591014));
    a(n+1,1)=a(n,1)+y(n,1);
    c=c+1;
    n=n+1;
    end
end

%1.6X 1200F Overloads
n1=1;  %cycle counter
while a1(n1,1)<(w-.01);
    b=1;
    c=1;
    while b<801 && a1(n1,1)<(w-.01);
    faw1(n1,1)=53.327*(a1(n1,1)/w)^6-
124.63*(a1(n1,1)/w)^5+112.87*(a1(n1,1)/w)^4-
48.17*(a1(n1,1)/w)^3+10.473*(a1(n1,1)/w)^2-0.5037*(a1(n1,1)/w)+1.1258;
    dk1(n1,1)=(smax-smin)*pirt*sqrt(a1(n1,1))*faw1(n1,1)/1000;
    y1(n1,1)=.000000131291*(dk1(n1,1).^(1.746187591014));
    a1(n1+1,1)=a1(n1,1)+y1(n1,1);
    b=b+1;
    n1=n1+1;
    end

    while c<2;
    faw1(n1,1)=53.327*(a1(n1,1)/w)^6-
124.63*(a1(n1,1)/w)^5+112.87*(a1(n1,1)/w)^4-
48.17*(a1(n1,1)/w)^3+10.473*(a1(n1,1)/w)^2-0.5037*(a1(n1,1)/w)+1.1258;
    dk1(n1,1)=(1.6*smax-smin)*pirt*sqrt(a1(n1,1))*faw1(n1,1)/1000;
    y1(n1,1)=.000000131291*(dk1(n1,1).^(1.746187591014));
    a1(n1+1,1)=a1(n1,1)+y1(n1,1);
    c=c+1;
    n1=n1+1;
    end
end

%1.3X 1200F Overloads
n100=1;  %cycle counter
while a100(n100,1)<(w-.01);
    b=1;
    c=1;
    while b<801 && a100(n100,1)<(w-.01);
    faw100(n100,1)=53.327*(a100(n100,1)/w)^6-
124.63*(a100(n100,1)/w)^5+112.87*(a100(n100,1)/w)^4-
48.17*(a100(n100,1)/w)^3+10.473*(a100(n100,1)/w)^2-
0.5037*(a100(n100,1)/w)+1.1258;
    dk100(n100,1)=(smax-
smin)*pirt*sqrt(a100(n100,1))*faw100(n100,1)/1000;
    y100(n100,1)=.000000131291*(dk100(n100,1).^(1.746187591014));
    a100(n100+1,1)=a100(n100,1)+y100(n100,1);
```

```
    b=b+1;
    n100=n100+1;
    end

    while c<2;
    faw100(n100,1)=53.327*(a100(n100,1)/w)^6-
124.63*(a100(n100,1)/w)^5+112.87*(a100(n100,1)/w)^4-
48.17*(a100(n100,1)/w)^3+10.473*(a100(n100,1)/w)^2-
0.5037*(a100(n100,1)/w)+1.1258;
    dk100(n100,1)=(1.3*smax-
smin)*pirt*sqrt(a100(n100,1))*faw100(n100,1)/1000;
    y100(n100,1)=.000000131291*(dk100(n100,1).^(1.746187591014));
    a100(n100+1,1)=a100(n100,1)+y100(n100,1);
    c=c+1;
    n100=n100+1;
    end

end

%Isothermal Constant Amplitude
n12=1;  %cycle counter
while a12(n12,1)<(w-.01);

    faw12(n12,1)=53.327*(a12(n12,1)/w)^6-
124.63*(a12(n12,1)/w)^5+112.87*(a12(n12,1)/w)^4-
48.17*(a12(n12,1)/w)^3+10.473*(a12(n12,1)/w)^2-
0.5037*(a12(n12,1)/w)+1.1258;
    dk12(n12,1)=sr*pirt*sqrt(a12(n12,1))*faw12(n12,1)/1000;
    y12(n12,1)=.000000131291*(dk12(n12,1).^(1.746187591014));
    a12(n12+1,1)=a12(n12,1)+y12(n12,1);
    n12=n12+1;

end

N=1:n;
N=N';

N1=1:n1;
N1=N1';

N100=1:n100;
N100=N100';

N12=1:n12;
N12=N12';

figure(1);
plot(N12,a12,N,a,N1,a1,N100,a100)
legend('\fontsize{16}1200^o','\fontsize{16}2X
Overload','\fontsize{16}1.6X Overload','\fontsize{16}1.3X Overload');
grid on
xlabel('\fontsize{16}Cycles')
ylabel('\fontsize{16}Crack Length (inches)')
title('\fontsize{16}Crack Length vs Cycles ')
```

A.6: SEM Stereo Pairs

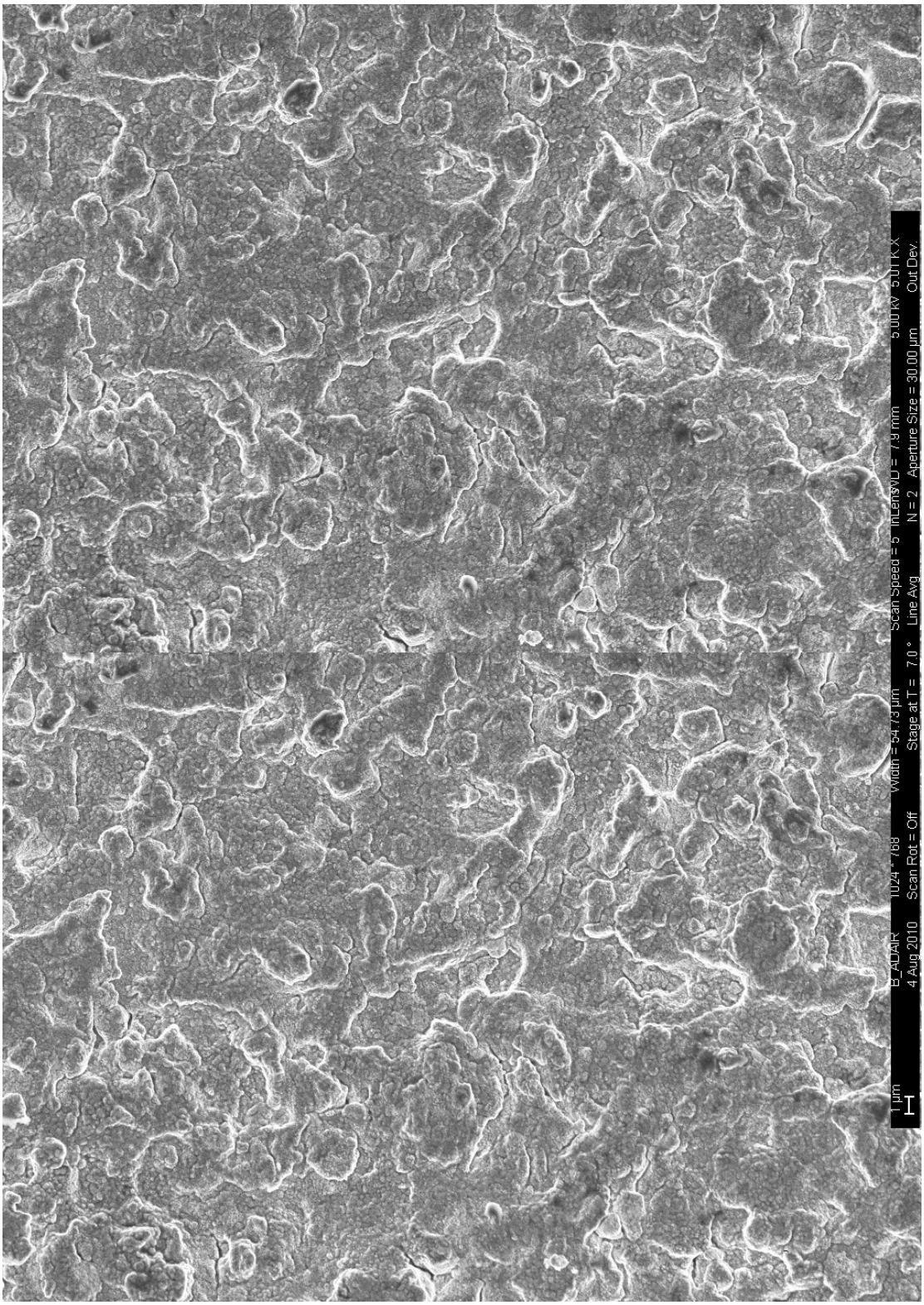

Figure A.1: 5000x SEM Stereo Pair Micrograph of IN100-6 tested at 649°C and 20 Hz at a ΔK of 22 MPa√m

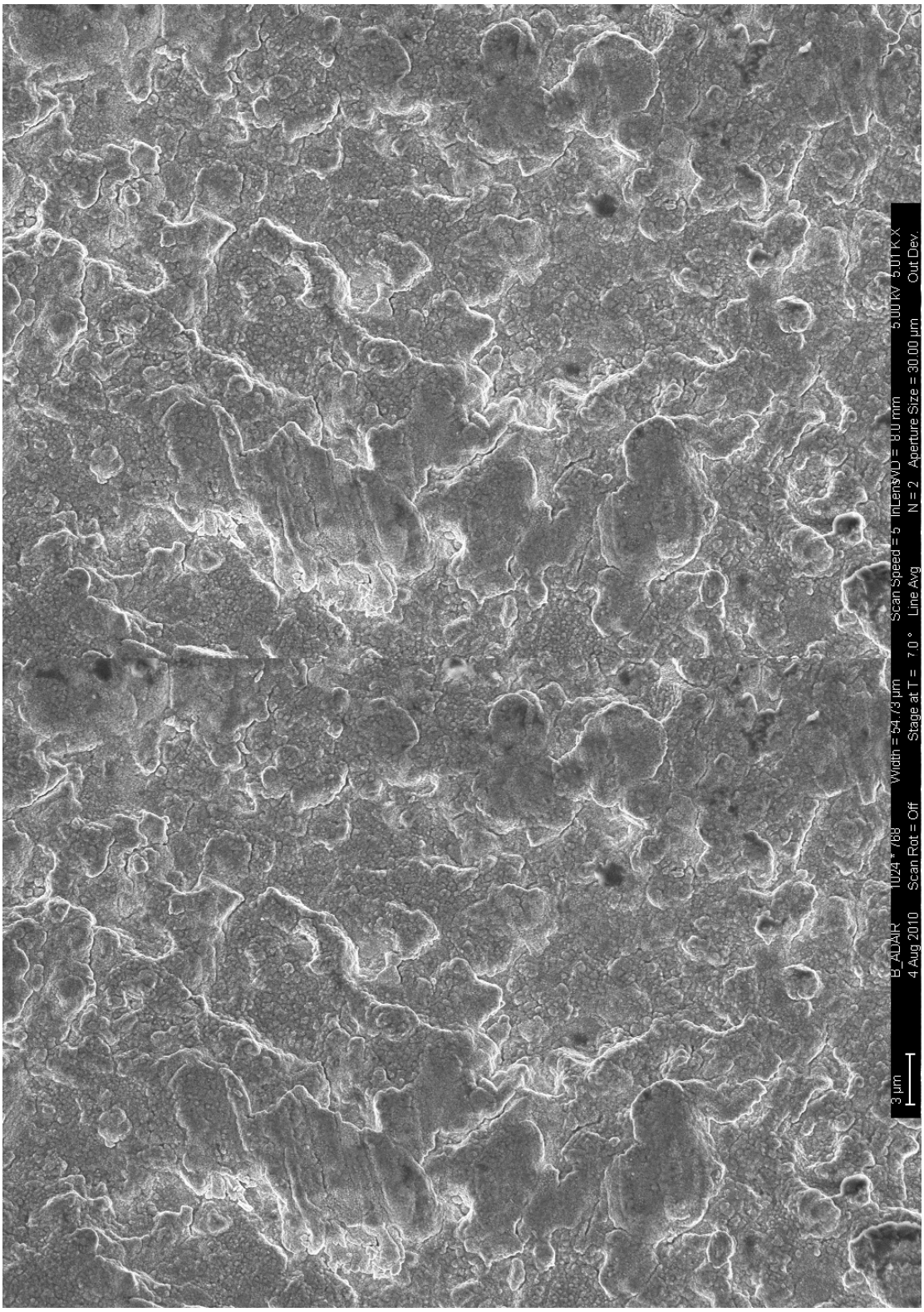

Figure A.2: 5000x SEM Stereo Pair Micrograph of IN100-6 tested at 649°C and 20 Hz at a ΔK of 33 MPa√m

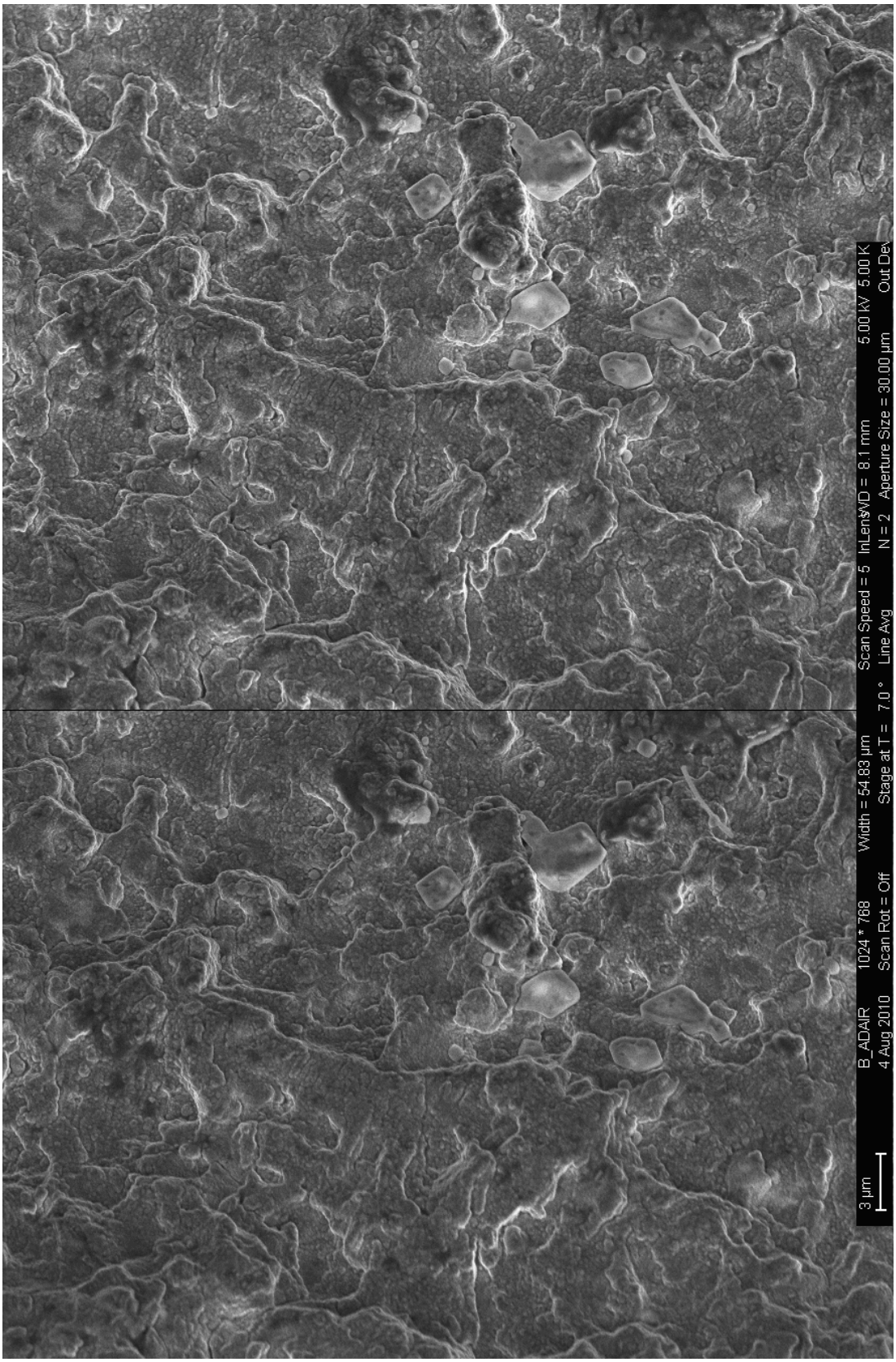

Figure A.3: 5000x SEM Stereo Pair Micrograph of IN100-6 tested at 649°C and 20 Hz at a ΔK of 44 MPa√m

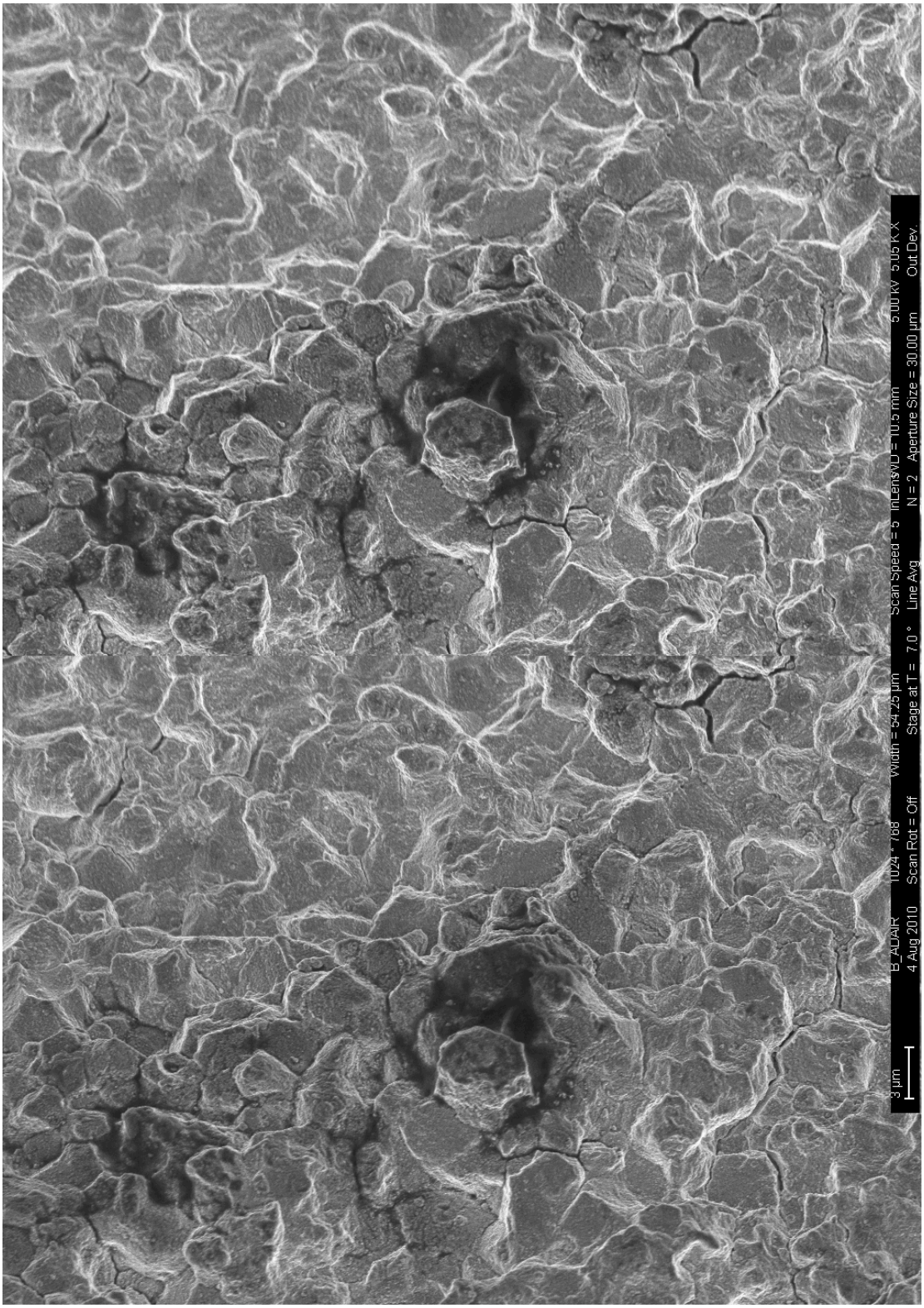

Figure A.4: 5000x SEM Stereo Pair Micrograph of IN100-10 tested at 649°C and 0.33 Hz at a ΔK of 22 MPa√m

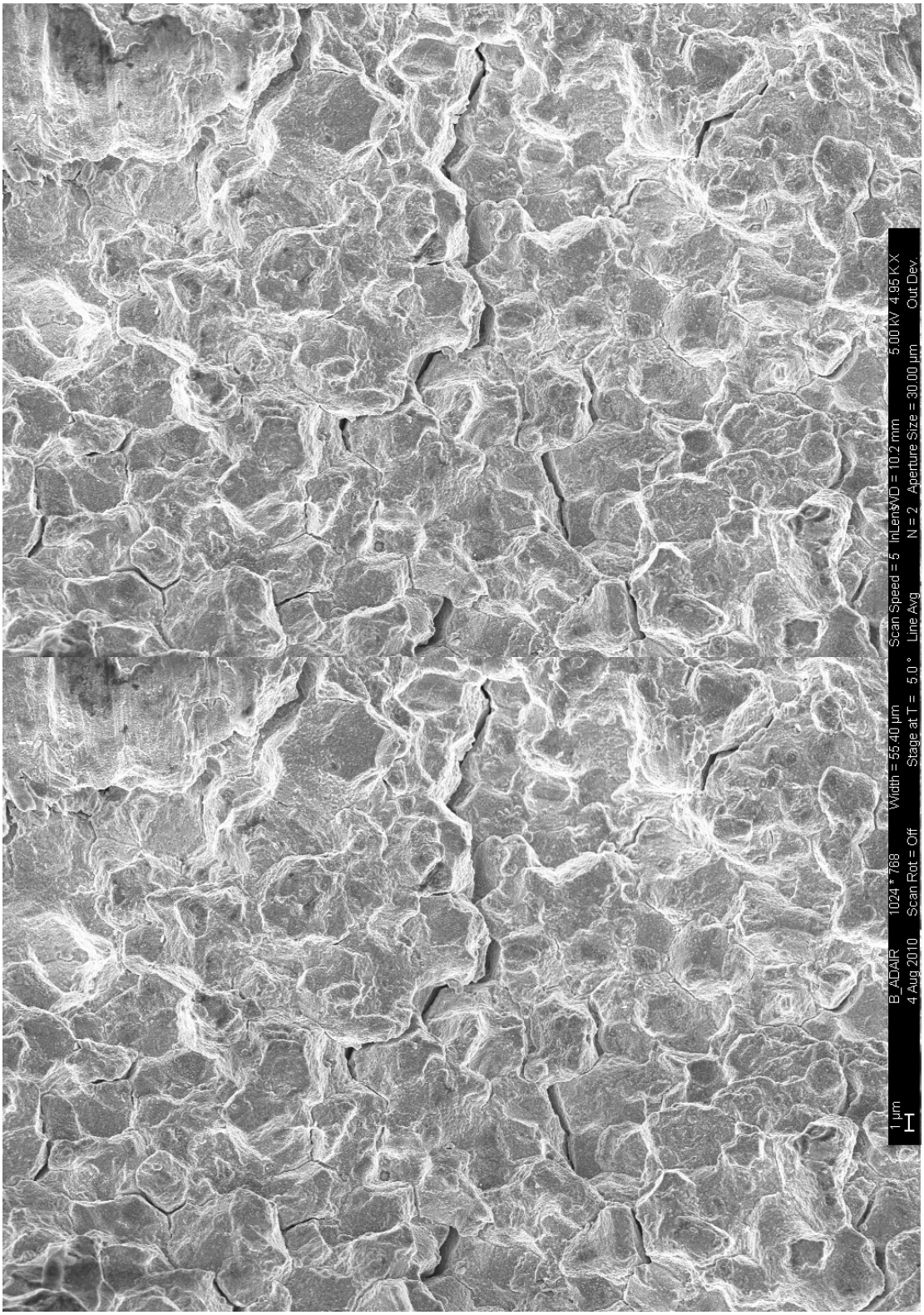

Figure A.5: 5000x SEM Stereo Pair Micrograph of IN100-10 tested at 649°C and 0.33 Hz at a ΔK of 33 MPa√m

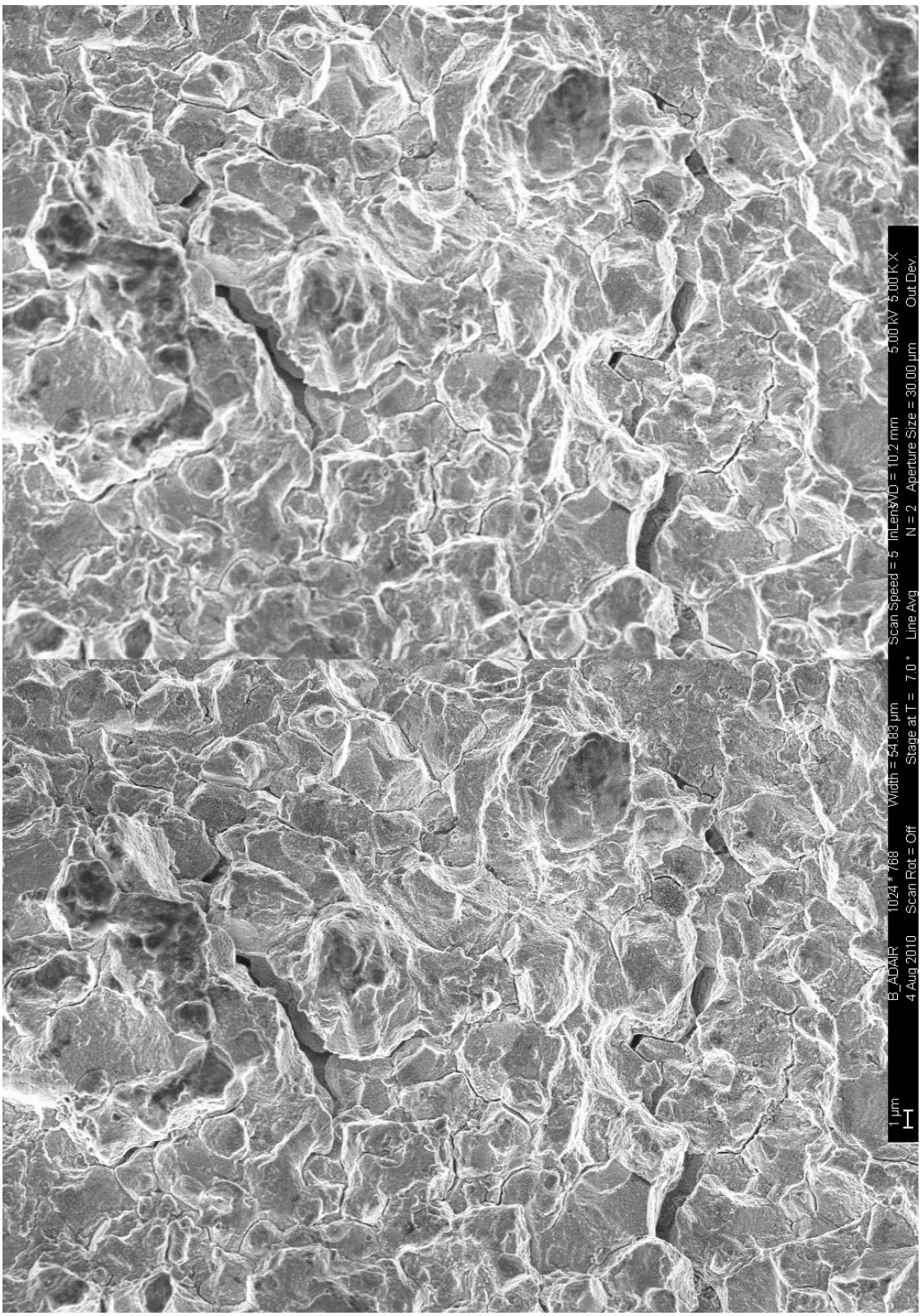

Figure A.6: 5000x SEM Stereo Pair Micrograph of IN100-10 tested at 649°C and 0.33 Hz at a ΔK of 44 MPa√m

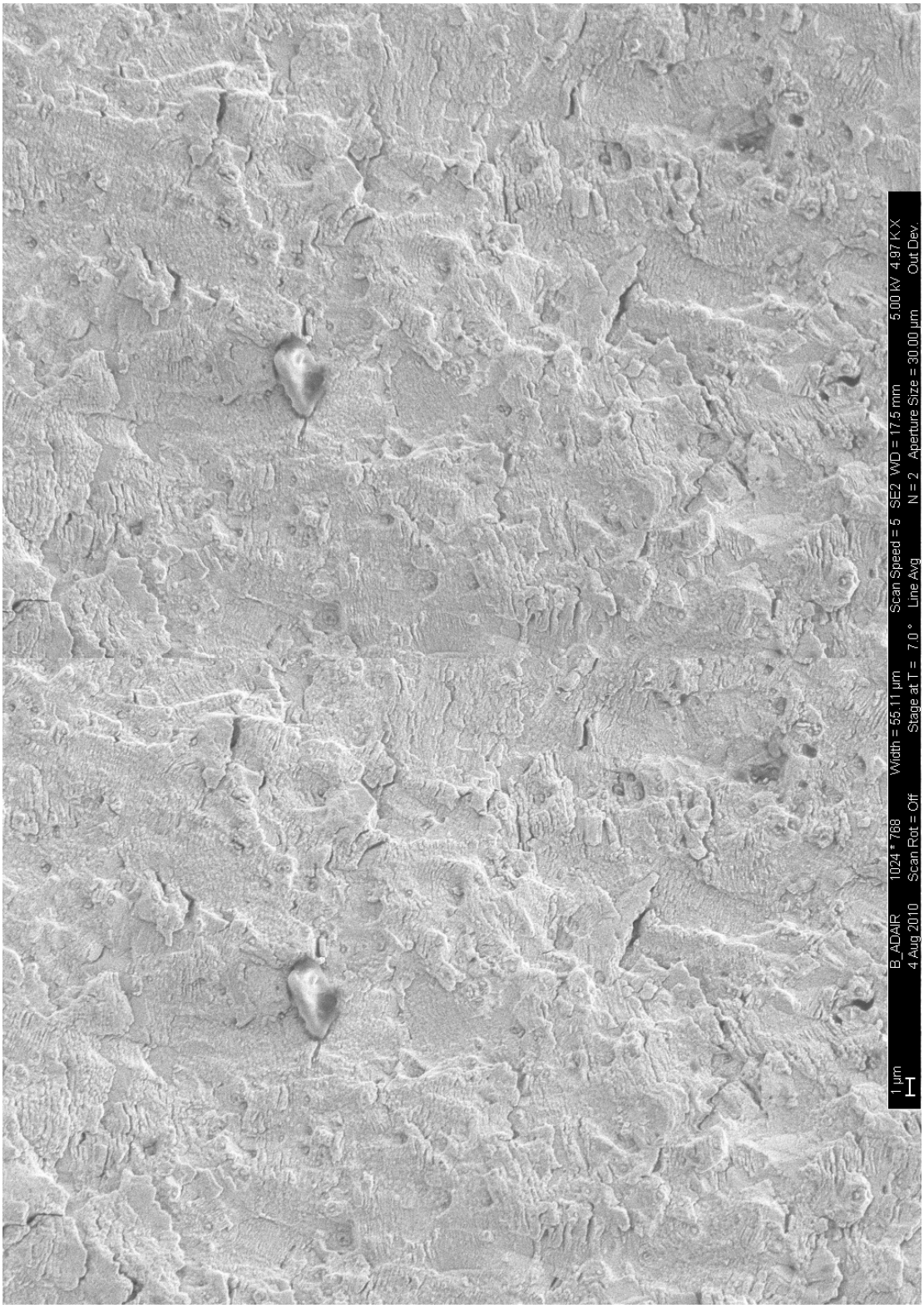

Figure A.7: 5000x SEM Stereo Pair Micrograph of IN100-1 tested at 316°C and 0.33 Hz at a ΔK of 22 MPa√m

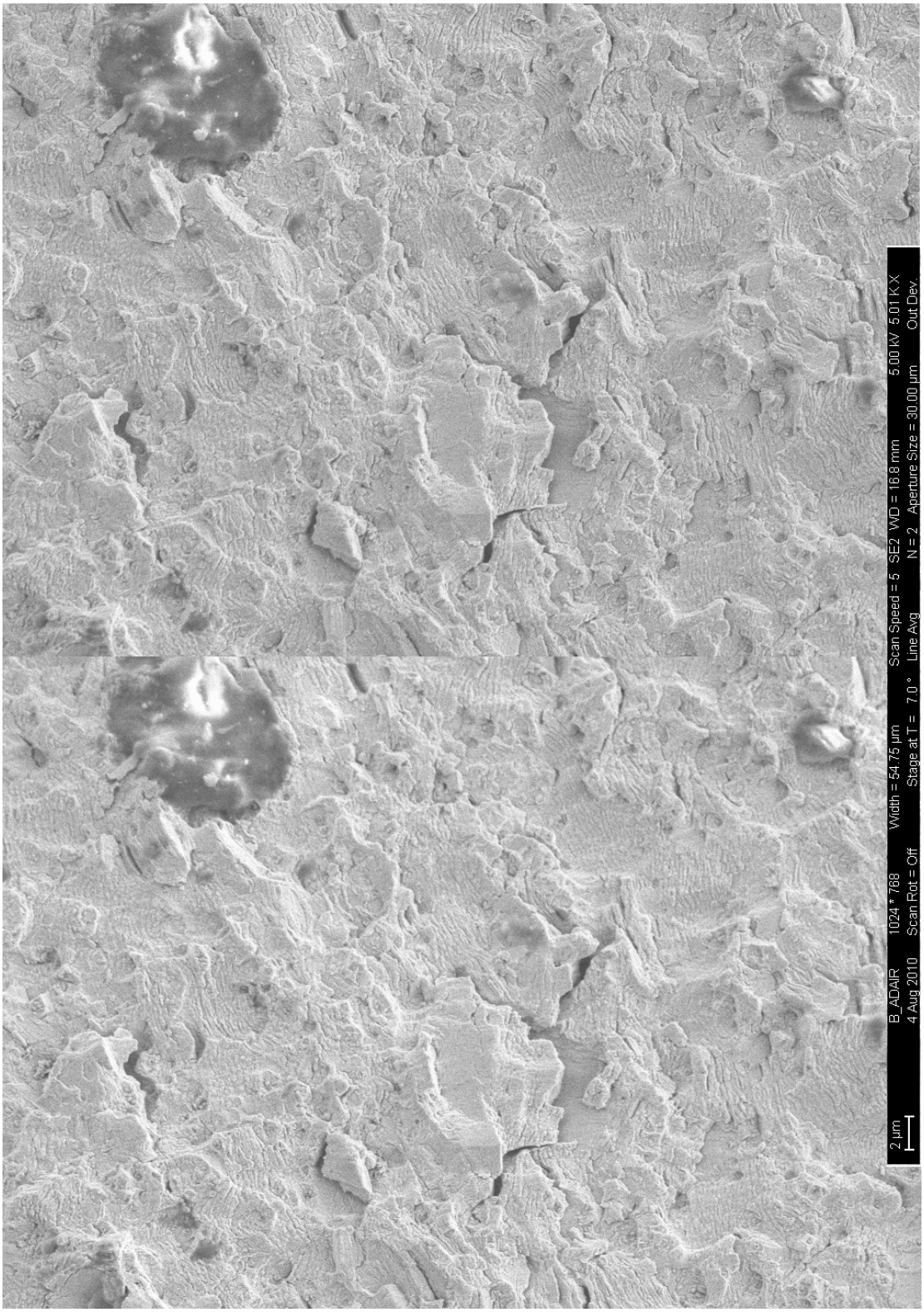

Figure A.8: 5000x SEM Stereo Pair Micrograph of IN100-1 tested at 316°C and 0.33 Hz at a ΔK of 33 MPa√m

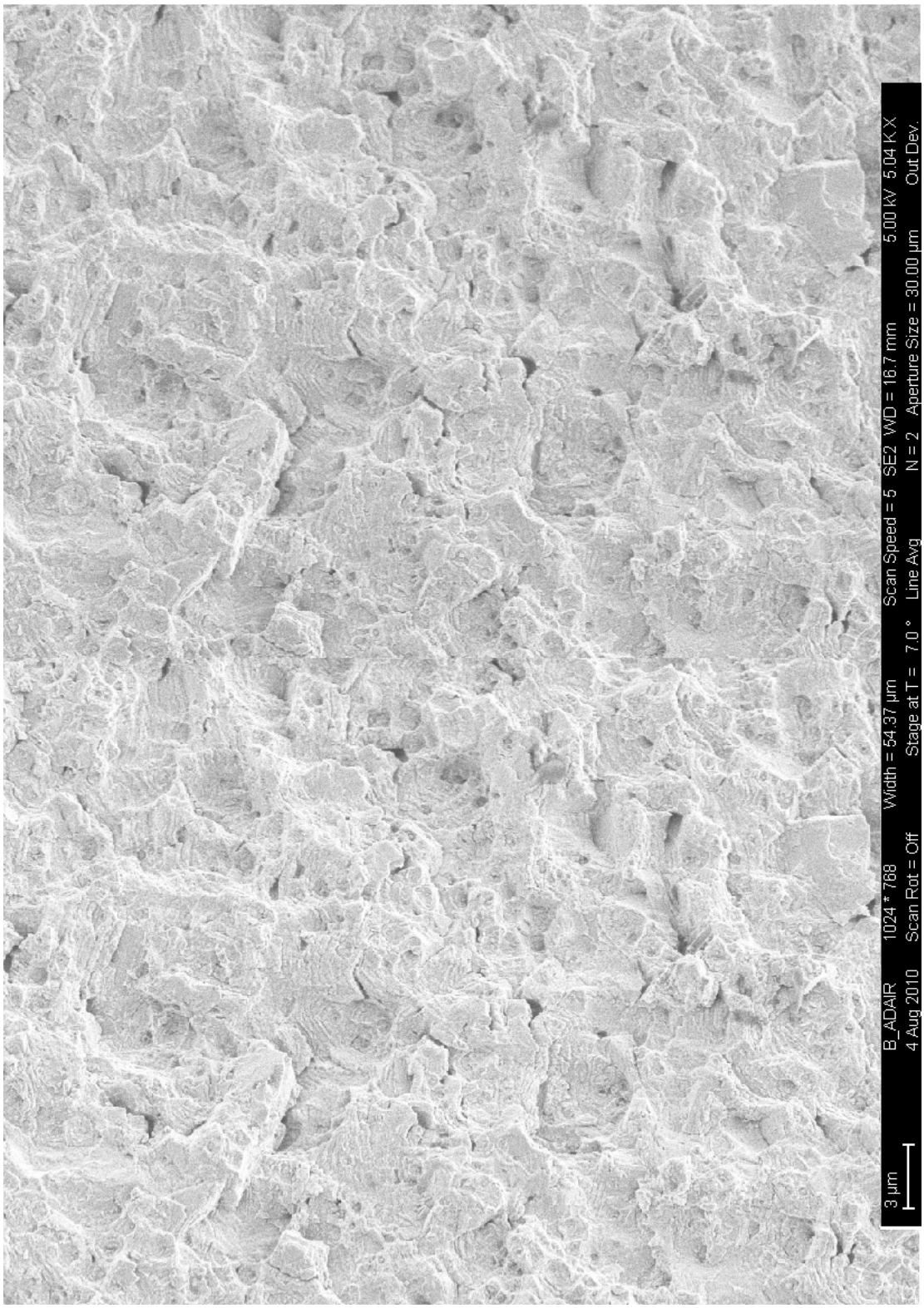

Figure A.9: 5000x SEM Stereo Pair Micrograph of IN100-1 tested at 316°C and 0.33 Hz at a ΔK of 44 MPa√m

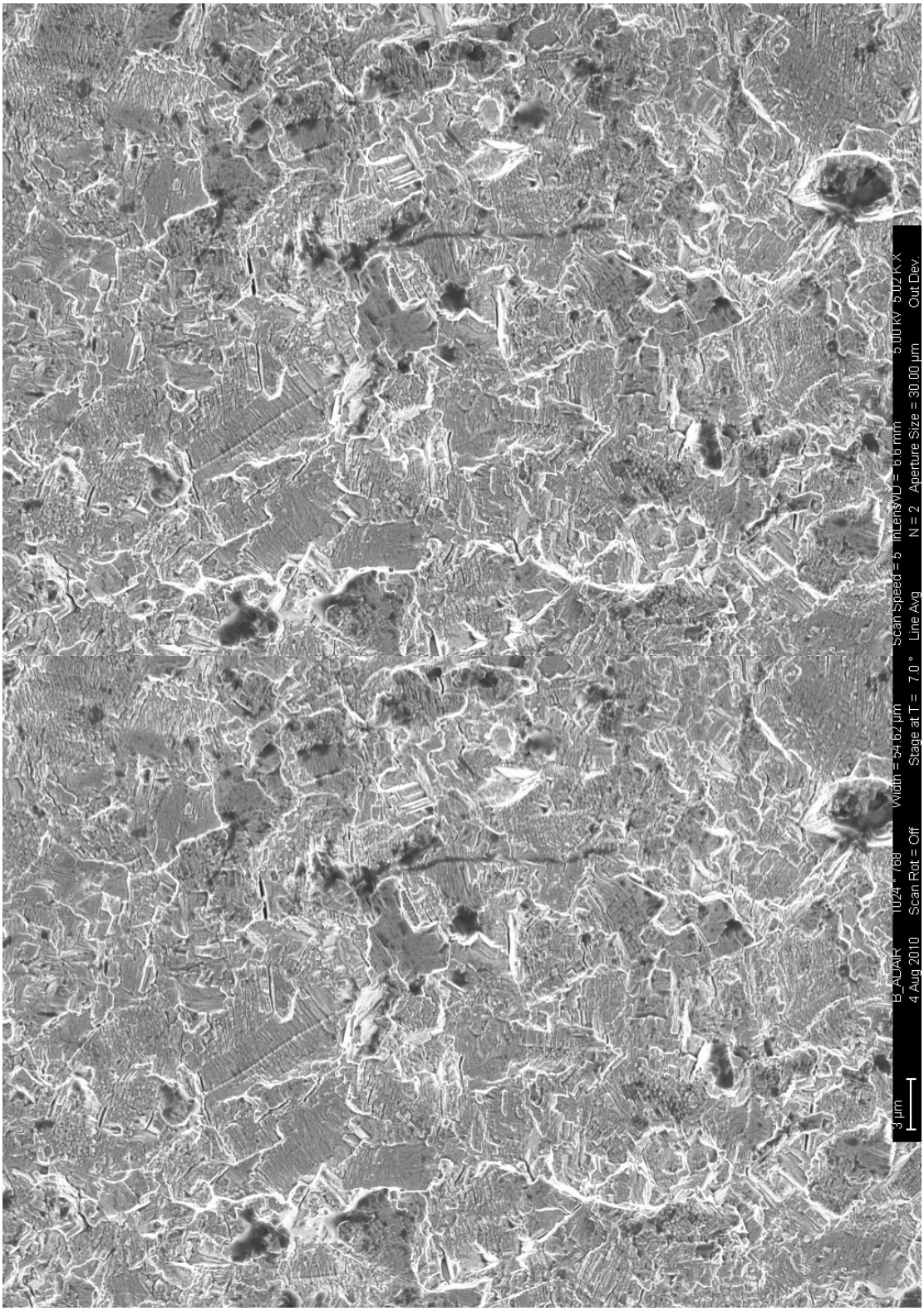

Figure A.10: 5000x SEM Stereo Pair Micrograph of IN100-8 tested at 22°C and 0.33 Hz at a ΔK of 22 MPa√m

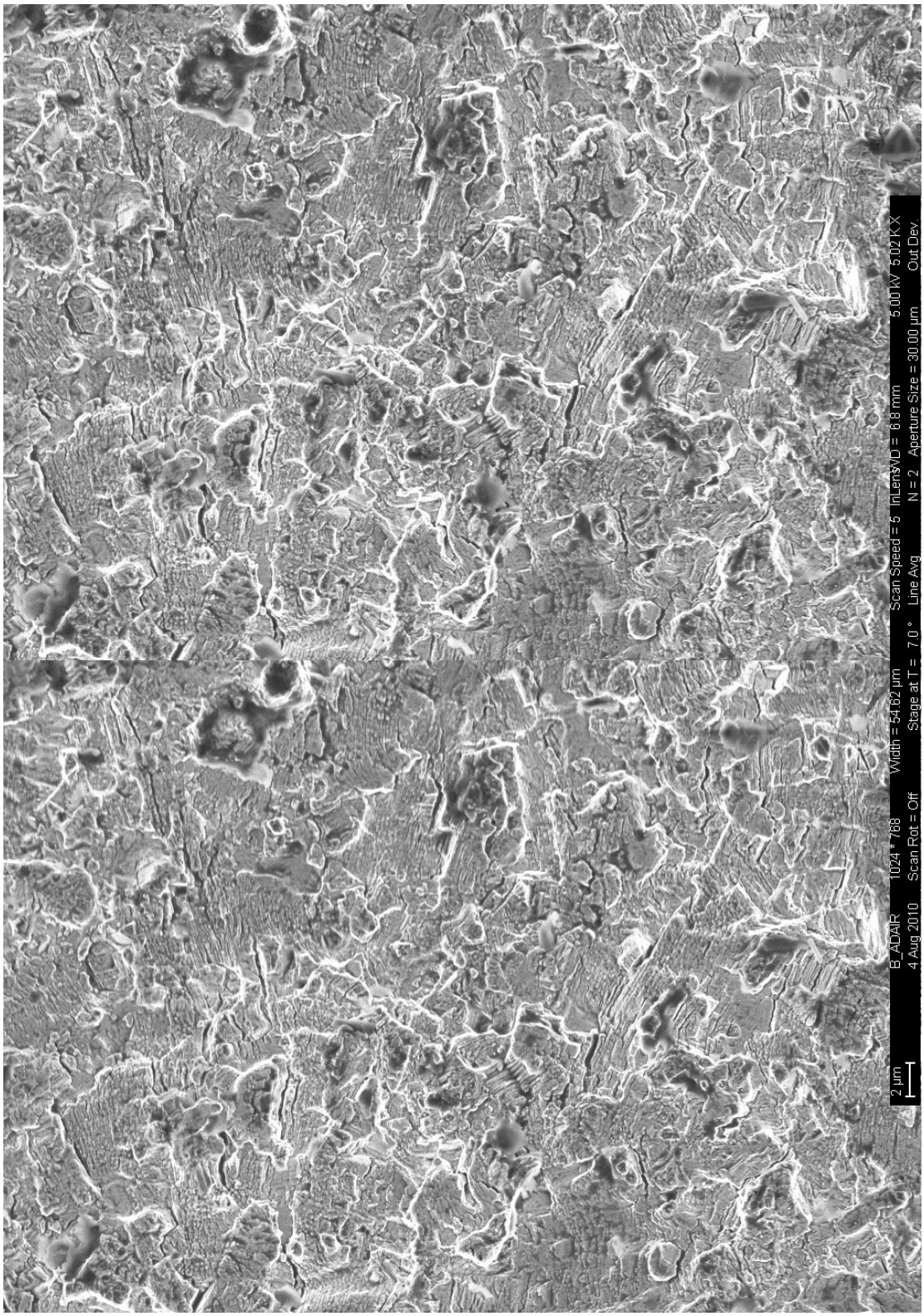

Figure A.11: 5000x SEM Stereo Pair Micrograph of IN100-8 tested at 22°C and 0.33 Hz at a ΔK of 33 MPa√m

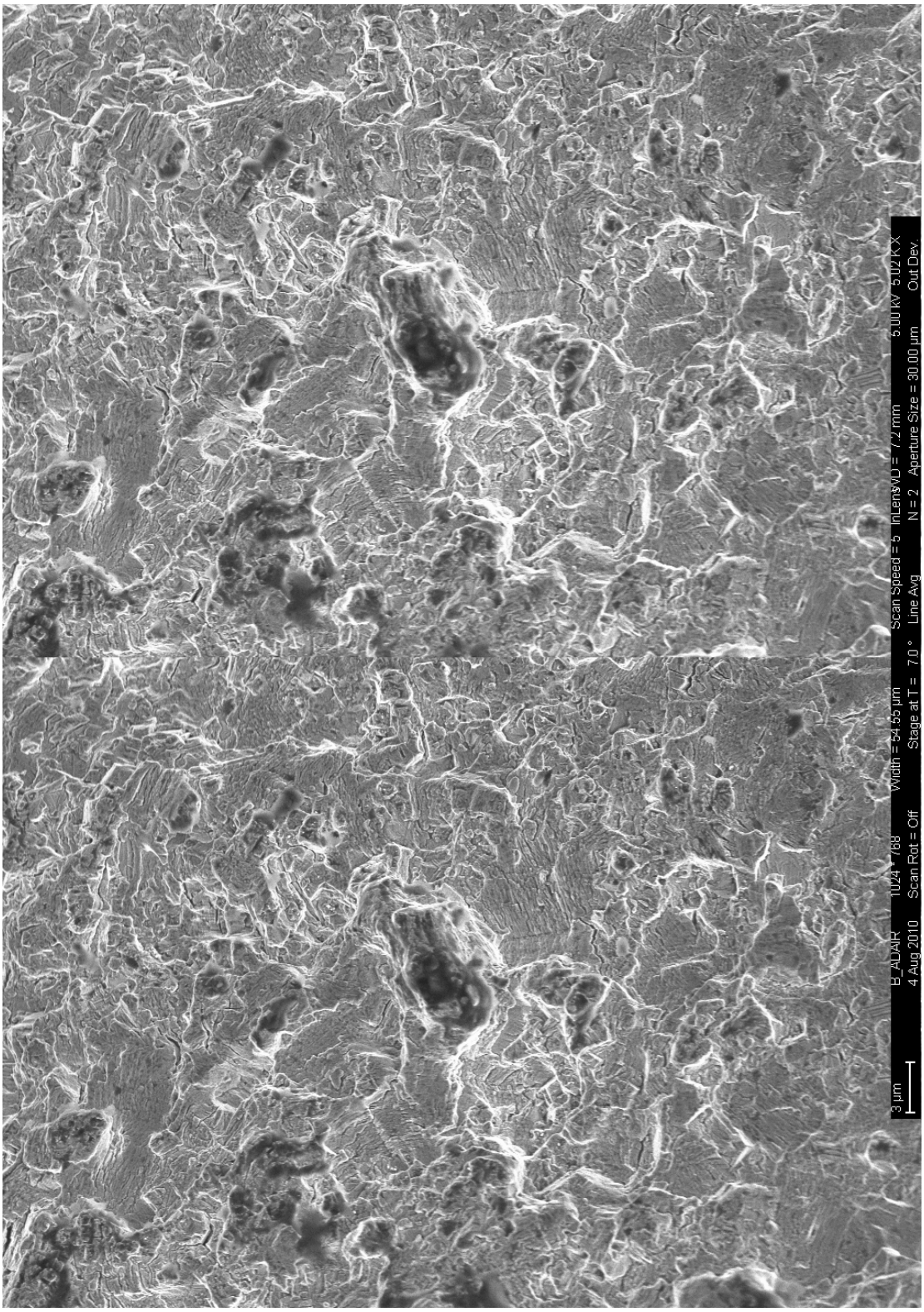

Figure A.12: 5000x SEM Stereo Pair Micrograph of IN100-8 tested at 22°C and 0.33 Hz at a ΔK of 44 MPa√m

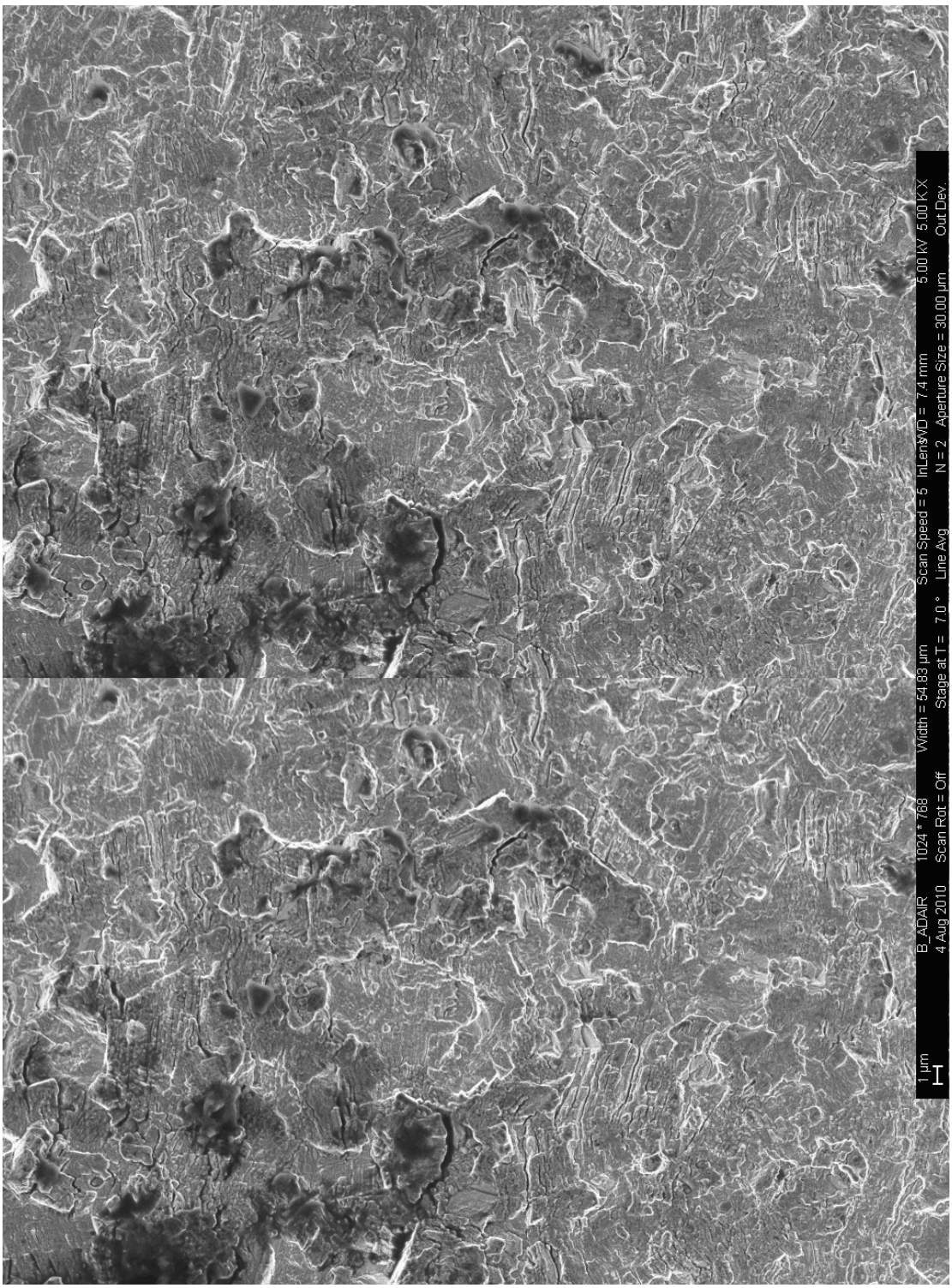

Figure A.13: 5000x SEM Stereo Pair Micrograph of IN100-2 tested at 22°C and 0.33 Hz at a ΔK of 26 MPa√m

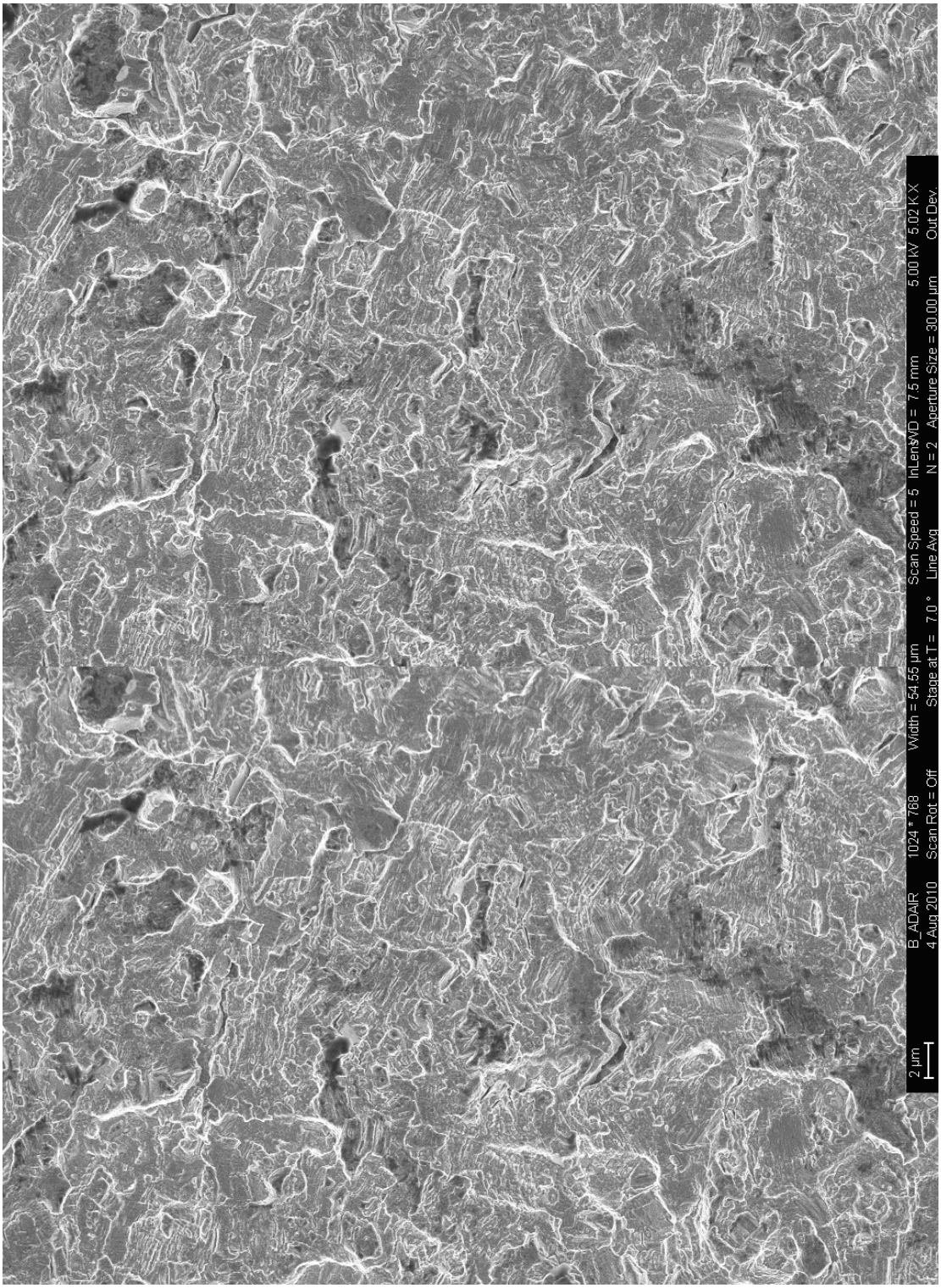

Figure A.14: 5000x SEM Stereo Pair Micrograph of IN100-2 tested at 22°C and 0.33 Hz at a ΔK of 32 MPa√m

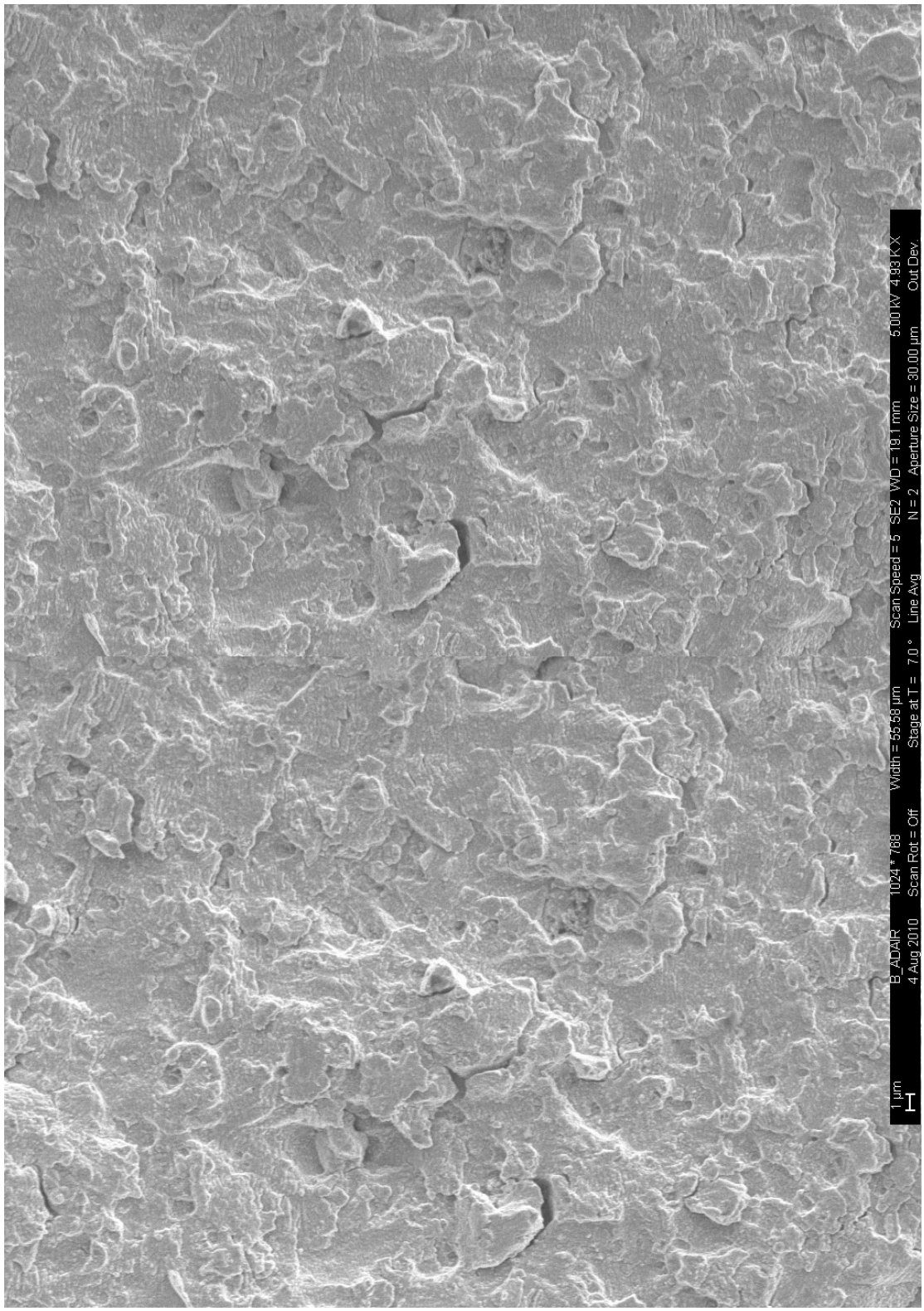

Figure A.15: 5000x SEM Stereo Pair Micrograph of IN100-3 tested at 482°C and 0.33 Hz at a ΔK of 22 MPa√m

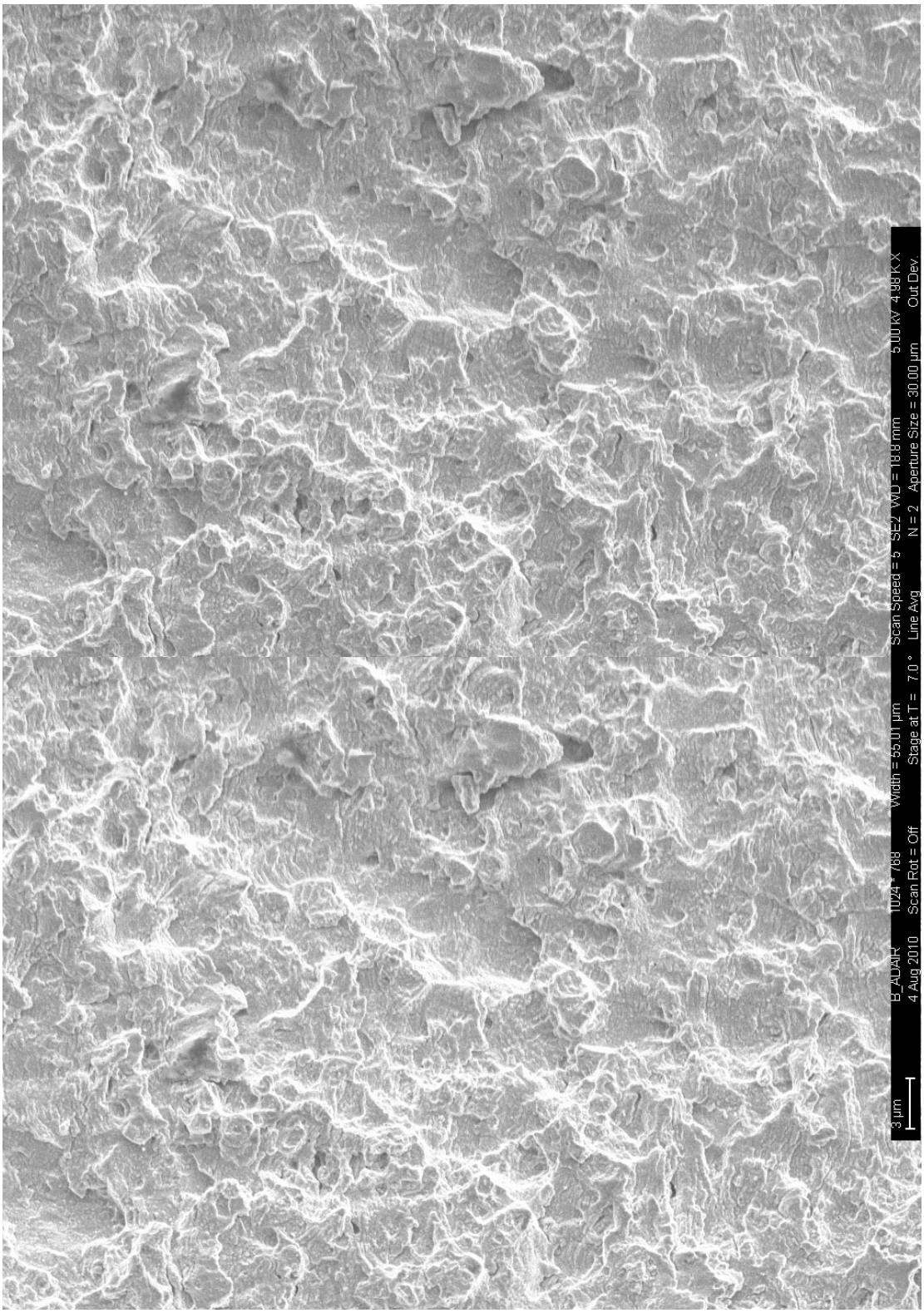

Figure A.16: 5000x SEM Stereo Pair Micrograph of IN100-3 tested at 482°C and 0.33 Hz at a ΔK of 33 MPa√m

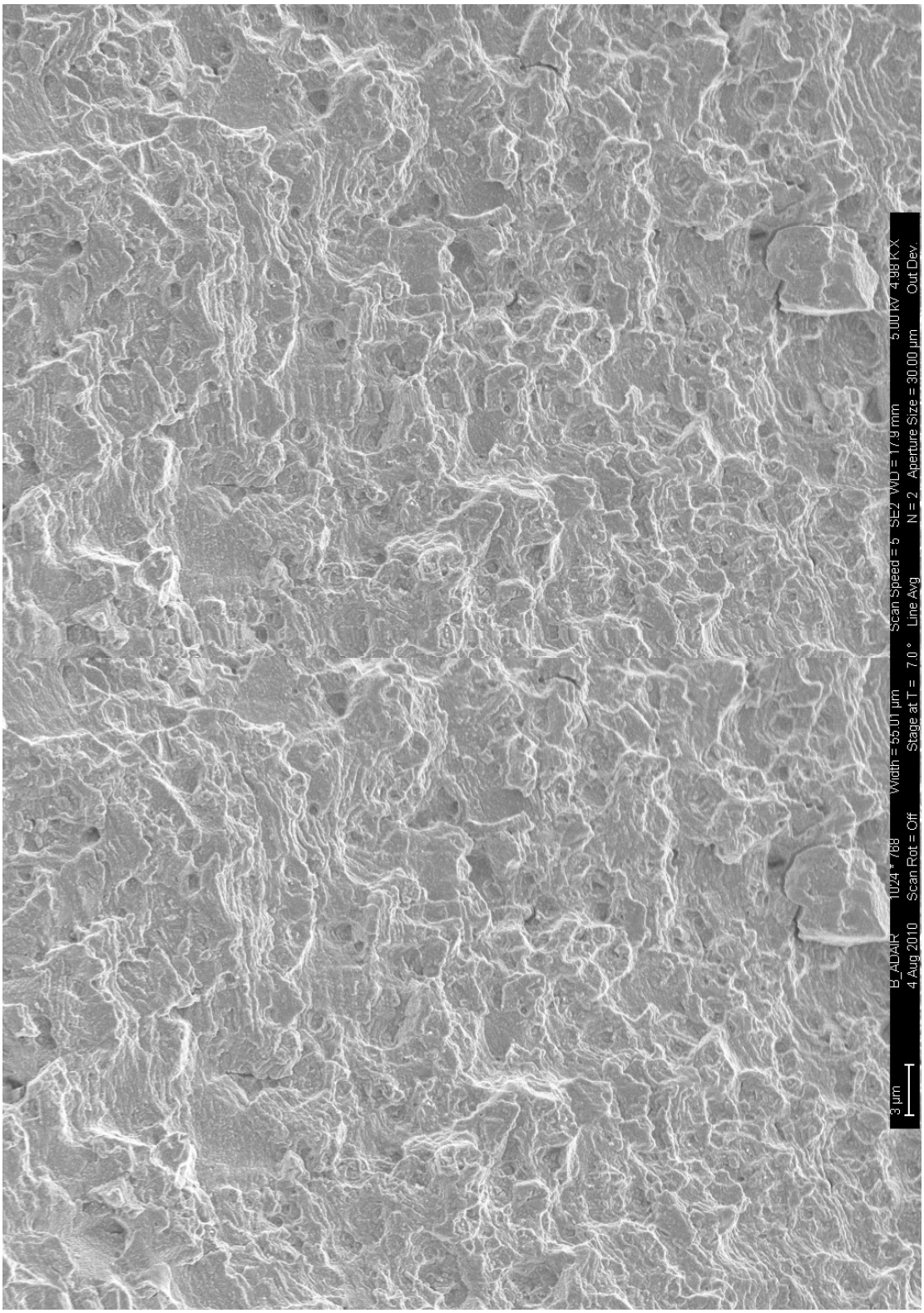

Figure A.17: 5000x SEM Stereo Pair Micrograph of IN100-3 tested at 482°C and 0.33 Hz at a ΔK of 44 MPa√m

A.7: Fatigue Fracture Surface Morphology Characteristics

Temperature	Frequency	
	0.33 Hz	**20 Hz**
22°C	Very transgranular fracture surface composed of fatigue striations and ductile rupture. Amount of ductile rupture and secondary cracking increases with increasing ΔK values. No intergranular fracture present.	No Test Data
316°C	Fracture surface is mostly transgranular in nature with a mix of fatigue striations and ductile rupture. As ΔK increases the amount of surface that failed by fatigue striations becomes more prevalent.	No Test Data
482°C	Considerable intergranular fracture surface and relatively less crystallographic fracture at low ΔK values. Slightly decreased intergranular fracture with small regions of fatigue striations and crystallographic fracture indicative of transgranular fracture at middle ΔK values. A mixture of intergranular fracture and transgranular fracture composed of crystallographic cracking with very small patches of fatigue striations at high ΔK values.	No Test Data
649°C	Fracture surface is very intergranular in nature. As ΔK increases the failure mechanism adds a very transgranular component. Grain boundary facet tearing normal to the crack growth direction becomes more prevalent as the stress intensity increases.	Fracture surface is very transgranular in nature. The surface is a mixture of fatigue striation patches and ductile rupture. As ΔK increases the fatigue striations become less and less prevalent while the amount of ductile rupture increases.

REFERENCES

1. *Airplane Flying Handbook.* U.S. Department of Transportation, Federal Aviation Administation - Flight Standards Service, 2004. **FAA-H-8083-3A**.

2. Blyth, N.R., *Examination of a Failed Cfm56-3c-1 Turbofan Engine - Boeing 737-476, Vh-Tjn.* Technical Analysis Report 3/01 (Reference BE/200000023) (Canberra, Australia: The Australian Transport Safety Bureau), 2001.

3. Rosenker, M.V., *Safety Recommendation, Ntsb Report on Los Angeles Engine Failure, Safety Recommendation.* 2006. **60-06 60-64**.

4. Suresh, S., *Fatigue of Materials*. 1998, Cambridge; New York: Cambridge University Press.

5. Schulz, U., C. Leyens, K. Fritscher, M. Peters, B. Saruhan-Brings, O. Lavigne, J.-M. Dorvaux, M. Poulain, R. Mevrel, and M. Caliez, *Some Recent Trends in Research and Technology of Advanced Thermal Barrier Coatings.* Aerospace Science and Technology, 2003. **7**(Compendex): p. 73-80.

6. Bondarenko, Y.A., E.N. Kablov, V.A. Surova, and A.B. Echin, *Effect of High-Gradient Directed Crystallization on the Structure and Properties of Rhenium-Bearing Single-Crystal Alloy.* Metal Science and Heat Treatment, 2006. **48**(Compendex): p. 360-363.

7. Sims, C.T., *Nickel Alloys. The Heart of Gas Turbine Engines.* 1970(Compendex).

8. Reed, R.C., *The Superalloys : Fundamentals and Applications*. 2008, Cambridge: Cambridge University Press. xv, 372 p.

9. Durand-Charre, M., *The Microstructure of Superalloys*. Other Information: Pbd: 1997. 1997. Medium: X; Size: 170 p.

10. Wusatowskasarnek, A., M. Blackburn, and M. Aindow, *Techniques for Microstructural Characterization of Powder-Processed Nickel-Based Superalloys.* Materials Science and Engineering A, 2003. **360**(1-2): p. 390-395.

11. Gessinger, G.H., *Recent Developments in Powder Metallurgy.* Metal Science Journal, 1974. **8**(Compendex): p. 394-396.

12. Sczerzenie, F. and G.E. Maurer, *Developments in Disc Materials.* Materials Science and Technology, 1986. **3**(Compendex): p. 733-742.

13. Moskowitz, L.N., R.M. Pelloux, and N.J. Grant, *Properties of in-100 Processed by Powder Metallurgy.* 1972(Compendex).

14. Nathal, M.V. *Nasa and Superalloys: A Customer, a Participant, and a Referee*. in *11th International Symposium on Superalloys, Superalloys 2008, September 14, 2008 - September 18, 2008*. 2008. Champion, PA, United states: Minerals, Metals and Materials Society.

15. Kear, B.H. and H.G.F. Wilsdorf, *Dislocation Configurations in Plastically Deformed Polycrystalline Cu3au Alloys.* Metallurgical Society of American Institute of Mining, Metallurgical and Petroleum Engineers -- Transactions, 1962. **224**(2): p. 382-386.

16. Bannantine, J., J. Comer, and J. Handrock, *Fundamentals of Metal Fatigue Analysis*. 1990: Prentice Hall.

17. Coffin, L.F.J., *A Study of the Effects of Cyclic Thermal Stresses on a Ductile Metal*, in *Other Information: Orig. Receipt Date: 31-DEC-53*. 1953. p. Medium: X; Size: Pages: 129.

18. Manson, S.S., *Behavior of Materials under Conditions of Thermal Stress*, in *Other Information: Orig. Receipt Date: 31-DEC-53*. 1953. p. Medium: X; Size: Pages: 105.

19. Romanoski, G.R., S.D. Antolovich, and R.M. Pelloux. *Model for Life Predictions of Nickel-Base Superalloys in High-Temperature Low Cycle Fatigue*. in *ASTM Spec Tech Publ 942, Low Cycle Fatigue, a Symp, September 30, 1987 - September 30, 1987*. 1987. Bolton Landing, NY, USA: ASTM.

20. Liaw, P.K., A. Saxena, and J. Perrin, *Life Extension Technology for Steam Pipe Systems-I. Development of Materials Properties.* Engineering Fracture Mechanics, 1993. **45**(Copyright 1993, IEE): p. 759-86.

21. Boyer, H.E., *Atlas of Fatigue Curves*. 1986. Medium: X; Size: Pages: 535.

22. Griffith, A.A., *The Phenomena of Rupture and Flow in Solids.* Philosophical Transactions of the Royal Society of London. Series A, Containing Papers of a Mathematical or Physical Character, 1921. **221**(582-593): p. 163-198.

23. Irwin, G.R., *Fracture Dynamics.* Fracturing of Metals, American Society for Metals, Cleveland, OH, 1948: p. 147-166.

24. Orowan, E., *Fracture and Strength of Solids.* Reports on Progress in Physics, 1949. **12**(1): p. 185.

25. Irwin, G.R., *Analysis of Stresses and Strains near the End of a Crack Traversing a Plate.* Journal of Applied Mechanics, 1957. **24**: p. 361-364.

26. Tada, H., *The Stress Analysis of Cracks Handbook*. 3rd ed. ed, ed. P.C. Paris and G.R. Irwin. 2000, New York :: ASME Press.

27. Anderson, T.L., *Fracture Mechanics : Fundamentals and Applications*. 3rd ed. ed. 2005, Boca Raton, FL :: Taylor & Francis.

28. Paris, P.C., M.P. Gomez, and W.E. Anderson, *A Rational Analytic Theory of Fatigue.* The Trend in Engineering, 1961. **1961**(13): p. 9-14.

29. Paris, P.C. and F. Erdogen, *A Critical Analysis of Crack Propagation La.* 1963(84.5): p. 528-534.

30. Walker, K., *The Effect of Stress Ratio During Crack Propagation and Fatigue for 2024-T3 and 7075-T6 Aluminum.* Effects of Environment and Complex Load History on Life, ASTM STP 462, American Society for Testing and Materials, 1970: p. 1.

31. Forman, R.G., V.E. Kearney, and R.M. Engle, *Numerical Analysis of Crack Propagation in Cyclic-Loaded Structures.* Transactions of the ASME. Series D, Journal of Basic Engineering, 1967. **89**(3): p. 459-464.

32. Beden, S.M., S. Abdullah, and A.K. Ariffin, *Review of Fatigue Crack Propagation Models for Metallic Components.* European Journal of Scientific Research, 2009. **28**(3): p. 364-397.

33. Preuss, M., J.Q. Da Fonseca, B. Grant, E. Knoche, R. Moat, and M. Daymond. *The Effect of ' Particle Size on the Deformation Mechanism in an Advanced Polycrystalline Nickel-Base Superalloy*. in *Superalloys 2008. Eleventh International Symposium on Superalloys, 14-18 Sept. 2008*. 2008. Warrendale, PA, USA: Minerals, Metals & Materials Society.

34. Wusatowska-Sarnek, A.M., M.J. Blackburn, and M. Aindow, *Γ' Precipitation Kinetics in P/M In100.* Materials Science Forum, 2003. **426-432**: p. 767-772.

35. Antolovich, S.D. and N. Jayaraman. *The Effect of Microstructure on the Fatigue Behavior of Ni Base Superalloys*. in *Fatigue. Environment and Temperature Effects. Proceedings of the 27th Sagamore Army Materials Research Conference, 14-18 July 1980*. 1983. New York, NY, USA: Plenum.

36. Antolovich, S.D. and N. Jayaraman, *Effects of Environment and Structural Stability on the Low Cycle Fatigue Behaviour of Nickel-Base Superalloys.* High Temperature Technology, 1984. **2**(Copyright 1984, IEE): p. 3-13.

37. Lerch, B.A., N. Jayaraman, and S.D. Antolovich, *A Study of Fatigue Damage Mechanisms in Waspaloy from 25 to 800c.* Material Science and Engineering, 1984. **66**(Copyright 1985, IEE): p. 151-66.

38. Bowman, R. and S.D. Antolovich, *Effect of Melt Spinning on the Microstructure and Mechanical Properties of Three Ni-Base Superalloys.* Metallurgical transactions. A, Physical metallurgy and materials science, 1988. **19 A**(Compendex): p. 93-103.

39. Boyd-Lee, A.D., *Fatigue Crack Growth Resistant Microstructures in Polycrystalline Ni-Base Superalloys for Aeroengines.* International Journal of Fatigue, 1999. **21**(Compendex): p. 393-405.

40. Gayda, J. and R.V. Miner, *Fatigue Crack Initiation and Propagation in Several Nickel-Base Superalloys at 650 Degree C.* International Journal of Fatigue, 1983. **5**(Compendex): p. 135-143.

41. Telesman, J., T.P. Gabb, A. Garg, P. Bonacuse, and J. Gayda. *Effect of Microstructure on Time Dependent Fatigue Crack Growth Behavior in a P/M Turbine Disk Alloy*. in *Superalloys 2008. Eleventh International Symposium on Superalloys, 14-18 Sept. 2008*. 2008. Warrendale, PA, USA: Minerals, Metals & Materials Society.

42. Gabb, T.P., J. Telesman, P.T. Kantzos, and A. Garg, *Effects of Temperature on Failure Modes for a Nickel-Base Disk Superalloy.* Journal of Failure Analysis and Prevention, 2007. **7**(1): p. 56-65.

43. Duhl, D.N., G. Maurer, S. Antolovich, C. Lund, and S. Reichman, *Superalloys 1988*. 1988. Medium: X; Size: Pages: (883 p).

44. Everitt, S., M.J. Starink, H.T. Pang, I.M. Wilcock, M.B. Henderson, and P.a.S. Reed, *A Comparison of High Temperature Fatigue Crack Propagation in Various Subsolvus Heat Treated Turbine Disc Alloys.* Materials Science and Technology, 2007. **23**(12): p. 1419-1423.

45. Caton, M.J. and A.H. Rosenberger. *Fatigue Crack Growth Variability in Waspaloy under Representative Loading Conditions*. in *Materials Damage Prognosis - a Symposium of the Materials Science and Technology 2004 Conference, September 26, 2004 - September 30, 2004*. 2005. New Orleans, LA, United states: Minerals, Metals and Materials Society.

46. Mall, S., H.K. Kim, W.J. Porter, J.F. Ownby, and A.G. Traylor, *High Temperature Fretting Fatigue Behavior of In100*. International Journal of Fatigue, 2010. **32**(8): p. 1289-1298.

47. Williams, J.C. and E.A. Starke, Jr., *Progress in Structural Materials for Aerospace Systems.* Acta Materialia, 2003. **51**(Copyright 2004, IEE): p. 5775-99.

48. Mourer, D.P. *Dual Heat Treat Process Development for Advanced Disk Applications*. in *Superalloys 2004. Proceedings of the Tenth International Symposium on Superalloys sponsored by the TMS Seven Springs International Symposium Committee, in Cooperation with the TMS High Temperature Alloys Committee and ASM International, 19-23 Sept. 2004*. 2004. Warrendale, PA, USA: TMS.

49. Larsen, J.M., A.H. Rosenberger, G.A. Hartman, S.M. Russ, and R. John, *The Role of Spectrum Loading in Damage-Tolerance Life-Management of Fracture Critical Turbine Engine Components.* 2003.

50. Pineau, A. and S.D. Antolovich, *High Temperature Fatigue of Nickel-Base Superalloys – a Review with Special Emphasis on Deformation Modes and Oxidation.* Engineering Failure Analysis, 2009. **16**(8): p. 2668-2697.

51. Reed, P.a.S., *Fatigue Crack Growth Mechanisms in Superalloys: Overview.* Materials Science and Technology, 2009. **25**(2): p. 258-270.

52. Liu, H.W. and Y. Oshida, *Grain Boundary Oxidation and Fatigue Crack Growth at Elevated Temperatures.* Theoretical and Applied Fracture Mechanics, 1986. **6**(2): p. 85-94.

53. Wei, R.P., C. Miller, Z. Huang, G.W. Simmons, and D.G. Harlow, *Oxygen Enhanced Crack Growth in Nickel-Based Superalloys and Materials Damage Prognosis.* Engineering Fracture Mechanics, 2009. **76**(5): p. 715-727.

54. Debussac, A. and S. Antolovich, *The Effects of Microstructure and Environment on the Fatigue Crack Propagation Behaviour of a Ni-Base Alloy.* Fatigue 2006, 2006.

55. Hancock, P., *The Influence of Environment on the Fatigue Behaviour of Superalloy Components at High Temperatures.* Corrosion Science, 1989. **29**(6): p. 657-671.

56. Hoffelner, W. *Effects of Environment on Crack Growth Behaviour of Superalloys under Various Loading Conditions*. in *Mechanical Behaviour of Superalloys, 10-11 June 1986*. 1987. UK.

57. Andrieu, E., R. Molins, H. Ghonem, and A. Pineau, *Intergranular Crack Tip Oxidation Mechanism in a Nickel-Based Superalloy.* Materials Science and Engineering A, 1992. **A154**(Compendex): p. 21-28.

58. Mercer, C., S. Shademan, and W.O. Soboyejo, *An Investigation of the Micromechanisms of Fatigue Crack Growth in Structural Gas Turbine Engine Alloys.* Journal of Materials Science, 2003. **38**(Compendex): p. 291-305.

59. Krueger, D.D., R.D. Kissinger, and R.G. Menzies. *Development and Introduction of a Damage Tolerant High Temperature Nickel-Base Disk Alloy, Rene88dt*. in *Proceedings of the Seventh International Symposium on Superalloys 1992, Sep 20 - 24 1992*. 1992. Champion, PA, USA: Publ by Minerals, Metals & Materials Soc (TMS).

60. Lawless, B.H. and A.W. Dix. *Effect of Processing/Microstructure on the Threshold Fatigue Crack Growth Behavior of Alloy 718 Forging*. in

SUPERALLOYS 718, 625, 706 and Various Derivatives, Jun 17 - 20 2001. 2001. Pittsburgh, PA, United states: Minerals, Metals and Materials Society.

61. Floreen, S. and R. Raj. *Environmental Effects in Nickel-Base Alloys*. in *Flow and Fracture at Elevated Temperatures, Papers Presented at the 1983 ASM Materials Science Seminar.* 1985. Philadelphia, PA, USA: ASM.

62. Zhang, C.-H., K.-X. Zhang, X.-S. Zhao, Q. Wang, and S. Zhang, *Isothermal Oxidation Behavior and Mechanisms of a Cast Ni-Base Superalloy K452.* Dongbei Daxue Xuebao/Journal of Northeastern University, 2010. **31**(Compendex): p. 181-184.

63. Starink, M. and P. Reed, *Thermal Activation of Fatigue Crack Growth: Analysing the Mechanisms of Fatigue Crack Propagation in Superalloys.* Materials Science and Engineering: A, 2008. **491**(1-2): p. 279-289.

64. *Scanning Electron Microscopy and X-Ray Microanalysis*. 3rd ed. ed, ed. J. Goldstein. 2003, New York :: Kluwer Academic/Plenum Publishers.

65. Woodruff, D.P., T.A. Delchar, and W. Plummer, *Modern Techniques of Surface Science.* Physics Today, 1995. **48**(9): p. 96-97.

66. Liu, C.T., J. Ma, and X.F. Sun, *Oxidation Behavior of a Single-Crystal Ni-Base Superalloy between 900 and 1000 C in Air.* Journal of Alloys and Compounds, 2010. **491**(Compendex): p. 522-526.

67. Cho, S., J. Hur, C. Seo, J. Yoon, and S. Park, *Hot Corrosion Behavior of Ni-Base Alloys in a Molten Salt under an Oxidizing Atmosphere.* Journal of Alloys and Compounds, 2009. **468**(1-2): p. 263-269.

68. Das, D.K., V. Singh, and S.V. Joshi, *High Temperature Oxidation Behaviour of Directionally Solidified Nickel Base Superalloy Cm–247lc.* Materials Science and Technology, 2003. **19**(6): p. 695-708.

69. Pfennig, A. and A. Kranzmann. *Oxidation of a Single Crystal Nickel-Base Superalloy at 950 C - a Kinetic and Microstructure Study*. in *Corrosion 2008, March 16, 2008 - March 20, 2008*. 2008. New Orleans, LO, United states: National Assoc. of Corrosion Engineers International.

70. Floreen, S. and R. Kane, *Effects of Environment on High-Temperature Fatigue Crack Growth in a Superalloy.* Metallurgical and Materials Transactions A, 1979. **10**(11): p. 1745-1751.

71. Boyd-Lee, A.D., G.F. Harrison, and M.B. Henderson, *Evaluation of Standard Life Assessment Procedures and Life Extension Methodologies for Fracture-Critical Components.* International Journal of Fatigue, 2001. **23**(Compendex): p. S11-S19.

72. Goswami, T.K. and G.F. Harrison, *Gas-Turbine Disk Lifting Philosophies - a Review.* International Journal of Turbo & Jet-Engines, 1995. **12**(1): p. 59-77.

73. Claudio, R.A., C.M. Branco, E.C. Gomes, J. Byrne, G.F. Harrison, and M.R. Winstone, *Fatigue Life Prediction and Failure Analysis of a Gas Turbine Disc Using the Finite-Element Method.* Fatigue and Fracture of Engineering Materials and Structures, 2004. **27**(Compendex): p. 849-860.

74. Cowie, W.D., *Turbine Engine Structural Integrity Program (Ensip).* Journal of Aircraft, 1975. **12**(Compendex): p. 366-369.

75. Johnson, W.S., *The History, Logic and Uses of the Equivalent Initial Flaw Size Approach to Total Fatigue Life Prediction.* Procedia Engineering, 2010. **2**(1): p. 47-58.

76. Wusatowska-Sarnek, A.M., G. Ghosh, G.B. Olson, M.J. Blackburn, and M. Aindow, *Characterization of the Microstructure and Phase Equilibria Calculations for the Powder Metallurgy Superalloy In100.* Journal of Materials Research, 2003. **18**(Compendex): p. 2653-2663.

77. Nissley, D.M., *Thermomechanical Fatigue Life Prediction in Gas Turbine Superalloys: A Fracture Mechanics Approach.* Journal Name: AIAA Journal; Journal Volume: 33; Journal Issue: 6; Other Information: PBD: Jun 1995, 1995: p. Medium: X; Size: pp. 1114-1120.

78. *Standard Test Method for Measurement of Fatigue Crack Growth Rate.* ASTM Standard E647, 2008.

79. *Standard Test Method for Linear-Elastic Plane-Strain Fracture Toughness Kic of Metallic Materials.* ASTM Standard E399, 2006.

80. Small, K.B., D.A. Englehart, and T.A. Christman, *Guide to Etching Specialty Alloys.* Advanced Materials and Processes, 2008. **166**(Compendex): p. 32-37.

81. Song, K. and M. Aindow, *A Hybrid Replication Technique for the Analysis of Precipitate-Boundary Interactions in Ni-Based Superalloys.* Journal of Materials Science, 2005. **40**(Compendex): p. 3403-3407.

82. Milligan, W.W., E.L. Orth, J.J. Schirra, and M.F. Savage. *Effects of Microstructure on the High Temperature Constitutive Behavior of In100*. in *SUPERALLOYS 2004 - Tenth International Symposium on Superalloys, September 19, 2004 - September 23, 2004*. 2004. Champion, PA, United states: Minerals, Metals and Materials Society.

83. Jha, S.K., M.J. Caton, and J.M. Larsen. *Mean Vs. Life-Limiting Fatigue Behavior of a Nickel-Based Superalloy*. in *11th International Symposium on Superalloys, Superalloys 2008, September 14, 2008 - September 18, 2008*. 2008. Champion, PA, United states: Minerals, Metals and Materials Society.

84. Wu, Newman, Zhao, Swain, Ding, and Phillips, *Small Crack Growth and Fatigue Life Predictions for High-Strength Aluminium Alloys: Part I—Experimental and Fracture Mechanics Analysis.* Fatigue & Fracture of Engineering Materials & Structures, 1998. **21**(11): p. 1289-1306.

85. Tan, P.W., I.S. Raju, and J.C. Newman, Jr., *Boundary Force Method for Analyzing Two-Dimensional Cracked Bodies.* Fracture Mechanics: Eighteenth Symposium. ASTM STP 945, 1988: p. 259-277.

86. Telesman, J. and L.J. Ghosn. *Fatigue Crack Growth Behavior of Pwa 1484 Single Crystal Superalloy at Elevated Temperatures*. in *Proceedings of the International Gas Turbine and Aeroengine Congress and Exposition, June 5, 1995 - June 8, 1995*. 1995. Houston, TX, USA: ASME.

87. Blatt, D., R. John, and D. Coker, *Stress Intensity Factor and Compliance Solutions for a Single Edge Notched Specimen with Clamped Ends.* Engineering Fracture Mechanics, 1994. **47**(4): p. 521-532.

88. John, R. and B. Rigling, *Effect of Height to Width Ratio on K and Cmod Solutions for a Single Edge Cracked Geometry with Clamped Ends.* Engineering Fracture Mechanics, 1998. **60**(2): p. 147-156.

89. Jones, I., *A Wide Range Weight Function for a Single Edge Cracked Geometry with Clamped Ends.* International Journal of Fracture, 1998. **89**(1): p. 1-18.

90. Mattoni, M. and F. Zok, *A Method for Determining the Stress Intensity Factor of a Single Edge-Notched Tensile Specimen.* International Journal of Fracture, 2003. **119**(1): p. L3-L8.

91. Tong, J., S. Dalby, J. Byrne, M.B. Henderson, and M.C. Hardy, *Creep, Fatigue and Oxidation in Crack Growth in Advanced Nickel Base Superalloys.* International Journal of Fatigue, 2001. **23**(Compendex): p. 897-902.

92. Pineau, A. *Intergranular Creep-Fatigue Crack Growth in Ni-Base Alloys*. in *Flow and Fracture at Elevated Temperatures, Papers Presented at the 1983 ASM Materials Science Seminar.* 1985. Philadelphia, PA, USA: ASM.

93. Nicholas, T. and T. Weerasooriya. *Hold-Time Effects in Elevated Temperature Fatigue Crack Propagation*. in *Fracture Mechanics: Seventeenth Volume, Seventeenth National Symposium on Fracture Mechanics.* 1986. Albany, NY, USA: ASTM.

94. Skinn, D.A., J.P. Gallagher, A.P. Berens, P.D. Huber, J. Smith, and I. Dayton Univ Oh Research. *Damage Tolerant Design Handbook. Volume 2. Chapter 5*. 1994; Available from: http://handle.dtic.mil/100.2/ADA311690.

95. Miller, M.P., D.L. Mcdowell, and R.L.T. Oehmke, *Creep-Fatigue-Oxidation Microcrack Propagation Model for Thermomechanical Fatigue.* Journal of

Engineering Materials and Technology, Transactions of the ASME, 1992. **114**(Compendex): p. 282-288.

96. Christ, H.-J., R. Teteruk, A. Jung, and H.J. Maier. *Using Fracture Mechanics Concepts for a Mechanism-Based Prediction of Thermomechanical Fatigue Life*. in *hermomechanical Fatigue Behavior of Materials: 4th Volume, November 7, 2001 - November 8, 2001*. 2003. Dallas, TX, United states: American Society for Testing and Materials.

97. Tang, N.Y. and A. Plumtree, *Fatigue-Creep-Environmental Interaction. A Kinetic Approach.* Materials Science and Engineering A, 1991. **A141**(Compendex): p. 55-61.

98. Wagner, C., *Diffusion and High Temperature Oxidation of Metals in Atom Movements.* Cleveland, OH: American Society of Metals., 1951.

99. Reuchet, J. and L. Remy, *Fatigue Oxidation Interaction in a Superalloy - Application to Life Prediction in High Temperature Low Cycle Fatigue.* Metallurgical transactions. A, Physical metallurgy and materials science, 1983. **14 A**(Compendex): p. 141-149.

100. Matsunaga, S. and T. Homma, *Influence on the Oxidation Kinetics of Metals by Control of the Structure of Oxide Scales.* Oxidation of Metals, 1976. **10**(Compendex): p. 361-376.

101. Antolovich, S.D., Baur, R., Liu, S., *A Mechanistically Based Model for High Temperature Lcf of Ni Base Superalloys.* Superalloys 1980, 1980: p. 605-613.

102. Boismier, D.A. and H. Sehitoglu, *Thermo-Mechanical Fatigue of Mar-M247. Part 1. Experiments.* Journal of Engineering Materials and Technology, Transactions of the ASME, 1990. **112**(Compendex): p. 68-79.

103. Antolovich, S.D., A. Saxena, and G.R. Chanani, *Model for Fatigue Crack Propagation.* Engineering Fracture Mechanics, 1975. **7**(Compendex): p. 649-652.

104. Woodworth, B., *Development of a Thermo-Mechanical Fatigue Test Apparatus with Crack Growth Monitoring Capability.* 2009: p. 110.